Uncooled unipolar receivers for 9 μm wavelength heterodyne detection

Azzurra Bigioli

UNIVERSITÉ DE PARIS

École Doctorale: Physique en Ile de France **ED564**

Laboratoire de Physique de l'École Normale Supérieure

Uncooled unipolar receivers for 9 μm wavelength heterodyne detection

présentée par

Azzurra BIGIOLI

Thèse de doctorat de physique

Présentée et soutenue publiquement le 2 Février 2021

Devant un jury composé de:

Pr. Jaime GÓMEZ RIVAS	Eindhoven University of Technology	*Rapporteur*
PD Dr. Harald SCHNEIDER	Helmholtz-Zentrum Dresden-Rossendorf	*Rapporteur*
Dr. Agnès DOLFI-BOUTEYRE	ONERA	*Examinatrice*
Dr. Jean-Philippe BERGER	IPAG	*Examinateur*
Pr. Giuseppe LEO	Université de Paris	*Président*
Pr. Angela VASANELLI	Université de Paris	*Invitée*
Pr. Carlo SIRTORI	École Normale Supérieure	*Directeur de thèse*

Abstract

The work of my PhD thesis focuses on the conception and realization of a sensitive detection set-up at 9 µm wavelength, where all components are uncooled semiconductor devices. The project is realized by exploiting two major advances: a metamaterial-enhanced detector and a heterodyne scheme with quantum cascade lasers. The investigated detectors are quantum cascade (QCD) and quantum well detectors (QWIP), unipolar devices where the optical transition takes place between confined electronic states in the conduction band. They are attractive for heterodyne detection as their carrier lifetime is extremely short and therefore, they have a fast and highly linear response under strong illumination. In this work, I describe the microscopic physics necessary to understand the device response to light solicitation, with an insight on the phenomena related to quantum electronic transport. I report the performances evaluation of a 9 µm QCD processed into an antenna-based metamaterial. The antenna increases the photon flux that impinges on the detector. This allows a reduction of the detector electrical area and consequently of the dark current, enabling much better performances at high-temperature. The detector sensitivity and bandwidth has been tested with a heterodyne system fully optimized using passive stabilization of the lasers and an accurate conception of the infrared optics. Finally, I demonstrate that the injection of microwave signal into the receivers shifts the heterodyne beating over the large bandwidth of the devices.

Keywords: High frequency optoelectronics devices, quantum cascade detectors, mid-infrared heterodyne detection, metamaterials

Résumé

Récepteurs unipolaires non-refroidis pour la détection hétérodyne dans la deuxième fenêtre de transparence atmosphérique

Mon travail de thèse de doctorat porte sur la conception et la réalisation d'un système de détection sensible à 9 µm de longueur d'onde, dans lequel tous les composants sont des dispositifs semi-conducteurs non refroidis. Cet objectif est atteint en exploitant deux avancées majeures : un détecteur amélioré par métamatériau et un schéma hétérodyne avec des lasers à cascade quantique. Les détecteurs étudiés sont des détecteurs à cascade quantique (QCD) et à puits quantiques (QWIP), dispositifs unipolaires où la transition optique a lieu entre des états électroniques confinés dans la bande de conduction. Ils sont intéressants pour la détection hétérodyne car leur temps de relaxation est extrêmement court et, par conséquent, ils ont une réponse rapide et hautement linéaire même sous un éclairage intense. Dans ce travail, je décris la physique microscopique nécessaire pour comprendre la réponse du dispositif à l'excitation lumineuse, avec un aperçu des phénomènes liés au transport électronique quantique. Je rapporte l'évaluation des performances d'un QCD à 9 µm inséré dans un métamatériau de type antenne. L'antenne augmente le flux de photons incident sur le détecteur. Ceci permet de réduire l'aire électrique du détecteur et donc le courant d'obscurité, qui améliore très significativement les performances à haute température. La sensibilité et la bande passante du détecteur ont été testées dans un système hétérodyne entièrement optimisé utilisant une stabilisation passive des lasers et une conception précise de l'optique infrarouge. Enfin, je démontre que l'injection de signal hyperfréquence dans les récepteurs décale le battement hétérodyne sur toute la large bande passante des détecteurs.

Mots-clés: Optoélectronique haute fréquence, détection hétérodyne dans l'infrarouge, détecteurs à cascade quantique, métamatériaux

Contents

Introduction

To conclude, if we call light, those rays which illuminate objects, and radiant heat, those which heat bodies, it may be inquired, whether light be essentially different from radiant heat? In answer to which I would suggest, that we are not allowed, by the rules of philosophizing, to admit two different causes to explain certain effects, if they may be accounted for by one.
W. Herschel, Phil. Trans., 1800

Herschel's first interpretation of thermal radiation as light was deduced by placing a mercury bulb thermometer beyond the red end of the rainbow, the visible spectrum spread out from a prism under sun illumination.
Although very precise thermometers were already available at Herschel's time, IR sensing development has been proceeded since then at a slow pace.
The main reason for this slow progress is that the world around us is very bright at infrared wavelengths. As stated by Planck's law, every object emits photons, the quanta of the eletromagnetic field. For bodies at room temperature (300 K - 25°C), the maximum of this radiation is for a wavelength of approximately 9 µm. In the very same way in which our eyes struggle to identify the moon scattering the sun radiation towards the earth in broad daylight, an IR detector has to distinguish the signal from the noise of the surrounding environment.
Nevertheless, the 9 µm wavelength is a very interesting band for spectroscopy and atmospheric science as it is the fingerprint region of many molecules. Portable semiconductor sensors could detect poisonous gases with great precision and rapidity. High-frequency free space communications could be implemented without deploying heavy infrastructures. In the long IR range and in adverse conditions, such as fog or dusty environment, an infrared electromagnetic signal propagates through the atmosphere much farther than at the wavelength of 1.55 µm widely used in telecommunications optical networks, securing communications more efficiently. Cool and dusty astronomical objects as exoplanets or newborn stars all emit in the infrared, and the vibrant search for extraterrestrial life or habitable places requires a sensitive detection of infrared radiation.
The most sensitive IR detectors are devices that change some properties (for instance the electrical resistance in bolometers) when heated by the illumination. The material cooling and heating rates determine their response time, which is therefore very low.
Faster devices than thermometers appeared after the consolidation of the quantum mechanics during the XX century. Early quantum mechanics physicists discovered that electrons in some materials called semiconductors interact with light by absorbing or emitting photons with a discrete energy. The consequent variation of their equilibrium state generates an electrical current that can be measured. When talking about detection and therefore absorption of photons, these semiconductor devices are called *photodetectors*.
Mercury-cadmium-telluride semiconducting alloy (HgCdTe or MCT) stands out among the infrared photonic detectors and dominates the market. This detector is composed of mercury, a polluting material banned by the last European safety regulations. Moreover, the MCT response time is limited by the recombination between negatively charged electrons and the positively charged holes they left behind after absorbing photons. MCT is also not adapted to intense laser light.

A ground-breaking innovation came from the possibility of assembling together atom by atom, without contaminations, thin layers of different semiconductor materials (heterostructures), and of inserting within them additional electrons called the doping electrons. Thus, the electron wavefunction, which quantum mechanically spreads along the whole semiconductor crystal lattice, can be engineered and confined in energy potential wells.
By confining the electrons, the capacitance caused by the separation of positive and negative charges and responsible for the frequency bandwidth damping is avoided. Therefore, the achievement of the equilibrium after light perturbation is very fast for detectors based on confined electrons in quantum wells (ps time scale).
Quantum well infrared detectors (QWIPs) and quantum cascade detectors (QCDs) result from this *wavefunction engineering* and benefit of rapid *unipolar* operations. They are currently the fastest infrared detectors, but they need to be cooled down. The necessity of cooling arises because of the quantum statistical nature (shot noise) and thermal agitation (Johnson noise) associated to the electrons. Infrared detectors are particularly affected by these noises as the detected energies (110-140 meV) start to be comparable to the room temperature thermal energy (25 meV). As a drawback, the cryogenic management increases the cost and the complexity of the detection. The *Johnson* noise and the *shot* noise add to the *background noise* and degrade the signal to noise ratio: the IR signal is constituted by few and energetically weak photons, immersed into a noise.
Applications require more advanced infrared devices; and more advanced detectors would enable new applications.
In this work, I analyse and propose some solutions using semiconductor quantum devices for sensitive, rapid, and uncooled detection systems in the long infrared range (at 9 µm). I tackled their development from the quantum modelling of electronic wavefunctions, to the clean room fabrication and the characterization, and up to their implementation in a system to make a working detector.
The different theoretical and experimental aspects of this research are treated in the next chapters as follows:
In **chapter 1**, I will introduce the general context of my research, by describing some fundamentals of infrared detection and of the physics of unipolar semiconductor detectors, with a particular attention for QWIPs and QCDs.
The **chapter 2** is dedicated to the theoretical description and modelling of the characteristics of quantum cascade detectors. As QCDs are relatively recent devices, no extensive work was so far dedicated to the microscopic device physics description under illumination. In this chapter, I propose a way to include the quantum effects in the analytical modelling of the detector photocurrent, resulting in a better predictive capability. The model is successfully compared to experimental observations.
The subject of **chapter 3** is the light-matter interaction enhanced by a meta-material acting as an antenna for the detector. The fabrication, theoretical model and experimental performance evaluation I realized are presented.
Chapter 4 is devoted to the implementation of a heterodyne system with all unipolar semiconductor devices operating at room temperature. The obtained noise equivalent power (NEP) is of tens of pW, which is an improvement of five orders of magnitude with respect to our previous results [1].

Part of the presented work is published in the papers cited as [2] and [3].

Chapter 1

IR detection and semiconductor quantum wells

1.1 Detection of the thermal infrared radiation

The infrared (IR) is the range of the electromagnetic spectrum between the red edge of the visible range (λ=700 nm) and the microwave range (λ=1 mm).
For optics and photonics, three spectral sub-bands are defined: the near infrared (NIR) with wavelength between 780 nm and 3 µm, the mid infrared (MIR) between 3 µm and 50 µm and the far infrared (FIR, known also as terahertz domain) between 30 µm and 1 mm. As the detector materials and performances vary widely within the MIR, the common appellation Long Wave Infrared Range (LWIR) is used for sensors in the band 8-14 µm.

This work intends to explore rapid and sensitive detection systems at:

$$\lambda \simeq 9 \text{ µm} \leftrightarrow E \simeq 140 \text{ meV} \leftrightarrow \nu \simeq 33 \text{ THz} \leftrightarrow k \simeq 1000 \text{ cm}^{-1} \tag{1.1}$$

where λ is the photon wavelenght, E the energy, ν the frequency and k is the wavevector.
The LWIR spectral range, also called "thermal band", has three characteristics:

- Some molecules as Ozone (O_3) present strong vibrational resonances in this range;
- Despite the abundance of molecular gases, the earth atmosphere is almost transparent in this band;
- Any object at temperature 300 K radiates in this band according to the Planck's law of blackbody radiation.

The atmospheric transmission together with a blackbody spectra at T=300 K (black line) are shown in fig. 1.1. The LWIR atmosphere transparency is mainly due to an absorption gap in the water vapor spectrum, while the upper limit is fixed by the carbon dioxide absorption spectrum. Around $\lambda \approx 10$ µm, ozone partly blocks the transmission. Thermal imaging, spectroscopy techniques and radiative cooling can be implemented without absorption loss by the molecules of the atmosphere.

The blackbody thermal radiation constitutes the standard calibration source for IR photodetectors. Every object at temperature T out of thermal equilibrium with the external radiation field, emits a power proportionally to its temperature [5]. The emitted power per wavelength interval $d\lambda$ radiated from a surface with area A is:

$$dP_\lambda = A\epsilon \frac{2\pi hc^2}{\lambda^5} \frac{1}{[\exp(hc/\lambda k_B T) - 1]} d\lambda \tag{1.2}$$

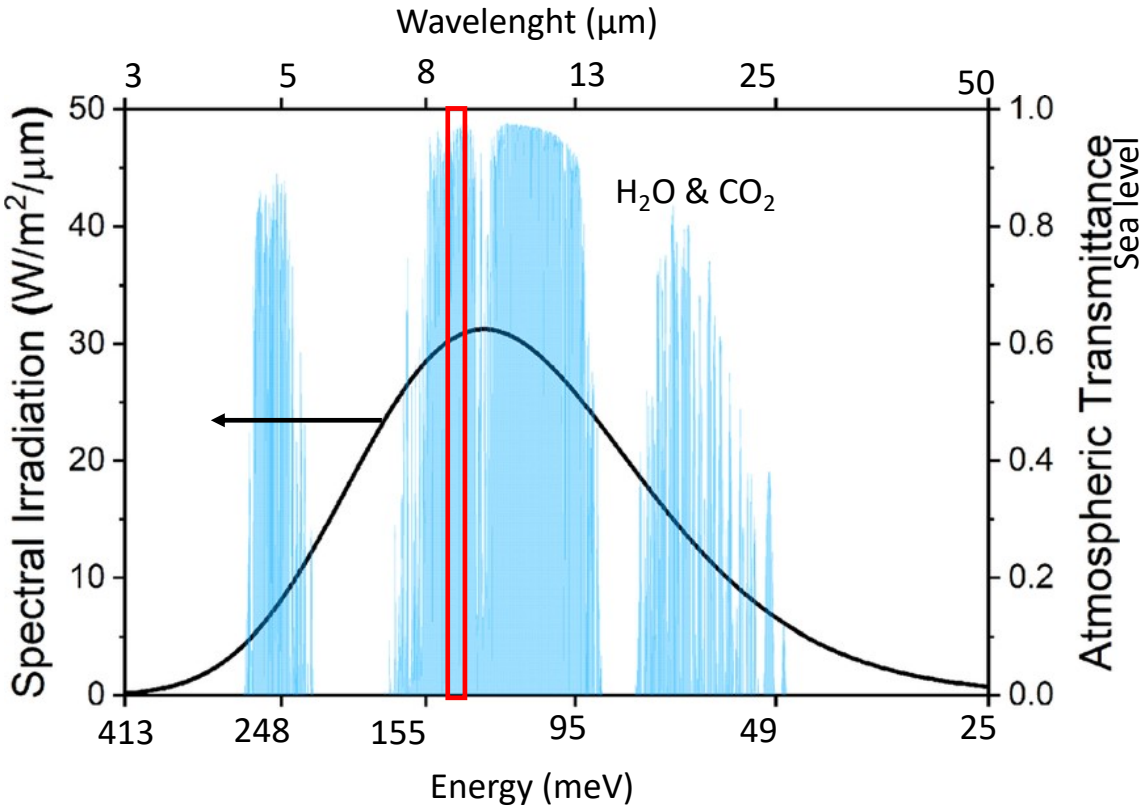

Figure 1.1: Atmosphere transmission spectrum at sea level and blackbody spectrum for T=300 K (black curve). A spectral transmission 'window' can be seen between 8 and 14 µm. In the same band, the peak emission wavelength of the ambient temperature blackbody occurs. From [4].

The emissivity ϵ represents the fraction of thermal radiation which is absorbed or emitted by real objects with non perfect black-body properties (for perfect blackbody ϵ=1). The speed of light is c $\simeq 3 \times 10^8$m/s, h is the Planck constant h=6.6×10^{-34}J/s, k_B=1.38×10^{-23}J/K is the Boltzmann constant, λ is the wavelength. When the temperature of a blackbody increases, the peak emission shifts to higher energies and the total emitted power increases. The incident black-body radiation is usually collected by an optical objective that focuses the radiation onto the detector. The irradiated power in eq. 1.2 is therefore corrected with the lens f-number F (focal length over lens diameter) as:

$$dP_{\lambda,lens} = \frac{1}{4F^2 + 1} dP_\lambda \tag{1.3}$$

The f-number defines the optical field of view of the detector.
The presence of a strong blackbody radiation at ambient temperature is a source of noise. Consequently, an infrared detection technique has to discriminate a signal against this background radiation. As it can be seen in fig. 1.1, at ambient conditions, LWIR detectors are more concerned than MIR detectors operating in the 3-5 µm atmospheric window.

1.1.1 Detectors classification

Within the multiplicity of systems/materials responsive to infrared light, two categories can be identified (for a detailed review of all types of IR detectors see reference [6]):

- Thermal detectors, where the impinging radiation causes a variation of the thermal state of the absorber. Some exploited phenomena can be gas expansion (Golay cell), electrical

resistance variation (Thermopile, Bolometers), pyroelectricity.

- Photonic detectors, where the light absorption derives by an electronic transition between two states in semiconductors.

In photonic detectors, the light excites electrons generating an electrical signal which is the output of the sensor, measured as a current in photoconductors or as a voltage in photovoltaic mode. There are two main types of photonic detectors, depending on two different electronic transitions [6]:

- Interband detectors, based on electronic transitions occurring between valence band and conduction band. The most used is the HgCdTe-alloy based detector;
- Intersubband detectors, exploiting electronic transitions occurring between bound states in quantum wells: III-V materials quantum well infrared photodetectors (QWIP), and III-V quantum cascade detectors (QCD), treated in this work, are among these ones.

LWIR thermal detectors are in general less sensitive to their operational temperature and at room temperature they present better signal to noise ratio than photonic detectors [7]. In semiconductor photonic detectors, the room temperature thermal energy kT $\approx$ 25 meV starts to be comparable to the transition energy of $\approx$ 140 meV. The direct consequence of this is a very high thermal generation rate of carriers, which causes a dark noise current. As a result, for LWIR detectors a cooling system is required adding considerable cost to the detector. However, thermal detectors are completely useless for very fast responses, as their response frequency cut-off is limited to few Hz.

1.1.2 Photonic detectors: figures of merit

The ideal detector is characterised by a signal to noise ratio (SNR) as large as possible. In this section we define the most important figures of merit for evaluating and comparing the performances of photonic IR detectors. The following definitions are partly based on reference [6] and [8].

Responsivity and intensity saturation

Responsivity measures the detector's electrical output for a given optical input. For a photoconductor, the responsivity (in [A/W]) is the amount of electrical current I_{photo} (in [A]) produced by the absorbed optical power P (in [W]). The responsivity is a spectral quantity $\mathcal{R}(\lambda)$, as the detector is sensitive only to a certain wavelength range over the blackbody spectrum. The responsivity is sometimes given as the maximum peak value $\mathcal{R}_p(\lambda_p)$, distinguished from the normalized spectral responsivity $\mathcal{R}_n(\lambda)$ as:

$$\mathcal{R}(\lambda) = \mathcal{R}_p \times \mathcal{R}_n(\lambda) \tag{1.4}$$

The normalized spectral response of a quantum cascade detector (QCD) with the blackbody spectrum at 1273 K is presented in fig. 1.2. If the relation between input power and output signal is linear there is a unique responsivity value (ideal situation). On the contrary, if the detector does not respond linearly to the input power, the responsivity is given as the local slope of the curve output current-input power. The responsivity saturation appears in particular when a powerful laser is used as source. An example of the photocurrent-laser power curve is given in fig.1.3. In blue, it is presented the response of a QWIP biased at 0.7 V and working at room temperature, the red points are for a thermoelectrically cooled Vigo HgCdTe detector. For the Vigo detector, the responsivity saturates at hundreds of µW, where no value of responsivity can be defined. We will explore in details the linearity of QWIP/QCDs in chapter 4.

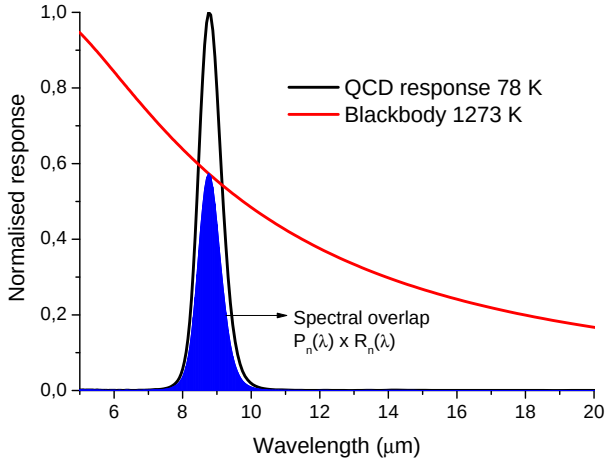

Figure 1.2: Normalized spectral response. The red line is the normalized responsivity of a QCD. The black line is the normalized blackbody radiation at T = 1273 K. In blue the product representing the overlap of the two responses.

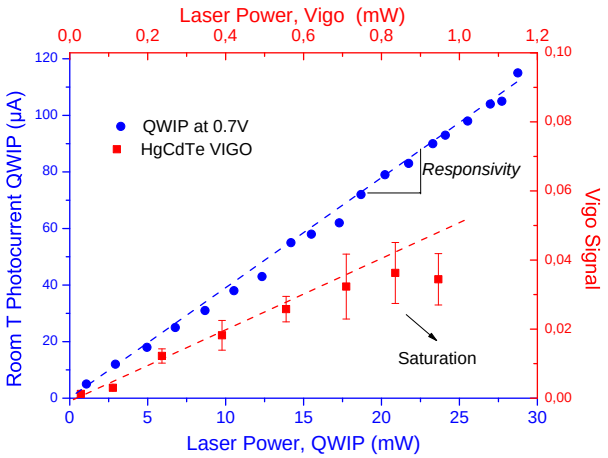

Figure 1.3: Photocurrent vs laser power for a RT QWIP (blue dots) and for a thermoeletrically cooled Vigo HgCdTe. The Vigo response saturates around a power of 400 μW, while the QWIP response is linear and a unique responsivity (slope) can be defined.

In a photonic device, the responsivity depends on the ratio of number of collected electrons over the number of *incident photons*, an important quantity called external quantum efficiency η. A very simple expression for responsivity is:

$$\mathcal{R}(\lambda) = \eta(\lambda)\frac{e\lambda[\mu\text{m}]}{hc} = \eta(\lambda)\frac{\lambda[\mu\text{m}]}{1,23895} \tag{1.5}$$

The detector quantum efficiency η should not be confused with the internal quantum efficiency of the detector, which is defined as the number of photoelectrons flowing in the external circuit per *absorbed photon*.

NEP

The noise equivalent power (NEP, in [W]) in direct detection is the incident power on the detector generating a signal output equal to the root mean square noise output current i_n, thus producing a signal-to-noise ratio (SNR) of 1. It can be written in terms of responsivity:

$$\text{NEP} = \frac{i_n}{\mathcal{R}} \tag{1.6}$$

The NEP is often referred to 1 Hz bandwidth.

Detectivity

The specific detectivity (D*), is defined as the inverse of the NEP of eq. 1.6, normalized by the detector area A and the measurement bandwidth Δf (in [cmHz$^{0.5}$/W]).

$$D^* = \frac{\sqrt{A\Delta f}}{\text{NEP}} = \frac{\mathcal{R}\sqrt{A\Delta f}}{i_n} \tag{1.7}$$

The specific detectivity is useful to compare detectors with different areas and measurement bandwidths. The noise current i_n can be written in terms of the noise spectral densities:

$$i_n^2 = [S_{dark} + S_{back} + \frac{4kT}{r}]\Delta f \tag{1.8}$$

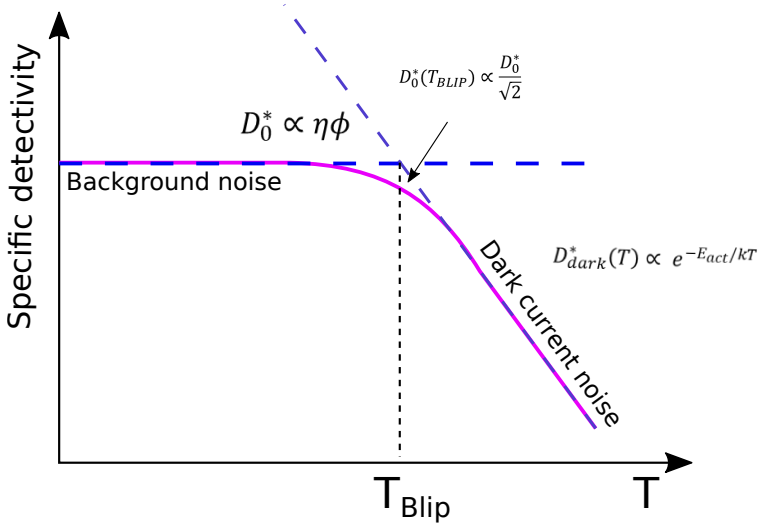

Figure 1.4: Definition of the BLIP temperature as the transition temperature between the background limiting regime and the dark limiting regime. The background noise is constant in temperature and depends on the quantum efficiency η and the blackbody flux Φ. The dark current noise is a thermally activated noise, with E_{act} the activation energy.

In this expression, S_{dark} is the dark noise spectral density, due to the current that flows in the photodetector in the absence of external radiation. It is a thermally activated noise. The noise spectral density S_{back} is caused by the photocurrent noise generated by the background radiation flux inside the detector field of view. The third contribution is the Johnson noise due to the device's resistance r. By replacing the current noise i_n of eq. 1.8 in eq. 1.7, we derive an explicit expression that strongly depends on the temperature T of the device:

$$D^*(T) = \frac{\mathcal{R}(T)\sqrt{A\Delta f}}{\sqrt{[S_{dark}(T) + S_{back} + \frac{4k_BT}{r}]\Delta f}} \tag{1.9}$$

where $\mathcal{R}(T)$ is the temperature-dependent responsivity of the device. The different contributions establish the device operation: the background signal limiting (at low temperature) or the detector dark noise limiting (at high temperature) regime. A schematic representation of the detectivity is given in eq. 1.7. The transition between the two regimes happens at the temperature when the noise under background illumination is equal to twice the noise in dark conditions. The transition temperature is called the Background Limited Infrared Performance temperature (T_{BLIP}). The BLIP temperature is the temperature below which it is useless to cool the detector further for obtaining better performances.

Frequency response

The frequency response of a detector can be modelled by the expression:

$$\mathcal{R}_f = \frac{\mathcal{R}_0}{\sqrt{1 + (2\pi f \tau_c)^2}} \tag{1.10}$$

where $\mathcal{R}_0$ is the direct current low frequency responsivity, and τ_c is the response time, related to the cut-off or 3 dB bandwidth f_c as $f_c = 1/(2\pi\tau_c)$. Flat responses out to the highest frequency of interest are required in laser heterodyning experiments. If the read-out system after the detector is perfectly RF impedance matched, the cut-off is set by the intrinsic carrier lifetime τ_c. The bandwidth foreseen for QWIPs/QCDs is $f_c \approx 100$ GHz as their carrier lifetime is in the ps range [9]. Their GHz bandwidth is a unique feature among any other detector technology in the LWIR.

1.2 Unipolar detectors

QCDs and QWIPs are semiconductor devices composed of heterostructures. The detection mechanism results from the optical transition between two bound electronic states in quantum wells, activated by the photon absorption.
Unlike optical photodiodes based on valence to conduction band transitions, QWIPs and QCDs are unipolar devices, meaning that just one type of majority carrier is involved in the optical transition and in transport (always electrons, that have a better mobility). Therefore, they don't exhibit a depletion charge region caused by the separation of holes and electrons. The transport involves tunnelling and scattering mechanisms and the carriers are characterised by short lifetime and transit time ($\tau \sim 5$ ps) [9]. The inherent fast dynamical processes underscore the intrinsic high modulation frequency characteristic of the unipolar optoelectronics which vastly comprises quantum cascade lasers (QCLs), detectors and modulators.

1.2.1 Band structure calculations and heterostructures

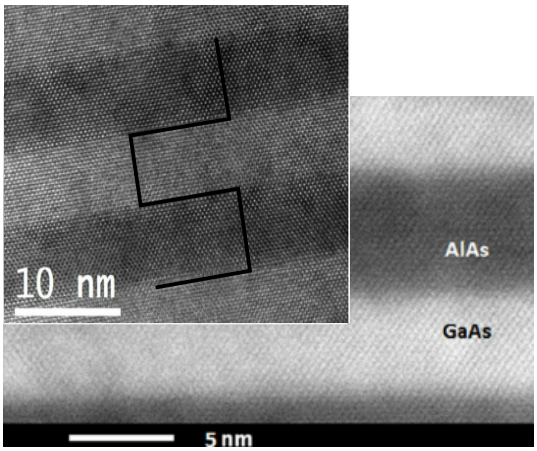

Figure 1.5: Transmission electron microscope image of a multiple QW structure made of AlGaAs (barriers) and GaAs (wells). From [10]

In this section, we outline the basics of the semiconductor quantum wells. A more detailed description can be found in references [11; 12]. All the scattering processes and the tunneling mechanism responsible for the electronic transport in intersubband based detectors will be introduced in chapter 2.
A semiconductor heterostructure is a sequence of nanometric semiconducting layers having different energy gaps but compatible lattice constants. These different layers are grown one on top of the other with atomic-precision techniques, such as molecular beam epitaxy or metalorganic vapour-phase epitaxy. Figure 1.5 shows a transmission electron microscope image of a multi quantum well structure, with alternating GaAs (well) and $Al_xGa_{1-x}As$ (barriers) layers, where x indicates the percentage of Al in the alloy. AlGaAs/GaAs system is a textbook example, it was the first heterostructure to be grown because the two materials have nearly the same lattice constant so that negligible strain affects the final structure.

Bulk III-V materials

AlGaAs/GaAs is a III-V semiconductor alloy and it is the material of the detectors studied in this work. Bulk III-V semiconductors are compounds of materials of group III and materials of group

V of the periodic table (like InAs, GaAs, and AlAs) that crystallize in the zinc blende structure. III-V semiconductors can have an indirect gap (as formed for instance by AlAs,BN, GaP) or a direct gap (e.g. GaAs, GaN, InAs). Figure 1.6 shows the band structure for GaAs, where both the minimum of the conduction band and the maximum of the valence band are at the Γ point, the center of the Brillouin zone.

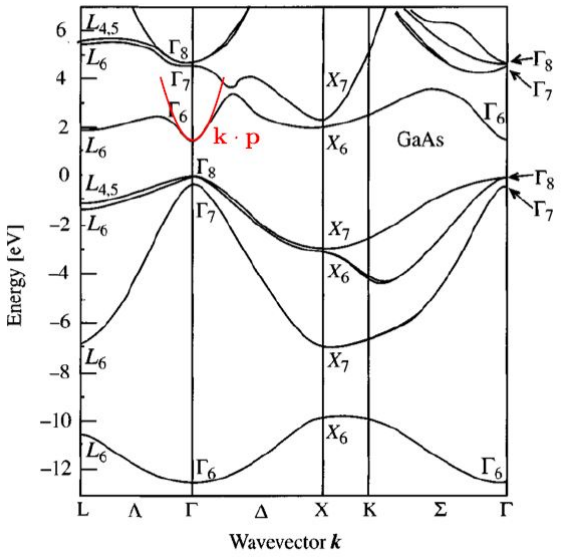

Figure 1.6: Electronic band structure of bulk GaAs calculated with the pseudopotential [13]. At the Γ point, the parabolic energy dispersion approximated with the k · p method is represented in red. From [14].

Band calculations: The bulk

The electronic states in a crystalline solid are determined by the time-independent Schrödinger equation:

$$\left[\frac{\mathbf{p}^2}{2m_0} + V(\mathbf{r})\right]\psi(\mathbf{r}) = E\psi(\mathbf{r}) \tag{1.11}$$

where $V(\mathbf{r})$ is the *periodic* potential of the crystal atomic structure and m_0 is the mass of the free electron. The eigenfunctions have the form stated by the Bloch theorem [13]:

$$\psi_{n,\mathbf{k}}(\mathbf{r}) = \frac{\mathrm{e}^{i\mathbf{k}\cdot\mathbf{r}}}{\sqrt{V}} u_{n,\mathbf{k}}(\mathbf{r}) \tag{1.12}$$

where V is the volume of the crystal, n is the band index, and $\mathbf{k}$ is a wavevector of the reciprocal space. The theorem states that the wavefunctions in a periodic structure are the product of a plane wave and a function with the same periodicity of the crystal.
The electronic and optical properties of infrared devices involve low energy photons and small momenta. Therefore, it is not necessary to calculate the full semiconductor band structure. All the processes happen from around the band edge $\mathbf{k}$=0 to a small range of $\mathbf{k}$ around it. In this case, the eigenenergies $E_{n\mathbf{k}}$ can be calculated within the $\mathbf{k}\cdot\mathbf{p}$ perturbative approximation as:

$$E_{nk} = E_{n0} + \frac{\hbar^2\mathbf{k}^2}{2m^*} \tag{1.13}$$

where m^* is the effective mass that in the $\mathbf{k}\cdot\mathbf{p}$ approximation is calculated as:

$$\frac{1}{m^*} = \frac{1}{m_0} + \frac{2}{m_0^2 k^2} \sum_{n' \neq n} \frac{|\langle u_{n\mathbf{0}} | \mathbf{k}\cdot\mathbf{p} | u_{n'\mathbf{0}} \rangle|^2}{E_{n\mathbf{0}} - E_{n'\mathbf{0}}} \tag{1.14}$$

The coupling between different bands n and n' induces a different electron mass via the term $\mathbf{k}\cdot\mathbf{p}$. The modification of the electronic behaviour due to the potential of the whole band structure on the electrons are contained in the use of the effective mass. The energy dispersion in eq.1.13 includes a parabolic term in $\mathbf{k}$ (in red in figure 1.6). When the influence of the valence band is strong, as for small energy gaps, the effective mass is lighter and the parabolic approximation has to be corrected. To account for this effect, a model has been developed by Kane [15] where the non-parabolicity is reformulated employing an effective mass that depends on the energy.

Band calculations: heterostructure and quantum wells

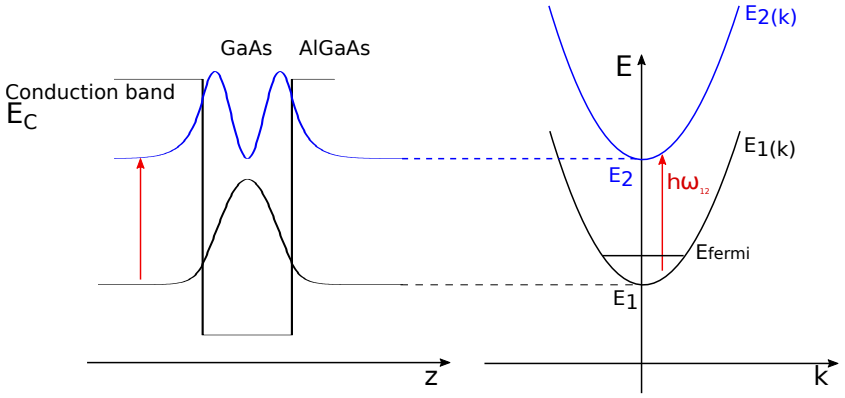

Figure 1.7: Schematic of a quantum well (QW) with the square moduli of the wavefunctions representing two bound states. The heterostructure is doped so the QW contains a two-dimensional electron gas (2DEG). Here, we study intersubband transitions between two subbands, 1 and 2. On the left, k-space representation, where the 2DEG populates the QW up to the Fermi energy E_f.

We consider now the calculations of the wavefunctions in heterostructures. The eigenstates are found in this case by defining an envelope function $\chi_{i\mathbf{k}} = \psi_i(z) e^{i\mathbf{k}_{||}\cdot\mathbf{r}_{||}}/\sqrt{S}$ slowly varying on the scale of the lattice constant, where S is the surface of the sample. The electrons in the conduction band are described by the envelope function including the effective mass due to the crystal potential, reported in eq. 1.14. The Schrödinger equation for the envelope function can be separated in its x-y plane component, where the electronic motion is that of a free particle, and in the z component, which is the growth direction. In the z direction it is expressed as:

$$\left[-\frac{\hbar^2}{2} \frac{\partial}{\partial z} \frac{1}{m^*(E_i, z)} \frac{\partial}{\partial z} + E_C(z) + V_{ext}(z) \right] \psi_i(z) = E_i \psi_i(z) \tag{1.15}$$

This equation includes the conduction potential profile $E_c(z)$ plus an external potential in the z direction in the case of an applied electric field.
The mismatch in conduction and valence energy band of two semiconductors with different energy gap provides an energy barrier that confine electrons in quantum wells (QW).
In this case, the electron energy is:

$$E_{ik} = E_i + \frac{\hbar^2 k_{||}^2}{2m^*(E)} \tag{1.16}$$

The index i labels a set of quantized states, called subbands, with a parabolic (ideally) dispersion relation (Figure 1.7) and different in-plane momenta. In the general case, the eigenvalues can be solved only with numerical techniques, as it is the case of square moduli of the wavenfunctions represented in fig. 1.7. If the effective mass is independent on the energy as in AlGaAs/GaAs, the separation energy between two subbands is constant in the reciprocal space, as it is sketched on the right side in fig. 1.7. In the case of the infinite potential well, it is possible to write an analytical solution for the energy levels inside the well:

$$E_{i,inf} = \frac{\hbar^2}{2m^*}\left(\frac{i\pi}{L_z}\right)^2 \tag{1.17}$$

where L_z indicatez the thickness of the well. This expression indicates that energy separation between two bound states can be engineered by modifying the well thickness. This is a fundamental feature for the design of unipolar optoelectronic devices.

The electron occupation within the subband is determined at equilibrium by the Fermionic statistical partition function. For intersubband transitions, the heterostructure must be doped in order to have the well ground state filled with electrons. The Fermi energy at zero temperature and for a single occupied state is thus fixed by the doping density $E_f = E_1 + (\pi\hbar^2/m^* n_{2D})$. We will describe with more details in chapter 2 the equilibrium carrier concentration in our detectors.

Numerical solution

The band structure calculations in this work are performed with a QUAD group developed program [16]. It is based on the Kane model including the coupling with the valence band. For AlGaAs/GaAs the non-parabolicity has a negligible effect. The bulk Kane model reformulated with the envelope function approximation is implemented following the reference [17]. The numerical method solving the Schrödinger equation under an applied bias is a shooting method, an iterative method for calculating point by point differential equations [18]. No correction for the heterostructure potential related to the Poisson solution is applied.

1.2.2 Light-matter interaction: intersubband absorption

In the optical intersubband transition, the dipole matrix element between two subbands (n and n') with different parity is:

$$e\langle z\rangle_{n,n'} = eL_z\frac{8}{\pi^2}\frac{nn'}{(n-n')^2} \tag{1.18}$$

The final and initial states change in energy but conserve the same in-plane momentum as the photon momentum is negligible compared to that of an electron (the photon is a massless particle, where its momentum is the inverse of the speed of light). The oscillator strength is:

$$f_{n,n'} \equiv \frac{2m^*\omega_{n,n'}}{\hbar}\langle z\rangle^2_{n,n'} = \frac{64}{\pi^2}\frac{nn'}{(n-n')^2} \tag{1.19}$$

It obeys the f-sum rule:

$$\sum_n f_{n,n'} = 1 \quad \text{for } n \neq n' \tag{1.20}$$

The oscillator strength for the transition n=1 to n'=2 in an infinitely deep well is $f_{1,2} \approx 0.96$. The lowest states in energy in a quantum well are therefore efficient for absorbing light since their

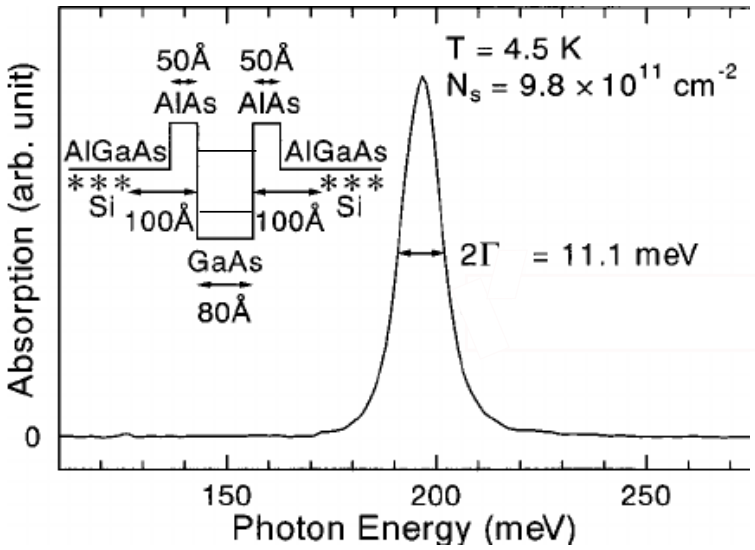

Figure 1.8: Intersubband absorption spectrum of a GaAs/AlGaAs single QW observed at 4.5 K. The typical linewidth of the Lorentzian shape is ≈ 10% of the peak energy. The inset represents the structure of the corresponding sample. From [19]

oscillator strength exhausts most of the f-sum rule. The absorption probability can be derived with the Fermi's Golden Rule [8] as:

$$\alpha_{2D} = \frac{e^2 h}{4\pi\epsilon_0\ n_r m^* c}\ n_{2D} f_{n,n'} \frac{\Gamma}{(E_{n,n'} - \hbar\omega)^2 + (\Gamma)^2} \tag{1.21}$$

where ϵ_0 is the vacuum permittivity, n_r is the refractive index. The absorption spectrum assumes a Lorentzian shape with broadening at half width of half the maximum Γ as it is shown in the absorption spectrum of a single QWs measured at 4 K, reported in fig. 1.8. This quantity is also called absorption quantum efficiency or absorption efficiency. The absorption depends on the doping density n_{2D} and on the effective mass. For a GaAs single well with an optical transition at $E_{1,2}$=140 meV, typical values are n_{2D}=5×10^{11} /cm^2, n_r=3.3, Γ=10 meV, f=0.96, m^*=0.067 m_e. The single well peak absorption probability is α_{2D}=0.0072.
When considering precisely the peak energy of the Lorentzian absorption, the collective behaviour of the electrons has to be taken into account as it causes the absorption resonance to be at larger energy than the transition energy. The so called depolarization shift of E_{dep} has to be added to $E_{n,n'}$[8]:

$$E_{dep} = \frac{e^2 \hbar^2 n_{2D} L_{qw} f_{12}}{2\epsilon_0 n_r E_{21} m^*} \tag{1.22}$$

where f_{12} is the oscillator strength, n_{2D} the doping density, L_{QW} the thickness of the doped well, E_{21} the transition energy. For the values given before E_{dep} is $E_{dep} \approx$ 4meV.

1.2.3 QWIP

We will give in this section an insight into the QWIPs physics, following reference [8]. The first demonstration of the QWIP detector was made in 1987 [20]. A QWIP detector is formed by quantum wells surrounded by thick barriers, as in the band diagram scheme in Fig.1.9. The well width and barrier height are adapted to build one confined state inside the quantum well and the excited level close to the top of the barrier. This enables to combine a strong oscillator strength for the optical transition and an efficient charge extraction (it is called bound to quasi-bound

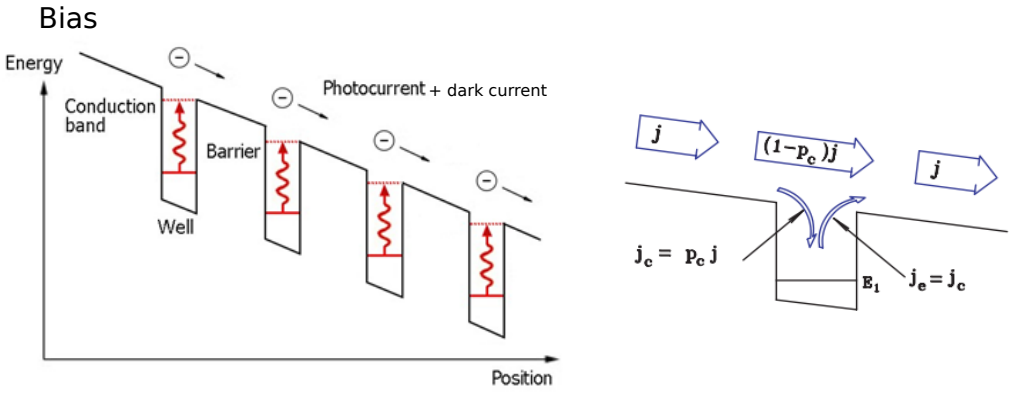

Figure 1.9: Conduction band diagram for a bound-to-quasi-bound QWIP. The QWIP structure is biased and a dark current is superimposed to the photocurrent. On the right, the total current over the well J is conserved as the contacts inject carriers compensating for the emitted electrons. From [8].

transition). An external bias is applied in order to collect the excited charge carriers and measure a photocurrent. This photocurrent is however superimposed on a significant dark current generated by the thermal carrier excitation or by the carrier tunnelling through the barriers.
Despite the simplicity of the structure, QWIPs device are rather difficult to model because of the different nature of the 2D quantum localized states and of the 3D states of the continuum. One of the most proper description is the emission-capture model. It pictures the current flowing in the QWIP structure by means of the probabilities of capture and emission of the electrons from the well [21]. A simplified schematic of the physical process is depicted in fig. 1.9. Under steady-state operation, the total current J is conserved as part of it is emitted from the well and part is injected by the contacts and captured into the well. The ratio between the emission and capture probabilities in a single well is called the single well gain:

$$g_1 = \frac{p_e}{p_c} \tag{1.23}$$

Dark current

In dark conditions, if we neglect the tunnel probability (thick barriers), the electrons can escape the well by a thermionic emission process. The dark current density is a function of the bias and it can be written as [8]:

$$I_{dark}(V) = \frac{e\ \sigma v(V)\tau_c}{\tau_{scatt}}\ \frac{m^*}{\pi\hbar^2 L_p}\ k_B T \mathrm{e}^{\frac{-E_{act}(V)}{k_b T}} \tag{1.24}$$

where τ_c is called the capture time, m^* is the effective mass in the barrier, σ is the electrical surface, τ_{scatt} is the scattering time involved in the emission process from the well to the continuum. The drift velocity depends on the applied electric field. Therefore in biased QWIPs, the dark current is an unavoidable contribution.
E_{act} is the activation energy, corresponding to the energy difference necessary to escape from the ground state $E_{act} = \Delta E_c - E_f$ where ΔE_c is the barrier height and E_f is the Fermi energy. It decreases when the voltage is increased because the top of the barrier becomes thinner at larger bias facilitating the tunnelling. It is also proportional to the doping density, through the Fermi Energy. The dark current noise is defined as:

$$i^2_{dark} = 4e g_{noise} I_{dark} \Delta f \tag{1.25}$$

where Δf is the integration bandwidth. The quantity $g_{noise} \equiv 1/(Np_c)$ is the noise gain, which can be different of a quantity p_e from the photoconductive one, which is the one defined in the eq. 1.23 divided by the number of wells N. For structures with $p_e << 1$ and $p_e \approx 1$, it is generally assumed that the noise and photoconductive gain are the same, as in an ideal photoconductor.

Photocurrent

The photocurrent from one well is given by:

$$i^{(1)}_{photo} = e\Phi\alpha_1\frac{p_e}{N} \tag{1.26}$$

where α_1 is the absorption efficiency (α_{2D} multiplied by the light-matter geometry factor explained in sec. 1.2.6) , Φ is the photon flux. The loss of electrons due to the emission from the well is compensated by the electrons capture. Therefore, the total photocurrent is:

$$I_{photo} = \frac{i^{(1)}_{photo}}{p_c} = e\Phi\alpha g_{photo} = e\Phi\alpha\frac{p_e}{Np_c} \tag{1.27}$$

where $g_{photo} = g_1/N$ is the total photoconductive gain, the single well gain in eq. 1.23 divided by N. In first approximation, the total photocurrent is independent on the number of wells as the absorption efficiency is N times the single well one $\alpha = \alpha_1 N$. This is valid for short structures, as we will see in sec.1.2.6. The evaluation of p_e depends on the position of the excited level with respect to the top barrier. The optimum condition for the photocurrent is the bound to quasi bound transition, for which we can suppose that the electrons always escape from the well while the probability of being captured is low: $p_e \approx 1$ and $p_c << 1$. In this case, the photoconductive gain can be rewritten as the ratio between the lifetime of an electron over its transit time between the two contacts, the common definition of the gain in photoconductive theory. It indicates the number of electrons reaching the external circuit for each absorbed photon and it depends on the temperature and voltage:

$$g_{photo}(V,T) = \frac{p_e}{Np_c} \approx \frac{\tau_c v(V,T)}{NL_p} \tag{1.28}$$

where τ_c= 5 ps is the capture time at low temperatures, v is the drift velocity, N is the number of quantum wells and $L_p \approx 40$ nm is the length of a period in the structure. The thermal dependence of the gain is related directly to the drift velocity and therefore to the electron mobility. The gain can be thus greater than 1, if the electron lifetime in the continuum is long enough. The capture probability p_c is an important but elusive parameter in QWIPs as p_c strongly depends on the sample [8]. From our devices having bound to quasi bound transitions, typical values at T=78 K are g=0.6-0.8 for N=5 QWs [1]. We also measure that at room temperature the photoconductive gain of QWIPs tends to 1/N, that means that p_c and p_e are close to 1 at high temperatures.

1.2.4 Photovoltaic QWIPs

In QWIPs, an externally applied electric field is necessary for extracting the photoexcited carriers, but is also responsible of a huge thermally activated noise. A different type of devices working without external bias has been proposed for low-noise operation. They all rely on some asymmetries in the potential of a multi quantum well structure, that generate an internal bias. A general scheme of the configuration for photovoltaic detection is represented in fig. 1.10a. The transport is engineered with the intention to prioritize one direction and block the other one (red cross in fig. 1.10). This asymmetry was achieved for instance by adding a tunnel barrier on one side of the QW and by using a modulation doping along the barrier, as in scheme presented in fig. 1.10

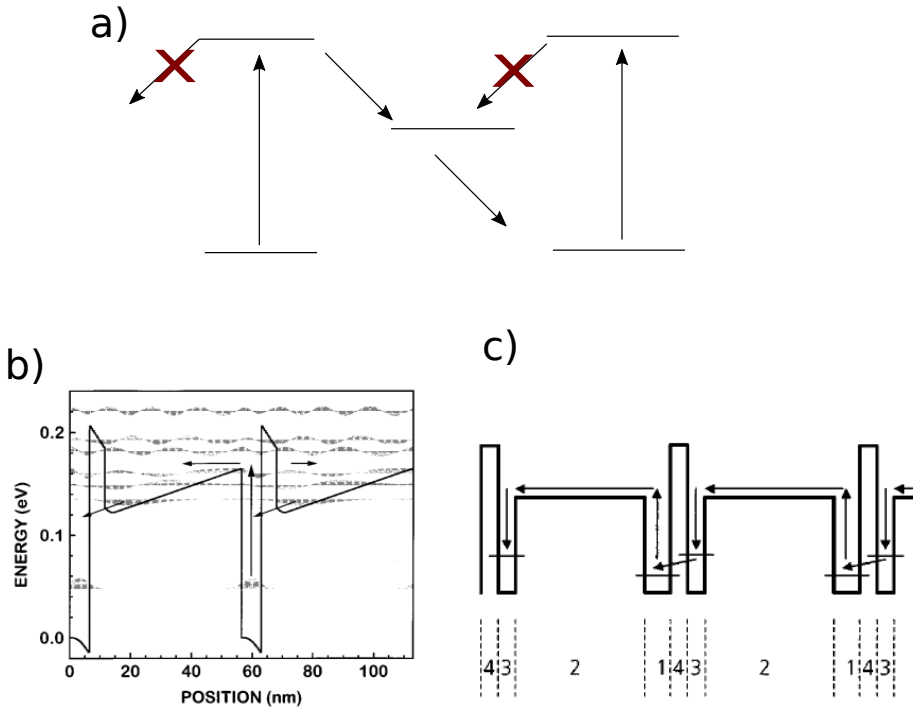

Figure 1.10: a) General subband configuration for a photovoltaic device, where the directionality of the current has to be enabled by a specifically generated internal potential (though modulation doping or phonon extraction, for example). b)Photovoltaic QWIP with modulation doping and one side barrier.From [22]. c)Four-zone photovoltaic QWIP. From [23].

[22]. Under illumination, electrons are excited from the lowest QW subband to the states into the quasi-continuum. Subsequently, the photoexcited electrons are accelerated by the band edge profile of the barrier (where a modulation doping is present) and relax to the following well. In an updated version of this device, another well with a higher energy subband was added to improve the capture probability into the doped well [23]. This led to the four-zone QWIP, whose band diagram is sketched in fig. 1.10. In the four-zone QWIP, the photoexcited carriers in the zone 1 drift through the quasi-continuum of the zone 2, relax first into 3 and then into the subsequent 1 through the barrier 4. In all these photovoltaic devices, the photoexcited electrons pass across a drift region within the continuum states. One problem of these photovoltaic QWIPs is that electrons in the continuum still have an high probability of moving back to the opposite direction (from 3 to 2 to 1 in fig. 1.10c), hindering high responsivities.

1.2.5 QCD

The four-zone QWIP together with the quantum cascade laser (QCL), demonstrated in 1994 [25], have inspired the QCD, which was introduced in 2004 [26],[27]. A recent review can be found in reference [28]. A simplified schematic of a QCL is reported in fig. 1.2.5a and the band diagram of a QCD in fig. 1.2.5b.
The QCL is a unipolar semiconductor laser emitting in the infrared, based on intersubband transition in multi quantum wells heterostructures. In a QCL, the population inversion necessary for lasing is achieved by fast depopulating the lower state by phonon-electron scattering (green arrow in fig. 1.2.5a). An injection region, forming an energy cascade, conveys electrons from one active region to the following and provides with doping the refilling of the superior level of the lasing transition.

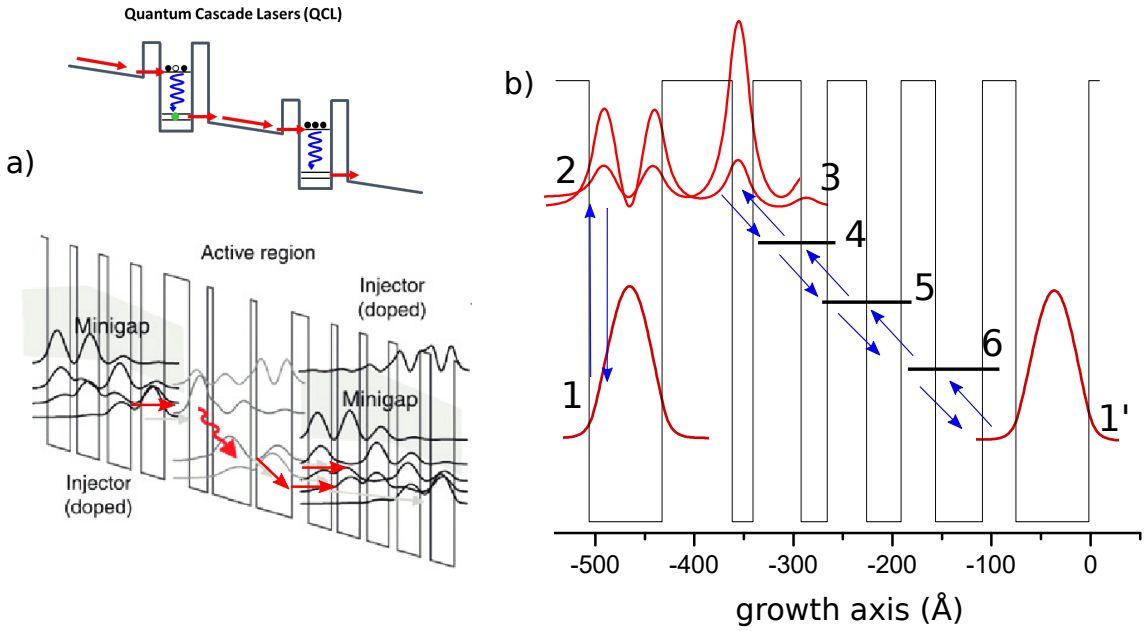

Figure 1.11: a) On top, simplified schematic of a QCL device. On bottom, the active region of the QCL where the square moduli of the wavefunctions are represented. The lower level is depopulated by the LO phonon-electron scattering. The electrons are extracted then re-injected into the upper state of the lasing transition. From [24]. b) Band diagram of the QCD, where the photocurrent can be extracted without bias using the asymmetry of the potential formed by the phonon-electron scattering cascade.

In a QCD, charge carriers are promoted by the light to the bound excited state of the doped well. After excitation, they are delocalized forming an extended doublet across the first barrier. The doublet provides a fast resonant tunnelling mechanism that avoids the relaxation back to the doped well. Then, part of the excited electrons relax into lower energy subbands engineered by varying the well and the barrier thickness, as in the injection region of a QCL. The energy spacing between the subbands is designed to be approximately equal to the longitudinal optical (LO) phonon energy ($\approx$ 36 meV in GaAs). In this via a resonant LO phonon-electron scattering the carriers are transported to the subsequent doped well. This structure is typically repeated for N periods for increasing the absorption.
The probability for an excited electron to reach the next period is called the extraction probability p_{ext}. The photocurrent can be written as:

$$I_{photo} = e\Phi\alpha\frac{p_{ext}}{N} \tag{1.29}$$

where $\alpha = N\alpha_1$ is N times the absorption efficiency of a single quantum well α_1, Φ is the photon flux, N the number of periods. The presence of the cascade generates a preferential direction for the transport and allows these devices to work without any external bias. The evaluation of p_{ext} for different temperatures and voltages will be the subject of the chapter 2.

1.2.6 Light coupling geometry and quantum efficiency

The absorption efficiency defined in eq. 1.21 takes into account only the number of electrons in the external circuit per absorbed photon, provided that all the photoelectrons are collected by the contacts and that all the incident photons are absorbed. The quantum efficiency for QWIPs and QCDs, defined as the number of collected photoelectrons per incident photon [30], depends on the external geometry. The geometry is imposed by the Fermi's Golden rule calculations [11]

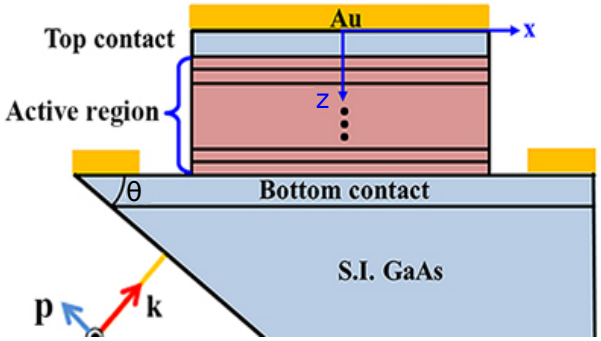

Figure 1.12: Schematic representation of a mesa geometry, with the 45°edge facet. The infrared radiation impinges normal to the facet surface. The substrate is semi insulating GaAs layer. From [29]

of the transition probability: only the light polarized along the growth direction can trigger the absorption in an intersubband transition. Therefore, for standard QWIPs and QCDs, a normal incidence geometry (light impinging normal to the wafer) cannot be used. The simplest geometry is a 45° polished edge facet called the mesa, depicted in figure 1.2.6. In this configuration the mesa absorption quantum efficiency is:

$$\alpha(\theta) = \frac{t_{sub}}{2}\left[1 - \exp\left(-2N\alpha_{2D}\,\frac{\sin^2\theta}{\cos\theta}\right)\right] \tag{1.30}$$

The factor $\sin^2\theta$ comes from the polarization selection rule. In this configuration, one half of the polarization is disregarded. The factor $t_{sub} = 4n/(1+n)^2 \approx 0.72$ is the transmission coefficient of the GaAs substrate with refractive index n=3.24, $\alpha_{2D} = 0.0072$ is the absorption efficiency from eq. 1.21, N=8 is the number of doped quantum wells, the factor 2 in the exponential accounts for the double passes. The absorption quantum efficiency for the QCD mesa with 8 periods is around $\alpha(45°)$=2.7%.
The total external quantum efficiency includes also the gain and the extraction probability for QWIPs and QCDs respectively:

$$\begin{aligned}\eta(\theta) &= \frac{p_e}{Np_c}\frac{t_{sub}}{2}\left[1 - \exp\left(-2N\alpha_{2D}\,\frac{\sin^2\theta}{\cos\theta}\right)\right] \quad \text{for QWIP}\\ \eta(\theta) &= \frac{p_{ext}}{N}\frac{t_{sub}}{2}\left[1 - \exp\left(-2N\alpha_{2D}\,\frac{\sin^2\theta}{\cos\theta}\right)\right] \quad \text{for QCD}\end{aligned} \tag{1.31}$$

where the factor $\frac{p_e}{Np_c}$ is the photoconductive gain in QWIPs (eq. 1.27), p_{ext} is the extraction probability in the QCD. The external quantum efficiency is included as η in the responsivity formula of eq. 1.5. The external quantum efficiency of QWIPs and QCDs mesas is usually low: if we consider N=8, α_{2D}=0.0072 as calculated with the eq. 1.21 with $n_{2D} = 5\times10^{11}$ cm^{-2}, t_{sub}=0.72, θ=45°, g=0.8 for QWIP and p_{ext}=0.7 for QCD at T=78 K, we find at T=78 K $\eta(45°)$=1.8% for QWIP and $\eta(45°)$=0.3% for QCDs.
A GaAs/AlGaAs QWIP mesa with nearly 100% absorption has been notably demonstrated using high doping density and N=100 quantum wells [31], at the cost of an important dark current.
For a lot of applications the facet geometry is very impractical. A number of alternative light-coupling geometries has been proposed [8]. In chapter 3 we will describe a photonic architecture that enables a normal incidence of radiation and that can be engineered to enhance the quantum efficiency without increasing the doping density.

1.2.7 State of the art

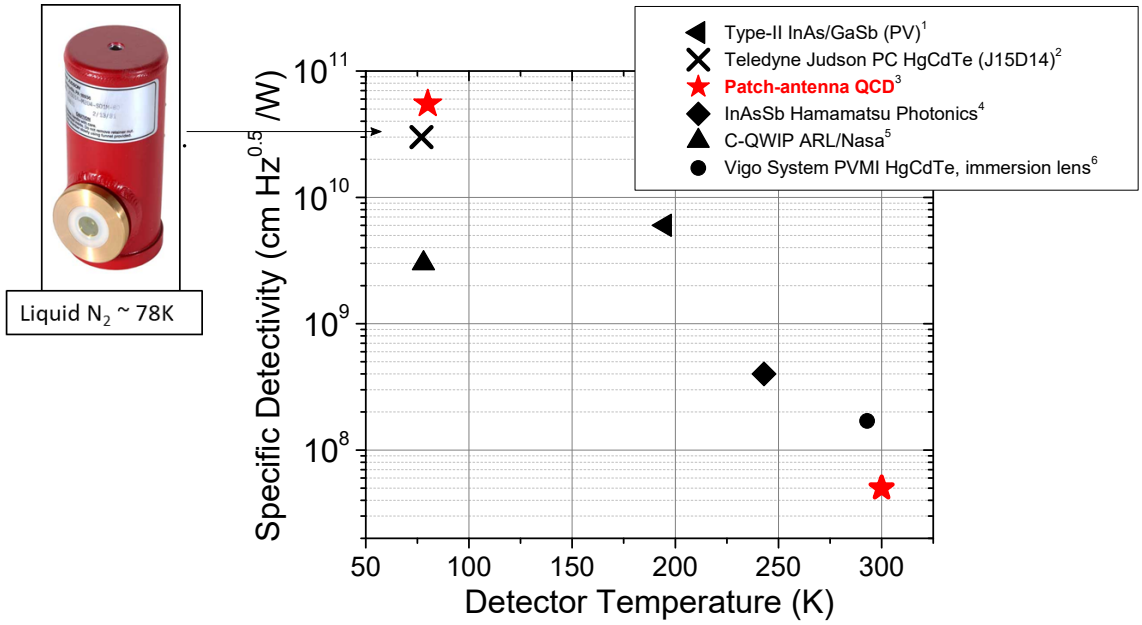

Figure 1.13: Specific detectivity for 60-deg FOV at λ=9µm as a function of the detector temperature. References: 1-[32]; 2-[33];3-[2]; 4-[34];5-[35]; 6-[36].

Whereas there exists a variety of IR photonic and thermal detection solutions at the laboratory level, the LWIR detector market is still monopolized by the HgCdTe detector. In fig.1.13, we report the value of the specific detectivity at 60-deg field of view for some detectors at the state of the art for λ=9 µm. This collection is not intended to be exhaustive but indicative of the targeted performances.
The HgCdTe detectors show highly competitive detectivity values from low temperatures (3×10^{10} cmHz$^{0.5}$/W) to high-temperatures (2×10^{8} cmHz$^{0.5}$/W), where optical immersion lenses are used for increasing the signal. In these detectors the quantum efficiency can reach up to a value of 70%. The HgCdTe is the detector used in every infrared lab and in spectroscopy systems, and it is affordable. With a dedicated electronics, its responsivity is flat up to a frequency of 1 GHz. However, they are limited by material non-uniformity, significant 1/f noise and intrinsic low-speed response. Moreover, the HgCdTe alloy is classified as non conform to safety standards by the Restriction of Hazardous Substances (RoHS), a European directive restricting the use of cadmium and mercury in electronic devices [37].
These limitations are absent in intersubband transitions based detectors such as QWIPs and QCDs. The development of High Operating Temperature InAs/GaSb type-II superlattices detectors is promising [32], but detailed studies about their time response are still missing in literature. QWIPs and QCDs are currently the only detectors in the LWIR with tens of GHz frequency response ($f_c \approx$ 100 GHz).
The engineering of the cooling system and the optical coupling are the most problematic and costly issues for QWIPs and QCDs devices. One way to optimize the detectors for high temperature operation is implementing resonant cavities and antennas to gather the photons from an area greater than the electrical area. Antenna-coupled QWIPs with detectivity more than 1×10^{7}cmHz$^{0.5}$/W at room temperature were recently demonstrated, opening new opportunities for high-frequencies uncooled unipolar devices [1]. Following this work, patch-antenna QWIPs detectors have been optimised for improved responsivity [38] and for high-frequency response [39].

Quantum Cascade Detectors represent the subject of an active research, although their commercial exploitation has not yet took off so far. Their appealing properties include the possibility of several GHz frequency cut-off, room temperature photovoltaic operations with laser light and integrated growth with quantum cascade lasers [40]. In this work we demonstrate the achievement of the state of the art performance of a meta-material enhanced LWIR QCD.

1.3 Infrared heterodyne detection

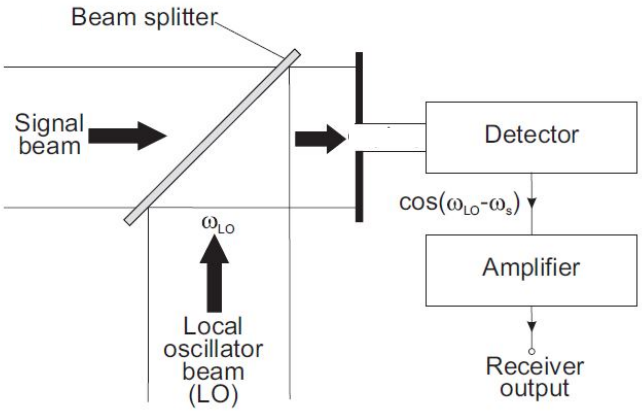

Figure 1.14: Scheme of the heterodyne detection, where a laser called local oscillator is mixed with the signal and detected by a power detector. The output is an AC signal at the beating frequency. From [6].

In previous sections, it was implicitly assumed that detector is operating in direct detection, the most used in applications. In section 1.1.2, we have seen that the ultimate limit of the background-limited NEP is set by the ambient background power P_B and the absorption quantum efficiency of the detector $\alpha(\theta)$:

$$\mathrm{NEP}_{limit} = \sqrt{\frac{4h\nu\ \Delta f\ P_B}{\alpha(\theta)}} \tag{1.32}$$

where $\alpha(\theta)$ is the geometry-dependent absorption efficiency in eq. 1.30 with θ the incident angle of radiation, Δf is the integration bandwidth, P_B is the spectrally integrated power density contained in the entire spectrum at ambient temperature. This formula is valid for a QWIP only if the photoconductive and the noise gain are equal. In direct detection, photonic detectors requires cooling to achieve this sensitivity.
If the detector is a power detector and its response is proportional to the square of the signal electric field E_s^2, there exists a workaround to ideally reach the single photon detection limit: the amplification and the selectivity provided by beating a laser with the signal in a heterodyne detection scheme. A sketch of the involved components is represented in fig. 1.14. The laser called local oscillator has a strong incident power P_{LO} at the frequency ω_{LO} which mixes with the signal at a slightly different frequency ω_S. The detector response has an AC component at the beating frequency $\omega_{LO} - \omega_s$. If the LO is strong enough to cancel out all the other detector noise contributions, the NEP ultimate limit is given by:

$$\mathrm{NEP}_{\mathrm{het}} = \frac{h\nu\ \Delta f}{\alpha(\theta)} \tag{1.33}$$

The heterodyne NEP is proportional to the measurement bandwidth and to the absorption efficiency dependent on the external geometry as in eq. 1.8. For absorption quantum efficiency close

to one the single photon power detection is possible. As another advantage of heterodyne is that the detection preserves the signal phase, the name coherent detection is often used. In chapter 4, we will give additional details about this technique, while here we will present a review of the available technology and of some possible applications.

1.3.1 Progresses in LWIR heterodyne technology

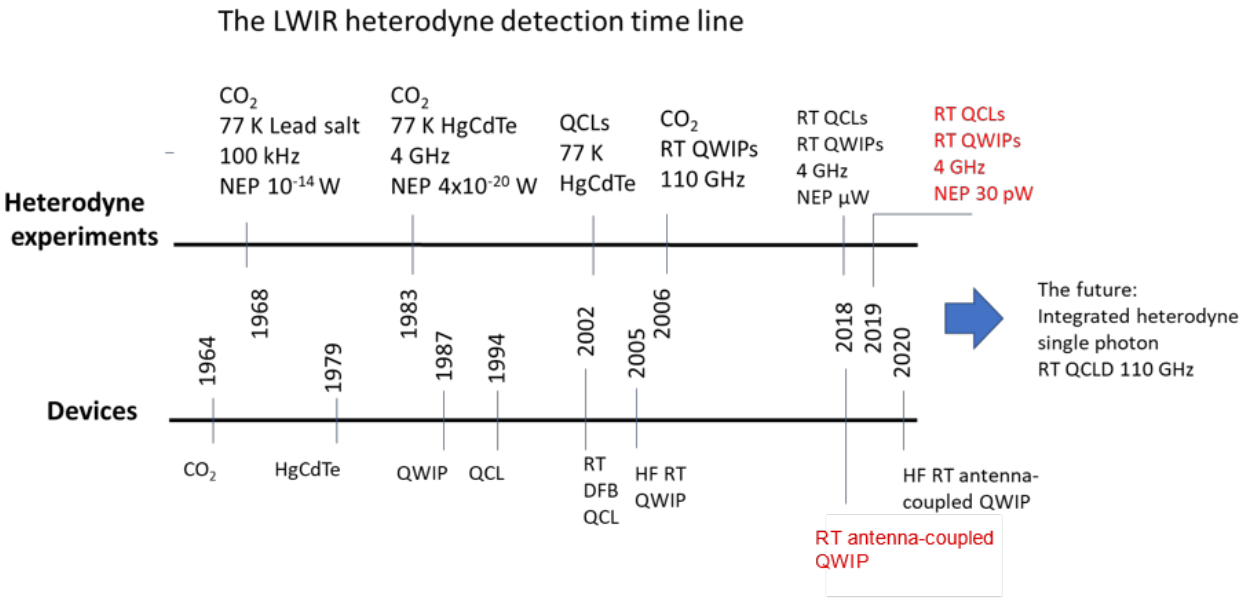

Figure 1.15: Time line of the performances of heterodyne detection system (top) and the corresponding device invention. RT stands for room temperature, HF for high frequency. The CO_2 is a single frequency gas laser, the quantum cascade laser (QCL) a semiconductor tunable laser. In red, the performances achieved in this work. In future, a single photon detection could be reached by HF integrated heterodyne sensors using bi-functional antenna-coupled QCLD (QCL with QCD).

In order to achieve the ultimate heterodyne performances, the detector has to satisfy some requirements:

- Large bandwidth, with a cut-off greater than the beating frequency;
- High saturation intensity, greater than the LO intensity;
- Good quantum efficiency.

The LO laser is instead selected for:

- Single-mode emission;
- Frequency stability;
- Frequency tunability.

In figure 1.15 we wrap up the main heterodyne realizations in terms of NEP and set-up simplicity over time. We remark that every heterodyne set-up's upgrade has always followed a breakthrough in infrared devices.
The first infrared heterodyne experiments were conducted in 1968 just after the CO_2 gas laser

invention, using nitrogen cooled lead salt photodiodes as receivers [41]. The obtained NEP was $\approx 2 \times 10^{-14}$ W for a beating frequency at 100 kHz and a bandwidth of $\Delta f \approx 65$ kHz. The HgCdTe detector was then widely exploited and optimized as heterodyne receiver [6]. With a λ=10.6 µm HgCdTe photodiode at 77 K, a NEP_{het} only a factor of 2 above the theoretical single photon quantum limit was measured at 1 GHz [42].
Despite the top sensitivities, the restriction to the fixed laser frequencies was a severe limitation of gas laser systems. It is only after the first room temperature CW (continuous waves) quantum cascade laser demonstration in 2002 [43], that the first heterodyne experiments with tunable QCLs were conducted with a HgCdTe receiver in a spectroscopy experiment [44; 45].
From the detector side, a great result was the demonstration of a 110 GHz heterodyne signal in 2006 obtained with a high frequency room temperature high-absorption QWIP and two CO_2 lasers [46]. This result proved that QWIPs detectors are very well suited for heterodyne detection. After that, in 2018 we demonstrated the first heterodyne experiment where all the components are room temperature semiconductor devices (QCLs and QWIPs) [1]. In this work, using an improved RT heterodyne configuration, we reached a NEP limit of 30 pW up to 4 GHz beating frequency [3].

1.3.2 Applications

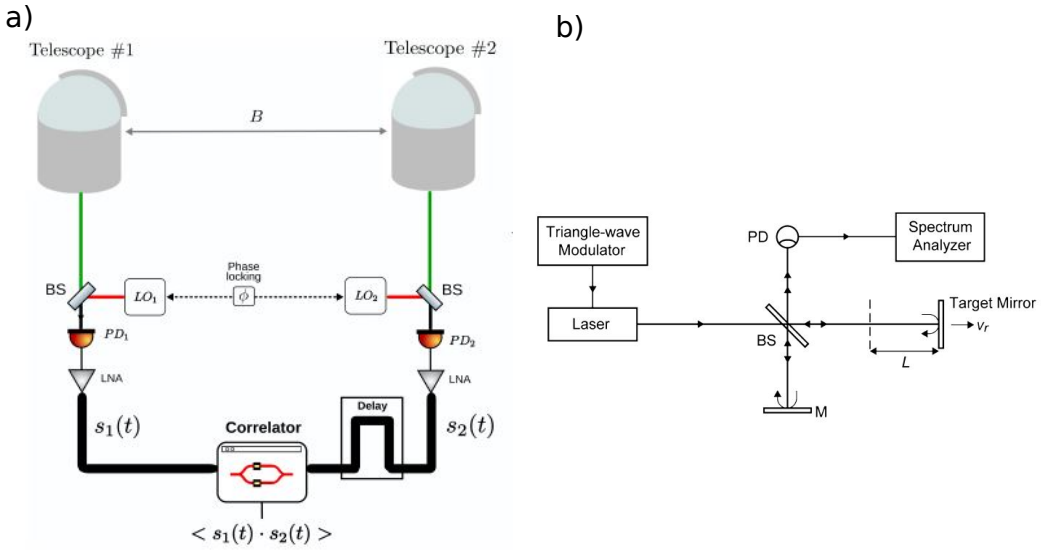

Figure 1.16: a) Scheme of a 2 telescopes heterodyne interferometer, where the starlight is mixed with two phase-locked local oscillators and detected by a fast photodetector. The two waveforms are then multiplied in a correlator whose output contains the coherent phase of the astronomical object. From [47]. b) Basic configuration of an frequency modulated continuous wave (FMCW) LIDAR with a triangularly frequency modulated laser; BS beam splitter. From [48].

A class of highly sensitive heterodyne receivers in the LWIR region is required for promoting technological applications and answering fundamental physical questions. This is relevant in observational astronomy and high resolution spectroscopy, already in demand for the development of low-noise and high frequency detection systems [49]. Ultrafast detectors are also required for coherent free-space LWIR communication platforms [50] and light detection and ranging (LIDAR) systems [51].

For instance, in an heterodyne interferometer composed of two distant telescopes (figure 1.16a) the incident light is coherently detected by the heterodyne mixing with two phase stabilized LO

lasers, on a fast power detector [52]. The beating signals are multiplied in a correlator. The resulting combined phase is proportional to the coherent flux of the astronomical object, which can thus be reconstructed by the Van Cittert-Zernike theorem [53].
The heterodyne interferometer is a common technique in the radio range. In the optical domain where the quantum photon noise is predominant over the blackbody background noise, heterodyne detection is not as efficient as a direct optical system. In the LWIR range, the advantage that an heterodyne interferometry detection can have over a direct detection depends on the availability of the devices technology. The heterodyne interferometer sensitivity is proportional to the square root of detector's bandwidth and to its quantum efficiency.
The only operated infrared heterodyne interferometer at Mount Wilson employed one HgCdTe detector with 1 GHz bandwidth and η=40% and one CO_2 laser for each telescope. For upgrading this interferometer, the possibility of QWIPs as receivers was suggested in 2000 [52] but then abandoned. Recently, after the advances in antenna-coupled QWIPs and the implementation of fast photonic correlators, the heterodyne interferometry technique has been proposed again [47]. With QWIPs or QCDs as receivers, the bandwidth would increase up to 100, gaining a factor of 10 in the overall performances. The use of QCLs also would bring more flexibility compared to the gas lasers.

The LWIR is a very much interesting region also for LIDAR systems, used in automotive vehicles and in stand-off detection of chemicals and aerosols. The 9 µm radiation is in fact particularly insensitive to fog and adverse conditions (which causes a scattering $\propto \lambda^{-2}$), to solar scintillations, to turbulence and offer eye-safe operation [54].
Heterodyne detection could be for example exploited in frequency modulated continuous-wave LWIR LIDAR (FMCW) for measuring distance and speed of a target using a frequency-swept QCL (figure 1.16b). In this system, the local oscillator is splitted in two: one part is a probe beam to be reflected by a moving distant target, then it is mixed with the other undelayed part by the square-law detector. From the obtained beat frequencies, the range and the speed of the target are retrieved.
The frequency sweep of the laser source and the detector bandwidth are critical for such systems as the resolution of the target size Δz is linked to the bandwidth of the modulation as $\Delta z = c/2\,\Delta f$.
To conclude the introductory chapter, we can state that the LWIR unipolar optoelectronics is very well adapted to coherent detection-based systems. QWIPs and QCDs response is in the GHz range, is linear under strong laser illumination and they can now work close to room temperature. All unique properties that are exploited in heterodyne platforms.

Chapter 2

Tunneling and transport in Quantum Cascade Detector

In this chapter we cover the basic physics of quantum cascade detectors (QCDs). We will present a density matrix theory for transport under illumination, and compare it to the response observed in measurements. We will then describe the theory of thermally activated electronic transport, in dark conditions.

2.1 Introduction

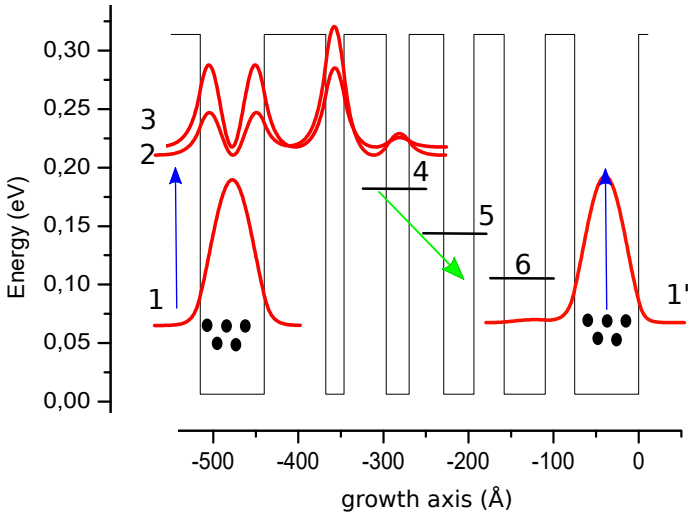

Figure 2.1: Band diagram of one period of the $Al_{0.3}GaAs/GaAs$ QCD at 0 V. The square moduli of the envelope functions involved in the detection are indicated in red. The black lines represent the extraction levels. The layer thickness in nm are $\underline{7}$/**6.7**/2/**4.6**/2.5/**3.8**/3.3/**3.3**/4.5/**3.2** with the first underlined layer doped at $n_{2D} = 5 \cdot 10^{11}$ cm^{-2} (black dots). Barriers are indicated in bold.

As introduced in section 1.2.5 of chapter 1, quantum cascade detectors (QCD) are unipolar intersubband devices, involving only electronic transitions. They can work, with appropriate well engineering, over a broad infrared range spanning from wavelength $\lambda = 3$ µm up to $\lambda = 18$ µm. The total device is a consecutive repetition of the same fundamental multilayer structure, called period. A representation of the square moduli of the envelope functions in the conduction band is

reported in fig. 2.1. Only one period is depicted. In every QCD period, the transport of the photoexcited carriers takes place through entirely confined electronic states, even without an applied bias. The carriers excited by light are extracted by a fast resonant tunnelling mechanism and flow toward the main well in the next period by a longitudinal optical (LO) phonon mediated relaxation. In photovoltaic mode, the photocurrent extraction is not degraded by a dark shot noise process, present in biased photoconductive detectors. The noise is still limited by the device's resistance, responsible for the Johnson noise.
The IV curve of a QCD device at room temperature is shown in fig. 2.2. Without illumination, a dark current flows into the device and vanishes at V=0 V. In this photovoltaic mode, when an illumination is applied, the I=0 point is shifted and an open circuit photo-voltage is generated. We

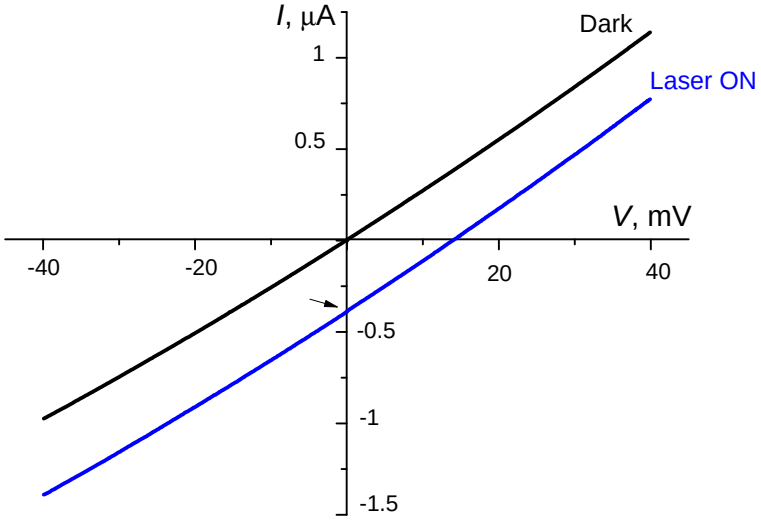

Figure 2.2: The volt-ampere characteristic of a QCD, at T=300 K for dark conditions (black) and under a 3 mW laser power (blue). The third quadrant (reverse voltage, reverse current) is the photodiode regime, the fourth quadrant (forward voltage, reverse current) is the photovoltaic effect.

are interested in the photocurrent generated at 0 bias (arrow in fig. 2.2), as at this point the dark current noise vanishes.
Maximizing the detector performances at 0 V bias is thus of prominent importance in the design of the QCD structure. This wavefunction engineering needs a simulation support capable to predict the main detector's characteristics. With this aim, the knowledge of the detector response under an applied bias, both in dark and under illumination, is a source of interesting information about electronic wavefunctions and doping, which reflects the quality of the device and of the grown heterostructure.
In this work we have developed a density matrix model for photocurrent, where non-resonant energy levels of the structure are treated with semiclassical rate equations while resonant ones are treated using coherent tunnelling processes. In the literature, QCD photocurrent transport has been analysed with rate equations in reference [55]. In this reference, the resonant tunnelling process between quantum states wasn't considered, despite it has the fundamental role to extract the photo-excited carriers from the upper state of the optical well. Density matrix models have been successfully developed for QCLs [56; 57; 58], and they will serve as a basis for the implementation of this formalism in QCDs. We will see that the proposed model is able to predict the performances of the studied QCD over a broad range of voltages and temperatures.
At the end of the chapter, we will also examine the dark electronic transport, starting from the analogy of a QCD with a Schottky diode developed in reference [59]. The aim is the extrapolation of the activation energy and resistance as a function of voltage and temperature. Dark current

noise voltage curves have already been described with quantitative agreement for a broad range of biases and temperatures, using a carrier hopping model of current [60]. In this work, we will present a simplified and easier to read, nevertheless efficient, description.

2.2 Sample structure and device description

The device used in this study is a GaAs/$Al_{0.35}Ga_{0.65}As$ QCD containing 8 periods, each composed of 5 quantum wells (QWs) and barriers, matched on a seminsulating GaAs substrate. Below and above the superlattice, two Si-doped ($n_{3D} = 6 \cdot 10^{18}$ cm^{-3}) GaAs contact layers were deposited with a thickness of 50 nm. The wafer reference is L1437 and its growth sheet is reported in Appendix A.1. The structure has been grown by MBE at the University of Leeds in the group of Prof. E.H. Linfield. The conduction band diagram associated to the nominal growth sheet is shown in figure 2.1 and the corresponding energy levels in fig. 2.5. The scheme in figure 2.1 represents as a black line the potential V(z), the conduction band edge of the heterostructure, in red the square moduli of the envelope functions involved in detection, at zero bias (see sec. 1.2.1 for the numerical implementation, in chapter 1). For wavefunctions 4,5 and 6 the square moduli have been replaced by a black line placed at the subband energy. Each quantum cascade detector period can be divided in two parts: a doped region where the absorption takes place (blue arrow) and an injection/extraction region where the excited carriers are feed to the next period (green arrow). In the absorption region of this device, the first quantum well contains three bound states (1,2 and 3 in figure 2.1), designed to provide an optical transition at a wavelength of $\lambda = 9$ µm, corresponding to an energy of 140 meV. The absorbing QW is Si-doped ($n_{3D} = 1.0 \cdot 10^{18}$ cm^{-3}) to act as an electronic reservoir (electrons as black dots). The excited bound state of the first well (2) and the ground bound state of the second well (wavefunction number 3) form an extended doublet across a barrier (6.7 nm), to enable an efficient extraction from the main well. The thickness of the following AlGaAs barriers and GaAs wells are designed in order to provide three bound states with an energy separation of the order of a longitudinal optical phonon E_{LO}=36 meV. They constitute a relaxation stage that scatters photo-excited electrons up to the following reservoir (number 4,5 and 6).
This sample has been fabricated as a standard mesa as described in section 1.2.6 in chapter 1, and as an array of double-metal patch resonators, whose process will be detailed in chapter 3. The patch device used in this study is composed of an array of wired 15x15 patches of size $s = 1.4$ µm for a total electrical surface of $A = 440 \times 10^{-8}$cm^2.

2.3 Building blocks for an efficient QC detector

In this section, we outline the theoretical groundwork for the study of the transport inside the QCD. Three basic blocks can be identified:

- Scattering processes between carriers;
- Carrier distribution at equilibrium in subbands;
- Intersubband optical absorption.

2.3.1 Scattering processes

Scattering mediates the carriers distribution and relaxation among levels, determining the electronic transport inside the device.
Three types of intersubband scattering are considered in this work:

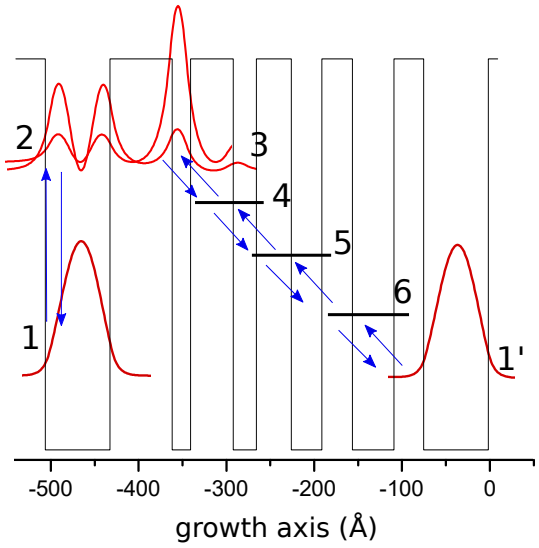

Figure 2.3: Band diagram presenting the main scattering transitions as blue arrows. Only adjacent levels are considered.

1. LO phonon spontaneous emission and absorption;
2. alloy disorder, caused by random disposition of different types of atoms;
3. interface roughness, caused by growth imperfection at the junctions.

Scattering rates are calculated using the Fermi Golden Rule, implemented in a QUAD-developed code described in [14] and based on reference [61].
Among these events, we can distinguish intrasubband transitions (electrons remain inside the subband but change their wavevector) and intersubband processes, as simplified in the scheme in figure 2.4 where transitions are represented by arrows. The scattering is inelastic if the final energy is different than the initial one (such as LO phonon scattering), or elastic, conserving energy (such as interface roughness scattering).

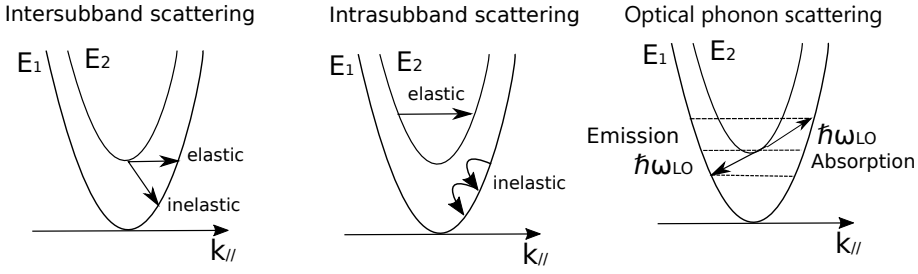

Figure 2.4: Schematic representation the parabolic dispersion relation of two subbands, with elastic and inelastic scattering processes as arrows (from left to the right): intersubband scattering, intrasubband scattering, intersubband emission and absorption of phonons

The intrasubband scattering rate is not included in our equilibrium model. It is generally between one and two orders of magnitude greater than the intersubband one and it is responsible for the thermalization of electrons inside the subband that happens in a fast time scale (order of 50-100 fs)[62]. In figure 2.3, the blue arrows indicate the main transitions. The approximation of a scattering involving only adjacent levels is appropriate whenever the overlap between non-consecutive wavefunctions is negligible and the excited levels are not significantly populated with

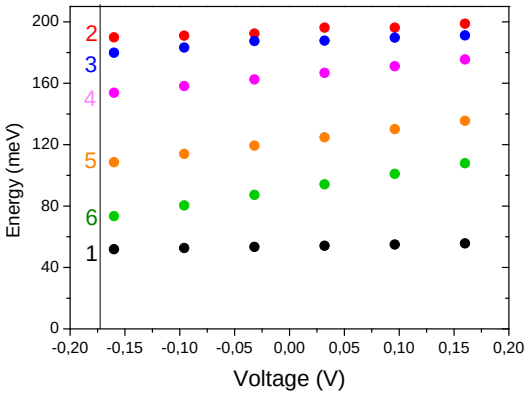

Figure 2.5: Level energies as a function of the voltage.

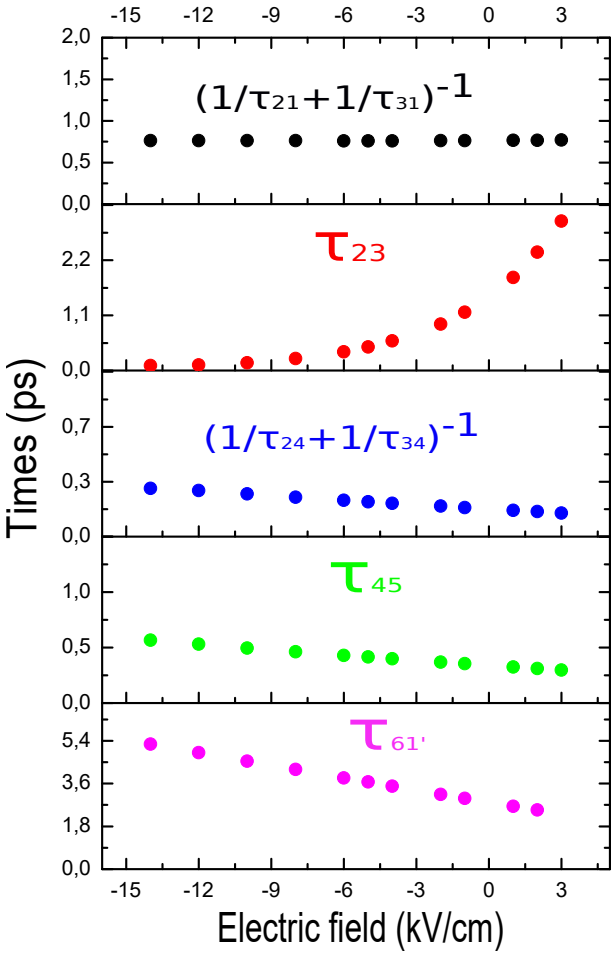

Figure 2.6: Calculated scattering times as a function of the applied bias at T=0 K.

respect to the doping density. To validate this approximation, table 2.1 reports the scattering times near V=0 V for transitions to the level 1, where carriers are mostly confined. Transitions

Table 2.1: Scattering times for transitions to level 1 from cascade levels, at 0 V and T= 0 K.

Transition	**Time** (ps)
2-1	0.82
3-1	12
4-1	86000
5-1	1.4E8

between 1-4 and 1-5 are less likely to happen since their scattering times is four and eight orders of magnitude slower than the times for transitions 1-2 and 1-3. For further levels, the transition probability rapidly decreases.
Scattering times for an electron at k=0 at T=0 K as a function of the applied electric field are shown in figure 2.6. As the levels 2 and 3 are tunnel coupled, for the transitions where the final level is 1 and 4, the total scattering time is presented. Times slightly depend on voltage, unless τ_{23} which is controlled by interface roughness and strongly depends on the bias-dependent spatial separation of the two envelope functions.
Table 2.2 reports the values of the scattering times for two transitions in the band diagram in figure 2.3. If the energy separation between subbands is larger than the phonon energy ($E_{LO} \approx 36.7$ meV in GaAs), the emission of a phonon is the dominant scattering process with a lifetime of nearly 1 ps at resonance. For lower energies, the emission of a phonon is forbidden. Therefore, the scattering is caused by a combination of the other mentioned mechanisms. In this case, interface roughness can provide a fast elastic transition between two states close in energy across a barrier [63].

Table 2.2: Scattering times in [ps] for transitions 2-3 and 5-6, at T=0 K and V=0 V.

Transition	**Energy separation**	$\tau_{\mathbf{LO}}$	$\tau_{\mathbf{IR}}$	$\tau_{\mathbf{tot}}$
2-3	10.7 meV	∞	0.27	0.26
5-6	37 meV	0.7	2.4	0.54

At finite temperature, the number of available phonons increases and also the phonon absorption becomes significant at room temperature. The Bose distribution factor $n_{LO} = \frac{1}{\exp(\frac{\hbar\omega_{LO}}{k_B T})-1}$ is included in the scattering time as:

$$\frac{1}{\tau_{ij,LO}(T)} = \frac{1}{\tau_{ij,LO}(0\text{K})}(n_{LO} + 1 \pm 1) \tag{2.1}$$

where the + is for phonon emission, and - for phonon absorption, the emission rate being always greater than the absorption rate. The other scattering mechanisms are considered independent on the temperature.

2.3.2 Equilibrium carrier distribution inside a QCD period

Whatever scattering event happens in a fermionic system at equilibrium, the average number of electrons that occupies a state is fixed by the Fermi-Dirac distribution function $f(E, E_F, T)$:

$$f(E, E_F, T) = \left[e^{\frac{E-E_F(T)}{k_B T}} + 1\right]^{-1} \tag{2.2}$$

The quantity $E_F(T)$ is the chemical potential, called Fermi Energy at T=0 K, where it sets the limit of occupied states. We will always consider the electron temperature to be the same as the lattice temperature, since the generated heat is negligible (unlike quantum cascade laser, an active device). The density of electrons per unit area in each subband i is given by the integral of the Fermi function starting from the energy E_i:

$$n_i = \int_{E_i}^{\infty} \frac{m^*}{\pi\hbar^2} f(E, E_F, T)\, dE = \frac{m^* k_B T}{\pi\hbar^2} \ln\left[1 + e^{\frac{E_F - E_i}{k_B T}}\right] \tag{2.3}$$

The total number of electrons is conserved (only 1 subband is occupied) and it is set by the doping density n_{2D} in the first well of each period. The doping density defines the E_F(0K) as:

$$E_F(0K) = \frac{n_{2D}\pi\hbar^2}{m^*} + E_1 \tag{2.4}$$

where E_1 is the energy of the first subband. With increasing temperature, electrons start to occupy states of subband 1 and the chemical potential for one well varies with the temperature as:

$$E_F(T) = k_B T \ln[e^{\frac{E_F(0)}{k_B T}} - 1] + E_1 \tag{2.5}$$

The chemical potential as a function of the temperature is shown in figure 2.7. The Fermi energy at 0 K is $E_F - E_1$=17.7 meV, for a doping density of $n_{3D} = 10^{18}\text{cm}^{-3}$ or $n_{2D} = 5 \times 10^{11}\text{cm}^{-2}$ in 5 nm doped well.

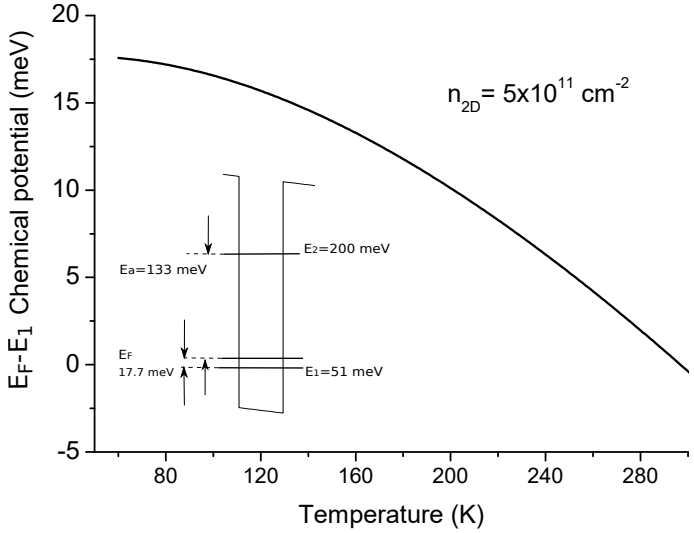

Figure 2.7: Calculated chemical potential relative to E_1 as a function of temperature.

When there is no external perturbation, such as an applied voltage or illumination, the QCD is in thermodynamic equilibrium and the Fermi-Dirac statistics holds. In this condition, we assume that a chemical potential is associated to every QCD period and it is independent on the applied bias [59]. We have now to define more precisely where the period starts and which levels are in balance with each other.

Inside the QCD structure, we remark that the relaxation time for transitions through the cascade, starting from subbands 2 and 3 down to 1' in figure 2.3, is lower (0.3-0.7 ps) than the scattering time of the transitions from 2 and 3 back to subband 1 τ_{21} (1 ps). Therefore, for definition, one period contains subbands 2,3,4,5,6 and 1', but not subband 1 (following the notation in figure 2.3).

Detailed balance

If a subband is at thermal equilibrium with the consecutive one, every electron's relaxation is always compensated by an electron's excitation mediated by the phonon absorption, for the thermodynamic principle of the detailed balance [59]. This means that for each pair of consecutive subbands (i,j) with energies $E_j > E_i$, the following equation must be satisfied:

$$n_i(V,T)W_{ij}^{abs}(V,T) = n_j(V,T)W_{ji}^{em}(V,T) \tag{2.6}$$

where n_i and n_j are the subbands occupation probabilities, W_{ij}^{abs} is the scattering rate for absorption and W_{ji}^{em} includes phonon emission rate $W_{LO} = (1 + n_{LO})/\tau_{LO}$ and the other scattering rates presented in the previous sec. 2.3.1, which do not depend on the temperature. The detailed balance relation is used to calculate the absorption rate, without including the k-space dispersion in the calculations. The absorption rate is thus derived from the Fermi-Dirac equilibrium population n_i and n_j and the LO phonon emission rate, which are exactly calculated. The subband probability n_j can be found from n_i by using equation 2.3:

$$n_j(V,T) = n_i(V,T)\frac{\ln\left[1 + e^{\frac{E_F(T)-E_j(V)}{k_BT}}\right]}{\ln\left[1 + e^{\frac{E_F(T)-E_i(V)}{k_BT}}\right]} \tag{2.7}$$

which simplifies for levels in the cascade far from the Fermi level $E_i - E_F >> k_BT$ as:

$$n_j(V,T) = n_i(V,T)\ e^{\frac{E_i-E_j}{k_BT}} \tag{2.8}$$

The eq. 2.8 is more adapted to an analytical study, while in our program we have implemented the complete one in eq. 2.7, valid for all temperatures. Knowing the equilibrium electron density, the absorption scattering rate is:

$$W_{ij}^{abs}(V,T) = W_{ji}^{em}(V,T)\ e^{\frac{E_j(V)-E_i(V)}{k_BT}} \tag{2.9}$$

From i=1' the chemical potential $E_F'(T)$ is taken into account:

$$W_{1'j}^{abs}(V,T) = W_{j1'}^{em}(V,T)\ e^{\frac{E_j(V)-E_F'(T)}{k_BT}} \tag{2.10}$$

The chemical potential $E_F'(T)$ is in this case calculated self-consistently, considering that the higher subbands start to be populated with increasing temperature but the carriers density is conserved. By solving the algebraic system for the 6 levels, including the charge conservation $\sum_i n_i = n_{2D}$, transition rates are found as a function of temperature and applied bias.
Figure 2.8 represents fraction of the population in each level as a function of the temperature for the electric field E=-1 kV/cm. On the right, a schematic of the population percentage in each subband, at temperatures T=78 K and T=300 K. The most populated level is 1', as expected. At T=78 K, the 1.6% of the total population is promoted in subband 5, the other subbands being almost empty. From the temperature of 150 K on, the population in higher energy subbands increases. The population incremental increase for level 2 is almost 6 orders of magnitude from T=78 K to T=300 K. This behaviour affects both the signal and noise detector properties, as we will see in the following sections.

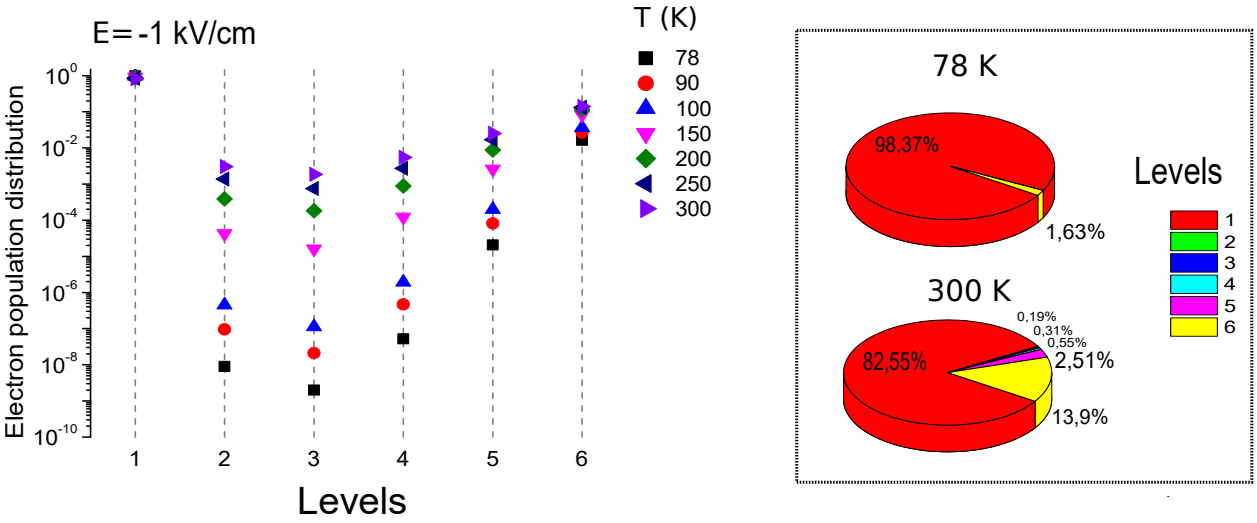

Figure 2.8: Electron distribution in each QCD subband as a function of the temperature in log scale. On the right, population percentage in each subband for T=78 K and T=300 K.

2.3.3 Intersubband absorption

When a radiation E_z with electric field in the z direction with frequency ω impinges on the QC detector with surface A, the electrons in the doped well are excited to subbands 2 and 3, which are tunnel coupled (diagram of fig. 2.3). The intensity I of this radiation is given by the Poynting theorem $I = 0.5\epsilon_0 ncE_z^2$ and results in a power $P_s = I\ A$. The adimensional absorption efficiency α_{2D} for a single quantum well is given in eq. 1.21 in chapter 1 [11], derived with the Fermi golden rule. We report its expression:

$$\alpha_{2D} = \frac{e^2 h}{4\pi\epsilon_0\ n_r m^* c}\ n_{2D} f_{n,n'} \frac{\Gamma}{(E_{n,n'} - \hbar\omega)^2 + (\Gamma)^2} \tag{2.11}$$

where ϵ_0 is the vacuum permittivity, n_r is the refractive index. The absorption spectrum assumes a Lorentzian shape with broadening at half width at half the maximum Γ usually around 10 meV. The oscillator strength $f_{n,n'}$ is defined in 1.19 in chapter 1. The absorption depends on the doping density n_{2D} and on the effective mass. For a GaAs single well with an optical transition at $E_{1,2}$=140 meV, typical values are n_{2D}=5×10^{11} /cm^2, n_r=3.3, Γ=10 meV, $f_{1,2}$=0.96, m^*=0.067 m_e. The single well peak absorption efficiency is α_{2D}=0.0072. If the device is processed as a mesa, the mesa absorption quantum efficiency has the expression defined in eq. 1.30 in 1.2.6. Since here we consider the electric field along the growth direction, the mesa absorption quantum efficiency we derive in simulations is not divided by the factor of 2 accounting for one polarization.
The simulated single-QW absorption spectrum is shown in figure 2.9 at T=78 K, for three different applied bias. The dashed lines in the same graph represent the spectrum for the individual transitions 1'-2 and 1'-3. As subbands 2 and 3 form a spatially extended doublet, in first approximation the total absorption coefficient is the sum of the absorption coefficients from 1' to 2 and from 1' to 3. The single spectrum contribution to the total sum depends on the oscillator strength of the transition, which again depends on the bias as the overlap of the envelope functions 2-3 depends on the voltage. In figure 2.10, the normalized oscillator strength is given for both transitions. For negative voltages the transition 1'-2 and 1'-3 share an equal oscillator strength, as 2 and 3 energy separation is comparable to their linewidth.
In the inset of fig. 2.9, the absorption for V= -30 mV is plotted as a function of temperature. The temperature decrease of the absorption from T=78 K to T=300 K represents a value of 14% and is mainly caused by doped well depopulation at high temperatures, as fig. 2.8 shows.

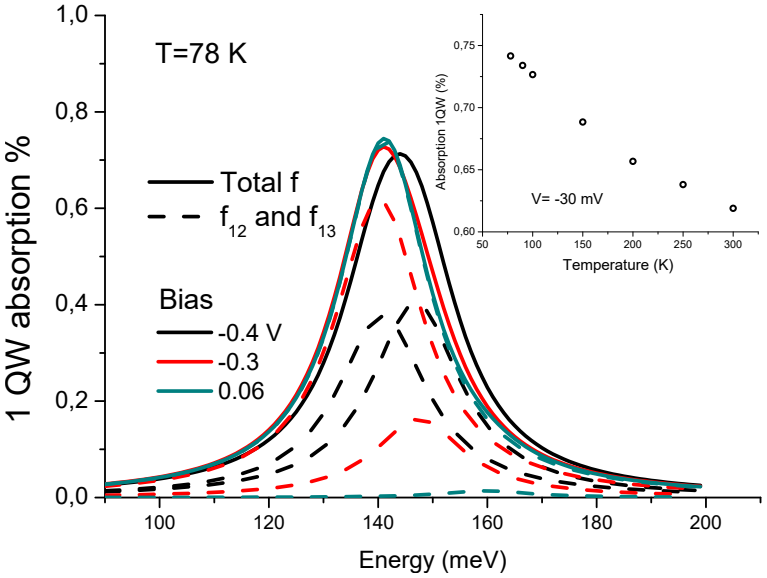

Figure 2.9: Simulated single QW absorption (α_{2D}) spectra for three different bias at T=78 K. The dashed lines shows the individual optical transitions of the tunnel coupled system: 1'-2 and 1'-3. In the inset, the absorption as a function of temperature for V=-30 mV.

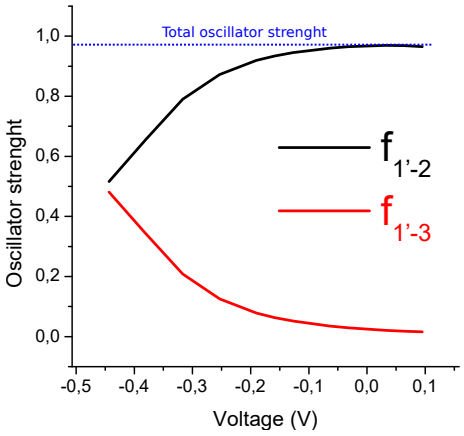

Figure 2.10: Oscillator strength for transition 1'-2 and 1'-3, involved in detection.

As it will be useful in the following section, we can derive an expression for the intersubband absorption time as:

$$\tau_{abs}(\omega) = \frac{\hbar\omega\ n_{2D}}{I\alpha_{2D}(\omega)} \tag{2.12}$$

where I is the radiation intensity, α_{2D} the absorption quantum efficiency, n_{2D} the doping density. The number of absorbed photons per second is in fact equivalent to $n_{ph}/s = A\ n_{2D}/\tau_{abs}$ which corresponds to the quantity $P\alpha_{\alpha_{2D}}/(\hbar\omega)$ as well.

In fig. 2.11, the calculated absorption time is plotted as a function of the incident intensity I (bottom axis) and corresponding power P for a photonic area of A=440 µm^2. For a blackbody source having an incident power of $P \approx 100$ nW the absorption time is $\tau_{abs} \approx 10$ µs, for a laser power of few mW it decreases to hundreds of ps. For high optical intensities, the rate of absorption becomes comparable to the inverse of the natural lifetime ($1/\tau_{LO}$), and the system saturates.

Absorption saturation The intensity reaches saturation when the electronic populations n_1 and n_2 become equal. The standard expression for absorption saturation for a single quantum well is [8]:

$$\alpha_{2D}(I) = \frac{\alpha_{2D,peak}}{1 + I/I_{sat}} \tag{2.13}$$

where the saturation intensity is I_{sat}. Referring to figure 2.11, saturation is reached when the absorption time is comparable to the relaxation time $\tau_{21} \approx 1$ ps which is around $I_{sat} = 300\ \mathrm{kW\,cm^{-2}}$. Commercial MIR QCLs deliver maximum power of $P \approx 100$ mW, therefore the absorption saturation intensity cannot be yet reached in tabletop experiments with QCLs.

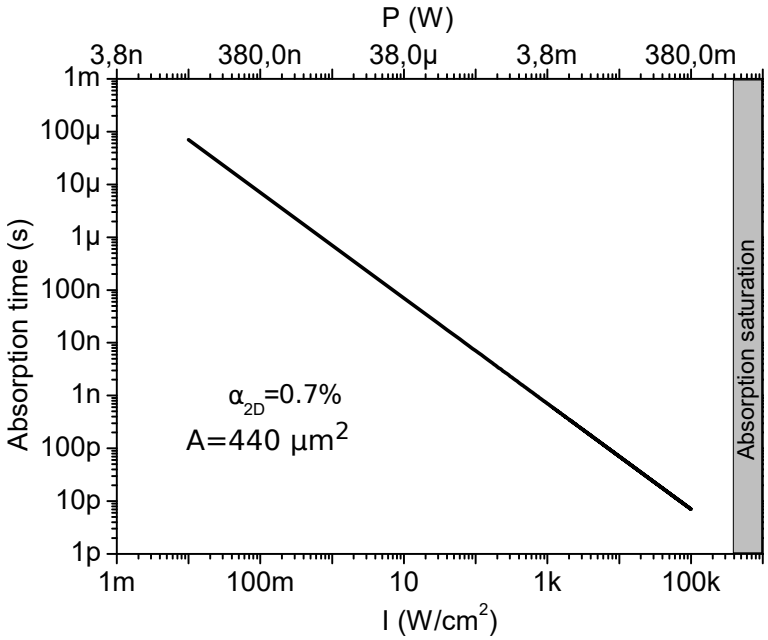

Figure 2.11: Absorption time as a function of the radiation intensity (bottom axis) and power (top axis) for a photonic area of 440 µm^2.

2.4 Electronic transport under illumination

In section 2.3.3, we have described the absorption mechanism occurring in the first doped quantum well of each period. For measuring a photocurrent signal at the contacts, absorption is not enough: only a fraction of the electrons are extracted with a probability p_{ext}, as introduced in section 1.2.5. Here we will detail its calculation. The photocurrent measured from a QCD processed in a mesa geometry can be written as (eq. 1.29):

$$I_{photo} = \frac{e\lambda}{hc} P_{inc,\lambda} \; 2 \; \alpha(\theta) \; \frac{p_{ext}}{N_p} \tag{2.14}$$

where $P_{inc,\lambda}$ is the incident power at wavelength λ, $\alpha(\theta)$ is the mesa absorption efficiency in eq. 2.11 which slightly depends on temperature as we saw in section 2.3.3 and p_{ext} is called extraction probability. The factor of 2 accounts for the fact that in our simulations the impinging electric field is only taken along the z direction. We note that as the number of periods N_p is also contained in the expression of $\alpha(\theta)$, for thin structures the photocurrent can be considered as independent on the number of periods.
A simple expression for p_{ext} is found considering that electrons can relax back to the main well, or they can relax down through the cascade. This is represented by the different arrows in the band diagram of fig.2.12. The total extraction probability p_{ext} is thus:

$$p_{ext} = \frac{\tau_{relax}}{\tau_{relax} + \tau_{ext}} \tag{2.15}$$

Since electrons undergo a tunnel transport across the middle barrier, the extraction comprises two mechanisms:

- Electrons oscillate between states 2 and 3;
- Electrons relax from subband 3 to 4.

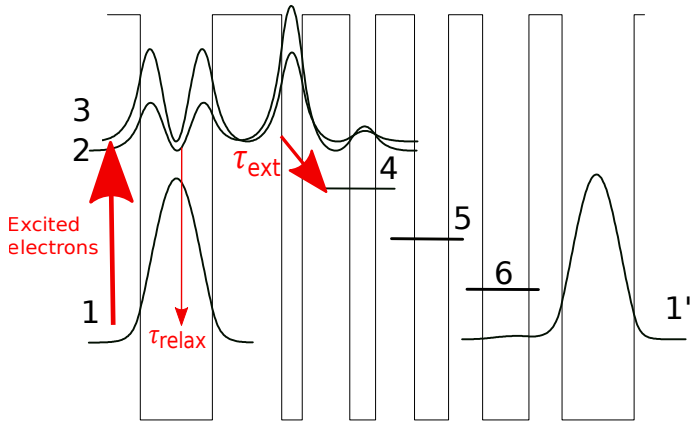

Figure 2.12: Band diagram of the device. The arrows represent, from the bigger to the smaller: the total excited electrons, the extracted ones and the electrons that relax back to the doped well.

These processes strongly depend on wavefunction's overlap, thus on the applied bias. In this section, we want to investigate the response as a function of the applied electric field. The starting point is to include the tunneling in the total Hamiltonian of the QCD system. In order to calculate the eigenstates of the system, two basis are possible, referred as *extended basis* and *localized basis*. The total hamiltonian is equivalently written as:

$$H_{eb} = H_0 + H_{tunnel} \tag{2.16}$$

where in the extended basis H_{eb} is the total diagonal hamiltonian where the tunnelling effect is included and the wavefunctions are delocalized over the whole structure. In the second framework, H_0 contains the kinetic energy and the unperturbed confinement potential. The tunnel is added as a coupling potential in H_{tunnel}. The localized basis does not diagonalize the total hamiltonian, but only H_0.

2.4.1 Tunnelling transport

In this section we will explain the two frameworks adapted to calculate the eigenstates for a given QCD potential, used in the model we have developed for the photocurrent. This section contains also the general rules we used to design an efficient QCD structure.

Extended basis

Firstly, the envelope function equation for the single carrier can be solved considering the set of wells and barriers as a whole potential. The subbands at k=0 are eigenstates of the associated Hamiltonian H_{eb}. The electron tunnelling across the barriers causes the delocalisation of the eigenstates between the first two wells. This basis is called *extended*, and it is used to calculate the spatial probability density distributions in figure 2.1.
The two wavefunctions in the first two wells involved in absorption are plotted in extended basis in figure 2.13 with numbers 2 and 3. Their minimum energy separation is the splitting energy Δ_{32}, which is the tunnelling coupling energy. The value of the minimum splitting energy is fixed by the barrier thickness, as reported in figure 2.15. The separation in energy of the two wavefunctions strongly depends on the bias, as shown in in figure 2.14. Our structure is designed to have the minimum splitting at 0 V (indicated by a red line in fig. 2.14), which is the ideal situation as the photocurrent is maximized for the point where the dark current noise is absent. At increasing bias,

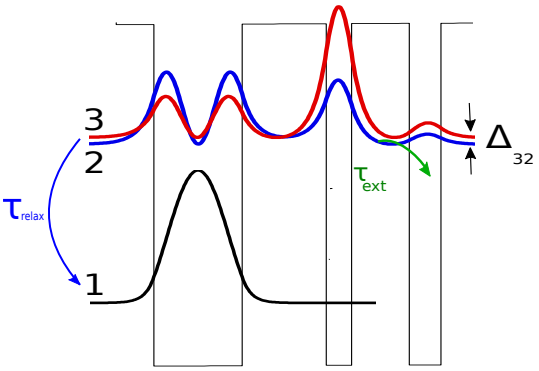

Figure 2.13: Section of the band diagram, with the extended doublet 2 and 3. 3 is the wavefunction more localized in the second well. Thickness in nm are 7,**6.7**, 2, **4.6**, 2.5 with barriers in bold.

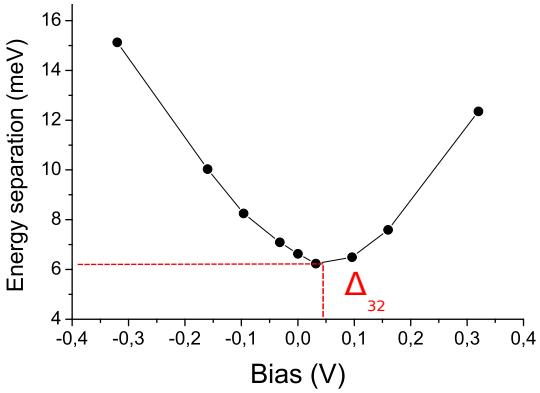

Figure 2.14: Energy separation between wavefunctions 2 and 3 as a function of the applied bias. The minimum is called Δ_{23} and is placed around 0 V for the nominal band structure.

the separation in energy between the two wavefunctions increases and the photoexcited electron extraction is less efficient.
Therefore, the photocurrent signal strongly depends on the applied bias and on the barrier's thickness. In order to choose the best barrier thickness, simulated photocurrent spectra at 0 bias as a function of the three barrier thickness are depicted in figure 2.16. We will see in the following how to calculate the photocurrent.

Choice of the barrier

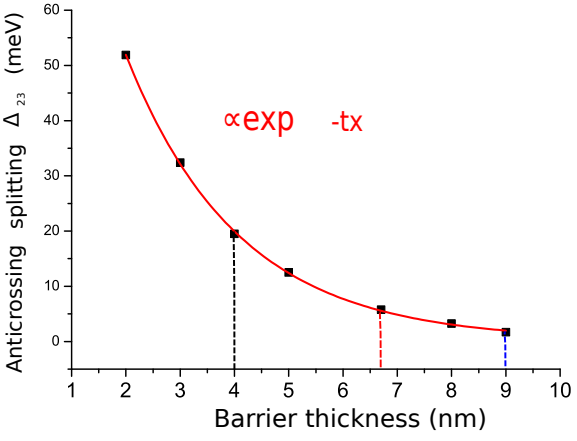

Figure 2.15: Anticrossing energy for different barrier thickness.

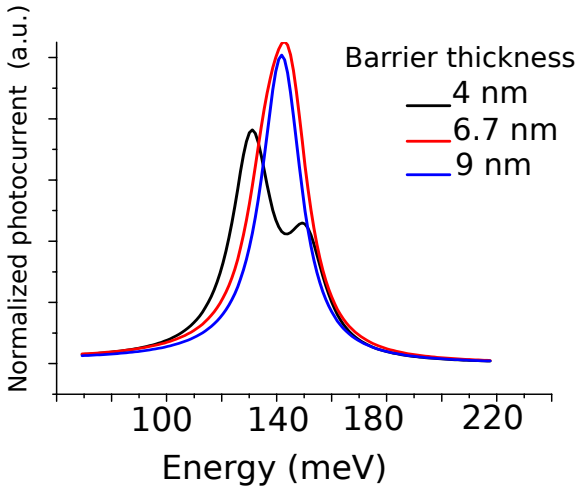

Figure 2.16: Simulated photocurrent spectra for three different barrier thickness at 0 bias.

We can consider three situations related to the choice of the middle barrier. When the wells are separated by a large distance, the coupling strength between the eigenstates is small and the quantum wells can be considered as independent. As the thickness of the central barrier is decreased, the energy levels interact to build a spatially extended doublet. In this case, the spectrum can be modelled with a Lorentzian function peaked at the energy 140 meV with a linewidth of Γ =10 meV (red curve in fig. 2.16). When increasing the barrier thickness, the photocurrent extraction

becomes less efficient. For thin barriers, the doublet is largely separated and the absorption spectrum consists of two curves separated in energy by Δ_{32}, each having a width of 10 meV (black line in fig. 2.16). The spectrum has the maximum signal when the barrier is such that the splitting Δ_{32} is around half the subband linewidth.
In our structure, the barrier width after the doped well has been fixed to 6.7 nm in order to have a splitting energy of 5.7 meV as in fig. 2.15 is indicated by a red dashed line, which corresponds to half the linewidth of a typical transition at λ=9 µm.
In this picture, the transport between the two tunnel coupled wavefunctions is approximated as instantaneous and no information about the coherence time of the tunnel coupled states is given. On the contrary, the dephasing time is considered in the localized basis framework.

Localized basis

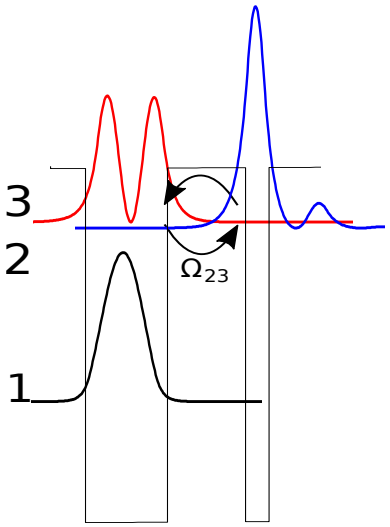

Figure 2.17: Section of the band diagram in localized basis

Alternatively, we can solve the Schrödinger equation in the form of localized wavefunctions in chosen subsets of the potential, for instance the QCD absorption and cascade region, separated by the 6.7 nm barrier as in figure 2.17. The tunnel is added as an energy coupling in a tight-binding approximation:

$$E_{tunnel} = \hbar\Omega_{32} = \Delta_{32} \tag{2.17}$$

The wavepacket coherently oscillates across the middle barrier, spending half of the time in either well with an angular frequency Ω_{32}. At resonance, the Rabi frequency is by design $\Delta_{32}/\hbar$. For the structure under consideration, with an anticrossing energy of Δ_{32}=5.7 meV (fig. 2.14), the associated Rabi frequency is Ω_{32}= 10 THz. The use of localised basis is no longer valid for very thin barriers, when the wavefunctions strongly overlap [14].

2.4.2 A density matrix model for QCD detection

The localized wavefunctions serve as a basis for implementing a density matrix formalism that describes the QCD photocurrent as a function of the applied bias and temperature. The theoretical basis about this formalism have been consulted in reference [64].
Our aim is to build an hybrid description including both resonant tunneling and scattering of electrons between localized states. Although this formalism has been extensively applied to describe

LIV curves in quantum cascade lasers, to our knowledge, a density matrix model has been applied to QCD only in reference [55] without considering the tunnelling effect.
For QCLs, a complete model can be found in ref. [56; 65]. In these references the QCL dynamics is described by including the resonant tunnelling into semi-classical rate equations. Dephasing, electronic populations and interaction with the optical field are calculated selfconsistently. Simplified and very useful versions can be found in references [66; 58; 14]. In the latter cases, temperature is not considered (electrons equally distributed in subbands) and the dephasing time is phenomenological.
QCDs differ from QCLs in their equilibrium conditions: while QCLs need an out-of-equilibrium condition to operate (population inversion), QCDs carriers at 0 bias are in thermodynamic equilibrium, as presented in section 2.3.2. Our approach, as we will see later in this section, combines the probabilistic nature of electron wavefunctions accounted by the density matrix formalism, with the macroscopic thermal equilibrium situation defined by the Fermi-Dirac statistics.

Theoretical definition

The ensemble of electrons in a QCD are in a quantum state constituted by a superposition of independently evolving states (each associated with a wavefunction $\psi(\mathbf{r},t)$) under the influence of various scattering events. Scattering events are responsible of the variation of the expectation value of the wavefunction and of its phase. As an example, for an arbitrary superposition of two states $|\psi\rangle = c_1|\phi_1\rangle + c_2|\phi_2\rangle$, the spatial probability density is $\langle\psi|\psi\rangle = |c_1|^2\langle\phi_1|\phi_1\rangle + |c_2|^2\langle\phi_2|\phi_2\rangle + c_1^*c_2\langle\phi_1|\phi_2\rangle + c_1c_2^*\langle\phi_2|\phi_1\rangle$. The first two terms do not depend on the phase, but the last two do as $c_1^*c_2 = |c_1||c_2|e^{i(\theta_2-\theta_1)}$. Moreover if $|\phi_1\rangle$ and $|\phi_2\rangle$ are eigenstates of the localised basis, the phase difference $\theta_2 - \theta_1$ will rotate at the energy difference, so that $|\psi|^2$ oscillates at the Rabi frequency Ω_{12}.
Coherent oscillations have been experimentally observed with pump and probe experiments in lasers structure for mid infrared frequencies.[67]
In a QCD, we expect the dephasing time to completely destroy the coherence, as the typical lifetime is of the order of 100-200 fs, comparable to the linewidth of the absorption spectrum[68]. More precisely, intersubband scattering events are responsible for population relaxation and for phase decoherence, and elastic intrasubband scattering events are responsible only for phase decoherence.
The density operator is defined as $\rho(t) = |\psi(t)\rangle\langle\psi(t)|$. Its matrix elements are ρ_{mn} and they represent:

- the diagonal elements ρ_{ii} are the probabilities to find the system in the state i. We will call them populations. The total probability is conserved,
  $Tr(\rho) = \sum_i^N \rho_{ii} = 1$ where N is the number of levels;

- the off-diagonal elements ρ_{ij} are related to the interferences between states i and j, they will be called coherences.

The equation of motion describing the time evolution of the density operator is the quantum Liouville equation:

$$\frac{\partial\rho}{\partial t} = -\frac{i}{\hbar}[H,\rho] \tag{2.18}$$

where H is the Hamiltonian of the system.

Hamiltonian of the system

The hamiltonian of a QCD device can be written as $H = H_{sp} + H' = H_0 + H_{tunnel} + H'$. H_{sp} can be written as:

$$H_{sp} = \begin{pmatrix} E_1 & 0 & 0 & 0 & 0 & 0 \\ 0 & E_2 & \hbar\Omega_{23} & \hbar\Omega_{24} & 0 & 0 \\ 0 & \hbar\Omega_{23} & E_3 & 0 & 0 & 0 \\ 0 & \hbar\Omega_{24} & 0 & E_4 & 0 & 0 \\ 0 & 0 & 0 & 0 & E_5 & 0 \\ 0 & 0 & 0 & 0 & 0 & E_6 \end{pmatrix}$$

States 2 and 3 are tunnel coupled with energy $\hbar\Omega_{23}$ and states 2 and 4 with $\hbar\Omega_{24}$. The other subbands have been considered uncoupled. Scattering and pure dephasing are incorporated in the matrix H' by considering that the intersubband relaxation times τ_i modifies ρ_{ii}, while the dephasing time, τ_{ij}, affects the coherence terms ρ_{ij}. The dissipative contribution to the Liouville equation can be written as:

$$\frac{1}{i\hbar}[H', \rho] = \begin{pmatrix} \frac{\rho_{11}}{\tau_1} - \frac{\rho_{22}}{\tau_2} - \frac{\rho_{66}}{\tau_6} - \frac{(\rho_{22}-\rho_{11})}{\tau_{abs}} & 0 & 0 & 0 & 0 & 0 \\ 0 & \frac{\rho_{22}}{\tau_2} - \frac{\rho_{11}}{\tau_1} + \frac{\rho_{22}-\rho_{11}}{\tau_{abs}} & \frac{\rho_{23}}{\tau_{23,//}} & \frac{\rho_{24}}{\tau_{24,//}} & 0 & 0 \\ 0 & \frac{\rho_{32}}{\tau_{32,//}} & \frac{\rho_{33}}{\tau_3} - \frac{\rho_{44}}{\tau_4} & 0 & 0 & 0 \\ 0 & \frac{\rho_{24}}{\tau_{24,//}} & 0 & \frac{\rho_{44}}{\tau_4} - \frac{\rho_{55}}{\tau_5} & 0 & 0 \\ 0 & 0 & 0 & 0 & \frac{\rho_{55}}{\tau_5} - \frac{\rho_{66}}{\tau_6} & 0 \\ 0 & 0 & 0 & 0 & 0 & \frac{\rho_{66}}{\tau_6} - \frac{\rho_{11}}{\tau_1} \end{pmatrix}$$

where $\tau_{ij,//}$ are the pure dephasing times of tunnelling electrons. τ_{abs} is the absorption time derived by the Fermi Golden Rule with a Lorentzian lineshape, from equation 2.12 and plotted in figure 2.11. The relaxation times τ_i are:

$$\begin{aligned} \tau_1^{-1} &= \frac{n_{LO}}{\tau_{12}^{LO,abs}} + \frac{n_{LO}}{\tau_{16}^{LO,abs}} \\ \tau_l^{-1} &= \frac{1+n_{LO}}{\tau_{l1}^{LO,emi}} + \frac{1}{\tau_{l1}^{alloy}} + \frac{1}{\tau_{l1}^{IR}} \quad \text{with } l = 2,3 \\ \tau_v^{-1} &= \frac{1+n_{LO}}{\tau_{v1}^{LO,emi}} + \frac{n_{LO}}{\tau_{1v}^{LO,abs}} + \frac{1}{\tau_{v1}^{alloy}} + \frac{1}{\tau_{v1}^{IR}} \quad \text{with } v = 4,5,6 \end{aligned} \tag{2.19}$$

where (LO,emi) accounts for the temperature dependent LO phonon emission and (LO,abs) for absorption. The absorption rate is calculated by means of the detailed balance in equation 2.6. All the scattering times are calculated as a function of the applied electric field with the Fermi Golden rule, as in figure 2.6.

Current density Classically, the current density is given by $\mathbf{j} = -ne\mathbf{v}$, where $\mathbf{v}$ is the velocity and n the volume electron density. We introduce the velocity operator for an electron motion along the growth direction z as:

$$v_z = \frac{i}{\hbar}[H_{sp}, z] \tag{2.20}$$

The operator expectation value is $< v_z >= Tr[\rho v_z]$, so the current is:

$$J = -ne\frac{i}{\hbar}Tr[\rho[H_{sp}, z]] \tag{2.21}$$

We define the matrix U as $U = \frac{1}{\hbar}[H_{sp}, z]$ whose elements are:

$$\begin{aligned} U_{ij} &= \frac{\Delta_{ij}}{\hbar} z_{ij} + \Omega_{ij}(z_{jj} - z_{ii}) \quad \text{for } i \neq j \\ U_{ij} &= 0 \quad \text{for } i = j \end{aligned} \tag{2.22}$$

where Δ_{ij} are the energy differences, z_{ij} is the matrix element of the position operator and $(z_{jj} - z_{ii})$ can be approximated as the length between the center of two consecutive wells. The current density is finally expressed in terms of matrices U and ρ:

$$J = -nei \sum_{i<j}^{6} U_{ij}(\rho_{ij} - \rho_{ji}) \tag{2.23}$$

In order to find the current density we need therefore to find an explicit expression for the different coherences, and this is done by solving the Liouville equation 2.18 at the steady state $\frac{\partial \rho}{\partial t} = 0$.

Density matrix with dissipation: superoperators

To simplify the numerical implementation and introduce the optical field, we remark that in the Liouville equation 2.18, the elements of the density operator ρ_{ij} undergo a linear transformation.[57; 65] In this representation, we can define some super-operators, operators that act on operators, representing dephasing and scattering. They couple directly the density matrix elements. The equation of motion of the density matrix can be rewritten as:

$$\frac{\partial \rho}{\partial t} = -\frac{i}{\hbar}[H, \rho] \equiv \mathcal{L}\rho \tag{2.24}$$

The super-operator $\mathcal{L}$ is called the Liouville operator or Liouvillian. If the observable ρ has the representation $\rho = (\rho_{11}, \rho_{12}, \ldots, \rho_{1N}, \rho_{21}, \ldots, \rho_{2N}, \ldots, \rho_{NN})$, its superoperator is therefore represented by a $\mathrm{N}^2 \times \mathrm{N}^2$ matrix. This formulation enables the use of standard linear algebra on superoperators and easy code implementation.

Two state system example: Kazarinov and Suris resonant tunneling

As a simplified example, we will write the superoperators included in our model for a two-state system, as the one represented in figure 2.17. This basic system has been treated firstly in the seminal paper [69] and reproposed for describing the current-voltage curve of a MIR quantum cascade laser in [70]. We will give here a reformulation of the current expression with Liouvillian superoperators. The two states in figure 2.17 here considered are 2 and 3, coupled across a barrier. The density matrix is therefore represented by a 2×2 matrix and the Liouville operator by a 4×4 matrix. Equivalently, the Liouvillian takes the form $\mathcal{L} = -\frac{i}{\hbar}[H_{sp},]$. If the density operator is $\rho = (\rho_{22}, \rho_{23}, \rho_{32}, \rho_{33})$, we can write the matrix of the Liouville operator $\mathcal{L}$ as:

$$\mathcal{L} = \begin{pmatrix} 0 & i\Omega_{23} & -i\Omega_{23} & 0 \\ i\Omega_{23} & -i\Delta E_{23}/\hbar & 0 & -i\Omega_{23} \\ -i\Omega_{23} & i\Delta E_{23}/\hbar & 0 & -i\Omega_{23} \\ 0 & -i\Omega_{23} & i\Omega_{23} & 0 \end{pmatrix}$$

where ΔE_{23} is the energy separation, called also detuning. The coherences decay with a dephasing time $\tau_{//,23}$ and the Liouville equations can be written as:

$$\begin{aligned} \dot{\rho_{23}} &= -\Omega_{23}(\rho_{22} - \rho_{33}) - i\frac{\Delta E_{23}}{\hbar}\rho_{32} - \tau_{//,23}^{-1}\rho_{23} \\ \dot{\rho_{32}} &= \Omega_{23}(\rho_{22} - \rho_{33}) + i\frac{\Delta E_{23}}{\hbar}\rho_{32} - \tau_{//,23}^{-1}\rho_{32} \end{aligned} \tag{2.25}$$

The corresponding damping superoperator $\mathcal{D}$ is thus:

$$\mathcal{D} = \begin{pmatrix} 0 & 0 & 0 & 0 \\ 0 & -\tau_{//,23}^{-1} & 0 & 0 \\ 0 & 0 & -\tau_{//,23}^{-1} & 0 \\ 0 & 0 & 0 & 0 \end{pmatrix}$$

Similarly, when adding the incoherent scattering between populations ρ_{22} and ρ_{33} the equation below follows:

$$\begin{aligned} \dot{\rho_{22}} &= \Omega_{23}(\rho_{23} - \rho_{32}) - \tau_2^{-1}\rho_{22} + \tau_3^{-1}\rho_{33} \\ \dot{\rho_{33}} &= -\Omega_{23}(\rho_{23} - \rho_{32}) + \tau_2^{-1}\rho_{22} - \tau_3^{-1}\rho_{33} \end{aligned} \tag{2.26}$$

The population relaxation is translated to a super-operator $\mathcal{F}$:

$$\mathcal{F} = \begin{pmatrix} -\tau_2^{-1} & 0 & 0 & \tau_3^{-1} \\ 0 & 0 & 0 & 0 \\ 0 & 0 & 0 & 0 \\ \tau_2^{-1} & 0 & 0 & -\tau_3^{-1} \end{pmatrix}$$

The equations of motion of the density matrix with dissipation for the steady state read:

$$\frac{\partial \rho}{\partial t} = [\mathcal{L} + \mathcal{D} + \mathcal{F}]\rho = 0 \tag{2.27}$$

By solving this algebraic system, we can find the populations and the coherences, that enter in the current equation 2.23. For the two level system, the current formula can be worked out analytically if we suppose that the matrix element z_{23} in 2.22 is negligible:

$$J = q\ n_{2D} \frac{2|\Omega_{23}|^2 \tau_{//,23}}{1 + (\frac{\Delta E_{23}}{\hbar})^2 \tau_{//,23}^2 + 4|\Omega_{23}|^2 \tau_3 \tau_{//,23}}. \tag{2.28}$$

where n_{2D} is the sheet electron density. The maximum current density is found when the two levels are in resonance, $\Delta E_{23} = 0$. As in reference [70], we can define two regimes depending on the values of Ω_{23}:

- weak coupling, if $4\Omega_{23}^2 \tau_{//} \tau_3 << 1$. For this value of Ω_{23}, the transport through the barrier is limited by the incoherent tunneling. For the detector, it corresponds to the situation of largest barrier depicted in 2.16, a sub-optimal condition due to the reduced extraction probability;
- strong coupling, if $4\Omega_{23}^2 \tau_{//} \tau_3 >> 1$. In this case the current is controlled by the lifetime τ_3, an optimal condition for the photocurrent.

The strong coupling regime corresponds to the situation where the energy splitting is comparable to the linewidth of the levels:

$$2\hbar\Omega_{23} \approx \text{FWHM} \equiv \hbar \left(\frac{1}{\tau_3} + \frac{2}{\tau_{//}} \right) \tag{2.29}$$

where FWHM is the full width half maximum of the intersubband transition as defined in ref. [71]. For the mesa processed device (the detector without the photonic architecture) the broadening of the spectrum is found to be FWHM$\approx$ 13 meV, and $2\hbar\Omega_{23}$ $\approx$13.52 meV which in turn set the dephasing time at $\tau_{//}$ $\approx$0.1 ps.

The two levels model can be used to evaluate the extraction time in the QCD extraction probability formula in 2.15 considering that:

$$\tau_{ext}^{-1}(V) = \frac{2|\Omega_{23}|^2\tau_{//,23}}{1+(\frac{\Delta E_{23}(V)}{\hbar})^2\tau_{//,23}^2+4|\Omega_{23}|^2\tau_3(V)\tau_{//,23}} \tag{2.30}$$

It is interesting to underscore from the formula an effective tunnel transport time across the barrier. We place the energies at resonance $\Delta E_{23}=0$. This enables to redefine:

$$\tau_{ext} = \frac{1+4|\Omega_{23}|^2\tau_3\tau_{//,23}}{2|\Omega_{23}|^2\tau_{//,23}} = \frac{1}{2\Omega^2\tau_{//,23}} + 2\tau_3 \tag{2.31}$$

In this expression the first term is the time taken by an electron to penetrate the tunnel barrier, $\tau_t = 1/(2\Omega^2\tau_{//,23})$. In our case it is $\tau_t \approx 50$ fs, which confirms the strong coupling regime controlled by the lifetime. The factor 2 comes from the resonant tunnelling process: as the electrons oscillate between the states in resonance, only one-half on average can be scattered in wells on each side of the barrier.
This simple equation has some limitations. Firstly, the current is limited by the lifetime of the level 3 without considering the relaxation through the next levels of the cascade. Secondly, it is limited to low temperatures where the carrier concentration in higher energy levels is negligible.
In this work, we have implemented a general model that calculates the photocurrent-voltage curve including the 6 levels, as a function of the temperature. The photocurrent as in eq. 2.14 is calculated from eq. 2.23. The two level model will be used to prove the quality of the general one. We adopted the numerical implementation presented in appendix C of ref. [14], that can also be easily re-adapted to an arbitrary number of levels and couplings.

Introduction of the optical field

In section 2.3.3 we have defined the absorption transition rate between two levels, under an incident radiation of intensity I. The absorption rate is given by the Fermi Golden Rule in eq. 2.11 and an absorption time, dependent on the incident radiation has been defined in eq. 2.12.
The core of our work is the adaptation and extension of the Liouvillian superoperator formalism to describe the photon absorption and the electron extraction through the cascade in a QCD, as a function of the temperature. Even under illumination, in QCDs the thermal equilibrium condition described in section 2.3.2 has to be always guaranteed. We will see here how this has been implemented.
In localized basis, the QCD ISB absorption can be seen as a pump mechanism that moves charge from the Fermi sea in subband 1 to subband 2. In this perturbative regime, the density of excited carriers is still negligible respect with respect to the doping density n_{2D}. A linear absorption superoperator containing the absorption rate $\mathcal{F}^{abs}$ can be defined. We assume that the superoperator $\mathcal{F}^{abs}$ acts as a perturbation on the equilibrium density operator ρ^0, by creating a charge difference $\delta\rho$:

$$\mathcal{F}^{abs} : \rho^0 \to \rho = \rho^0 + \delta\rho \tag{2.32}$$

Light does not create nor destroy charge, therefore the following charge conservation relations must hold:

$$\begin{aligned} \mathrm{Tr}(\rho^0) &= 1 \\ \mathrm{Tr}(\delta\rho) &= 0 \end{aligned} \tag{2.33}$$

The Liouville equation 2.27 becomes:

$$[\mathcal{L}+\mathcal{D}+\mathcal{F}']\rho = [\mathcal{L}+\mathcal{D}+\mathcal{F}'-\mathcal{F}^{abs}+\mathcal{F}^{abs}](\rho^0+\delta\rho) = 0 \tag{2.34}$$

where the superoperator $\mathcal{F} = \mathcal{F}' - \mathcal{F}^{abs}$ is the scattering superoperator without the absorption time. The equilibrium condition imposes that:

$$[\mathcal{L} + \mathcal{D} + \mathcal{F}](\rho^0) = 0 \tag{2.35}$$

The equilibrium density operator ρ^0 contains the equilibrium populations defined in section 2.3.2 and evaluated at each temperature. Therefore the final system reads:

$$[\mathcal{L} + \mathcal{D} + \mathcal{F}'](\delta\rho) = -\mathcal{F}^{abs}\rho^0 \tag{2.36}$$

By solving this last equation along with the charge conservation condition, we find the density operator $\delta\rho(V, T)$, therefore the photocurrent density. In the following sections, the results for the QCD under study are given and compared to the experimental results.

2.4.3 Results and comparison with experiments

The model gives the photocurrent density (in [Acm^{-2}]) as a function of the applied voltage, given an intensity I (in [Wcm^{-2}]) and temperature T, at the resonant absorption wavelength. The responsivity ($\mathcal{R}$ in [A/W]) is defined as the value of the photocurrent density J_{phot} divided by the incident intensity I impinging on the photodetector.
In this work, we have evaluated the performances of an AlGaAs/GaAs based QCD coupled to a photonic antenna. The study of its performances related to the photonic architecture will be treated in detail in the chapter 3. In this chapter, these measurements will be used as a test for proving the quality of the proposed model. AlGaAs/GaAs is a standard heterostructure, whose growth is now well controlled, thus a good benchmark for a theoretical model.

Approximations

In order to compare the simulated responsivity to the experimental one, two adjustments have been done concerning:

- Grown structure deviation from the nominal structure;
- Light-matter coupling geometry.

For the first point, although the device is supposed to work in a photovoltaic mode, experiments show that a small voltage is necessary to align the envelope functions 2 and 3 in resonance and maximize the performances. Real energy positions can significantly vary with respect to the simulated ones. As a consequence, the QCD nominal structure used for simulations has been slightly modified by raising up the energy of the subbands. The thickness of the wells in [nm] reported in bold, have been decreased with respect to the nominal structure as:

- nominal: [7, 6.7, **2**, 4.6, **2.5**, 3.8, **3.3**, 3.3, **4.5**, 3.2]
- modified: [7, 6.7, **1.9**, 4.6, **2.3**, 3.8, **3.1**, 3.3, **4.3**, 3.2]

The variations are uniform and always of the same order. In this way, the two extractor levels are in resonance at around -10 kV/cm, as it is observed in experiments.

In order to account for the photonic architecture, the simulated responsivity has been multiplied by a factor of 5.5 which takes into account the absorption enhancement due to patch-antenna geometry (whose experimental data are used for verification) with respect to a mesa device with an incident angle of θ=45°and with polarized light (eq. 2.14). This factor is given in eq. 3.19 and will be explained in detail in section 3.5.2.

Responsivity-voltage curves

Firstly, we present the dependence of the responsivity curves on the applied bias. Results for

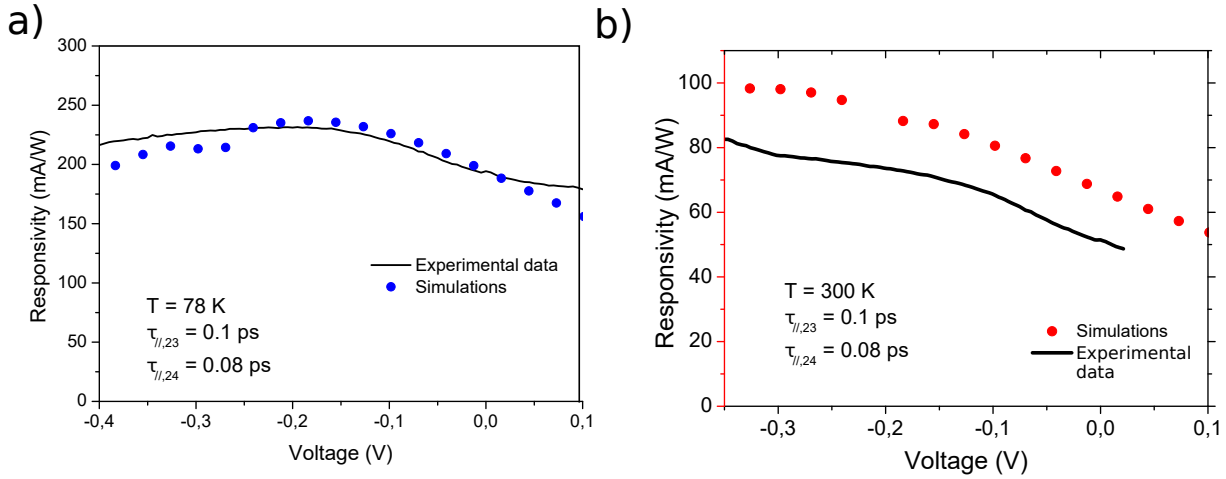

Figure 2.18: Photocurrent-voltage curves, a) for T=78 K b) T=300 K. Black lines are the experimental results.

simulations at T=78 K are shown in figure 2.18a) as blue points and in 2.18b) for T=300 K as red points. The black lines represent the experimental responsivity curves measured with a calibrated black-body source. The dephasing time between states 2 and 3 is set to $\tau_{23,//}$=0.1 ps and for states 3 and 4 $\tau_{24,//}$=0.08 ps resulting in a broadening comparable to that of the linewidth (FWHM=13 meV) of a mesa processed device, as explained in the previous section. These values are also confirmed by photocurrent spectroscopy measurements in quantum wells [68]. From the negative bias V=-0.2 V wavefunctions 2 and 3 start to align. In this resonant condition, the tunnelling is very efficient and the escape rate is solely limited by the inelastic scattering time 0.3 ps. This is why the curves are quite broad in this voltage range and don't present a very sharp maximum, as it would be for longer coherences. Simulations are consistent with experimental results in the voltage range from V= -0.4 to 0.1 V.

Extraction probability as a function of the temperature

QCD devices are very interesting for high temperature operation. However, their responsivity decreases as temperature increases. A factor of 2-4 for responsivity loss is systematically observed in the literature [72], whatever the structure used (i.e without resonant tunnelling as extraction mechanism). It is mainly caused by a degradation of the extraction rate in temperature. To give an insight into this phenomenon, we explicitly rewrite the extraction probability simply with phonon scattering rates between states 1,2,3, and 4 as:

$$p_e = \frac{W_3}{W_3 + W_2} = \frac{W_{34}^{em} - W_{43}^{abs}}{W_{21}^{em} - W_{12}^{abs} + W_{34}^{em} - W_{43}^{abs}} \tag{2.37}$$

where we have considered in the emission rate only the LO phonon scattering. We apply the detailed balance in eq. 2.6 to find the absorption rate as a function of the emission rate, then rewrite the temperature dependent extraction probability expression as:

$$p_e(T) = \frac{1}{1 + \frac{\tau_{34,0K}}{\tau_{21,0K}} \frac{[1-e^{-(E_2-E_1-E_{LO})/kT}]}{[1-e^{-(E_3-E_4-E_{LO})/kT}]}} \tag{2.38}$$

The phonon energy E_{LO} comes from the ratio between the absorption and emission Bose factors $n_{LO}/(1+n_{LO})$ reported in eq. 2.1. From this simplified formula, we can deduce why the responsivity degrades in temperature. Since the transition $E_2 - E_1 \approx 140$ meV is greater than the energy differences in the cascade $E_3 - E_4 \approx 20$ meV, the level 3 is populated and depopulated faster than the level 2. Therefore for the principle of the detailed balance, the relaxation rate W_{21} increases in temperature at the detriment of the responsivity. In figure 2.19 the simulated responsivity for a fixed V=-0.1 V is compared to the experimental one as a function of temperature. The extraction

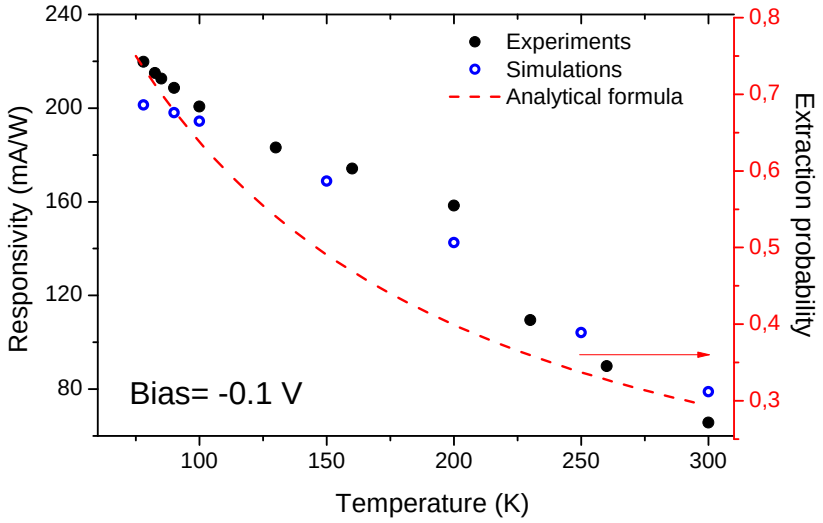

Figure 2.19: Responsivity as a function of the temperature for a voltage of V=-0.1 V: empty blue circles simulations, black dots experimental data and dashed line the behaviour predicted by the analytical expression 2.38.

probability calculated with the analytical expression in eq.2.38 is depicted as red dashed line. The responsivity decreases of a factor of ≈3 in the density matrix model in agreement with experimental results and with the analytical model.

Photocurrent saturation

In section 2.3.3, we have found that the absorption saturation intensity is of the order of $I_{sat} = 300\ \mathrm{kW\,cm^{-2}}$. We can further prove the quality of our model by studying the linearity of the photocurrent, as a function of the incident intensity. Simulated photocurrent density curves are plotted in 2.20 at T=300 K and V=-0.1 V. The radiation shot noise current density ($\sqrt{\frac{2e}{N_p} J_{photo}}$, with N_p the number of periods) in 1 Hz bandwidth has also been plotted, as it sets the ultimate limit of the detector's NEP. Johnson and dark current noise have been neglected for simplicity. The model predicts the correct saturation intensity and a theoretical dynamical range of 180 dB. This is a very wide range and one of the major advantages of the intersubband devices for heterodyne detection, as we will see in chapter 4.

Extraction probability: comparison with the two levels model

It is interesting to check the validity of our model compared to the extraction probability formula for the two state models given in 2.28. In the figure 2.21a) the calculated extraction probability at

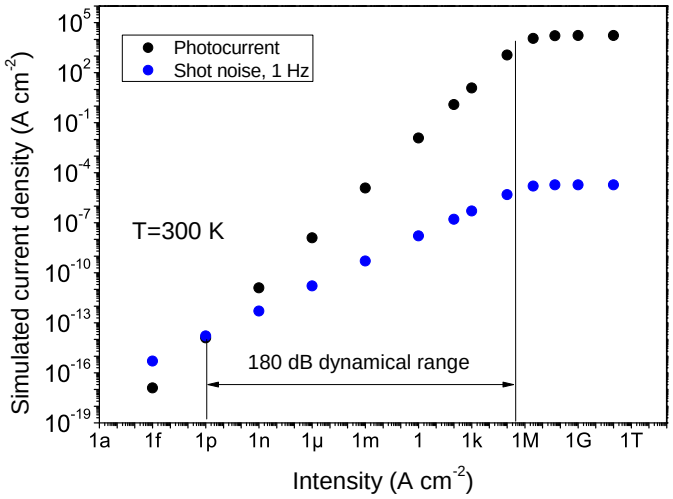

Figure 2.20: Simulated photocurrent density as a function of the radiation intensity at T=300 K (black points), and corresponding shot noise current density for 1 Hz (blue points)

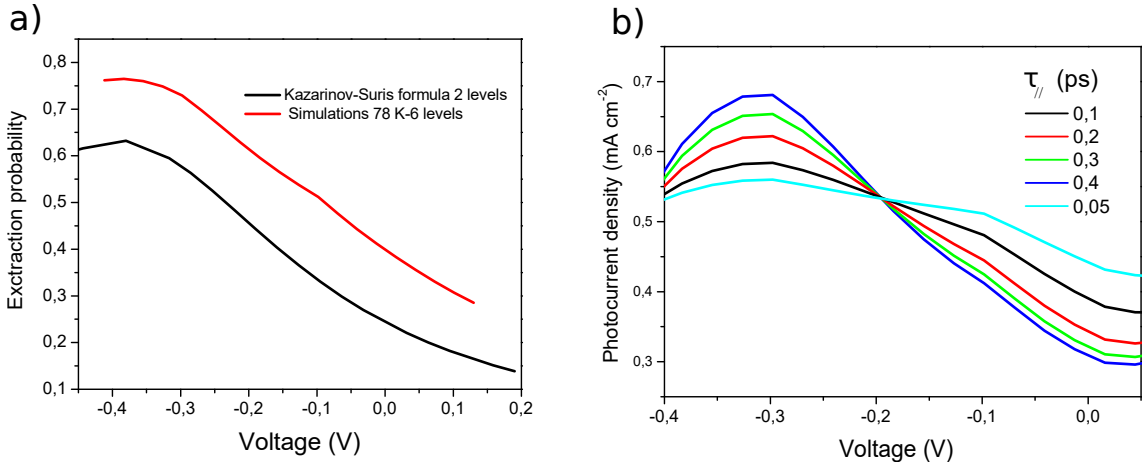

Figure 2.21: Left: escape probability calculated with the general model at T=78 K(red line) compared to the Kazarinov-Suris formula for two levels. Right: Simulated photocurrent density for different dephasing times at T=78 K.

T=78 K is represented in red, while the two levels model is given in black. The agreement between the two models is very good. Our model gives a greater maximum probability value of $p_{ext} = 0.75$ instead of 0.65.
Figure 2.21b) presents the simulated photocurrent density-voltage curve for different values of the coherence time $\tau_{//,23}$. As also expected from the formula 2.28, the curves have a Lorentzian shape, whose width is determined by the coherence time.

2.4.4 Extended and localized basis comparison

Throughout the section 2.4, we have made use of localized basis, with wave functions localized on either side of the barrier coupled coherently via tunnelling matrix elements.
We demonstrated that in our system the coherent transport is not a bottleneck for the current,

therefore it is interesting to compare this description of the photocurrent calculated in localized basis to an equivalent model based on semiclassical rate equations in extended basis.
In figure 2.22 we show the comparison between the responsivity as a function of voltage for localized basis with $\tau_{//,23} = 0.1$ ps (red line) and the responsivity calculated in extended basis (full and empty circles). The black dots represent the values obtained when the transport between states 2 and 3 is taken as instantaneous. The empty circles instead are values that consider a short transport time dominated by the interface roughness scattering time (IR).

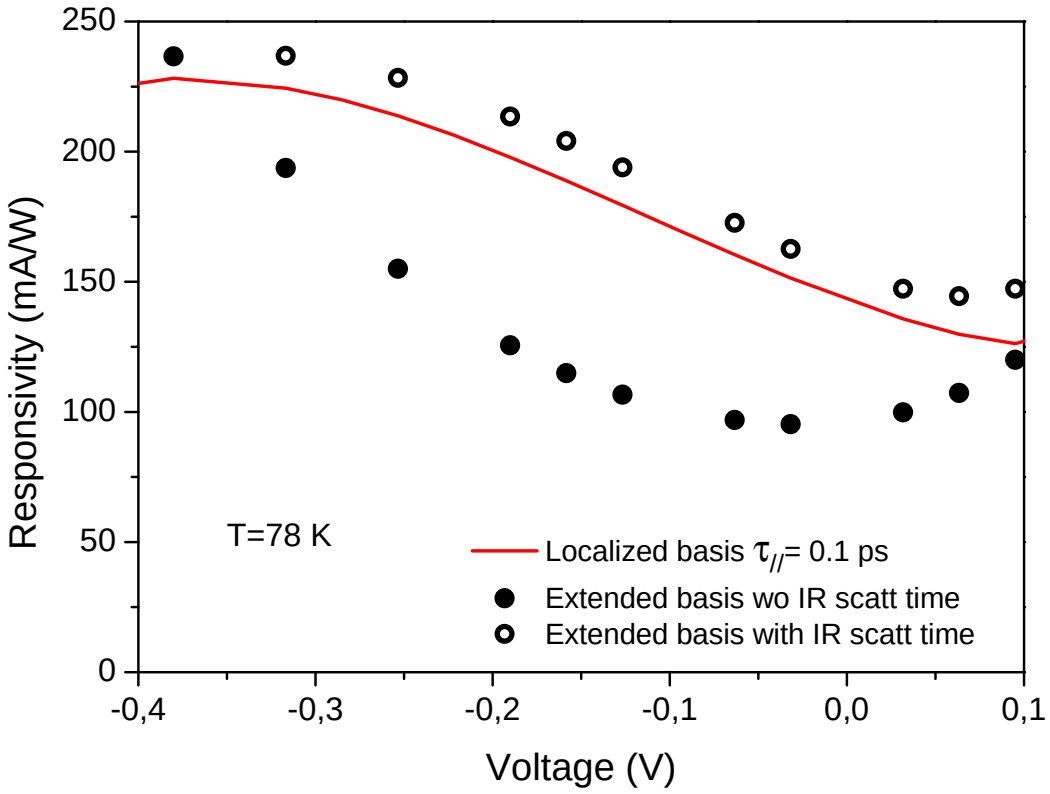

Figure 2.22: Comparison between responsivity calculated with extended (dots) and localized basis (red line). The empty circles are the calculations considering the interface roughness (IR) scattering time. The black dots are without including the IR time into the rate equations.

We deduce that in this case the extended basis formulation is equivalent to the localized basis as far as a short time between 2 and 3 is considered.
Interface roughness scattering arises because the separation between two epitaxially grown layers is never perfectly plane. This calculation, that can be found in reference [19; 63], assumes a phenomenological estimation of the defects concentration, penetration depth in the well/barrier and lateral extension. It can therefore be applied only to known interfaces, as in the case of AlGaAs/GaAs, and may not reproduce the variability of each MBE growth process. Therefore, the use of a coherent tunnelling time within localized basis gives a more accurate description than the extended basis model.

In conclusion, the density matrix formalism is a reliable and easy to read model where a phenomenological dephasing time is used for transport in tunnel coupled levels. It can be generalized to any number of levels, designs and different materials while avoiding heavy numerical procedures.

2.5 Electronic transport in dark conditions

In this section we will outline the basic principles underlying the detector's noise, in absence of illumination. More rigorous explanations can be found in references [73; 74]. We will neglect 1/f noise (high frequencies approximation). All the description will be done considering extended basis, and neglecting dephasing in tunnel coupling. In a QCD the noise spectral density (S) when a voltage is applied is usually written as the sum of two independent contributions, shot noise and Johnson noise:

$$S = \frac{2e|I_{dark}|}{N_p} + \frac{4k_BT}{r} \tag{2.39}$$

where I_{dark} is the measured dark current, N_p the number of periods, r the device's differential resistance.
In figure 2.23 the dark current noise spectral density S_{dark} and Johnson noise $S_{Johnson}$ for T=300 K are presented. It is clear from the figure that the most favourable regime is V=0 V, where S_{dark}=0 and as far as a small voltage is applied the dark current noise becomes dominant. In the following

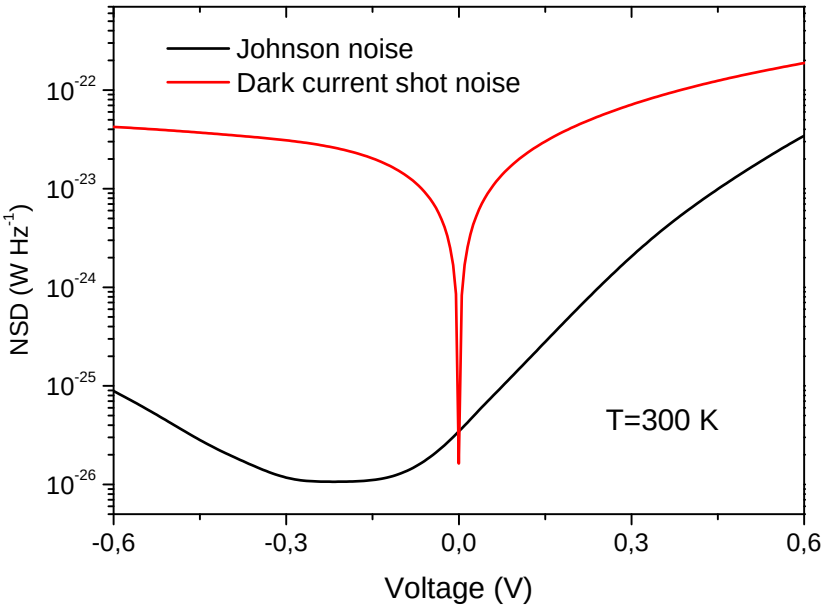

Figure 2.23: Experimental data. Noise spectral density as a function of the voltage for T=300 K. In red, the dark current shot noise. In black, the Johnson noise related to the differential resistance.

sections we will present a model describing the dark current and the Johnson noise.

2.5.1 Dark current

Dark shot noise current refers to the experimental situation where no IR illumination is impinging on the device, which means that the sample is surrounded by a shield kept at a temperature equal to or lower than the device's temperature. When no bias is applied, all periods share the same chemical potential and the total current density is zero.[75] When a bias is applied, the equilibrium is perturbed and the use of a single Fermi level for all the periods is no more valid. We adopt the notion of separate quasi-Fermi levels to describe the non-equilibrium populations between two consecutive periods (in photodiodes, it is used for populations in valence and conduction bands).[76; 75] Consider the band diagram given in fig. 2.24. All the subbands forming the cascade are in equilibrium (in figure 2.24, subbands in equilibrium with each other are depicted with the same color),

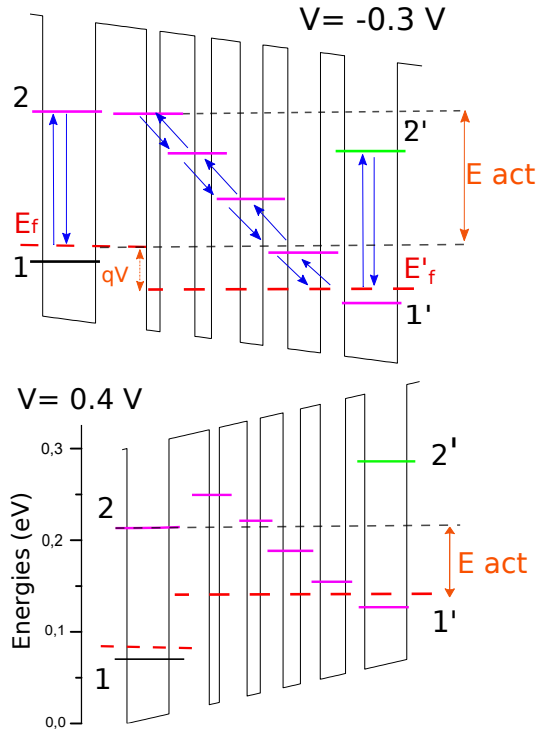

Figure 2.24: Band diagram for negative (up) and positive voltages (down). The subbands in equilibrium with each other are depicted in fuchsia. The orange dashed line represents the Fermi chemical potential. The activation energy, indicated by the orange arrow, is the energy difference between the chemical potential and the subband 2 energy.

since they are closer in energy with respect to the subbands forming the optical transition. Therefore, we define a quasi Fermi level from level 2 to level 1' and another quasi Fermi level in the previous period up to level 1. The difference between the two quasi Fermi levels $E_F - E'_F$ is the quantity qV, where V is the voltage drop between two periods. The total dark current density is the difference between the flow of electrons that enters and exits in one period from the level 1' and the flow that enters and exits to that period from level 1. This difference is proportional to the voltage drop between 1 and 1', qV.

$$J(V,T) = q\frac{\Delta n_1}{\tau_{21}} = q\frac{n_2(V,T)}{\tau_{21}(V,T)}\left[e^{-(E_2-E_F(T)-qV)/kT} - e^{-(E_2-E_F(T))/k_BT}\right] \tag{2.40}$$

which gives the total dark current density as:

$$J(V,T) = q\frac{n_2(V,T)}{\tau_{21}(V,T)}\, e^{-\frac{E_2(V)-E_F(T)}{k_BT}}\left[e^{qV/kT} - 1\right] \tag{2.41}$$

where n_2 is the equilibrium population density of subband 2 reported in section 2.3.2, τ_{21} is the temperature and voltage dependent phonon emission time reported in sec. 2.3.1. This expression has been implemented to obtain simulations of the dark J-V curves as a function of the temperature, presented in fig 2.25b). The experimental data as a function of temperature in the range from liquid nitrogen temperature (78 K) to room temperature (300 K) are shown in figure 2.25a).
As expected, the dark current vanishes at 0 voltage. At low temperatures the IV curve is asymmetric between negative and positive voltages, showing a rectifying behaviour as in photodiodes (for positive applied bias the device is more conductive as all the subbands start to align). However, moving closer to room temperature an increasingly symmetric behaviour between the two polarizations is observed. The main characteristics of the curves are well reproduced by eq. 2.41. We

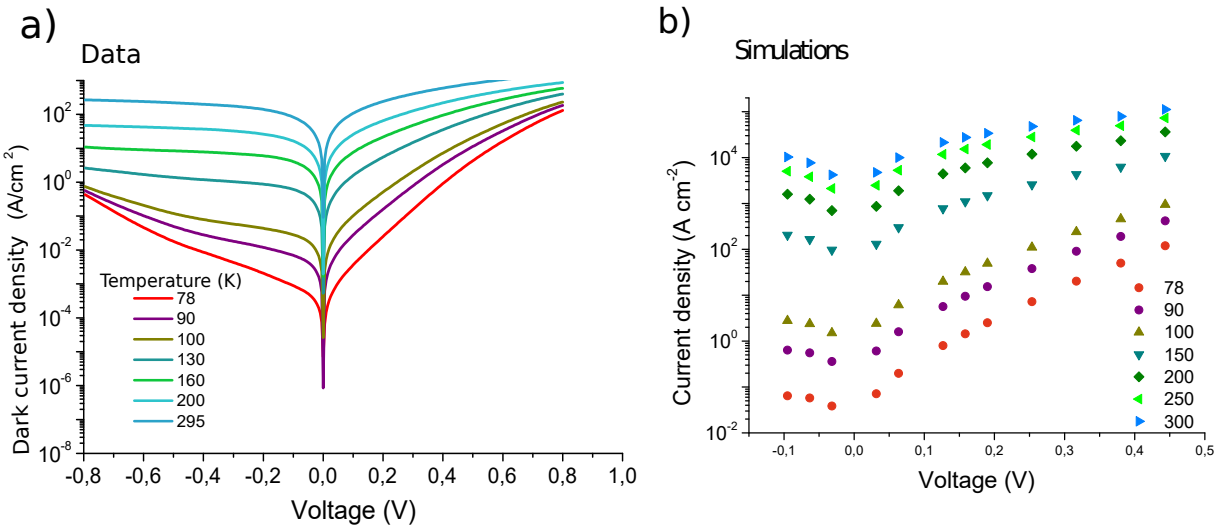

Figure 2.25: Dark current density-voltage curves for different temperatures. a) Experiments b) Simulations

note that in the measurements the dark current density is lower than in simulations, in particular at higher temperatures. This can be caused by an incomplete etching of the heterostructure during the processing of the patch cavity (therefore the electrical area of the heterostructure is greater than the one accounting for the top gold contact).

Diffusion regime

The dark transport in QCD can be related to the diffusion current in a Schottky diode [59]. Namely, the QCD has barrier height greater than k_BT and activation energy $E_a = E_2 - E_F$ which is the analogous of the Schottky barrier potential [77]. The diffusion takes place from a high density region (the doped well) to a low density region (cascade) and it is thermally activated. In the expression for the current density in eq 2.41, we can rewrite the subband population n_2 as a function of the population in subband 1 (taken as the doping density n_{2D}) and emission/absorption rate by using the detailed balance 2.6:

$$J(V,T) = q\frac{n_{2D}(V,T)}{l}\ \frac{l}{\tau_{12}(V,T)}\ e^{-\frac{E_2(V)-E_F(T)}{k_BT}}\ \left[e^{qV/k_BT}-1\right] \tag{2.42}$$

where we have multiplied and divided by l, a period length. The term l/τ_{12} can be considered as a velocity related to the motion of electrons from the doped well of one period to the next one. For small electric field, the velocity can be written as a mobility μ times the electric field on one period $v = \mu E$. By making use of the Einstein relations ([77]) for the diffusion, the mobility can be related to a diffusion coefficient as $\mu = -\frac{qD}{k_BT}$.
Therefore, the dark current- voltage characteristics of eq. 2.42 can be rewritten as [78]:

$$J(V) = q^2\ \frac{n_{2D}}{l^2}\frac{D}{k_BT}V\mathrm{e}^{-\frac{E_a}{k_BT}}\left[e^{-\frac{qV}{k_BT}}-1\right] \tag{2.43}$$

where V=E/l is the applied voltage on one period. This formulation is interesting because it enables to extract the activation energy as a function of the voltage, and therefore infer the information on the doping density. This is easier to see by reformulating an Arrhenius equation of the type:

$$\ln\left[\frac{JT}{J_0T_0}\right] \approx -\frac{E_a}{k_B\ T} \tag{2.44}$$

where $J_0T_0 = \ln\left[q^2\frac{n_{2D}}{l^2}\frac{DV}{k_B}\right]$ contains the diffusion coefficient. The factor $\left[e^{-\frac{qV}{k_BT}} - 1\right]$ has been neglected as at first approximation $qV > k_BT$.
An Arrhenius-type plot of ln(J T / J_0T_0) as a function of 1/T is expected to yield a straight line with slope equal to E_a/k_B. We performed the Arrhenius plot both for experimental dark current density J presented in fig. 2.25a) and for simulated one presented in fig. 2.25b). The results for some temperatures are presented as full circles in fig. 2.26a) and c) for simulations, and b) and d) for experimental data, for negative and positive voltages. The straight line represents the linear fit from eq. 2.44. In this way both experiments and simulations (from eq.2.41) are studied within the diffusion current analogy. Two parameters for the fit have been used: the diffusion coefficient and the activation energy.

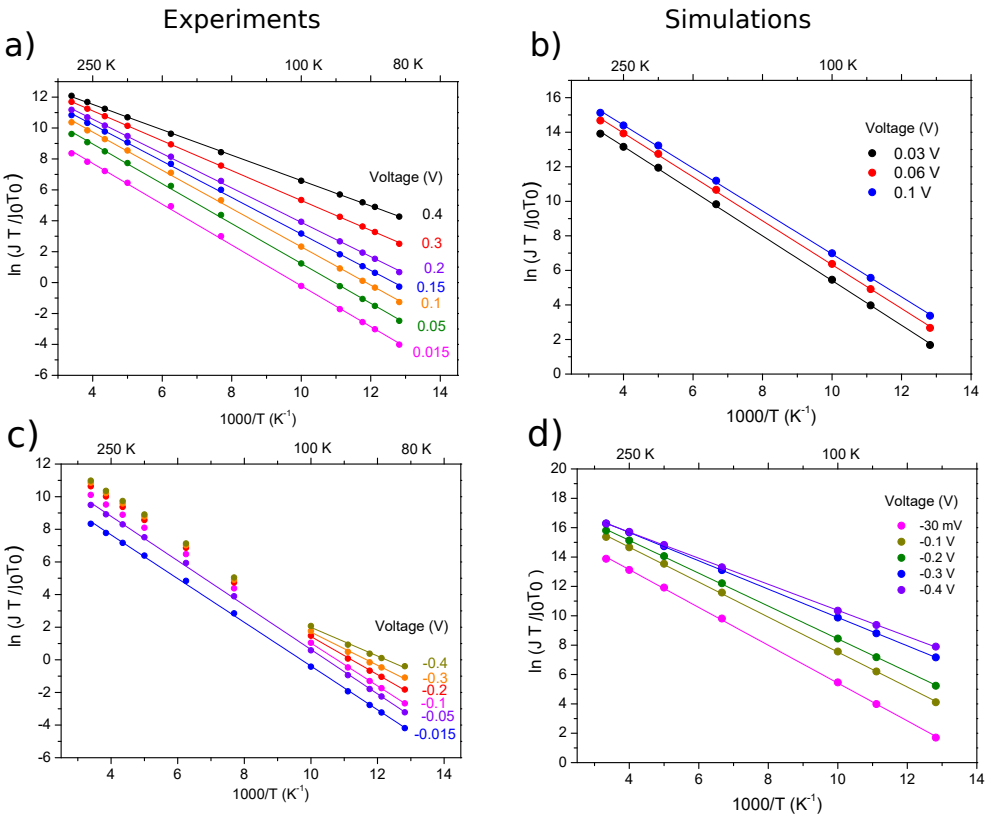

Figure 2.26: Arrhenius plot for: a)-c) Experimental dark current densities for positive and negative voltages; b)-d) Simulated dark current densities for positive and negative voltages. The curves are fitted with a linear function derived by the diffusion theory of a Schottky diode.

For experimental data, curves are fitted linearly for all the temperatures for positive bias (fig. 2.26a)), while in negative bias (fig. 2.26c)) two regimes with two different slopes can be defined. In reverse bis, the fit with equation 2.44 is valid only up to 120 K and for biases close to 0, our region of interest. From fig. 2.26 b) and d), we observe that simulated curves fit linearly for both positive and negative bias. This agreement suggests that the diffusion model of eq. 2.44 is qualitatively valid for small voltages across all the temperature ranges for experiments and simulations. The Schottky diode model was firstly proposed in the literature [79]. The difference with respect to this work stands in the fact that we have considered only consecutive electronic transitions as indicated in section 2.3.1. Concerning the parameters used for the fit, the quantitative estimation of the diffusion coefficient is currently under investigation as we didn't retrieve a good agreement between

simulations and experiments. This can be likely due to the underestimation of the electrical surface for the patch-antenna device, as explained in the previous paragraph. We have instead correctly retrieved the activation energy E_a, as presented in the following paragraph.

Activation energy

The activation energy used as parameter in the linear fit of 2.44 is shown in fig.2.27 as a function of the applied bias. In fig. 2.27 the black dots represent the values from the fit of the simulated curves

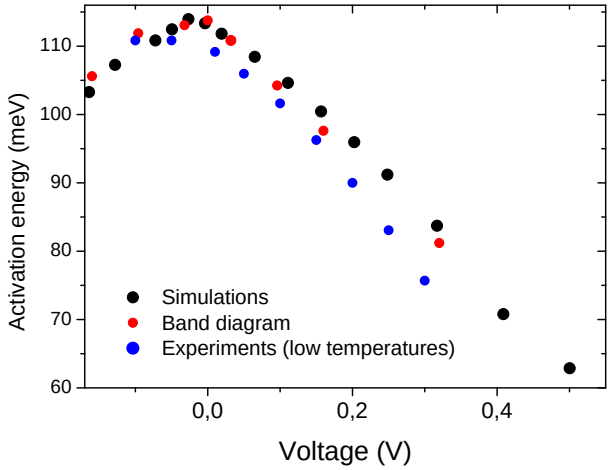

Figure 2.27: Activation energy for experimental data (blue), for simulations (black) and from the band diagram (red), as a function of the bias.

in fig. 2.26b) and c), the blue dots the values from the fit of the experimental data in fig. 2.26a) and c). In red, we report the activation energy obtained from the QCD band diagram, considering that the activation energy is defined as the energy between Fermi level E_f ($E_f - E_1$=17.7 meV using equation 2.4) and the subband 2 in the band diagram of figure 2.24. Activation energy is indicated with an orange arrow to the left of the figure 2.24, for negative and positive voltages. The values for experiments and simulations all agree with each other and with the theoretical value $E_2 - E_f \approx 120$ meV.
The maximum activation energy is found for 0 bias. When a positive bias is applied the energy separation is contracted, facilitating the electron flux from one period to the next and decreasing the activation energy. For negative voltages, the activation energy is supposed to be constant as the subbands separation is increased and then for higher voltages decrease as the subband 2 becomes closer to 1. We remark that energy activation is derived using the nominal doping density, which is a mark of the high quality of the growth of the heterostructure. Greater values of the activation energy are desired to build low-noise detectors, but the optical transition energy constitutes an upper limit. This implies that for a given wavelength, the only free parameter to keep a large activation energy is a low doping density.

2.5.2 Resistance

The Johnson noise in 2.39 depends on the differential resistance of the structure, which also depends on the temperature, the diffusion coefficient, and on the activation energy. From the dark J-V experimental curves in figure 2.25, the differential resistance as a function of the applied bias is presented in figure 2.28, from T=78 K up to room temperature. The low temperature resistance has a maximum of r=30 MΩ at 0 bias and it reaches at room temperature the value of r=260 Ω at

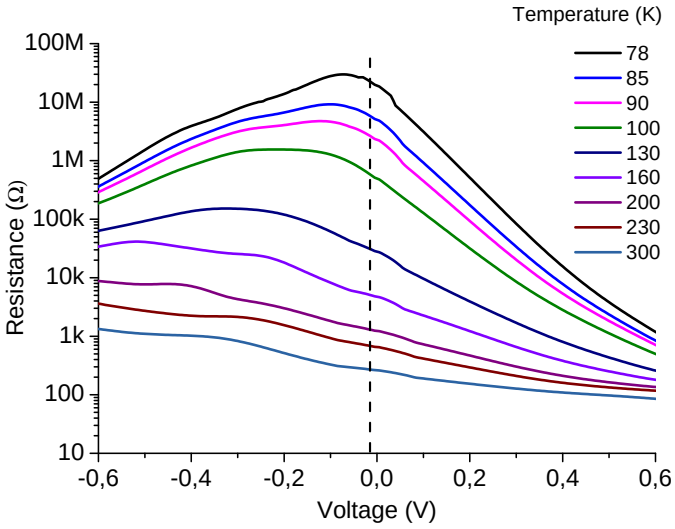

Figure 2.28: Experimental resistance-voltage curves for different temperatures.

0 V. We note that for negative bias, the differential resistance increases at high temperatures with respect to its value at 0 V: this is the regime where the diffusion is slower as a consequence of a wider subbands separation. The differential resistance can be also calculated from the derivation of eq. 2.41 and from the diffusion current of equation 2.43 as:

$$\mathcal{R}(V)A = \left(\frac{dJ}{dV}\right)^{-1} = \frac{l^2 k_B T^2}{q^2\ D\ n_{2D}}\ \ e^{\frac{E_a - qV}{k_B\ T}} \tag{2.45}$$

This formula can be used to study the differential resistance dependence on temperature. To this aim, we plot as empty dots the experimental and simulated differential resistances for a fixed applied bias of V$\sim$ 0 V respectively in fig. 2.29a) and 2.29b), as a function of the temperature. The data are fitted with the expression given in 2.45, depicted with a dashed line. The fitting parameters are again the activation energy E_a and the diffusion coefficient D.

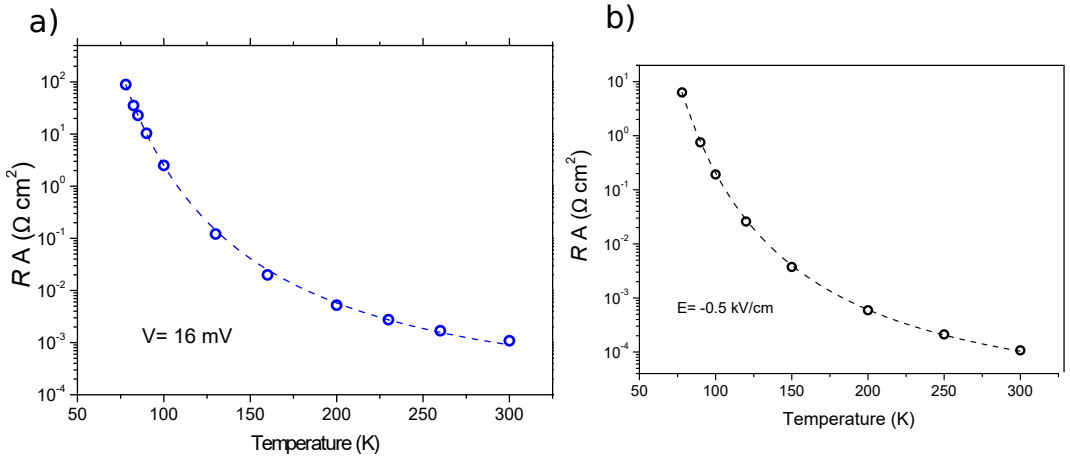

Figure 2.29: Resistance times the surface as a function of temperature for experimental data a) and simulations b). The dashed line is a fit from eq. 2.45

The fit accurately reproduces the value of the activation energy E_a=115 meV for experiences and

110 meV for simulations, in excellent agreement with the previously derived activation energy values. On the contrary, the diffusion coefficient is under investigation, and the discrepancy we obtain is likely related to an underestimation of the electrical area of the patch device.
In conclusion, in the section we have analysed the properties characterising the noise of a QCD device, such as the activation energy and the resistance. The use of the purely diffusion current for the Schottky diode, with a 1/T dependence in 2.44 is the different approach with respect to the literature where the thermionic emission current, with a T^2 dependence, is commonly used [79]. The fit of the resistance derived from 2.44 is in agreement with the experimental values of resistance for all temperatures, considering only consecutive levels.

Chapter 3

Meta-material for enhanced light-matter coupling

3.1 Introduction

In this chapter we analyse the detector's light-matter interaction. In this work, the photonic architecture that mediates the coupling of the detector with the external radiation is realized by inserting the QCD heterostructure in a double-metal cavity (a patch-antenna), patterned as an array [1]. The use of the double-metal cavity has several advantages for QWs detectors:

- it's a way to overcome the polarization selection rule for the ISB transition, permitting a simplified light-coupling geometry with respect to the mesa configuration with a 45°facet presented in sec. 1.2.6;
- the photon collection area is distinguished from the electrical area. The detector size is reduced, resulting in less dark noise without affecting the photocurrent signal. This antenna effect enables high-temperature operating devices;
- The incident electric field is enhanced locally by the cavity effect, which strengthen its interaction with the QWs.

In the first part of the chapter, we describe the geometry and the procedure we followed for the fabrication in clean room. We then provide a theoretical framework based on Coupled Mode Theory (CMT) equations, for describing how the meta-material enhances the performances of the low-doped detectors. This CMT analysis greatly simplifies the previous theoretical models, based on the resolution of the Poynting theorem in double metal cavities[80],[81]. While the CMT equations are already used to study light-matter strong coupling regimes in QWs [82], they were never used for the optimisation of weak-coupled detectors as our QCD. We will demonstrate that, with an appropriate choice of geometry it is possible to combine a large absorption quantum efficiency to an enhanced signal-to-noise ratio.
In the second part of the chapter, we present the experimental performance evaluation of the patch-antenna QCD, reported in reference [2]. These detectors have outperformed state-of-the-art QCDs at λ=9 µm with a room temperature responsivity of $\mathcal{R}$=80 mA/W. In conclusion, we indicate an optimization strategy of the patch-antenna detector which summarizes all the theoretical considerations of the chapter 2 and 3 and predicts a two-fold enhancement for the QCD responsivity at 0 bias.

3.2 Device description

The QCD heterostructure is inserted in an array of double-metal patch resonators, which provide sub-wavelength electric field confinement and act as antennas and contacts. The top layer is a Pd/Ge/Ti/Au ohmic contact and serves to extract the photocurrent. The array is visible in the electron microscopy image of fig.3.1. Each array is composed of 15x15 patches, electrically connected by 130 nm wide wires where a Ti/Au Schottky contact has been evaporated in order to prevent the flow of dark current from the underlying heterostructure. The resonant wavelength is defined by the lateral patch size s according to $\lambda = 2\ s\ n_{eff}$, where n_{eff}=3.3 is the effective modal index, higher than the GaAs bulk index. For $\lambda = 9$ µm wavelength, the size is of the order of $s = 1.4$ µm. The distance between each patch is fixed at a= 2 µm. A coupling efficiency of 80% has been confirmed by reflectivity measurements (which we will see later does not guarantee the maximum absorption quantum efficiency). The wires end to a contact pad isolated from the metal ground by a SiO_2 layer 800 nm thick. The contact pad and metal ground are connected by a wire bonding to a voltage source.

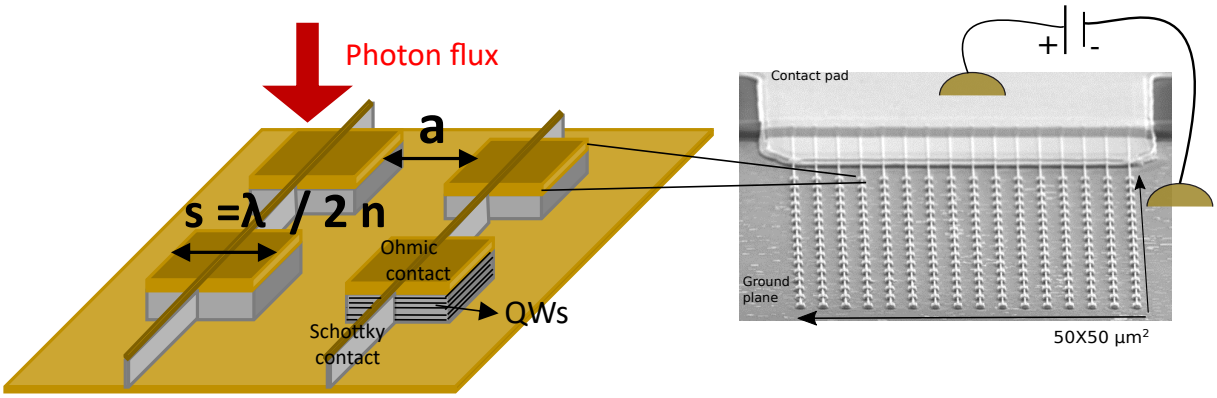

Figure 3.1: On the left, schematic of a series of patches of size s composing the device. The patches are separated by a distance a. The yellow colour stands for gold, the grey lined part between the two gold plates represents the heterostructure. Patches are connected with nano-wires 130 nm thick. On the right, SEM image of a device where the sketched wiring contacts connect ground and top metal.

3.3 Fabrication process

The fabrication of the double-metal patches is based on a thermocompressive wafer-bonding technique and it requires the use of electron beam lithography (EBL). It was mostly performed at the clean room of MPQ laboratory, Université de Paris. Here we resume the basic steps.

Definition of the cavity bottom gold layer

The fabrication starts with an ohmic contact evaporation (Pd/Ge/Ti/Au with thickness of 25/75/10/500 nm) onto the MBE detector structure and onto a host GaAs substrate (fig. 3.2). The two gold layers are fused together by thermocompression at 300°C, a procedure called wafer-bonding. This step is made at the University of Leeds, in the group of Prof. Edmund Linfield. The sample is flipped and the original GaAs substrate is etched, first mechanically then with a chemically selective citric acid solution $H_2O : H_2O_2 : C_6H_8O_7$ up to the etch stop layer. The etch stop layer is removed by pure Hydrofluoric acid and wash out with water. Care must paid to avoid edges etching and inhomogeneous surfaces. Angles can cause unreal estimation of distances during electron beam writing.

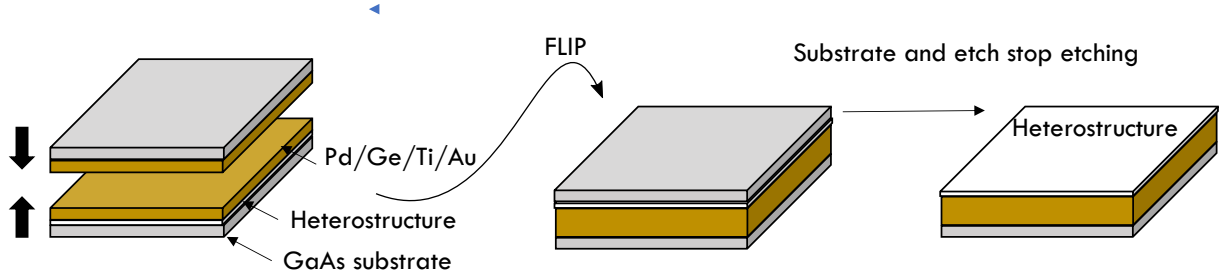

Figure 3.2: Schematic of the fabrication process. The white part is the heterostructure, in grey the GaAs substrate, in yellow the Pd/Ge/Ti/Au alloy. From left to right: the two gold layer are fused together by wafer-bonding. The sample is flipped and the GaAs substrate above the heterostructure is etched away.

Definition of the cavity top gold layer and wires

The array is composed of patches connected by wires 130 nm wide. In this step the top contact of the microcavity is defined. Before the EBL, the sample is spinned with a PMMA A6 (poly-methyl methacrylate) solution diluted in Anisole (ratio 2:1). There are two steps of EBL, one for the array of patches and the second for the wires. An alignment procedure is therefore required between the two, and constitutes the finest step. The two steps are necessary to permit an evaporation of an ohmic contact on the patches Pd/Ge/Ti/Au (15/45/5/85 nm) and a Schottky contact on wires (Ti/Au 15/75). The ohmic contact is diffused into the heterostructure by a post annealing of 1' at T=260°C. After the EBL, the semiconductor is removed everywhere except in a region around the cavities defined by UV lithography. In this way, the ground plane of gold is revealed.

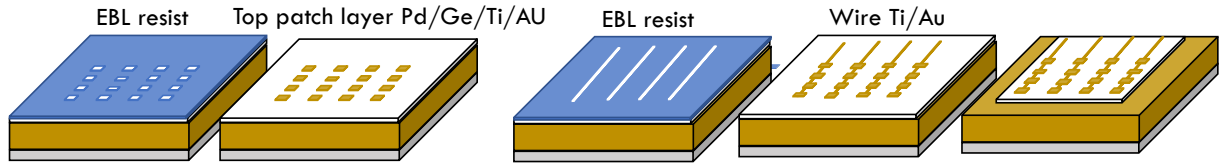

Figure 3.3: From left to right: EBL steps for the patches, with following Pd/Ge/Ti/Au evaporation. Second EBL alignment for wires and its Ti/Au evaporation. Optical lithography is then used to reveal the ground plane at the bottom.

Electrical contacts

Optical lithography is used to define the electrical read-out contacts. An insulating layer is necessary to electrically disconnect the ground plan of gold (the bottom of the cavity) from the top of the cavity. A layer of 800 nm thick SiO_2 is deposited throughout the sample by Plasma-Enhanced Chemical Vapor at 280°C and with a rate of 400 nm/min. It is then removed from the metallic parts by Reactive Ion Etching (RIE). Above the insulating layer, a gold contact, designed with a positive optical lithography, is evaporated (Ti/Au in 10/400 nm). For this, the sample is tilted in order to electrically link the wires to the top pad.

Final etching

After cleaning the sample, an Inductively Coupled Plasma (ICP) final etching of the 300 nm semiconductor around the patches is operated with a fast rate of around 25 nm/s. The gold on top serves as mask. This is a very disruptive etching, but enables a fine undercut of the cavity.

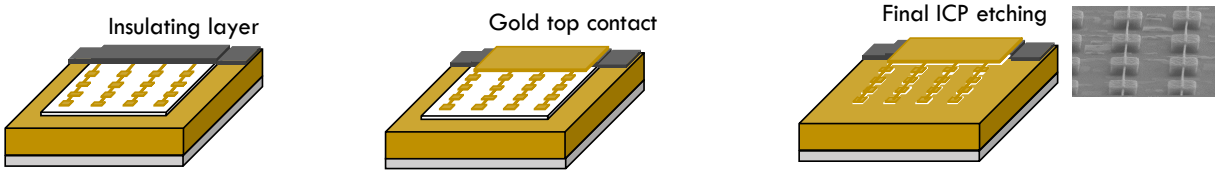

Figure 3.4: From left to right: deposition of the 800 nm SiO_2 insulating layer, then Ti/Au contact pad and final ICP etching where the semiconductor is left only within the cavity and wires.

3.3.1 Process yield and list of samples

The double-metal architecture was applied to enhance the performances of a LWIR quantum well infrared detector (QWIP) for the first time in 2014. [83] Over the years, the process improvements targeted at the elimination of any possible parasitic contribution to the detector dark current and Schottky contacts. In ref. [83], it was demonstrated that dark current was substantially reduced when the semiconductor part around each cavity was etched away by ICP. In 2018, an optimised LWIR QWIP reached unprecedented performances, notably at room temperature. [1] This was possible thanks to a general processing optimisation, including the use of two different contact depositions for wires (a Schottky contact) and patches (an ohmic contact), aimed to extract the current solely from the double-metal patches.
At this stage, the maturity of the device technology was promising enough for the transfer to industrial partners for commercialization. However, the process fabrication had a yield as low as 10%, and devices suffered in particular of electrical breakdown.
During this PhD work, the fabrication variability has been reduced and its reliability increased. A key issue was the quality of the insulating layer under the contact pad. A top view of two devices is shown in fig. 3.5 on the left and a lateral section of the contact pad on the right. Devices

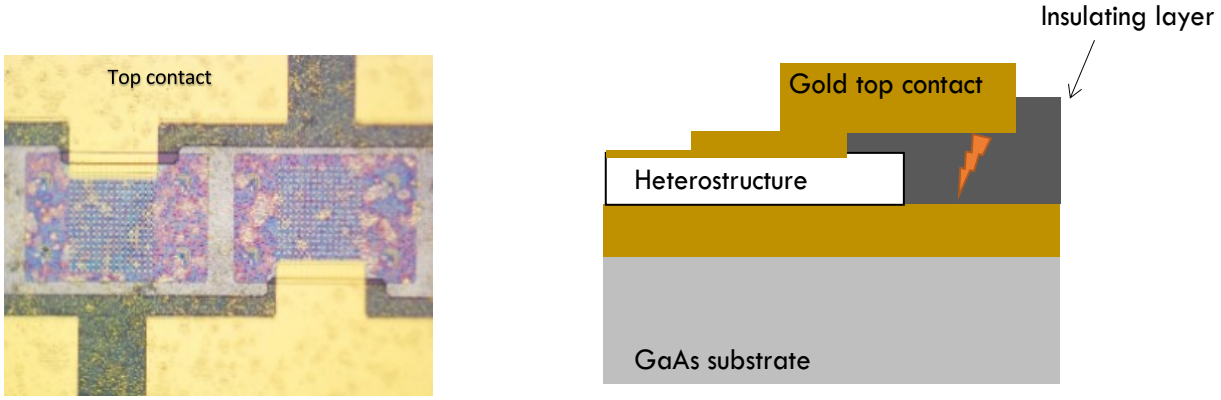

Figure 3.5: On the left, optical microscope image view of two finished devices. On the right, schematic of the lateral section of the contact pad showing the insulator layer, where parasitic current leakages can cause a breakdown.

degradation can be caused by dielectric breakdown and electrostatic discharge (ESD). Charges are injected inside the insulator by tunnelling, and there reside in very long lived traps. Traps are often constituted by interfaces and defects whose presence depends on the insulator deposition rate and temperature. For the patch-antenna devices, Si_3N_4 with a deposition temperature of 150 °C was used because the wafer-bonding was supposed to break at higher temperatures. In this work, this material was replaced by a 280°C SiO_2, known also to have a better stoichiometry. The total deposition time was reduced to 2 min, during which the gold bonding has proven to resist.
Two different heterostructures were processed (growth sheet in appendix, growth from University

of Leeds):

- L1436 QWIP, for a total of 200 devices;
- L1437 QCD, for a total of 410 devices.

From the QCD batch, all the devices tested having an array composed of 15x15 patches worked properly. In the same batch, devices with a single patch measuring just s=1.4×1.4 µm^2 were also inserted. Despite the small surface, a yield of 70% was obtained for them. For the QWIP batch 90% worked as intended. Stability over time has been proved. Patch-antenna QWIPs with an optimised active region served as fast heterodyne receivers, as presented in chapter 4. Patch-antenna QCD performances will be discussed in this chapter.

3.4 Coupled mode theory for IR antenna-coupled detection

In chapter 2 we described the photocurrent vs voltage curve in a QCD using a density matrix model, without providing details of the external light coupling geometry.
The detector light-matter coupling is the topic of this section. We expect from a photonic architecture to be beneficial both for the quantum effiency and for the signal to noise ratio. In this work, the QWs heterostructure is embedded between two gold layers that act as a cavity and as an antenna. This modifies the detector's absorption and increases the coupling with the external radiation. In this section, the effect of the metamaterial is analysed in the framework of the coupled mode theory (CMT), adapted from previous work on strong light-matter coupling regime [82], to our weakly doped low-noise detectors. These equations serve to describe the patch-antenna detector in use in section 3.2 and to sketch an optimization strategy for the meta-material.

3.4.1 Sub-wavelength double metal cavities

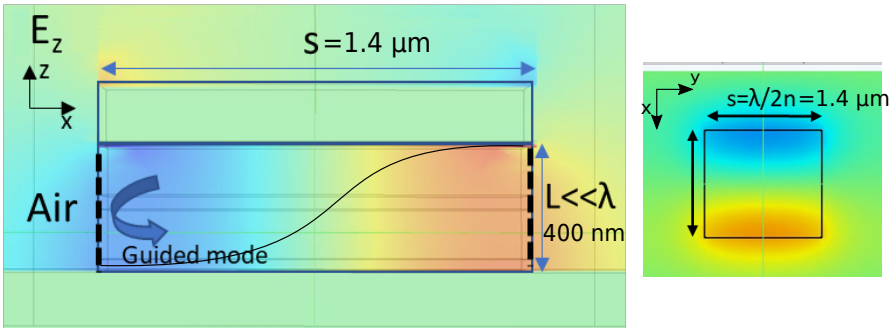

Figure 3.6: Lateral and top view schematic of the resonator geometry. The color plot indicates the TM_0 component of the electric field, with in red the maximal value and the minima in blue. The black line is the electric field E_z. In the x-y plane, the field undergoes an impedance mismatch at the openings between the air and the semiconductor. For the simulation, a polarized light was used.

Before introducing the CMT, we remind some electromagnetic properties inherent to a double-metal Fabry-Perot geometry with sub-wavelength dimensions.
The optical absorption rate between two confined states is proportional to the matrix element $|e < z > \cdot \mathbf{E}|^2$, where $e < z >$ is the dipolar matrix element between the subbands involved in the optical transition, as defined in eq. 1.18. In the presence of a cavity, the internal local field can

be written as $\mathbf{E} = (1 + f)\mathbf{E_0}$, with f the local field enhancement factor and E_0 the incident field. For intersubband dipoles, f is proportional to the ratio of the wavelength λ to the cavity thickness L [84]. The confinement can therefore be very strong for sub-wavelength microcavity thickness $L << \lambda$, up to achieve the strong and ultrastrong light-matter regimes[85].
In the double-metal resonator under study, the electromagnetic modes are confined in three directions. A color plot of the electric field inside the resonator is given in fig. 3.6. In the z direction, the resonator has a sub-wavelength thickness L«λ and the confined mode corresponds to the TM_0 of a planar waveguide [86], with homogeneous electric field along z, the growth direction. The ISBT selection rule is automatically satisfied with normal shining radiation (θ=0). In the x-y directions, as the cavities are etched, there is a discontinuity of the effective index at the openings between the single-metal and double-metal regions causing an impedance mismatch [80]. A Fabry-Perot standing wave is formed inside the semiconductor, represented by the blue arrow in fig. 3.6. The resonant frequency for this first order mode is:

$$\nu_{a,0} = \frac{c}{2\ n_{eff}\ s} \tag{3.1}$$

where s is the size of the patch, n_{eff} the effective index. The size can be chosen so that the resonance frequency happens where the ISB absorption occurs.

3.4.2 Coupled mode theory

In the following considerations, it is essential to discern the properties that are intrinsic to the absorber, the quantum well, and those related to its environment. A schematic representation of the coupled system consisting in the QW and the resonator is given in fig. 3.7. This interacting

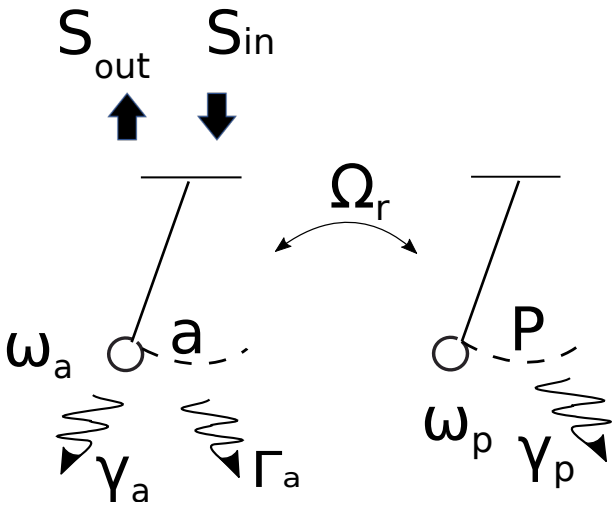

Figure 3.7: Schematic representation of a two level system at frequency ω_p coupled to a photonic resonator at frequency ω_a. The resonator mode can decay either via the radiative losses at rate Γ_a or via the non radiative losses at rate γ_a. The matter loses energy at rate γ_p. The incident radiation is described by the amplitude S_{in} and the outgoing field is S_{out}.

system can be modelled within the semiclassical framework of the coupled mode theory (CMT) [87]. CMT is very useful to describe the temporal evolution of the mode amplitude of an oscillator, under a variety of couplings and dampings [86]. It has been applied to cavity-coupled quantum wells in ref. [88] and recently in [82], to describe QW absorption engineering in the strong-coupling regime. In CMT, the quantum well is treated as an oscillator with resonance frequency ω_p and

with internal polarization field $\mathbf{P}$, coupled to a resonator (the microcavity) with amplitude field $\mathbf{a}$. After excitation by the external radiation $\mathbf{S_{in}}$, the polarization field decays at a rate γ_p which is the inverse of the lifetime of the excited subband in the QW. As only inelastic scattering events contribute to the dissipation and not the dephasing events, we consider a lifetime of 0.5 ps that fixes $\gamma_p \approx 2$ THz (see sec. 2.4.2 chapter 2). The coupling between the matter excitation and the electromagnetic field occurs at the Rabi angular frequency $\Omega_r \propto (N_e/V_{eff})^{1/2}$ with N_e the total number of electrons and V_{eff} is the effective volume accounting for the overlap of the mode with the heterostructure:

$$\Omega_r = \sqrt{\frac{\Psi^2 e^2}{4\epsilon_0 n_r^2 m^*} \frac{f_{12} N_p N_e}{SL}} \tag{3.2}$$

where $n_s = N_e/S$ is the doping sheet density, S the electrical surface, L the cavity thickness, $m^* = 0.067 m_e$ the GaAs effective mass, f_{12} the oscillator strength defined in 1.19, N_p the number of periods. The dimensionless overlap factor Ψ represents the fraction of the electromagnetic field energy coupled into the z-component of the electric field and overlapping with the semiconductor layers [89]. In our case, Ψ is supposed to be close to 1, but the incomplete etching of the cavities (section 3.3) can cause a weaker overlap. The Rabi frequency characterizes the coupling strength of the interaction between the QW and the patch-antenna and can be tuned for example with the doping and the thickness of the absorber. The resonator mode $\mathbf{a}$ can relax either radiatively (emitting photons outside the cavity at a rate Γ_a) or non-radiatively due to the ohmic losses in the mirrors (at a rate γ_a).
The CMT rate equations of the system read [82]:

$$\begin{aligned} \frac{d\mathbf{P}}{dt} &= (i\omega_p - \gamma_p)\mathbf{P} + i\Omega_r \mathbf{a} \\ \frac{d\mathbf{a}}{dt} &= (i\omega_a - \gamma_a - \Gamma_a)\mathbf{a} + i\Omega_r \mathbf{P} + \sqrt{2\Gamma_a}\mathbf{S_{in}} \\ \mathbf{S_{out}} &= -\mathbf{S_{in}} + \sqrt{2\Gamma_a}\mathbf{a} \end{aligned} \tag{3.3}$$

For a monochromatic excitation at frequency ω, $\mathbf{S_{in}} = S_0 e^{i\omega t}$, these equations can be worked out analytically for the steady state. Two main characteristics of the detectors can be derived from these equations:

- The cavity absorption quantum efficiency called η_{2D};
- The photon collection area A_{coll}.

The cavity absorption quantum efficiency is given by the absorbed intensity in the cavity (the power dissipated via ohmic losses in the metal is excluded since it doesn't contribute to the photocurrent) $2\gamma_p|\mathbf{P}|^2$ over the incident intensity $|\mathbf{S_{in}}|^2$ as [82]:

$$\eta_{2D} = \frac{2\gamma_p |\mathbf{P}|^2}{|\mathbf{S_{in}}|^2} \tag{3.4}$$

The expression is found by deriving $\mathbf{P}$ from eq. 3.3 and inserting it into eq. 3.4:

$$\eta_{2D}(\omega) = \frac{4\gamma_p \Gamma_a \Omega_r^2}{[\gamma_p(\omega - \omega_a) + (\gamma_a + \Gamma_a)(\omega - \omega_p)]^2 + [\gamma_p(\gamma_a + \Gamma_a) + \Omega_r^2 - (\omega - \omega_a)(\omega - \omega_p)]^2} \tag{3.5}$$

If the intersubband transition is resonant with the cavity $\omega_a = \omega_p$, we can rewrite η_{2D} as:

$$\eta_{2D}(\omega) = \frac{4\gamma_p \Gamma_a \Omega_r^2}{[(\omega - \omega_a)(\gamma_a + \Gamma_a + \gamma_p)]^2 + [\gamma_p(\gamma_a + \Gamma_a) + \Omega_r^2 - (\omega - \omega_a)^2]^2} \tag{3.6}$$

As the cavity operates as an antenna mediating the coupling of the QWs to the free-space, we can define a photon collection area for each patch as [90]:

$$A_{coll} = C\Sigma \tag{3.7}$$

where C, the contrast, is the fraction of collected photons and Σ the unit cell area around a single patch. The contrast is defined as $1 - R(\omega)$ where $R(\omega)$ is the reflectivity of the sample:

$$R(\omega) = \frac{|\mathbf{S_{out}}|^2}{|\mathbf{S_{in}}|^2} = \frac{[(\omega-\omega_a)(\Gamma_a-\gamma_a-\gamma_p)]^2 + [(\omega-\omega_a)^2 + \gamma_p(\Gamma_a-\gamma_a) - \Omega_r^2]^2}{[(\omega-\omega_a)(\gamma_a+\Gamma_a+\gamma_p)]^2 + [\gamma_p(\gamma_a+\Gamma_a) + \Omega_r^2 - (\omega-\omega_a)^2]^2} \tag{3.8}$$

The photon collection area is directly related to the signal to noise ratio and should be maximized with respect to the electrical area in order to reduce the noise. By conservation of the energy, the contrast C could also be expressed as the sum of the absorption quantum efficiency η_{2D} and of an other term corresponding to power dissipation due to ohmic losses in the metal. This term causes an absorption and increases the contrast but it does not contribute to the photocurrent, so it should be discarded when evaluating the device efficiency.

3.4.3 Absorption study of the patch-antenna array

We have derived the analytical expressions of the collection area A_{coll} and of the cavity absorption quantum efficiency η_{2D}, the quantities that characterize the meta-material coupled detector. The Rabi frequency Ω_r in eq. 3.2 is mostly set by the doping density and γ_p by the properties of the QW absorber. The loss rates Γ_a and γ_a depend on the geometry of the resonator and are extracted by measuring reflectivity spectra by means of the FTIR spectroscopy.
In this section, we present the optical characterization of the patch-antenna detector described in section 3.2.

Reflectivity spectra

The reflectivity measurements were performed on GaAs/AlGaAs superlattice samples with thickness L=386 nm (5 periods) inserted between two gold layers. The QWs are doped with n_{2D}=7 $\times$ 10^{11}cm^{-2} and have an absorption wavelength of approximately 9 µm. Their absorption properties are very similar both to the QWIP and to the QCD structures used in the rest of this thesis. No electrical contacts were realized. The samples were processed with different metamaterial geometries in order to find the optimum parameters. A FTIR was used for this experiment, and the reflected intensity was collected by a cooled MCT detector under an incident angle of θ=15 °. As a source, we used the normal incident beam of a Globar. A reference spectrum was measured on a simple gold layer. The reflectivity spectra for s=1.3 µm and different grating distances (p=s+a) are reported in fig. 3.8. The experimental data were modelled by the reflectivity expression given in eq. 3.8 (red line). For this fit we assumed $\omega_p = \omega_a$, and we fixed γ_p = 2 THz and Ω_r = 1.1 THz, to extract the values of the parameters Γ_a and γ_a. The value of the Rabi frequency Ω_r is given by the formula 3.2 and that of γ_p is determined from the calculation of the scattering time described in 2.3.1. The estimation of these two parameters is subject to some approximations and they are not known exactly, but we checked that the values extracted from the fit did not depend critically on that of the parameters Ω_r and γ_p.
The contrast C=1-R, reaches a maximum of 0.8 for p=3.3 µm when the radiative and ohmic losses are equal to $\Gamma_a = \gamma_a = 2$ THz, corresponding to the critical coupling condition for the empty cavity. The contrast disappears when the period p becomes comparable to the wavelength. This is due to the drop of the radiative rate Γ_a with increasing period p, as evidenced on fig. 3.9, that reports

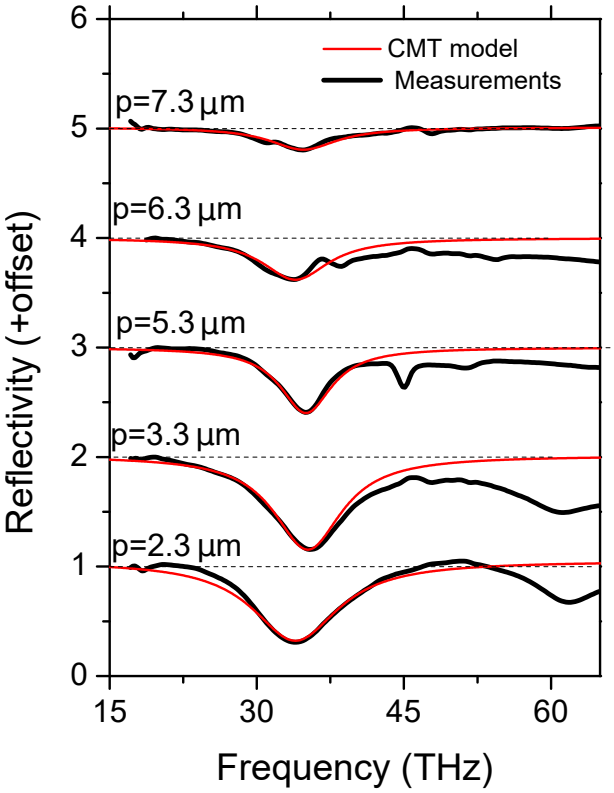

Figure 3.8: Reflectivity spectra for a sample having s=1.3µm and different grating distances. The red lines are the fit using CM theory. The Rabi frequency is given by the formula 3.2 and it is around $\Omega_r = 1.1$ THz, while we set γ_p= 2 THz.

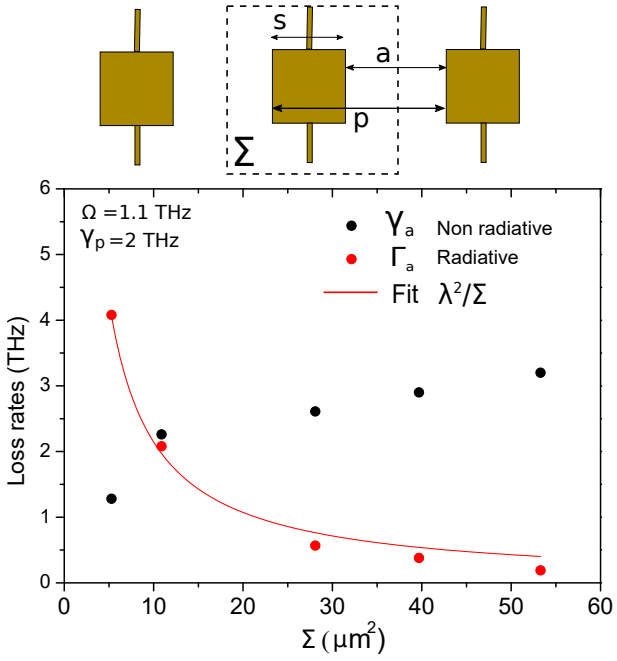

Figure 3.9: The dots are the fit parameters for radiative (red) and non radiative losses (black). The continuous red line is the fit for radiative loss in an array of resonators. The Rabi frequency is Ω_r=1.1 THz.

the parameters extracted from the model as a function of the unit cell area defined as $\Sigma = (a+s)^2$ and indicated by the dashed line around the schematic on top of the fig. 3.9.
The radiative losses are strongly influenced by the separation between each resonator. For a single patch (i.e. in the limit $p \to \infty$), the radiative rate Γ_a can be estimated from the classical equations of antenna theory, where double-metal patches are known in the microwave region as microstrip antenna. [91] We consider a single microstrip antenna with sub-wavelength dimensions and frequency ν_a that radiates a power P_{rad} to the far-field free space. Its radiative loss rate can be written as:

$$\Gamma_{a,1} = \nu_a \frac{P_{rad}}{U_0} \tag{3.9}$$

where U_0 is the radiation intensity of an isotropic point source (the reference) and P_{rad} is related to the far-field intensity:

$$P_{rad} = \int_0^{2\pi} \int_0^{\pi} \frac{1}{2Z} |\mathbf{E}(\theta,\phi)|^2 \sin\theta d\theta d\phi \tag{3.10}$$

where Z is the impedance of free space and $E(\theta,\phi)$ is the electric field radiated by a microstrip antenna. The expression for $E(\theta,\phi)$ can be found in [91] and the corresponding intensity is directly proportional to the cavity thickness L. From equations 3.9 and 3.10, the radiative decay loss rate is found to be $\Gamma_{a,1}$=0.15 THz for a thickness of L=386 nm and patch lateral size s=1.3 µm.
The radiated power can be increased by combining multiple patches to form an array, where the periodicity of the system defined as p=s+a plays an important role [90]. Indeed, in this regime, the oscillators are coupled via their interaction with the electromagnetic field and they display a collective behaviour known as superradiance, first described by Dicke [92] and as observed for arrays of split ring resonators [93]. In the superradiant regime, we expect the radiative rate to be inversely proportional to the density of the resonators $1/\Sigma$:

$$\Gamma_a = \Gamma_0 \frac{\lambda^2}{\Sigma} \tag{3.11}$$

The results of fig.3.9 are consistent with all these observations: for dense arrays, we recover the λ^2/Σ dependence (red line), while in the large Σ limit, the values obtained for Γ_a become close to the estimation of $\Gamma_{a,1}$ from microstrip antenna theory.

Absorption enhancement

We now have all the parameters to be inserted in the CMT analysis for the device described in 3.2. These detectors have been fabricated according to the guidelines following the theoretical approach developed by Palaferri et al. in [81] based on the solution of the Poynting theorem. The critical coupling condition $\Gamma_a = \gamma_a$ for the empty cavity was supposed to be the best condition, as the contrast is at maximum as we can see in fig. 3.8. Therefore, the distance between patches has been fixed at a=2 µm. We will see later that this approach does not optimize the cavity absorption quantum efficiency η_{2D} and is therefore slightly misleading.
The absorption quantum efficiency η_{2D} can be calculated with the expression 3.5. The resulting absorption spectrum is presented in fig. 3.10. In this figure, we compare the cavity absorption (black curve) to the mesa absorption for an equivalent structure of 8 periods (red curve) which has a $\alpha(\theta)$=2.7% (45°, one polarization and decaying of the electric field included, see 1.30). The maximum cavity absorption is η_{2D}=22%, which would be equivalent to use 95 periods in a standard mesa geometry. One of the advantages to use the meta-material to increase the absorption is to avoid the need for structures with large number of periods, because it would imply detrimental effects such as band bending due to non-homogeneous field, responsivity saturation, and malfunction of the first and last periods. As a consequence, it is found that the detectivity is maximized when the number of periods is less than 15 [94].

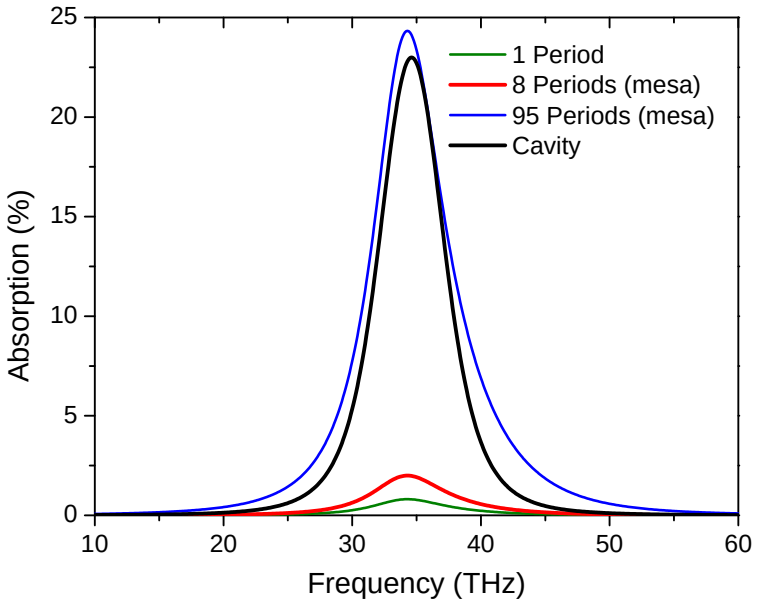

Figure 3.10: Absorption quantum efficiency η_{2D} for cavity sample (black curve) compared to the absorption calculated for an equivalent mesa device (45°) with 8 periods (red), with just a single period (green) and with 95 periods (blue).

Collection area

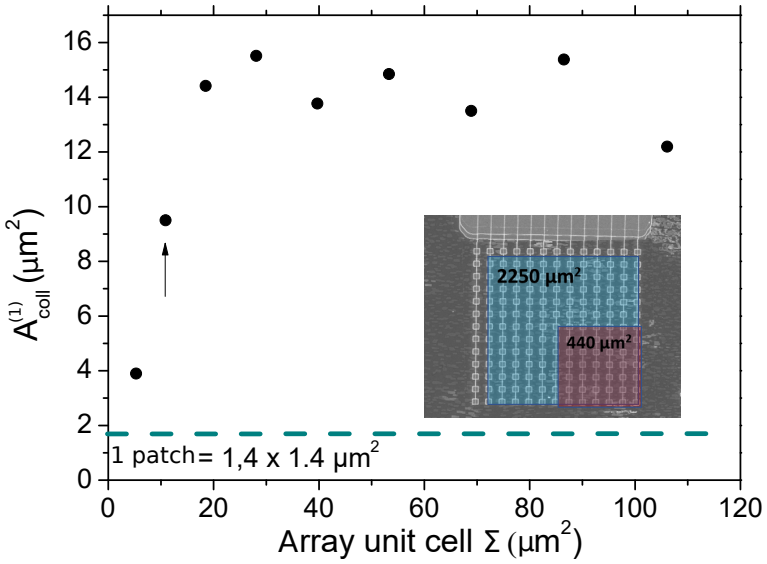

Figure 3.11: Collection area for a single patch as a function of the unit cell area. The dashed line is set at the electric surface of one patch. In the inset a reproduction of the detector array, where the total collection area is represented by the blue transparent square. The total collection area is $NA^{(1)}_{coll}$ with N the number of patches in the array, it represents $C \simeq 80\%$ of the device physical area for the detectors under study (marked with a black arrow). The purple transparent square indicates the electric area for the same device.

From the contrast extracted from the reflectivity measurements shown in fig. 3.8, we can calculate the photon collection area as defined in eq. 3.7. The collection area $A^{(1)}_{coll} = A_{coll}/N$ is shown in figure 3.11 as a function of the array unit cell Σ. For the detectors used in the rest of this

work, with a period p=3.4 µm (marked by a black arrow in fig. 3.7), the collection area is five-fold greater than the electrical area (dashed line). For the whole detector, the total collection area is $A_{coll} = 2250$ µm^2, represented by the blue transparent part in the inset in figure 3.11, while its total electric surface is just $\sigma = 440$ µm^2, the purple transparent square in scale. Since the photocurrent depends on the collection area and the dark current is proportional to the electrical area, the antenna array enables improving the signal-to-noise ratio.
The collection area saturates for larger periods and converges towards the collection area of the single element, which is the best configuration for the SNR.

3.4.4 Coupling regimes

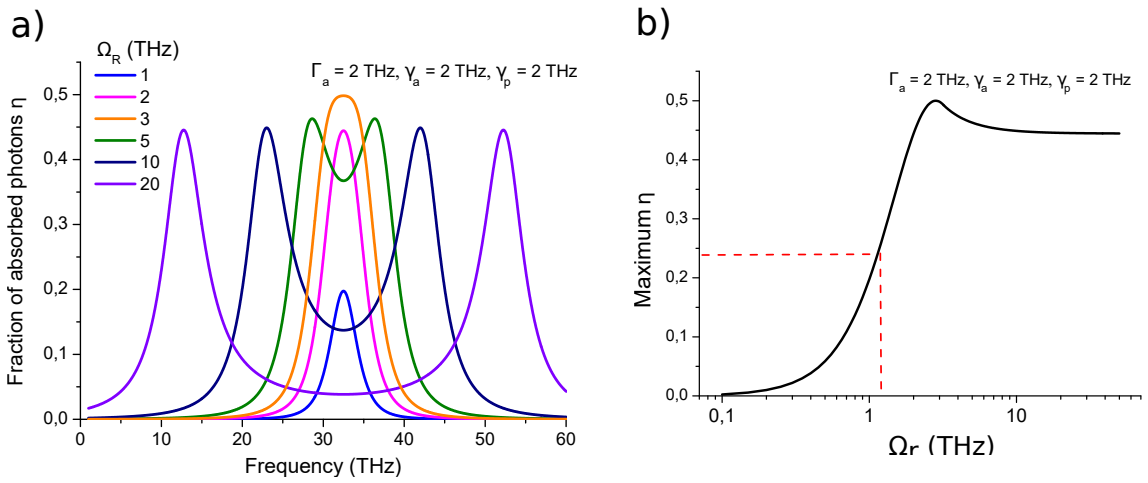

Figure 3.12: a) Spectrum of η_{2D} for different the coupling strength Ω_r, with Γ_a=γ_a=γ_p=2 THz. The system is first in weak coupling regime, with a single peak whose height rises with increasing Ω_R, until the peak value reaches a maximum and begins to decrease. For further increase of Ω_R, the system enters the strong coupling regime in which the spectrum splits gradually into two polaritonic peaks, whose intensity saturates to a constant value. b)Peak value of η_{2D}. The red dashed line indicates the value of η_{2D} of the current detector. The maximum is is obtained at Ω_r=2.7 THz around the transition from the weak to the strong coupling regime.

In this section, we explore in more details the CMT equations defined in section 3.3. We develop a more general analysis with respect to reference [82],which is adapted for both weak and strong coupling regimes.
We infer from the CMT equations an optimisation procedure for the meta-material.
Firstly, we analyse the spectral dependency of the quantum efficiency $\eta_{2D}(\omega)$ as a function of the coupling strength Ω_r. The absorption spectra for different values of the coupling strength Ω_r are shown in fig. 3.12 for the parameters of the detector in use Γ_a=γ_a=γ_p=2 THz, as reported in section 3.4.3. We are interested to know at which spectral frequencies the absorption quantum efficiency is maximized, therefore we apply to the expression $\eta_{2D}(\omega)$ in 3.6 the condition:

$$\frac{\partial\ \eta_{2D}(\omega)}{\partial\ \omega} = 0 \quad \text{and} \quad \frac{\partial^2\ \eta_{2D}(\omega)}{\partial\ \omega^2}\bigg|_{\omega=\omega_{max}} < 0 \tag{3.12}$$

This equation is satisfied for two sets of values that depend on the coupling strength Ω_r^2 and define two regimes (in all this analysis, we consider a resonant configuration: $\omega_a = \omega_p$):

- Weak coupling for $\Omega_r^2 \leq \frac{1}{2}[\gamma_p^2 + (\gamma_a + \Gamma_a)^2]$.
  The maximum absorption η_{2D} is at the frequency $\omega = \omega_a$; In fig. 3.12b the weak coupling regime persists until Ω_r= 2.7 THz.

- Strong coupling for $\Omega_r^2 > \frac{1}{2}[\gamma_p^2 + (\gamma_a + \Gamma_a)^2]$.
  Two polariton peaks appear at frequencies $\omega = \omega_a \pm \sqrt{\Omega_r^2 - \frac{1}{2}[\gamma_p^2 + (\gamma_a + \Gamma_a)^2]}$, as identifiable in fig. 3.12a; For even greater Rabi frequencies, $\Omega_r^2 >> \frac{1}{2}[\gamma_p^2 + (\gamma_a + \Gamma_a)^2]$ we can approximate the polaritonic frequencies as $\omega = \omega_a \pm \Omega_r$.

The corresponding expressions for the maximum absorption quantum efficiency are found by replacing these frequencies back into eq. 3.6 to obtain:

$$\begin{aligned} \eta_{2D,max} &= \frac{4\gamma_p \Gamma_a \Omega_r^2}{[\gamma_p(\Gamma_a + \gamma_a) + \Omega_r^2]^2} \quad \text{for weak coupling;} \\ \eta_{2D,max} &= \frac{4\gamma_p \Gamma_a \Omega_r^2}{(\gamma_p + \Gamma_a + \gamma_a)^2[\Omega_r^2 - \frac{1}{4}(\gamma_p - \Gamma_a - \gamma_a)^2]} \quad \text{for strong coupling.} \end{aligned} \tag{3.13}$$

In figure 3.12b, we plot the max value of the η_{2D} as a function of different values of the coupling strength Ω_r. The red dashed line denotes the value of η_{2D}= 22% and Ω_r=1.1 THz related to the antenna-coupled detector in use, whose performances will be detailed in the next section. From this graph, we can infer that, in this configuration, the maximum absorption value is reached for Ω_r=2.7 THz, just before the splitting of the two polaritonic states. After a maximum, the absorption saturates to a lower constant value. This is a general result valid for all coupling parameters, not yet considered in the literature [95; 82]. The formula in eq. 3.13 enables us to find also some new conditions for obtaining a better absorption than the current η_{2D}= 22%.
In the weak coupling regime, the maximum absorption occurs for the following condition:

$$\frac{\Omega_r^2}{\gamma_p} = \Gamma_a + \gamma_a \tag{3.14}$$

By substituting eq. 3.14 into eq. 3.13, we obtain:

$$\eta_{\omega_p,max} = \frac{\Gamma_a}{\Gamma_a + \gamma_a} \tag{3.15}$$

The maximum absorption in weak coupling can be reached if:

$$\begin{aligned} \gamma_a &\to 0 \\ \Gamma_a &\to \frac{\Omega_r^2}{\gamma_p} \end{aligned} \tag{3.16}$$

It is intuitive that an optimal meta-material should have minimum ohmic losses. These conditions also express the critical coupling condition for these systems.

3.4.5 Strategies for an optimised metamaterial

In section 3.4.3, we derived the absorption and the collection area for the patch-antenna device described in 3.1, whose performances will be presented in the next section. This device has a total thickness of L=386 nm for N_p=8 periods.
The geometry of the meta-material was misleadingly selected with the aim of satisfying the critical coupling for the empty cavity $\Gamma_a = \gamma_a$. This condition was found to maximize the contrast but it does not guarantee an optimal absorption efficiency η_{2D}, as we noted previously that the contrast can consist either in absorption in the QW or in ohmic losses in the metal.
Although the obtained value of η_{2D}=22% is enhanced with respect to an equivalent mesa structure, from the expressions 3.16 we can now engineer a better absorption. We start by fixing the value of

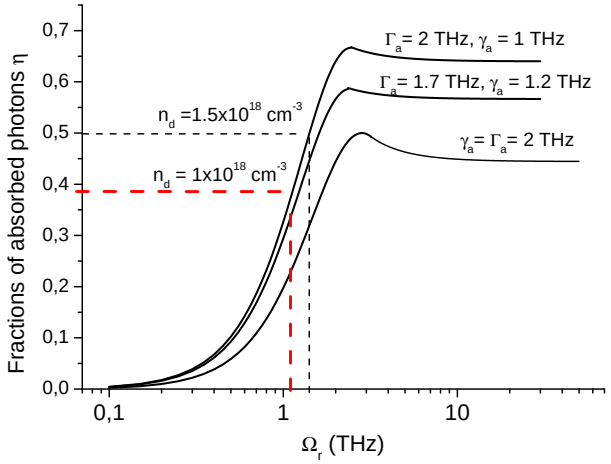

Figure 3.13: Peak fraction of absorbed photons η_{2D} as a function of the coupling strength Ω_r, for three different sets of Γ_a and γ_a. The red dashed line indicates the current value Ω_r=1.1 THz, the black dashed line is for an increased doping density n_{2D}=1.5 × 10^{18}cm^{-3}.

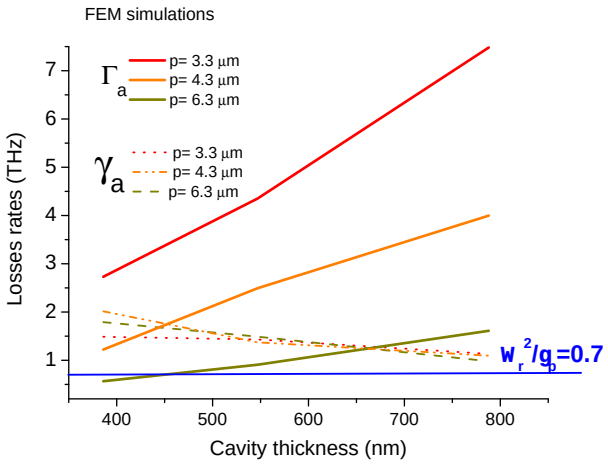

Figure 3.14: COMSOL simulations. The radiative losses rate Γ_a, in continuous lines, and the non radiative losses, as dashed lines, as a function of the cavity thickness for different patches separation. The blue continuous line is the limit Ω_r^2/γ_p=0.7 THz. p is the period of the array defined as p=s+a.

γ_p= 2 THz, because it represents the lifetime of the excited state fixed by the design of the QCD band diagram.

The absorption strongly depends on Ω_r, hence mostly on the doping density (eq. 3.2). An increase of the doping density would increase the noise: while the Rabi frequency Ω_r varies as the square root of the doping density, the activation energy described in sec. 2.5.1 is linearly proportional to it. Moreover, we observed in the previous section that a value of η_{2D} close to 1 can be achieved remaining in a low doping weak coupling regime. Therefore, we can modify the geometrical properties of the cavity by choosing Γ_a and γ_a in order to satisfy the conditions in 3.16. In fig.3.13 we plotted the peak value of η_{2D} as a function of the coupling strength Ω_r for three different values of the cavity loss rates. In order to shift the peak of the curve to lower values of Ω_r, γ_a should be smaller than the radiative loss Γ_a.

The variations of the two cavity rates γ_a and Γ_a depend on the geometry and can be predicted with FEM simulations. In fig.3.14, we reported FEM simulations performed with COMSOL for the patch-antenna array. This graph shows the extracted loss rates, radiative (continuous lines) and non radiative (dashed and dotted lines), as a function of the cavity thickness (x-axis) and for different grating periods $p = s + a$ as a parameter. The curve in red color is the current non-optimised situation. The radiative losses increase almost linearly with the thickness and decrease with the periodicity as predicted by eq. 3.11. The ohmic losses decrease with the cavity thickness and are almost constant with the periodicity. In order to reduce the ohmic losses, thicker cavities are desired, meaning more periods added to the quantum structure. At the same time the radiative losses should approach the quantity Ω_r^2/γ_p, indicated by the blue line in fig.3.14 and they should be greater than γ_a: this can be selected by tailoring the distance between patches. For instance, if we suppose to increase the number of periods from 8 to 15, the thickness of the cavity is increased to L=0.770 µm. For this thickness, the non radiative loss rates could reach the values of γ_a=1 THz, while the radiative loss rates are set to Γ_a=2 THz by fixing the distance between the patches at around a=4 µm. As we can retrieve from the fig.3.13, the loss rates γ_a = 1 THz, Γ_a = 2 THz correspond to a peak of nearly η_{2D}=40% for n_d= 1 × 10^{18}cm^{-3}. A greater periodicity implies also a maximum in the collection area, as observed in fig. 3.7. Just adding some periods, we could combine an enhanced signal to noise ratio and a factor of 2 in the absorption efficiency.

This strategy constitutes a short-term effortless improvement of the detector. However, the optimum condition $\gamma_a \rightarrow 0$ is very hard to implement by using metallic patches. Dielectric cavities would resolve this problem and have been already used for second harmonic generation (SHG) in QWs, but their electrical connections for detectors are difficult to realize [96]. High Q factors will also limit the acceptance bandwidth of the detector.

3.5 Experimental results

3.5.1 Spectral Photoresponse of the patch-antenna LWIR QCD

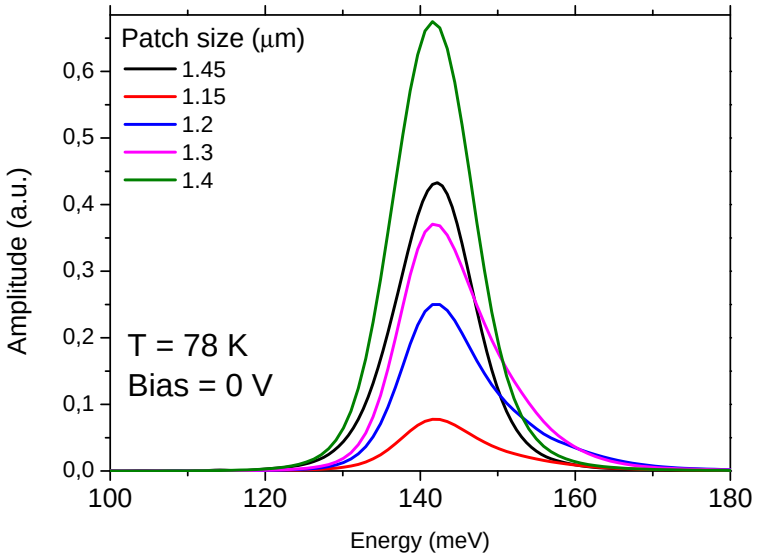

Figure 3.15: Photocurrent spectra measured at 78 K and 0 bias for five different patch sizes.

Patches of different dimensions have been processed in order to determine the structure with a mode resonant with the intersubband absorption, thus optimizing the cavity effect. Here, we will report and discuss their photocurrent spectra, taken using the globar source of the FTIR interferometer Bruker (Vertex) and rapid scan mode. Fig.3.15 illustrates photocurrent spectra for 5 devices with patch sizes s = 1.15, 1.26, 1.3, 1.4, 1.45 µm measured at 78 K and 0 V. For s = 1.4 µm the spectrum has a symmetric shape as the two peaks, associated with the cavity mode and the intersubband transition, converge into one resonance. The integral of the photocurrent spectra in fig. 3.15 is proportional to the responsivity of the device and is plotted in fig. 3.16 as a function of the patch lateral size, s (red points). The integral value shows a net drop of the responsivity when the cavity is detuned from the intersubband transition. The x-error-bars are associated to a 20 nm offset of the electron beam lithography (EBL) patterning. Experimental data are compared to the integral of the absorption spectrum given in 3.5, as derived from the CMT equations (black points).
In the weak-coupling regime, this is equivalent to calculate the integral of the product of the spectral response of the bare detector, $S_{ISB}(\omega)$ and the empty microcavity absorptivity $S_{cavity}(\omega)$ as:

$$S_\eta(s) = \int S_{ISB}(\omega) \times S_{cavity}(\omega, s)\, d\omega \tag{3.17}$$

The result of this integral as a function of the cavity size s is represented as a black curve in figure 3.16. The quantity $S_{ISB}(\omega)$ represents the mesa photocurrent spectrum reported in red in figure 3.17. $S_{ISB}(\omega)$ is the same for all processed samples. On the contrary, $S_{cavity}(\omega, s)$, also represented

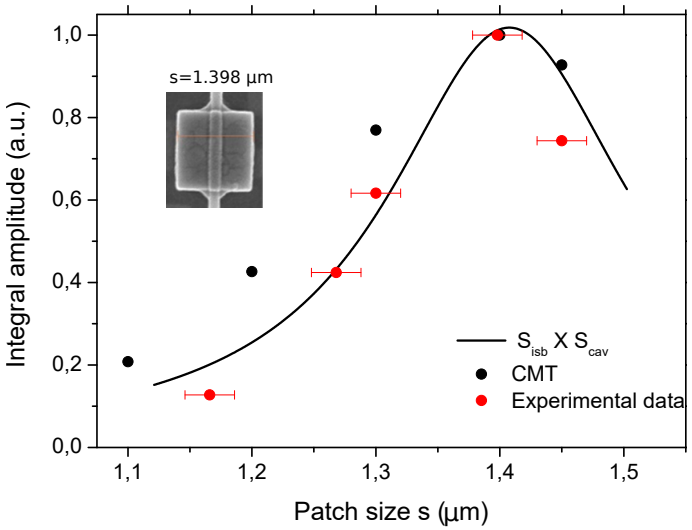

Figure 3.16: Integral amplitude of the photocurrent spectra at varying patch sizes is given as red dots with the EBL dimensional error. The black curve is a Lorentzian model accounting for the combined intersubband and cavity absorption. In the upper-left corner, a SEM top-view of the 1.4 µm single patch is given. Black dots are calculated from CMT simulations.

in fig.3.17 as a dashed line, is a Lorentzian curve that peaks at different energies as a function of the size s:

$$S_{\text{cavity}}(\omega, s) = \frac{2(\Gamma_a^2 + \gamma_a^2)}{[\omega - \omega_a(s)]^2 + (\Gamma_a + \gamma_a)^2} \tag{3.18}$$

where $\omega_a = 2\pi\nu_a$ with ν_a the resonant frequency depending on s as given in eq. 3.1, γ_a and Γ_a are the ohmic and the radiative losses, deduced from the reflectivity spectra in fig. 3.8. The model

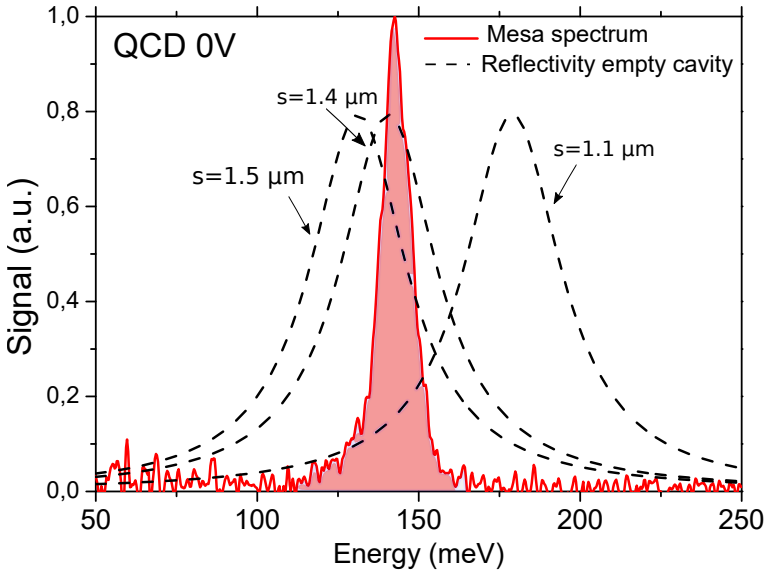

Figure 3.17: Normalized photocurrent spectra of the mesa (red) at 0V and reflectivity for patches with dimensions s =1.1 µm, s =1.5 µm, s =1.4 µm.

reproduces accurately the data and suggests that the optical cavity acts as a broad band-pass filter on the photocurrent of the bare intersubband transition. Notice that the spectra peak always at the same energy (Fig. 3.15), as the linewidth of the bare photocurrent spectrum is narrower than

that of the cavity ($\gamma_p < \gamma_a + \Gamma_a$). The difference between the black dots and the measured values in fig. 3.16 stands for the fact that in CMT we didn't take in consideration any photocurrent transport but only the absorption.
We can also notice that a shift of $\Delta s \approx$20 nm in the dimension of the cavity or of $\Delta E \approx 3$ meV in the ISB peak energy will not produce a considerable drop in responsivity. This is important for considering the processing of patches with higher quality factors, as it would require a finer EBL tuning in order to match the resonance.
The model confirms that optimal performances are achieved for the device with dimension s=1.4 µm, where the empty cavity is resonant with the optical transition. In the rest of the chapter, we concentrate on the performance characterization of this resonant QC device.

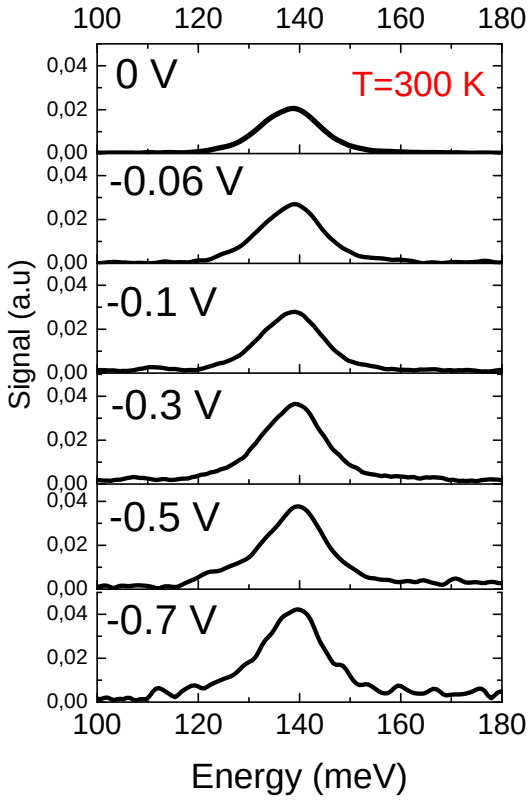

Figure 3.18: Photocurrent spectra for QCD at T=300 K for different voltages.

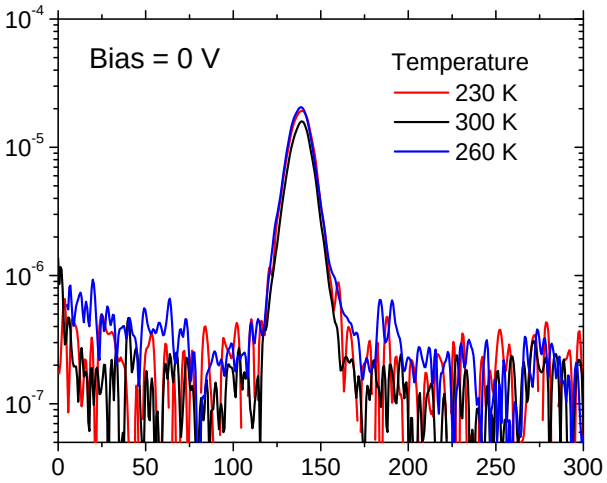

Figure 3.19: Photocurrent spectra at V=0 bias for high temperatures, in log scale.

Photocurrent spectra at room temperature could only be obtained for the resonant device, as reported in fig. 3.18. In these measurements, the temperature was T=300 K and different negative voltages were applied (for positive voltages, the noise was too high). As demonstrated in the previous chapter, due to the tunnel alignment the response is maximized when increasing the negative voltage (see fig. 2.18b). At 0 bias, the spectra show a constant response for temperatures T>210 K, as presented in fig. 3.19. This thermal range can be achieved with a Peltier-cooling system.

3.5.2 Responsivity

The responsivity is defined as the ratio between the generated photocurrent I_{photo} and the corresponding absorbed power P, as described in sec. 1.1.2. Peak responsivity curves are reported in fig. 3.20 for several temperatures for the unbiased mesa device (black hollow dots) and for the

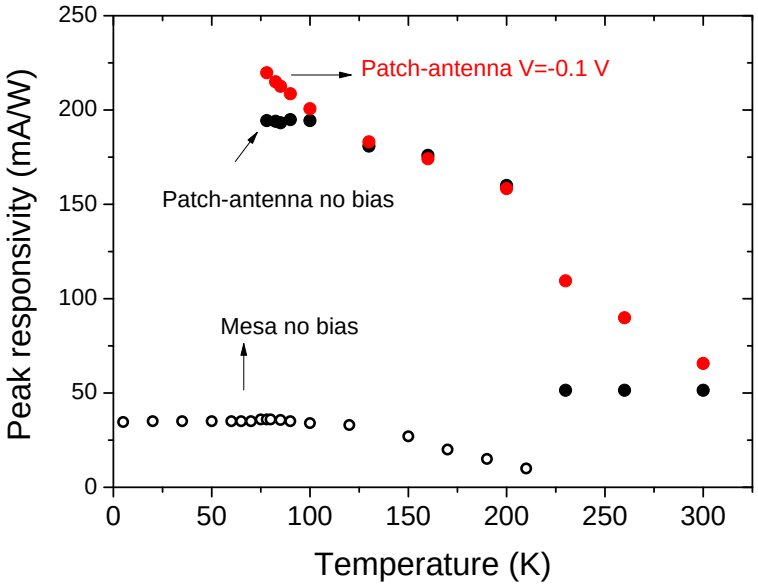

Figure 3.20: Peak value of responsivity for a mesa device at 0 bias (black hollow dots) and an antenna-coupled detector at 0 bias(black dots) and -0.1 V (red dots) sharing the same heterostructure. The responsivity reaches the record value of 50 mA/W with no bias, ambient temperature conditions.

antenna-coupled detector at 0 bias (black dots) and V=-0.1 V (red dots). The peak responsivity of the mesa detector is $\mathcal{R} \approx 40$ mA/W and drops below the noise level after T=200 K. The patch antenna detector shows a five-fold enhancement of the responsivity at low temperatures and 0 bias, reaching a maximum value of $\mathcal{R}$= 200 mA/W. The enhancement is due to augmented absorption of the antenna-coupled geometry presented in section 3.4.3. The ratio between the responsivities of the mesa and of the cavity detector sharing the same heterostructure can be estimated as:

$$\frac{\mathcal{R}_{cavity}}{\mathcal{R}_{mesa}} = \frac{\epsilon_{wires}\ \eta_{2D,cavity}}{\alpha(\theta)} \approx 5.5 \tag{3.19}$$

In the cavity responsivity the array polarization factor due to the presence of the wires in one direction $\epsilon_{wires} \approx 0.7$ [1] is also considered. The cavity absorption quantum efficiency η_{2D} =22% was given in section 3.4.3. The responsivity for the mesa is calculated with $\alpha(45°)$=2.8% given in eq. 1.30 in chapter 1. The experimental ratio $\frac{\mathcal{R}_{cavity}}{\mathcal{R}_{mesa}}$=5.3 is in agreement with the estimated calculation from the CMT. Note that the extraction probability is the same in both devices.
For the antenna-coupled QCD the total detector quantum efficiency is given by:

$$\eta(\omega) = \eta_{2D}(\omega)\epsilon_{wires}\frac{p_{ext}}{N_p} \tag{3.20}$$

where p_{ext} was calculated in section 2.4.3 in chapter 1. At 78 K, we find a peak value of $\eta \approx 1.3\%$ to be compared to the mesa total quantum efficiency of $\eta(45°)\approx 0.3\%$ (eq. 1.31). At room temperature the cavity total quantum efficiency η drops to 0.57%. The dependence of the responsivity in temperature has been studied and modelled in sec. 2.4.3.

Most importantly, the antenna-coupled QCD reaches a record value responsivity at T=300 K of 50 mA/W at 0 bias and 80 mA/W for V=-0.1 V, overperforming of a factor of 3 the QCD state-of-the-art at λ=9 µm and at room temperature [72]. Moreover, here a normal incident radiation is used, which could greatly simplify pixels scheme and integrated geometries.

Experimental methods

The evaluation of the responsivity requires the determination of the photocurrent generated by the detector and of the corresponding effective incident power. Here we present their calibration procedure.
The experimental set-up used for the calibration is sketched in fig. 3.21. An optical system

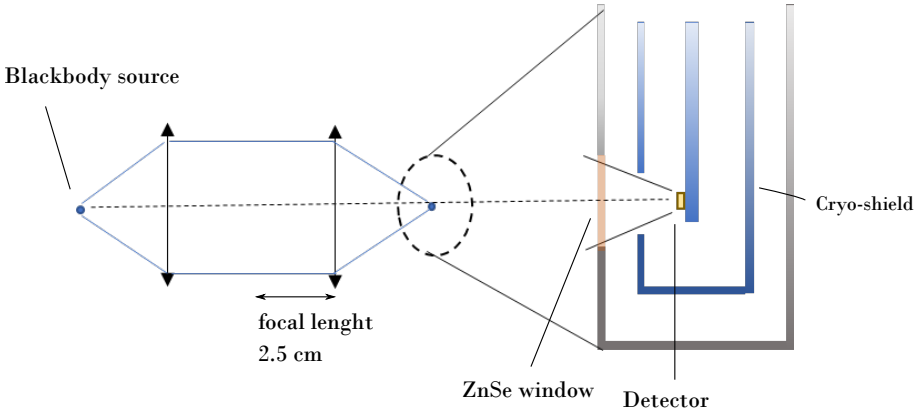

Figure 3.21: Schematic of the optical system used for calibrating the responsivity.

composed of two lenses with f-number F=0.5 collects the light from a black body source kept at 1000° and converge it onto the detector. The incident power P is estimated by means of a commercial calibrated detector (Teledyne Judson MCT, model J15D22), with a responsivity curve $\mathcal{R}_{MCT}(\lambda)$ provided by the manufacturer. The peak QCD responsivity is thus calculated considering the peak value of the MCT responsivity:

$$\mathcal{R}_{p,QCD} = \mathcal{R}_{p,MCT} \frac{I_{p,QCD}}{V_{p,MCT}} \frac{\alpha_{MCT}}{\alpha_{QCD}} \frac{A_{MCT}}{A_{QCD}} \frac{\int V_{n,MCT} \times dP_\lambda}{\int I_{n,QCD} \times dP_\lambda} \tag{3.21}$$

where the ratio between the QCD/MCT areas is $\frac{A_{MCT}}{A_{QCD}} \approx 1600$, $R_{p,MCT}$ =36 V/W is the MCT peak responsivity, $I_{p,QCD}$ is the measured QCD peak photocurrent and $V_{n,MCT}$ is the measured photovoltage of the MCT. The integrals represent the spectral factor taken as the overlap between the normalized spectrum of the devices and the black-body spectrum, as given in eq. 1.2 in chapter 1. The ratio of the spectral factors between the MCT (which has a broader response) and QC detectors is around 10. The quantity α denotes the field of view: (i) the QC detector field of view is given by a cooled cryo-shield with aperture giving the same FOV than the MCT (60°), therefore the ratio of the α factors is 1; (ii) the optical 4f system reproduces a beam spot identical to the aperture of the black body. We choose the source diameter that matches the size of the detector (0.05" for the QCD and 0.2" for the MCT) and we align the focal position of the QCD and the MCT to maximize their signal.
The photocurrent $I_{p,QCD}$ is measured by a lock-in technique. Figure 3.22 shows the equivalent electrical circuit for the photocurrent measurements of the QC detector. The QCD can be modelled as a current source in parallel with a device resistance r_d. It consists of three current generators: (i) the photocurrent due to the blackbody radiation I_{ph} (ii) the background photocurrent I_{back}; and (iii) the dark current I_{dark}. I_{ph} is measured by a synchronous detection at the light modulation frequency provided by a mechanical chopper placed in front of the source (f=1 kHz). The total current I flows through a shunt resistor with resistance R_{shunt} = 220 Ω, creating a voltage drop V_{lock} across it. This voltage is amplified by a Stanford Research Systems SR560 low noise voltage preamplifier with gain G = 104 and then sent to the input of the lock-in amplifier. The effective

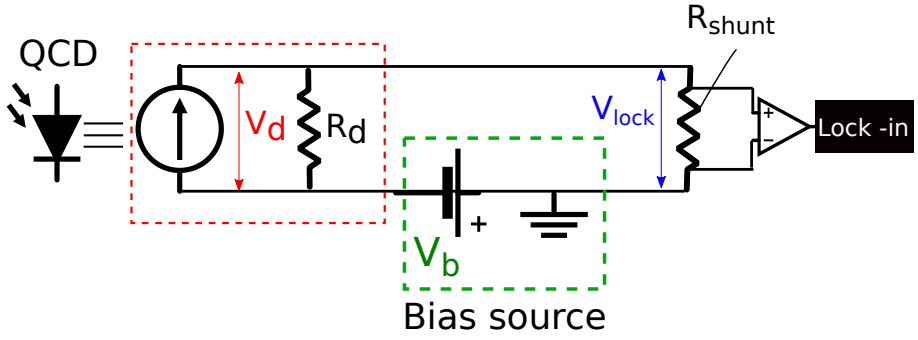

Figure 3.22: Equivalent electrical circuit for measuring the photocurrent of the QCD device, schematized as a current generator and parallel resistance r_d. The QCD bias is V_b and the photocurrent is measured by a lock-in through a shunt resistance R_{shunt}.

voltage applied to the device is calculated by solving the equivalent circuit using Thévenin' s theorem:

$$V_d = \frac{r_d}{r_d + R_{shunt}}(V_b - I\ R_{shunt}) \tag{3.22}$$

where V_b is the voltage applied by the voltage generator (Keythley 2450). In this expression r_d is the device differential resistance dI/dV measured with an IV curve under a blackbody illumination, without R_{shunt} in the circuit. The photocurrent is thus the signal read on the lock-in divided by an equivalent resistance r_{eq}:

$$\begin{aligned} I_{ph} &= \frac{\pi V_{lock}}{\sqrt{2}\ r_{eq}} \\ r_{eq} &= \frac{r_d R_{shunt}}{r_d + R_{shunt}} \end{aligned} \tag{3.23}$$

The lock-in input resistance (10 MΩ) and the cable impedance give a negligible contribution.
For the MCT, the same technique is used except for an additional voltage divider in the circuit that prevents the output from the MCT amplifier to overcome the maximum input voltage accepted by the lock-in. We measured a value of $V_{p,MCT} = 43,2$ mV. Lastly, the obtained incident power from the black body impinging into the QCD is found to be:

$$P_{in,QCD} = 90 \text{ nW} \tag{3.24}$$

3.5.3 Detectivity and Blip condition

Patch antenna microcavities enhance the signal to noise ratio, as the antennas permit the detector to gather photons on a collection area A_{coll}, which is much larger than its geometrical surface σ (see sec. 3.4.3). The signal to noise ratio of the detector is expressed by the background limited detectivity D^*_{BL} which contains the background current shot noise and the Johnson noise:

$$D^*_{BL}(T,V) = \frac{\mathcal{R}(T,V)\sqrt{A_{coll}\ \Delta f}}{\sqrt{\left[\frac{2eI_{back}(T,V)}{N_p} + \frac{4k_BT}{r(T,V)}\right]\Delta f}} \tag{3.25}$$

where the $\mathcal{R}$(T,V) is the responsivity reported in the previous section, N_p is the number of periods, r the resistance described in sec. 2.5.2, Δf the integration bandwidth. The I_{back}-voltage curve is measured with the same FOV=60° as the responsivity. It also depends on the collection area:

$$I_{back} = \mathcal{R}\ E_{21}\ \Phi\ A_{coll} \tag{3.26}$$

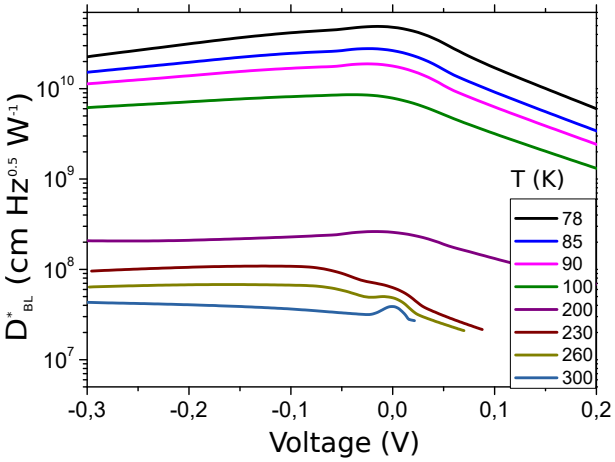

Figure 3.23: Background Limited Detectivity as a function of the applied voltage, for several temperatures. The FOV is 60-deg and the background temperature 293 K.

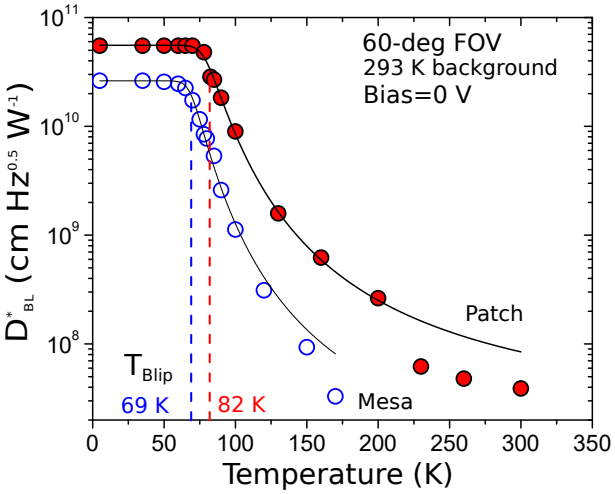

Figure 3.24: BL detectivity vs. temperature for the mesa device as blue dots and for the patch detector in red, at 0 bias. The fit curves are calculated using eq. 3.25 and the expression for the resistance in eq. 2.45 in chapter 2.

where Φ is the integrated background photon number flux at 293 K incident on the detector. The detectivity is reported in fig. 3.23 as a function of the voltage, for the range from T= 78 K to ambient temperature. The values of detectivity for V=0 V are reported in fig. 3.24 as a function of the temperature. Here, the patch-antenna detector measurements, in red dots, are compared with those in blue of a device with the same active region but processed in a mesa geometry.
At low temperatures, the QCD noise is dominated by the background current noise. In this limit, the advantage of the patch antenna device is given by the cavity effect that increases the absorption and the responsivity, as we saw in the previous section with eq. 3.19. The measured ratio $D^*_{BL,patch}/D^*_{BL,mesa}$ at low temperatures is consistent with the square root ratio of the responsivity for the patch and mesa device patch in eq. 3.19:

$$\frac{D^*_{BL,patch}}{D^*_{BL,mesa}} \approx \sqrt{\frac{R_{patch}}{R_{mesa}}} \approx 2.3 \tag{3.27}$$

This is also in agreement with the description given in ref. [1]. At these temperatures, the background-limited detectivity for the patch device is $D^*_{BL,patch} = 5.5 \times 10^{10}$ cmHz^{0,5}/W, nearly half the value of the ideal blackbody-limited detection at λ=9 µm for a background temperature T=293 K and 60-deg FOV (the ideal $D^*_{BL,ideal} = 1.2 \times 10^{11}$ cmHz^{0,5}/W is given for a quantum efficiency of 100%). In this regime, the $D^*_{BL,patch}$ depends only on the quantum efficiency and the background photon flux[8].
The BLIP temperature is found when the noise under illumination is equal to twice the noise in dark conditions (see sec. 1.1.2 for a definition of T_{Blip}):

$$D^*_{BL}(T = T_{Blip}) = \frac{D^*_{BL}(T < T_{Blip})}{\sqrt{2}} \tag{3.28}$$

This condition is marked as a blue dashed line for mesa and red dashed line for the patch in fig. 3.24. Notably, the reduction of the dark current in the patch-antenna array increases the BLIP (background limited infrared photo-detector) temperature from 69 K to 82 K.
At high temperatures, the detector noise is dominated by the Johnson noise, which is proportional

to the electrical resistance of the device, r. The resistance, extracted from the dark current voltage measurements, as a function of the temperature for the patch device is reported in fig. 2.29a). In a patch antenna device, the electrical area σ is reduced with respect to its collection photon area A_{coll}. This increases the device resistance of a factor A_{coll}/σ with respect to a standard device, where A_{coll} coincides with the electric area, as it is apparent from the high temperature limit of the detectivity $D^*_{BL}(T > T_{Blip})$:

$$D^*_{BL}(T > T_{Blip}) = \frac{R}{\sqrt{\frac{4kT}{r_{surf}}}} \sqrt{\frac{A_{coll}}{\sigma}} \tag{3.29}$$

where $r_{surf} = r\sigma$ is a surface resistance in units of $[\Omega\,\mathrm{cm}^2]$. This expression of detectivity is significant as it underlines the net improvement on the signal to noise that can be obtained at high temperatures by increasing A_{coll} with respect to σ. Notice that $D^*_{BL,patch}$ at 300 K has the same value as $D^*_{BL,mesa}$ at 160 K, which means an increase of 140 K in the operating temperature in agreement with the previous results for quantum well infrared photodetectors having the same ratio A_{coll}/σ. [1] By substituting the expression of the resistance given in eq. 2.45 into eq. 3.25, it is possible to model the detectivity values as a function of the temperature, as shown in fig. 3.24 by the black line for the mesa structure and for the patch-antenna device. The model fits the data until T=200 K and it confirms an activation energy of E_a=116 meV (see sec. 2.5.1). The loss of accuracy in the detectivity model at high temperatures and no bias may stem from thermally induced charge transfer from the doped well to other higher energy levels. The resulting internal electric field may reduce the tunnelling extraction of electrons from the excited state of the optical transition with a negative impact on the responsivity.

3.6 Patch-antenna QWIP vs QCD

We conclude the chapter with a comparison between QWIPs and QCDs in a patch-antenna geometry at room temperature. We presented the QWIP detector in sec. 1.2.3 of chapter 1. Here we compare the patch-antenna QCD described in this chapter with an antenna-coupled QWIP optimized with respect to the device studied in ref. [1] and presented in [3].
The optimization intended to improve this type of metamaterial high temperature detectors. In particular, the doping density per well has been decreased with respect to the previous work from $n_{2D} = 7.0 \times 10^{11}/\mathrm{cm}^2$ to $n_{2D} = 4 \times 10^{11}/\mathrm{cm}^2$, in order to reduce the Fermi energy of 10 meV and consequently increase the activation energy. The associated lower absorption has been compensated employing eight quantum wells instead of five. The total QWIP cavity quantum efficiency is $\eta = \epsilon_{wires}\eta_{2D}\ g$ =1.8% at T=300 K, where η_{2D} is 21%, the room temperature photoconductive gain is g=1/N=0.125 and the wire polarization factor is ϵ_{wires}=0.7 (eq. 3.19). The thickness of the absorbing region, without taking into account the contact layers, is therefore increased from L = 236 nm to L = 339 nm. The thicker active region also reduces the ohmic losses of the cavity resulting in a higher cavity quality factor Q. The patch-antenna QCD and QWIP have therefore the same number of doped well, the same cavity thickness and were processed with the same metamaterial. The QCD total room temperature quantum efficiency is η=0.2% given in eq. 3.20. This important difference in quantum efficiency resides in their operations: the QWIP is a biased photoconductive detector when a single well gain>1 can occur, while the QCD is a photovoltaic device where the p_{ext} for one period can be at max 1.
Spectra at high temperatures of the new QWIP device are shown in fig. 3.25. With respect to the previous spectra in ref. [1], they were measured at room temperature with the FTIR rapid scan mode instead of using a step scan mode through a lock- in amplifier. The rapid scan mode enables a factor 2.5 less of integration time.

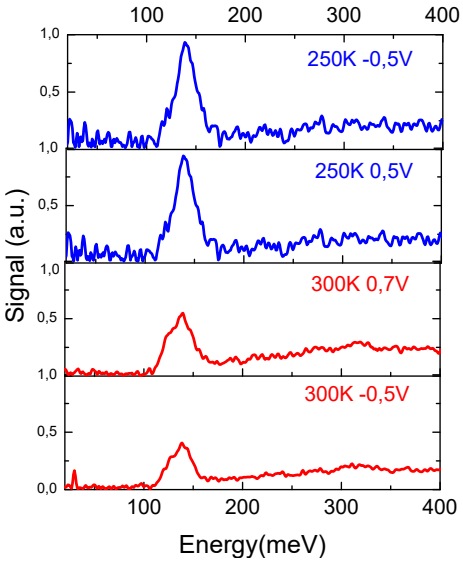

Figure 3.25: Photocurrent spectra for the optimized antenna-coupled QWIP at 250 K and 300 K, rapid scan mode.

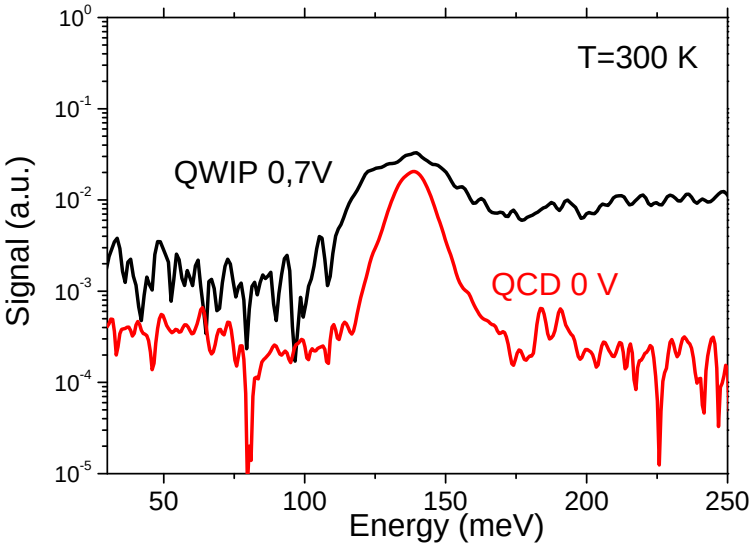

Figure 3.26: Photocurrent spectra at 300 K for the patch-antenna QWIP (black line) and QCD (red line).

In fig. 3.26, we compare the spectra of the two resonant antenna-coupled QWIP and QCD at room temperature. The QWIP is biased at 0.7 V and the QCD is unbiased. It's apparent from the spectra that even if the QWIP's peak signal is greater of a factor of 1.15 given by the difference in the quantum efficiency, it also has a higher noise level than the QCD. This is confirmed also by the detectivity as a function of the bias, measured in the same conditions, in fig. 3.27. The QCD

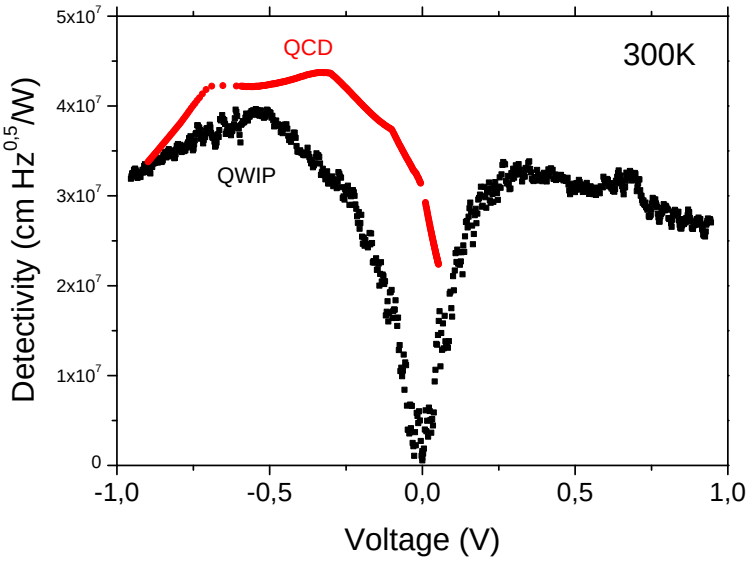

Figure 3.27: Background Limited Detectivity for a patch-antenna QCD (red) and QWIP (black) measured under a 60-deg FOV.

detectivity is represented as a red curve, and it doesn't vanish at 0 V. The QWIP's detectivity is the black line, which vanishes for no bias. The QCD can be operated without bias with a detectivity that is comparable to the value for QWIPs at V= 0.7 V. Despite the weaker response, the QCD has always a slightly better detectivity when it is biased.

These results imply that, for high temperature operation, patch antenna QCD are very adapted, but they need to be modified. Both the quantum region and the metamaterial can be improved. In

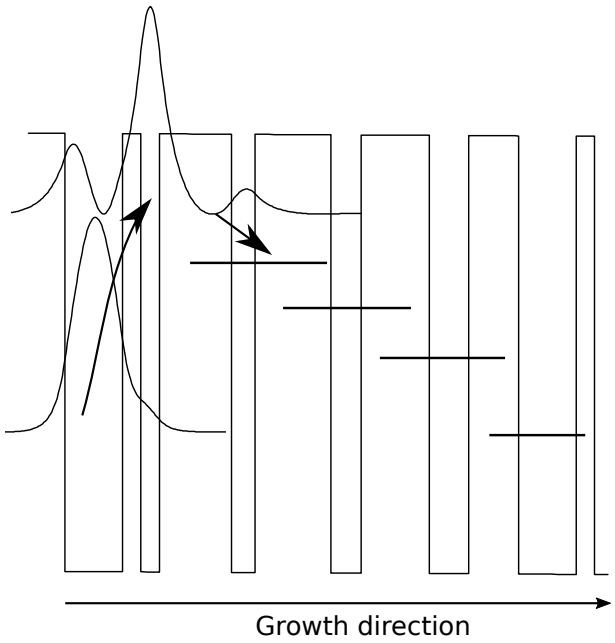

Figure 3.28: Band diagram for an optimised QCD at 9 µm at 0 bias. The thicknesses are 4.4, **1.4**, 1.4, **5.5**, 1.8, **5.8**, 2.3, **5.2**, 3, **3.8** in [nm], where the underline denotes the doped well at n_{3D}=1×10^{18}cm^{-3} and the bold denotes the barriers.

particular, working at 0 bias is very advantageous for integration purposes: the use of a higher gain amplifier is possible and the set-up is simplified. The current structure is not optimised for 0-bias operation, as the tunnel coupled levels require to be aligned with a bias (see sec. 2.4 in chapter 2). A diagonal optical transition, as represented in the band diagram in fig.3.28, would be more insensitive to the bias with respect to the vertical one. The use of a diagonal transition will also increase the resistance and reduce the electron probability to relax back into the doped well. As described in section 3.4.5, the absorption quantum efficiency can be increased by selecting a better meta-material:

- Increased number of periods up to 15. The cavity thickness is increased, the ohmic losses reduced. An absorption of 40%-50% could be obtained;
- A greater separation between the patches (up to a=4 µm) to increase the ratio A_{coll}/σ.

In the next chapter we will present a smart way to overcome the noise: the AC heterodyne detection.

Chapter 4

Unipolar heterodyne receivers

4.1 Introduction

In this chapter, we present progresses on heterodyne detection using room temperature metamaterial QWIP and QCD receivers and quantum cascade lasers (QCLs). In the previous part, we described a photonic based solution for exalting the absorption and reducing the noise of the detector. Most importantly, this enabled a sensitive operation of the device at high temperatures and the removal of complex cooling systems. However, the noise is still limited by the background radiation and the Johnson noise. A complementary solution to the issue of noise, proposed for the infrared range after the discovery of the CO_2 lasers, is the use of the amplification provided by beating, on a fast detector, a weak signal at frequency ω_S with a powerful local oscillator (LO) at frequency ω_{LO}, slightly shifted [41].
For this configuration, known as heterodyne, QWIPs and QCDs are the ideal devices as they are power detectors and their ultrafast dynamics provides a wide frequency range and a very high linearity before intensity saturation. The infrared heterodyne detection and the available technology are introduced in sec. 1.3 of chapter 1.
We remind here the basic equations and the main advantages of this technique. A schematic is given in fig. 4.1.
For convenience, we assume that the signal and the LO beams have linearly polarised electric fields. Therefore, the combination of their electric fields E_{LO} and E_S near the sensitive area of the photodetector can be described as follows:

$$\begin{aligned} E_h(t) &= [E_S \cos(\omega_S t + \phi_S) + E_{LO} \cos(\omega_{LO} t + \phi_{LO})]^2 \approx \\ &\approx \frac{1}{2}E_S^2 + \frac{1}{2}E_{LO}^2 \\ &+ 2E_{LO}E_S \cos[(\omega_s - \omega_{LO})t] \cos(\phi_s - \phi_{LO})t \end{aligned} \tag{4.1}$$

where E_{LO} and E_S are the amplitude optical fields of the LO and signal, respectively, ϕ_{LO} and ϕ_S are the constant phases. The first two terms are proportional to the average (DC) power absorbed. The term at the sum frequency is neglected as it is beyond the cut-off of the detector. The AC amplitude photocurrent generated by the detector at the beating frequency $\omega_h = \omega_{LO} - \omega_S$ is proportional to:

$$|I_{het}| \propto \mathcal{R} \, |E_S||E_{LO}| \tag{4.2}$$

where $\mathcal{R}$ is the responsivity of the detector.

Power detectors and gain The equation 4.2 is valid because QWIP and QCD are square-law detectors: they respond to the photon energy so the energy flux scales as the square of the

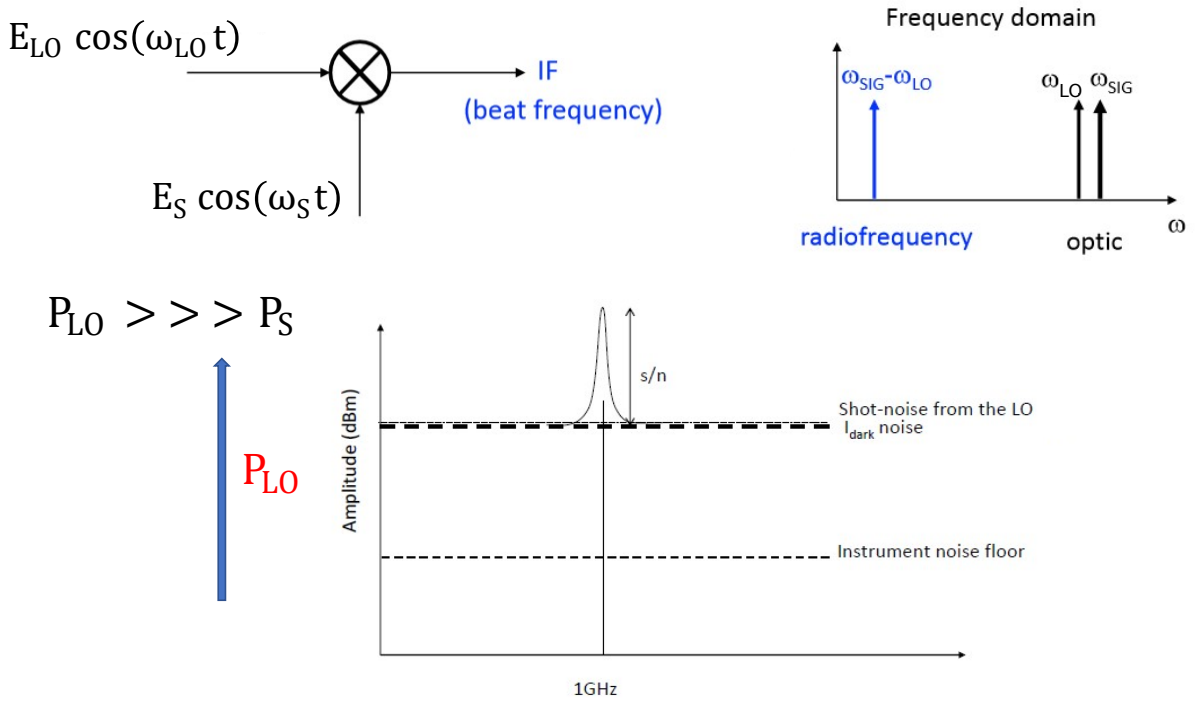

Figure 4.1: Schematic of the heterodyne detection principle: two beams illuminate a power detector , causing the square of their terahertz fields to combine and have a term at the difference frequency in the RF range. If the local oscillator laser is more powerful than the signal to be detected, the noise floor is ultimately limited by the photon shot noise of the laser and not by detector and amplifier noise.

electric field. Therefore the formula can also be written in terms of the incident power:

$$|I_{het}| = 2\mathcal{R}\sqrt{P_{LO}P_S} \tag{4.3}$$

The advantage, in applications when the signal power is weaker than the LO, $E_{LO} > E_S$, is that an amplification occurs because the energy flux in the difference frequency is greater than the DC energy flux of the signal by itself:

$$E_{LO} > E_S \rightarrow E_S\ E_{LO} > E_S^2 \tag{4.4}$$

Coherent detection Another benefit of heterodyne detection is that it preserves the phase of the signal to be detected if a phase reference is established in eq. 4.1. In our experiments, we considered that the phase difference is zero as no phase modulation on reference is employed (for instance through a modulator or a reflecting target).
The detection of the heterodyne AC component has also the advantage of a high resolution if the detector's bandpass is in the GHz range ($\nu/\Delta\nu > 1 \times 10^4$ where ν is the beating frequency). This results in a strong rejection of the blackbody background signal at λ=9 µm. The signal is also transferred from the THz to the RF frequencies where electronic filters and amplifier are available.

Noise reduction to the shot noise level The heterodyne signal to noise ratio is ultimately limited by the absorption quantum efficiency of the detector, independently of the dark current (see also eq. 1.33). When the LO photon noise overcomes all other noises, the signal to

noise ratio can be written as:

$$\frac{S}{N} = \frac{2\mathcal{R}\sqrt{P_{LO}P_S}}{\sqrt{4eg\ \Delta f\ \mathcal{R}P_{LO}}} = \frac{\alpha P_S}{E_{12}\Delta f} \tag{4.5}$$

where g is the photoconductive gain for photoconductive detectors defined in sec. 1.2.3, α is the geometry dependent absorption quantum efficiency, E_{12} the optical transition energy, Δf the integration bandwidth. The Noise Equivalent Power NEP is the signal power when the S/N is equal to one:

$$\text{NEP} = \frac{E_{12}\Delta f}{\alpha} \tag{4.6}$$

This fundamental result is only true if the photon noise is not affected by the laser Relative Intensity Noise (RIN). RIN can nevertheless be suppressed by using balanced photodetectors [97]. The potential of this detection technique at λ=9 µm has been exploited with QWIP detectors and two CO_2 lasers in 2006 in ref. [46]. In this reference a beating signal up to a frequency of 100 GHz was detected. Single line gas lasers are now replaced by quantum cascade lasers, which offer a power of $\approx$ 100 mW and can be precisely frequency-tuned with temperature [98]. This is a great advantage for the heterodyne scheme that can rely today on compact and efficient semiconductor local oscillators. The work presented in this chapter integrates and extends the study in ref.[1], by achieving a record result of a NEP=30 pW at room temperature at λ= 9 µm [3]. Some further work following these results is now in preparation, in particular regarding the high frequency impedance matching of the patch antenna devices [39].

4.2 Heterodyne detection with patch-antenna QWIP

The main innovation of our experimental set-up used for heterodyne experiments is the use of all semiconductor devices at room temperature at λ=9µm. Many efforts have been made in the last twenty years to reach high-temperature operations with devices where the order of magnitude of the involved energies (100-140 meV) is so close to the room temperature thermal energy (25 meV). The results presented in the ref. [3] constitute the main part of this chapter. They are obtained with an antenna-coupled quantum well infrared photodetector (QWIP) and two Distributed Feedback (DFB) QCLs.

4.2.1 The lasers

The QCLs emitting at λ=8.36 µm were provided by the group of Pr. J. Faist, ETH, Zurich. They are single-frequency, continuous wave (CW) devices working at room temperature (RT). The first RT CW lasers start to appear in 2002 [43] and since then mid-infrared applications using QCLs have thrived. A strong limitation for CW RT operation is imposed by the large QCL dissipated electrical power density, typically 10-50 kW cm^{-2} at RT, which are responsible for strong self-heating effects. In order to reduce the high thermal resistance imposed by the thick and layered active region, it is necessary to mount the laser junction down, so that the active region, where power is dissipated, is in contact with the copper heat sink. These optimised heat extraction has enabled operation with hundreds of milliwatts of single-mode emitted power at temperatures achievable with a Peltier cooler. The light and bias-versus-current (LIV) characteristics of the two DFBs QCL 1 and QCL 2 in use, are reported in figure 4.2 and 4.3. QCL 1 is characterised at T=293 K and T=273 K (left panel), with respective threshold currents 0.20 A and 0.22 A. QCL 2 is measured at 253 K, with similar threshold current at 0.22 A. The optical power is detected using a power-meter thermopile Ophir.

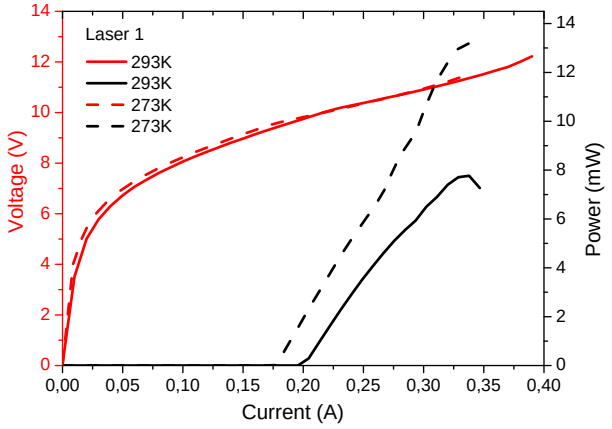

Figure 4.2: Light intensity and bias-versus-current characteristics of the DFB QCL 1

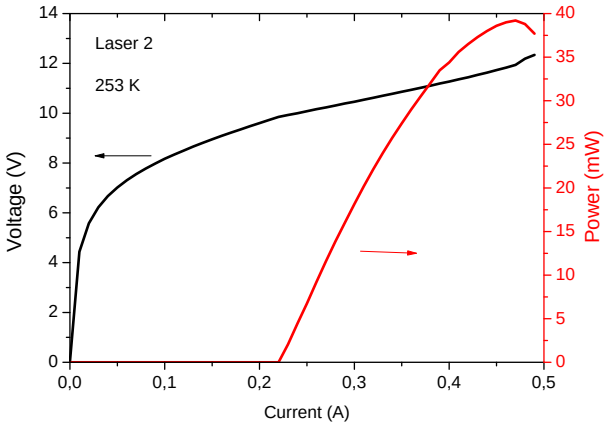

Figure 4.3: Light intensity and bias-versus-current characteristics of the DFB QCL 2

Tuning the frequency

Wavelength control for local oscillator laser is of primary importance for heterodyne detection. In order to achieve a single mode operation at the targeted frequency the two lasers have been processed in a buried distributed feedback cavity (DFB). In DFB, a grating is implemented inside the active region. It induces periodical changes in the effective index of the waveguide selecting specific propagating and counter- propagating modes. The emission frequency can be tuned by changing the refractive index using the laser substrate temperature and the current.

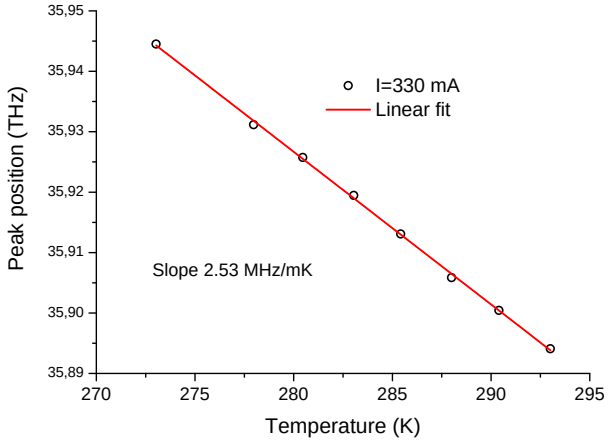

Figure 4.4: Peak frequency of the QCL 1 as a function of the laser substrate temperature for fixed current I=330 mA.

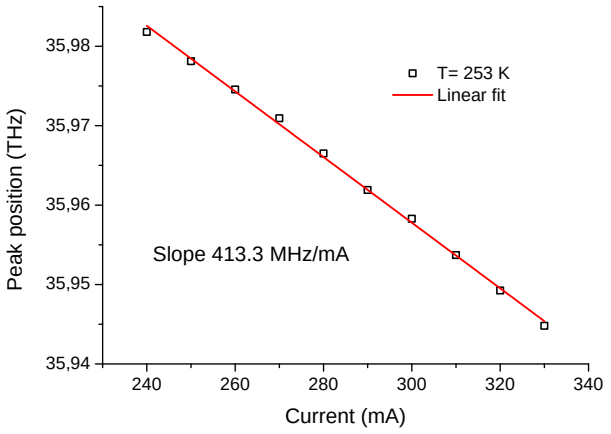

Figure 4.5: Peak frequency of the QCL 1 as a function of the current for substrate T=253 K.

Temperature

The emitted wavelength of a DFB QCL is fixed by the Bragg condition of the grating [98]:

$$\lambda(T) = 2\ n_{eff}(T)\ \Lambda(T) \tag{4.7}$$

where n_{eff} is the mode effective index ($n_{eff} \approx 3.2 - 3.3$ for grating in InGaAs layer and an InP regrowth) and Λ is the periodicity of the grating. The variations of the frequency emission in

temperature come from two contributions: the temperature change of the refractive index and the thermal expansion of the semiconductor material. The latter change is an order of magnitude smaller, therefore we consider just the first one for the tuning coefficient:

$$\beta = \frac{1}{\lambda}\frac{d\lambda}{dT} \approx \frac{1}{n_{eff}}\frac{dn_{eff}}{dT} \tag{4.8}$$

From the peak emitted frequency as a function of the temperature, reported in fig. 4.4 for laser 1, we can extract the temperature tuning coefficient. For both lasers the tuning coefficient is $\beta = -7.6 \times 10^{-5}$/K which corresponds to a frequency variation of 2.50 MHz for 1 mK of temperature drift. In the heterodyne experiments, the temperature is normally kept fixed, as its stabilisation down to the mK range requires at least tens of milliseconds.

Current

As the laser current is varied, the temperature inside the active region changes which causes again a modification of the effective index. The tuning of the frequency with injected current can be very fine. In the heterodyne experiments, current is varied to adjust the peak frequency beating of both lasers (for example, to give a beating at 1 GHz frequency). The QCL 1 peak frequency as a function of the current is reported in fig. 4.5 for a fixed temperature of T=253 K. The current tuning coefficient is β_c= 378.6 MHz/mA for laser 2 and 413 MHz/mA for the laser 1.

In laser free-running configuration, the frequency stability is therefore limited by the laser current, temperature fluctuations and optical feedback. The adjustments devoted to reduce the sources of thermal and electronic noise affecting the laser frequency stability are called passive frequency stabilisation techniques. The use of an external oscillator that forces the laser frequency to be stable is defined as an active stabilization technique. We will see in this chapter how the frequency stability ultimately contributes to the heterodyne SNR.

4.2.2 The receivers

The QWIP (1.2.3) is based on a GaAs/$Al_{0.25}Ga_{0.75}As$ heterostructure containing $N_{qw} = 8$ quantum wells absorbing at a wavelength of 8.9 µm at room temperature (139 meV). The QWIP has been designed with a bound-to-quasi-bound structure, formed by 33 nm thick barriers and 5.2 nm thick wells. The growth sheet is reported in appendix A.2. It has been processed into an array of double-metal patch resonators (chapter 3). The band diagram at E=-20 kV/cm and a SEM image of the device are depicted in fig. 4.7. The resonance with the peak absorption of the detector is achieved for structures with patch size s = 1.35 µm. The meta-material enables to differentiate the photon collection area from the electrical area, which is around 380 μm^2 for this device. The doping density per well is $n_{2D} = 4 \times 10^{11}$ /cm^2.
A photocurrent spectrum at room temperature and V= 0.7 V is reported in fig. 4.6, together with the emission line of a QCL as a red line. From fig. 4.6, we remark that the detector responsivity at the laser wavelength is 50% of the peak responsivity, which is not the optimal condition.

Responsivity and Saturation Intensity

Heterodyne detection requires a receiver that has a linear response without saturation due to the power from the local oscillator. The first step in the calibration procedure of an heterodyne detection set-up is therefore to test the receiver for increasing intensities and extract its responsivity value.

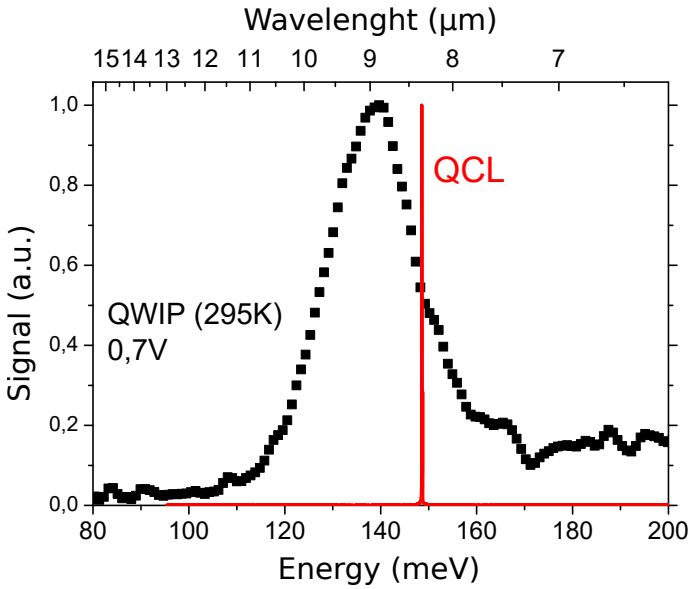

Figure 4.6: Photocurrent spectrum at room temperature with an applied bias of 0.7 V. In red the DFB QCL emission line.

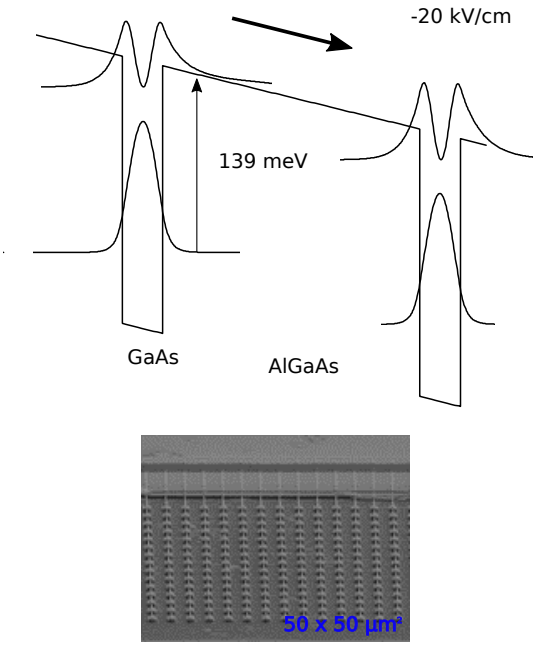

Figure 4.7: On top, band diagram under E=-20 kV/cm of the GaAs/$Al_{0.25}Ga_{0.75}As$ QWIP with 33 nm thick barriers and 5.2 nm thick wells. The excited level is resonant with the top of the well, forming a bound-to-quasi-bound structure. The structure is repeated for 8 periods. On the bottom, a SEM image of the patch-antenna device.

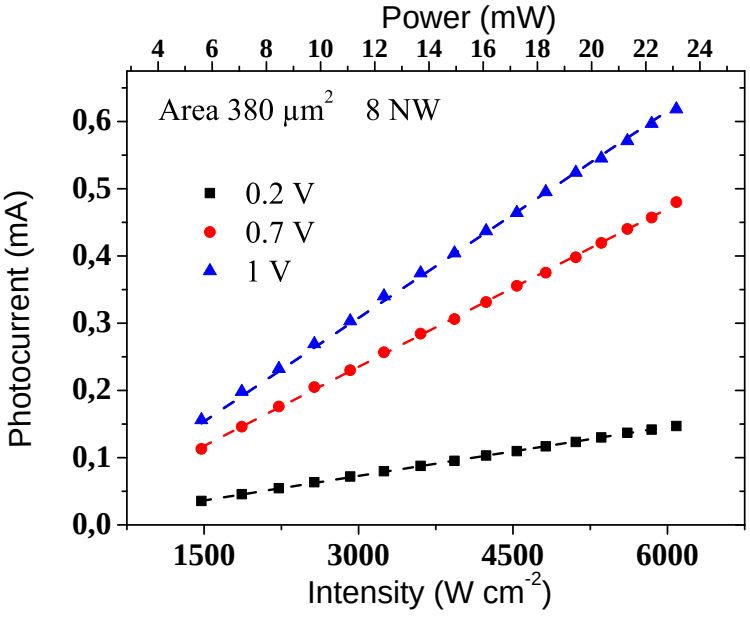

Figure 4.8: Photocurrent curves as a function of the incident intensity for three different bias voltages applied to the device, at room temperature. The dashed lines are linear fits. The intensity is calculated by dividing the optical power by the electrical area of the device (380 µm^2).

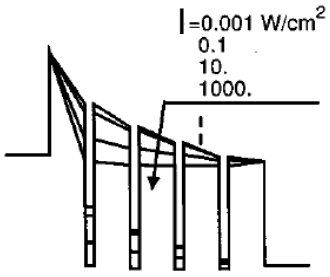

Figure 4.9: Conduction band-edge profile at an average field of 15 kV/cm under different illumination intensities (after ref. [99]).

In figure 4.8, we report photocurrent curves as a function of the incident power supplied by the QCL, for three different biases applied to the device. The detector was kept at ambient temperature. For these measurements the collimated beam from the QCL was focused on the detector using an anti-reflection coating aspheric lens (NA=0.56, focal lenght 6 mm). Since the QCL output beam is divergent, an optical system was used for collimation. After the focusing lens, the beam has a waist of 25 µm. The polarization of the laser was chosen to be orthogonal to the wires among patches in the device, which is the optimal condition to operate the QWIP. The power was calibrated by a thermopile Ophir.
No saturation effects appear even at intensities of several kW cm^{-2}.
Notably these values are far above the saturation intensity of MCT detectors. As a comparison, we have characterized with the same setup a Vigo MCT (model PVI-4TE-10.6), showing that it saturates at about 400 µW for an area of 0.25x0.25 mm^2, corresponding to 64 W cm^{-2}.
The linearity of the photocurrent over several orders of magnitude stands undoubtedly as an appealing advantage of QWIPs as heterodyne receivers. However, it is possible only as a consequence of a high dark current, which avoids the contact charge depletion caused by the photocurrent.
The quench of the photocurrent in short QWIPs structures can happen much before the intrinsic saturation of intersubband absorption in QWs due to the depletion of electrons from the ground state (in sec. 2.3.3 in chapter 2, $I_{sat} \approx 300$ kWcm^{-2}). It can be explained in terms of electric field inhomogeneity along the QWIP structure. See fig. 4.9 and references [8; 100; 99] for detailed studies.
Ideally, the electric field E is constant across the length of the structure L and it is given by the applied voltage V as E=V/L.The dependence of the QWIP responsivity $\mathcal{R}(E)$ on the electric field E is expressed as:

$$\mathcal{R}(E) = \frac{e}{h\nu}\alpha\ g_{photo}(E) = \frac{e}{h\nu}\alpha\frac{\tau_c(E)\ v(E)}{N_{qw}\ L_p} \tag{4.9}$$

where $g_{photo}(E)$ is the photoconductive gain (see also eq. 1.27), α is the quantum efficiency, τ_c is the photoexcited carrier lifetime, $v(E)$ the drift velocity, N_{qw} the number of wells, L_p the period length. A schematic representation of the conduction band edge profile at different intensities is reproduced in fig. 4.9, after [99]. The electric field can be very high at the contact if the total current increases due to a strong illumination, eventually becoming comparable to the applied field. In order to re-establish the equilibrium, the electric field on the wells in the middle of the structure is consequently reduced: in equation 4.9 the drift velocity is reduced and the responsivity drops. For this reason, it is observed that a non linear behaviour already occurs even at the thermal background power (mW cm^{-2} regime), in particular in devices with few periods and at low temperatures, where the contact effects are more important. On the contrary, in presence of a high dark current the thermionic transport through the contact barrier increases and therefore a drift current regime always supplies the carriers to refill the wells depopulated by photoemission.
The contradiction resides in the fact that the high suitable regime where the photocurrent overcomes the dark current, at the same time engenders a saturation of the responsivity. We will see in the next section that QCD devices are in principle not affected by contact saturation effects, as they don't present the dark current at 0 bias.
In fig. 4.10, we show the responsivity extracted from fig. 4.8 as a function of the applied bias as black dots. At room temperature and with an applied bias of 0.7 V, the detectors show a responsivity of 80 mA W^{-1}. This value is a factor 2.5 less than the peak responsivity calibrated with a black body, represented as a black line in fig. 4.10. The discrepancy can be attributed to the difference between the laser emission wavelength and peak responsivity, reported in fig. 4.6. Part of the light is also reflected back if the beam spot is larger than the device size, causing deviations in the estimation of power. In the rest of the chapter, we will use as reference the responsivity value obtained with the laser.

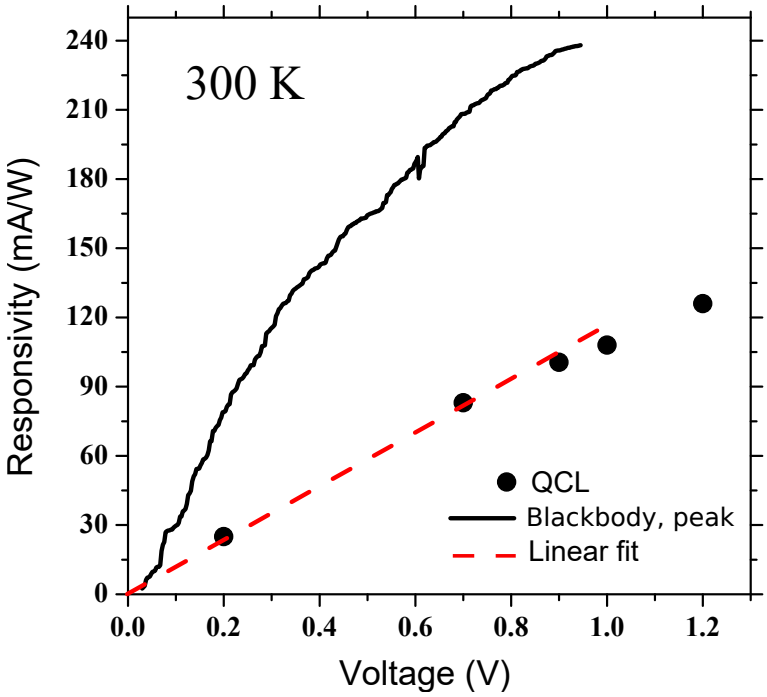

Figure 4.10: Responsivity of the detector as a function of the voltage applied to the device. The dots are the measurements with the QCL as a source, the black line is using a calibrated blackbody. The red dashed curve is the linear fit for small voltages.

Noise characterization

A second calibration step concerns the investigation of the current noise properties of the device. The photocurrent at room temperature for a laser power of $\approx$ 10 mW is I_{ph}=0.2 mA, one order of magnitude smaller than I_{dark} = 3.7 mA at V=0.7 V. Dark current at room temperature is presented in fig. 4.11.
The receiver has been characterised by measuring its noise power spectrum. Five contributions are distinguished:

- Dark current shot noise $i_{n,dark} = \sqrt{4egI_{dark}\Delta f} = 1.7 \times 10^{-11}$A (with gain g=0.125 and I_{dark}=3.7 mA, Δf=1 Hz);
- QWIP Johnson noise $\sqrt{4k_BT\Delta_f/r_d} = 5 \times 10^{-12}$A with r_d=200 Ω;
- Photocurrent shot noise $i_{n,shot} = \sqrt{4egI_{photo}\Delta_f} = 4 \times 10^{-12}$A with I_{photo}=0.2 mA;
- Amplifier and power supply noise, given by the datasheet and associated to the amplifier gain resistance;
- Flicker noise, at low frequencies proportional to $1/f$.

We observed in the noise spectral power measurement shown in fig. 4.12, that the noise is dominated by the dark current shot noise.
In these noise measurements, the detector was biased with a trans-impedance amplifier (femto DLPCA-200) connected to a signal analyser [101]. Each measurement comprises the average of 100 acquisitions up to 100 kHz, limited by the bandwidth of the transimpedance amplifier. The variable gain resistance was set to $r_G = 1$kΩ.

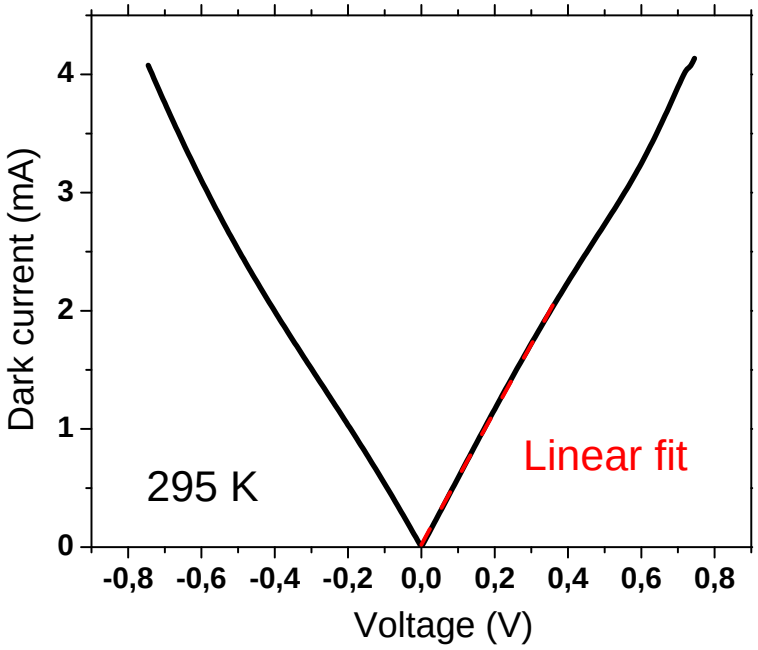

Figure 4.11: Dark current curves as a function of voltage at 295 K. The red dashed curve is the linear fit of small voltages data.

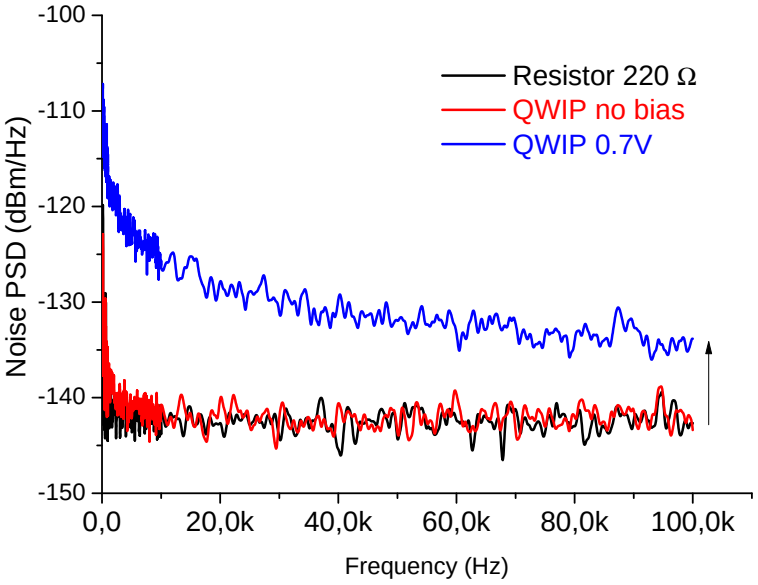

Figure 4.12: Noise power spectral density with 30 dB amplification at T=300 K for a resistor of 220 Ω (black curve), the unbiased QWIP (red curve) and for the QWIP under a bias of 0.7 V (blue curve).

Firstly, the noise contributions from the electronic set up have been calibrated using different input resistances. The QWIP detector has a resistance of 200 Ω, whose Johnson noise dominates over the amplifier noise (for greater input resistance, the amplifier noise dominates). In fig. 4.12, the black curve represents the noise from a calibrated resistance of 220 Ω, which is the resistance of the device at 0 V. The red curve is the connected unbiased detector. The blue curve is when the applied bias on the detector is 0.7 V: the noise floor increases 10 dBm above the Johnson noise when the dark current circulates in the device. This curve shows that the 1/f noise is visible only at frequencies below 40 kHz. As it is apparent from the figure at higher frequencies the noise flattens

and therefore, at our heterodyne frequencies, the flicker noise can be neglected. This is confirmed by noise calculation for our devices, where at room temperature the dark current shot noise is close to an order of magnitude greater than the other noise sources.

4.2.3 Heterodyne experimental set-up

The schematic of the experimental set-up is shown in fig. 4.13 and a photo is given in fig. 4.14. The black dot indicates the elements placed in a positionable stage (three coordinates plus rotation).

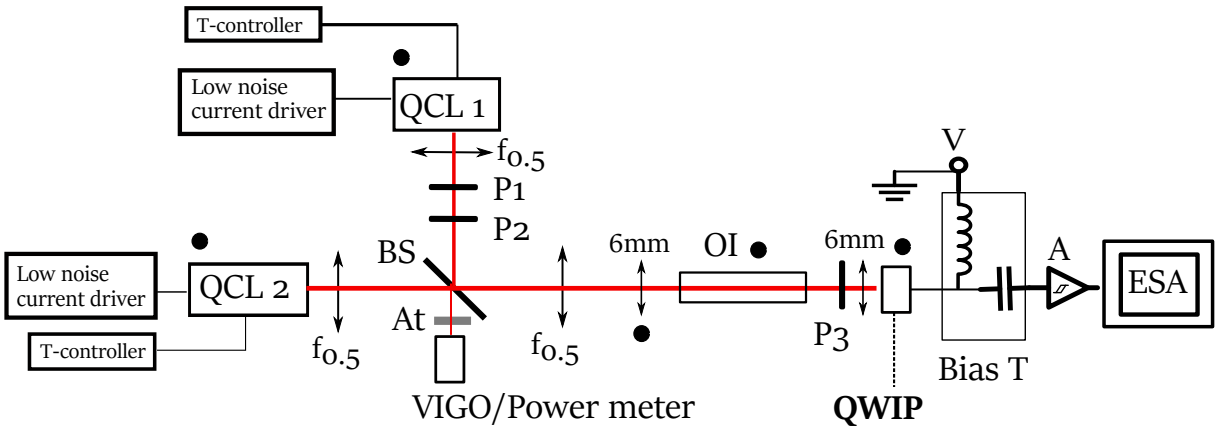

Figure 4.13: Schematic of the heterodyne detection set-up. A-power amplifier; OI-optical isolator; BS-beam splitter; P-polarizer; V- voltage supplier; At- power attenuator. The black dot indicates a movable element.

In our heterodyne experiment, the QCLs cooling is provided by a chilled water circuit and a Peltier module operated by a commercial temperature controller. The QCLs are driven with two home-made low noise current sources supplied by the Laboratoire de Physique de Lasers (LPL) at University Paris 13, with a current noise of only 100 pA/Hz$^{0.5}$. The optical power from each DFB quantum cascade laser is collected by two aspheric AR $f_{0.5}$ lenses and then made collinear using a ZnSe 50% beam-splitter (BS). One part of the beam serves as reference, impinging on a power meter or a VIGO detector. The other part is collimated and then passes through a telescope composed by a $f_{0.5}$ lens and a movable 6 mm focal length lens, providing a beam reduction of a factor 4. In this way, after the telescope, the diameter of the beam matches the aperture of an optical isolator (Innovation Photonics) having a diameter of 4 mm and mounted in a three-stages plus horizontal angle positionable platform. The resulting beams are focused and made collinear onto the patch antenna QWIP detector with a f = 6 mm lens.
The QWIP is biased with a Keithley 2450 source meter. The heterodyne signal from the detector is sent through a bias tee to the spectrum analyser Agilent E4407B (ESA). The signal is amplified by a low noise power amplifier (33-LN-S+, 18 dB gain). The QWIP is mounted on a copper holder without any cooling system. By means of a precision rotation stage, the detector angle can be selected. We remind that the QWIP response is partially polarized as the wires reduce the coupling for an incoming light polarized along their direction. Therefore the DFB QCL polarization is in the orthogonal direction to the wires, as it schematically represented in fig. 4.13. Three polarizers are used in order to control the power and keeping the same polarization for a correct estimation of the responsivity of the detector. Among the two wire grid polarizers in front of laser 1, one is rotated in order to attenuate the power, while the second is fixed with vertical grid in order to keep the laser polarization horizontal. A third wire grid anti- reflection coated polarizer in front of the detector is placed after the optical isolator enabling just the horizontal polarization to enter.

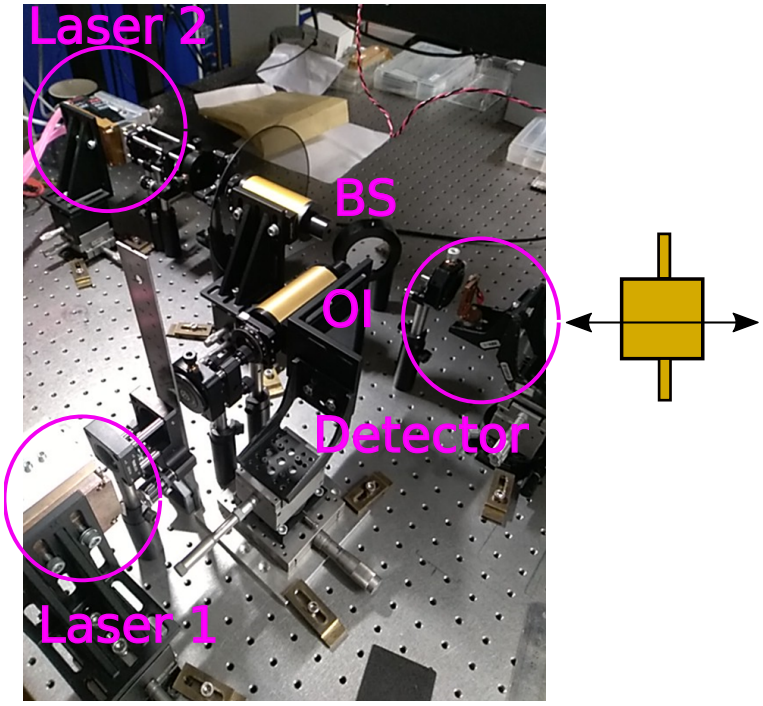

Figure 4.14: Photo of the heterodyne detection set-up, with two optical isolators. OI-optical isolator; BS-beam splitter; Note the cumbersome size of the optical isolator in the MIR range (15 mm length). On the side, schematic representation of one patch with wires and the orthogonal laser polarization.

With this set up we have evaluated the frequency response of the heterodyne signal (sweeping the laser current, hence the beating) and calibrated the signal to noise ratio and the Noise Equivalent Power (NEP).
As the laser beam is divergent, the alignment can be complex and the power calibration requires a precise procedure:

- At the beginning, the first and second laser beams (without telescope and optical isolator) are adjusted in order to form the two waists very far (ideally at infinity). The power at this distant point is measured with a power meter and must correspond to the calibrated LIV curve given in fig. 4.2 and 4.3.

- The telescope introduction into the optical beam has to preserve the power measured by the power meter at the distant position. To this aim, a lens is fixed and the other is moved parallel to the optical axis. The second laser is eventually adjusted to be collinear with the first one.

- Alignment of the optical isolator. The power is attenuated by a factor of 2, specified by the manufacturer.

- The polarizers are placed and the power is calibrated in both arms of the beam splitters.

- The detector is aligned with respect to one of the laser beams (by chopping the light and using a lock-in), then the second laser is eventually adjusted to the detector. Most importantly, the receiver isn't considered aligned until the same DC responsivity is measured from both lasers, considering their power individually.

4.2.4 Results

When the detector is illuminated by both lasers, an heterodyne signal appears on the spectrum analyser centred at the beating frequency. This signal is characterized by:

- Frequency position;
- Peak amplitude;
- Linewidth;
- Noise floor;

In this section we will explain how these parameters determine the SNR of the system and we will extrapolate its NEP. As the power from one laser is attenuated by means of a polarizer, the signal decreases and vanishes under the noise floor. The last detectable point sets the NEP of our system.

Detector frequency bandwidth

In fig. 4.15, we show heterodyne signals up to a frequency cut-off 5 GHz. The beating frequency is swept by varying one laser current. An amplification of 20 dB is used. In figure 4.16, the data are renormalized by the amplifier frequency response. The -3 dB bandwidth is f_c= 2 GHz. Although it is comparable to the frequency response of the VIGO MCT detector, our QWIP's bandwidth is at present strongly limited by the RF connections and the impedance mismatch between the detector and the external circuit. This mismatch is also responsible for RF spikes in the noise floor of the spectrum analyser, in particular within the MHz band. In this case, the huge potential in terms of high-speed operation for these devices is underexploited: the metal-insulator-metal contact pad and the wire-bonding for connections represent severe complex impedances detrimental for high-frequency operations.

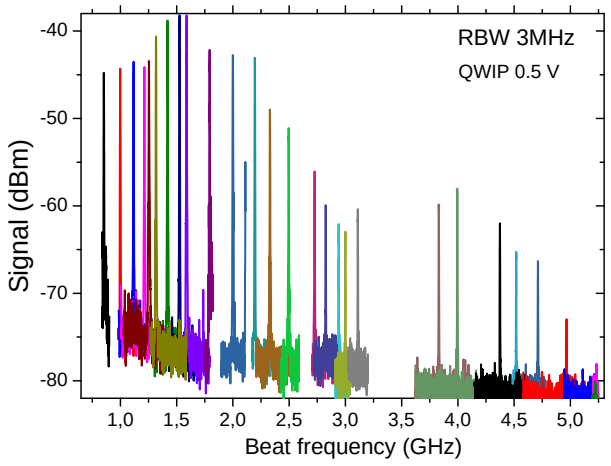

Figure 4.15: Heterodyne beatings at different frequencies. The RBW is 1 MHz and the amplification is 20 dB.

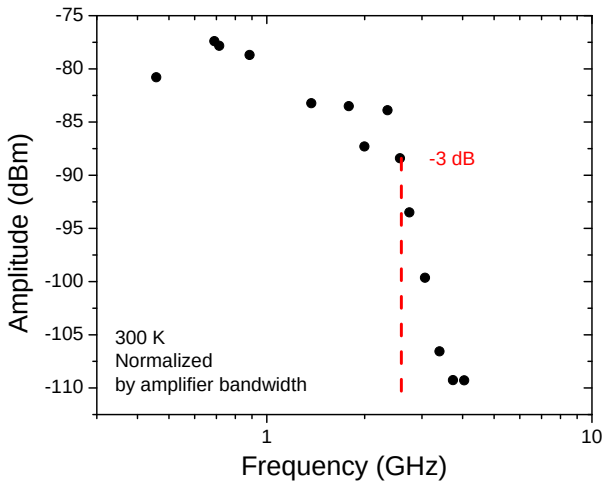

Figure 4.16: Normalized bandwidth of the detector. The 3 dB cut-off is at ≈ 2 GHz.

In the measurements presented in this chapter, a frequency range of 1-1.8 GHz was selected. The RF noise was kept low by using the shortest connections possible and accurately avoiding any ground loops in the set-up.

Signal to noise and NEP at room temperature

In direct detection, the noise equivalent power (NEP) is in the µW range, as the peak detectivity, calibrated with a blackbody source, is only D* = 3.3×10^7cmHz$^{0.5}$/W at room temperature.
In heterodyne detection, this limit can be overcome by using a strong local oscillator impinging on the detector. The signal to noise ratio is in this case:

$$\frac{S}{N} = \frac{I_{het}}{I_{noise}} = \frac{2\ \mathcal{R}\sqrt{P_{LO}P_S}}{\sqrt{[4eg(I_{dark} + I_{photo}) + \frac{4k_BT}{r_d}]\Delta f}} \tag{4.10}$$

where $\mathcal{R}$ is the responsivity, P_{LO} is the local oscillator power, P_S is the signal power, g is the photoconductive gain of the device, r_d is the QWIP resistance. We have neglected the amplifier noise.
The noise of the QWIP, in a unit frequency band, is calculated using the measured gain of g=0.125 and dark current at room temperature, reported in section 4.2.2 in fig. 4.11.
The heterodyne current I_{het} is extracted from the signal in the spectrum analyser, whose amplitude is in dBm for a spectral frequency range. After conversion to mW, the power spectral density PSD is introduced to renormalise the amplitude by the chosen resolution bandwidth (RBW): PSD = P_{mW}/RBW. The total signal is the integral over the frequency window:

$$P_{tot} = \int \text{PSD}\ d\omega \tag{4.11}$$

A noise baseline is selected for the integration, defined by a reference spectrum taken with the lasers off. After removing the amplifier gain G, the total heterodyne current is calculated as the power dissipated through the input load:

$$I_{het} = \sqrt{\frac{P_{tot}}{2G \times 50\Omega}} \tag{4.12}$$

The measured signal to noise ratio multiplied by the bandwidth of 1 Hz is shown in fig. 4.17 as a function of the incident signal power. This figure shows a comparison between measurements in the current set-up (red, green and fuchsia points for different methods of calibration) and the data from our previous work, black symbols [1]. In this graph, the y-axis is the signal to noise ratio (S/N) multiplied by the square root of the integration bandwidth $\sqrt{\Delta f}$, while on the x-axis one can read the incident power from the signal-laser, P_S.
The signal power is attenuated by changing the angle of the first polariser P1, depicted in fig. 4.13. The heterodyne spectra corresponding to different signal powers are reported in fig. 4.18. The power calibration cannot be simply effectuated with the thermopile, as it isn't sensitive enough. It has been done in two ways:

- with the known responsivity of the device (red points);
- with a VIGO detector and power meter on the other arm of the beam splitter (hollow pink dots).

In the first method, care must be paid to align for each measurement the detector to both lasers in order to obtain the expected total DC photocurrent. Since we know the responsivity, the local oscillator power from the thermopile and the heterodyne current given by the signal, we can estimate the signal power as:

$$P_S = \frac{(I_{het}/2\mathcal{R})^2}{P_{LO}} \tag{4.13}$$

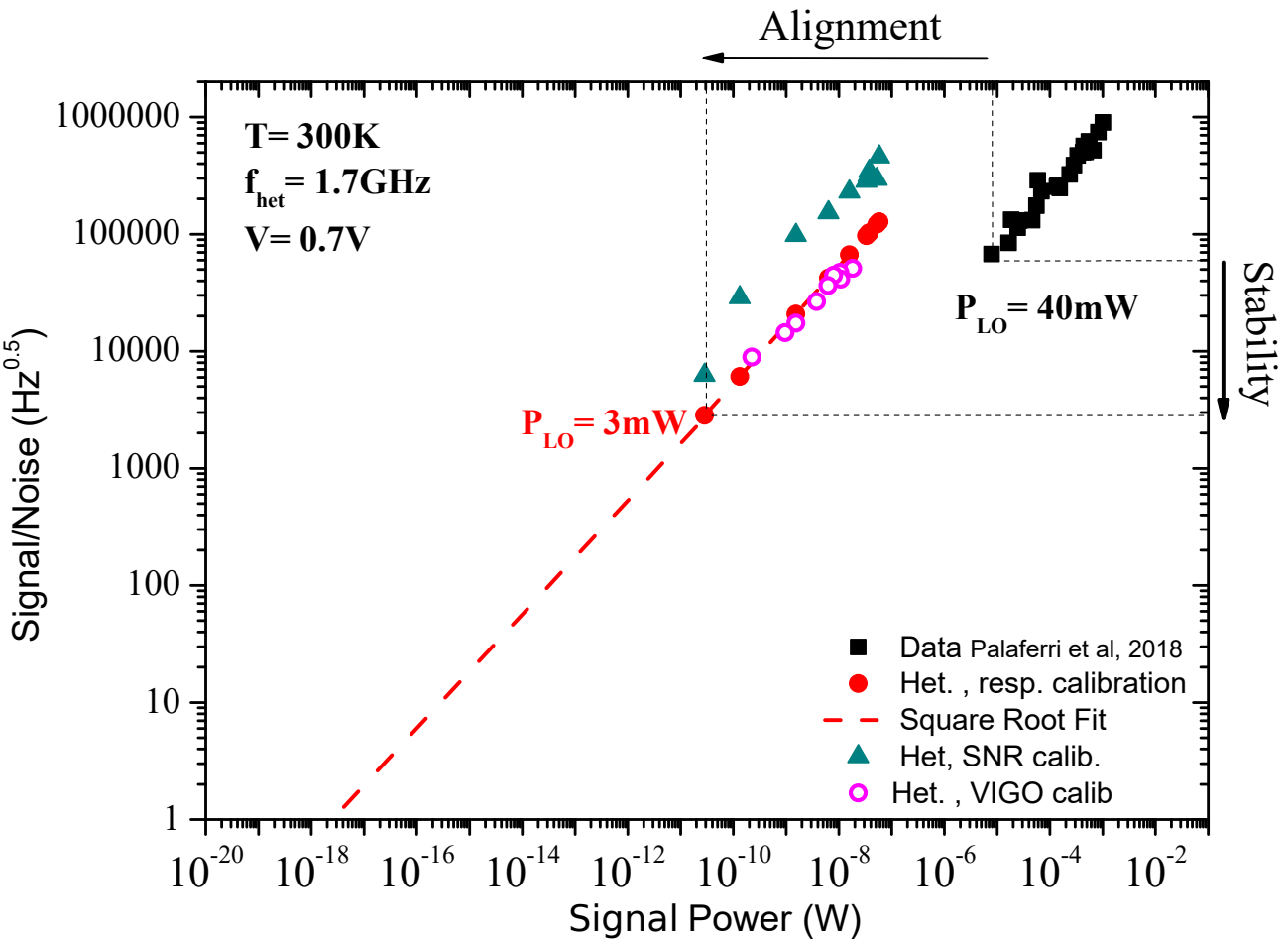

Figure 4.17: Log-log plot of the signal-to-noise ratio as a function of the QCL power. The noise of the QWIP is calculated using the measured gain and dark current values at room temperature. Black points are data from ref. [1], while red points are the current measurements. The improvement was possible in the horizontal scale thanks to a greater responsivity, in the vertical scale to a better stability.

An alternative method is to use the other arm of the beam splitter. If the ratio of the power between the two arms is known, we can then calibrate the power in the second arm with a VIGO when it doesn't saturate or a power meter for higher powers. Both methods give an equivalent estimation, as we report in figure 4.17. The results are also compared with the signal to noise ratio (SNR) computed as the difference between the maximum and minimum of the power spectrum, multiplied by the RBW and divided by the gain amplifier (+18 dB) (see fig. 4.18). They are presented as green triangles in fig. 4.17. This last method depends on the noise floor fluctuations and has a larger error, but a similar NEP is retrieved.

The lowest detectable power on the x-axis is the NEP of the system. The measured NEP is 30 pW for the present set-up, to be compared to the value of 8 µW in ref. [1], corresponding to an increase in sensitivity of five orders of magnitude. Notice that the measurements in previous set-up implemented in the group were taken with a local oscillator power $P_{LO} = 40$ mW, while in the present configuration the LO power is at most $P_{LO} = 3$ mW, because of the losses induced by optical elements added on the beam path. For an integration bandwidth of 1 Hz, the theoretical NEP at 0.7 V is $\approx 1 \times 10^{-18}$ W at 300 K.
The power of one single photon at $\lambda = 9\mu$m is $h\nu\Delta f \approx 2 \times 10^{-20}$ W for Δf=1 Hz: it is easy to

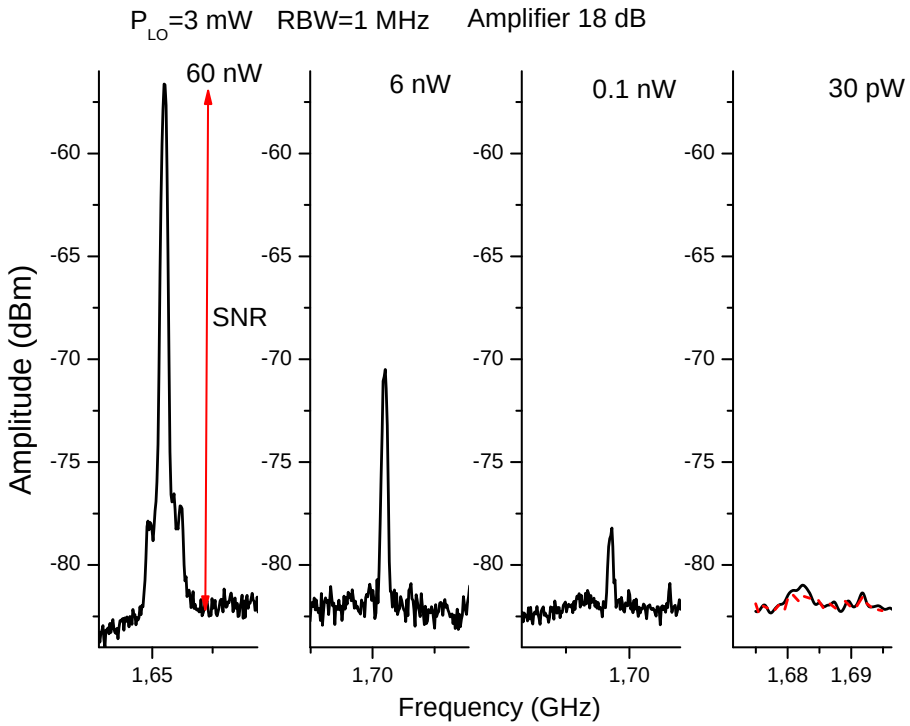

Figure 4.18: Heterodyne spectra for different signal powers, for a P_{LO}= 3 mW and an amplifier gain of 18 dB. The resolution bandwidth is 1 MHz. The red arrow indicates the SNR. In the last figure, the red dashed line is the reference spectrum with lasers off.

compute that our theoretical NEP corresponds to the detection of 100 9 µm photons per second, while the NEP of our uncooled system is sufficient to detect 15×10^8 photons, the equivalent radiation emitted by a surface of 10 µm^2 of an opaque object with perfect emissivity at a temperature of T=300 K in a 1 µm spectral band.

The lower NEP of the improved set-up has been obtained by addressing two main issues:

- Alignment;
- Stability.

A better alignment of the LO provides larger responsivity. This can be readily observed in fig. 4.17, where the enhanced stability corresponds to a reduced Δf (shift in the vertical direction) while the larger responsivity gives a shift on the horizontal axis. We recall that careful alignment between the LO and signal beams is necessary in order to maintain a constant phase difference over the whole surface of the photodetector [102]. The overlap of wave fronts between signal and LO beam is regulated by the relation $A_d\Omega = \lambda^2$, where A_d is the detector area and Ω is the solid angle of incidence of the radiation and λ is the wavelength. At $\lambda = 9$ µm and for our detector area, $A_d = 2500$ µm^2, the correct photomixing is valid for a maximum angular tolerance of 32 mrad.

Heterodyne signal linewidth and stability

A substantial improvement of the sensitivity was achieved by reducing the integration bandwidth Δf with a passive stabilization of the laser frequencies. To this end, we have minimized all the external sources of noise that compromise the laser frequency stability:

- fluctuations of the laser temperature;

- noise from the laser current generator;
- spurious optical feedback.

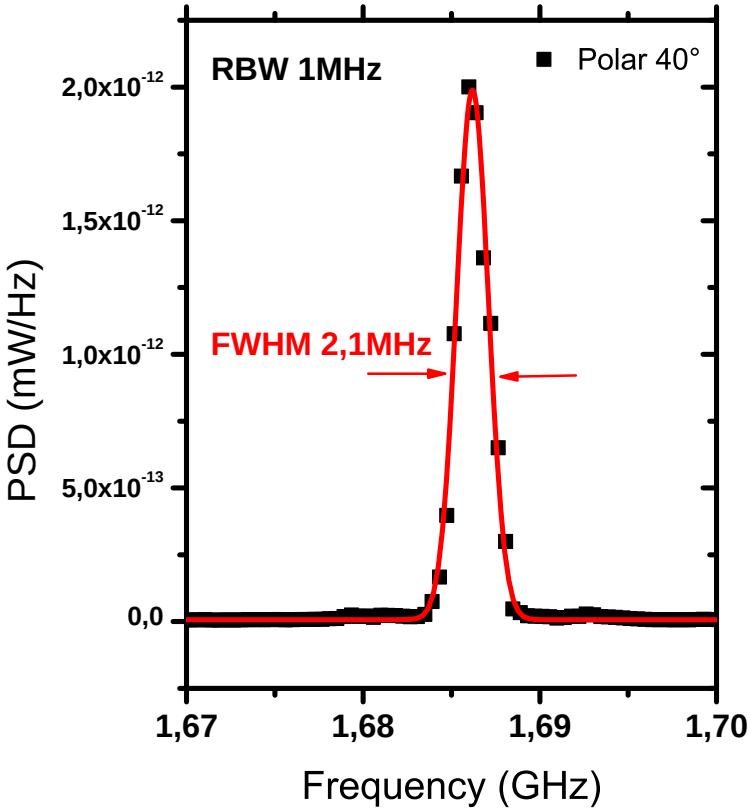

Figure 4.19: Heterodyne signal taken with a RBW of 1 MHz, an amplification of 20 dB for a polarizer angle of 40°. The red line is a Gaussian fit with FWHM of 2,1 MHz.

Temperature instabilities were minimized by an accurate regulation of the temperature controller PID, up to the mK, while current noise was reduced by using two low noise dedicated current drivers (100 pAHz$^{-0.5}$) [103].
Spurious optical feedback (OF) consists in reinjecting part of the light emitted by the laser after reflection from the optical elements in the set-up. It affects the laser properties if the reinjected fraction of power f_{OF} is larger than [104]:

$$f_{OF} >> \left(\frac{\text{Linewidth}}{\Delta\nu}\right)^2 \tag{4.14}$$

where the free-running laser linewidth is around 1 MHz and the longitudinal mode spacing for the effective cavity length L=2 mm is $\Delta\nu = c/(2nL) \approx 23$ GHz. The main feedback contribution in our set-up comes from the detector: if perfectly aligned, it acts as a partial reflector forming a Fabry-Perot cavity with the laser facet. The patch-antenna QWIP, as we described in chapter 2, is processed with a highly reflective bottom gold plane and an absorption contrast of 80%. Consequently, the feedback introduced is expected to be at least 10%, considering the BS present in the path. This feedback fraction of f_{OF} ≈-10 dB is far more than the -87 dB calculated from eq. 4.14 and should strongly affect the QCL lasing properties. The QCL behaviour under OF has been studied in [105] as a function of the length of an adapted external cavity. In our set-up, the external cavity is twice the distance between the laser and the detector, approximately 60 cm. Following

the cartography given in [105], the feedback level in our set up of -10 dB corresponds to the third operational regime. In these conditions, the QCL mode is forced to the external Fabry-Perot cavity and a linewidth narrowing can happen. The output power of the laser and its threshold are indeed strongly modified. This is an undesired situation for power calibration, as on the contrary the thermopile doesn't produce feedback. Moreover the modulation of the laser power produced by the standing wave pattern is subjected to the fluctuations of the refractive index of air, and therefore to the ambient temperature instabilities (that can be changed for example as a person walks in proximity of the experiment). As our aim is to calibrate the set-up, tilting the detector did not appear to be a suitable solution since it reduced the power at the detector. The best method is found to be the employment of an Innovation Photonics MIR isolator based on Faraday rotator principle, although its transmission is only 50% and it is difficult to align.
All these arrangements enabled the use of an integration time of around 100 ns (Δf = 8 MHz) to be compared to around 200 ps (Δf = 4.5 GHz) in ref. [1].
We can derive the effective integration time from the fig. 4.17, as the SNR in the y-axis is normalized by the integration bandwidth. The last measurable power of NEP=30 pW corresponds to a SNR of 2842. This value is equivalent to have a SNR= 1 for an integration bandwidth of $\Delta_f = (\mathrm{SNR})^2 \approx 8$ MHz.
The reduction of the technical noise provided us with a stability which is the maximum achievable in this configuration as it is comparable to the sum of the linewidths of the two DFB QC lasers, reported to be in the MHz range in the literature [24]. The easiest way to characterize the spectral purity of an heterodyne signal is by the full width at half maximum (FWHM) linewidth of the optical lineshape [106]. An heterodyne signal measured with a RBW=1 MHz, is reported in fig. 4.19, along with the Gaussian fit with a FWHM $\approx$ 2 MHz (red line).
In presence of electronic noise and temperature noise, flicker noise severely affects any free-running QCL, therefore the real linewidth is much broader than the intrinsic linewidth predicted by the Shawlow-Townes formula and measured to be as narrow as 500 Hz [107]. In this noisy case, the spectral profile of the two free-running DFB lasers can be modelled by random fluctuations with Gaussian functions with center frequencies ω_{DFB} and variance of Γ_{DFB}. As a result of the superposition of the electric fields of the two laser beams E_0, the power spectrum of the heterodyne signal at the beat frequency is calculated as:

$$P_{het}(\omega) = \frac{|E_0|^2}{2\eta_0} \frac{1}{\sqrt{2\pi}\sigma_{het}} \exp\left(-\frac{(\omega-\omega_b)^2}{2\sigma_{het}^2}\right) \tag{4.15}$$

where η_0 is the characteristic impedance of free space, $\omega_b = \omega_{DFB}^{(1)} - \omega_{DFB}^{(2)}$ is the beating frequency set to be in the GHz range. It is well a Gaussian spectrum with a FWHM linewidth of $\sqrt{2\ln 2}\,\sigma_{het}$ where $\sigma_{het} = (\sqrt{2}\Gamma_{DFB,1}^2 + \sqrt{2}\Gamma_{DFB,2}^2)^{1/2}$ which confirms the $\Gamma_{DFB} \approx 1$ MHz limit of our set-up.

Mixing properties

The improved stability of our system has allowed us to explore other important functions of these ultrafast receivers. In particular, we have investigated the ability of frequency shifting the heterodyne signal, which is of great interest for signal processing and for future active stabilization of the beating. This function has been obtained by injecting into the detector a microwave excitation through a -10 dB directional coupler in order to modulate the heterodyne signal within the receiver itself, with or without an applied dc bias. A schematic of the setup is shown in fig. 4.20a.
After setting a DC voltage V_0, the detector is modulated through an applied microwave voltage $\mathbf{v_u} = |v|\ cos(\omega_u t)$ around a working point $I_0(V_0)$. The injected AC bias at frequency ω_u causes a modulation of the device responsivity $\mathcal{R}(V_0 + \mathbf{v_u})$, which allows us to expand the heterodyne

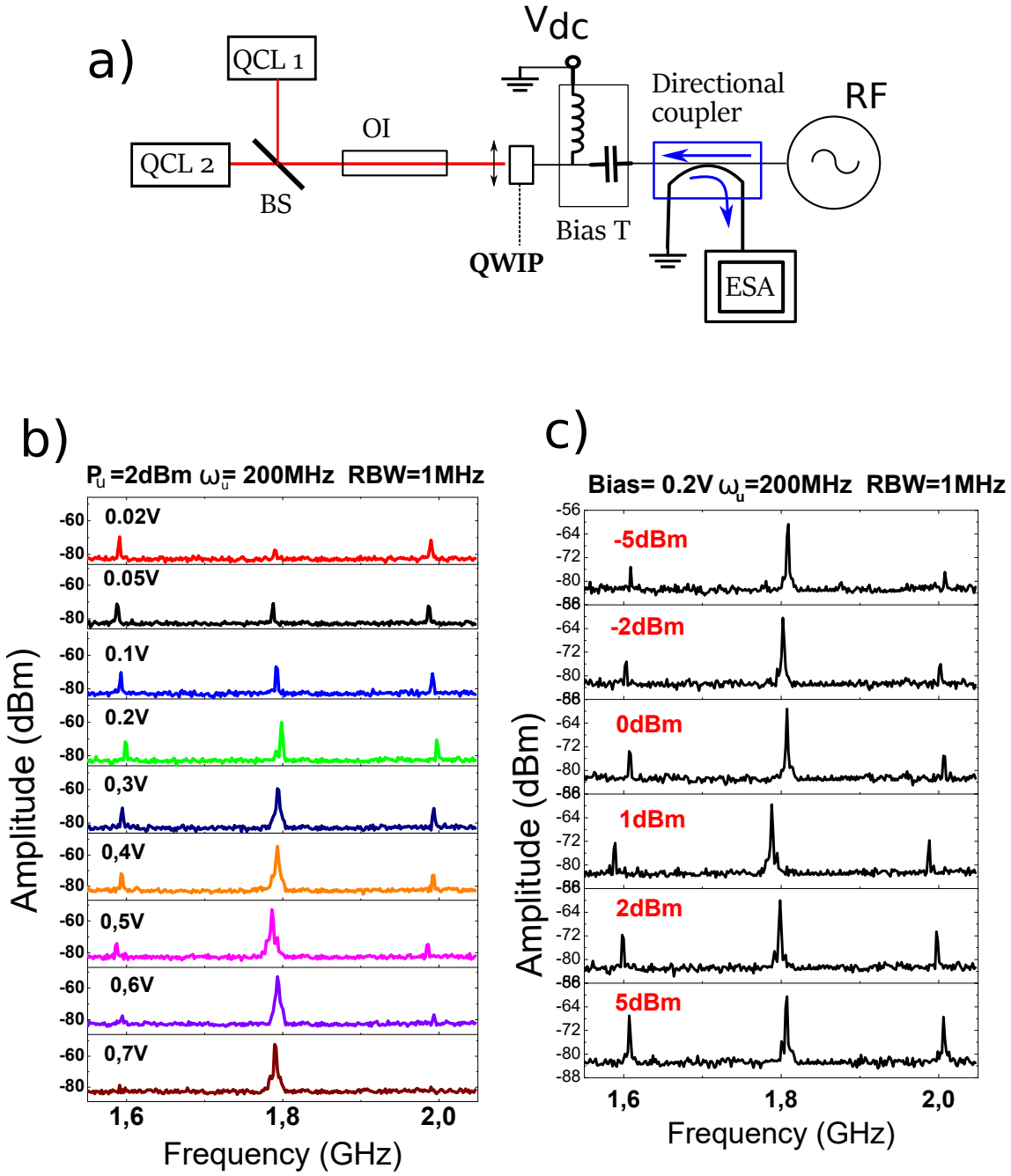

Figure 4.20: a) Schematic of the microwave mixing experiment. The detector has a DC bias on which is added an RF signal, through a bias T. b) Signals with RF power P_u=2 dBm and different applied DC voltages. c) Spectrum analyzer signals with a DC bias of V = 0.2 V, for different injected RF powers. The heterodyne signal has a frequency of 1.8 GHz, and the two sidebands are shifted of ±200 MHz.

current at the first order as:

$$\begin{aligned} I_{het} &= 2\mathcal{R}(V_0 + \mathbf{v_u})\sqrt{P_{LO}P_s}\cos(\omega_h\ t) = \\ &= I_{het}(\omega_h) + 2\ v\ \frac{\partial \mathcal{R}}{\partial V}\sqrt{P_{LO}P_S}\cos(\omega_h\ t)\ cos(\omega_u\ t) \\ &= I_{het}(\omega_h) + I_{het}(\omega_h \pm \omega_u) \end{aligned} \tag{4.16}$$

The heterodyne current is therefore composed of a signal at the frequency ω_h and two sidebands at $\omega_h \pm \omega_u$. Notice that the component at ω_h disappears if no DC bias is applied to the device, as $\mathcal{R}(0) = 0$. Figure 4.20 b) and c) show measurements recorded with a spectrum analyzer of a heterodyne signal at 1.8 GHz. In figure 4.20b the detector has a constant microwave power P_u=2 dBm and the voltage is varied. In figure 4.20c the detector has a constant applied bias V_0= 0.2 V, while the microwave power is increasing top down in the figure. Two sidebands appear at $\omega_h \pm 200$ MHz, corresponding to the frequency of the injected microwave. The signal power of the sidebands is:

$$\begin{aligned} P_{side} &= R_L v_u^2 \left(\frac{\partial \mathcal{R}}{\partial V}\right)^2 P_{LO}P_S \\ &= R_L Z(\omega_h \pm \omega_u)\ P_u\ \left(\frac{\partial \mathcal{R}}{\partial V}\right)^2 P_{LO}P_S \end{aligned} \tag{4.17}$$

where R_L is the load resistance of the transmission line, P_u is the applied microwave power and Z is the frequency dependent complex impedance of the QWIP. In this expression, we suppose that the microwave voltage across the device is $|v_u|^2 = |Z||P_u|$. Z could be obtained from the reflection coefficients S_{11} parameters measured with a VNA analyzer. For impedance matched devices, it should be equal to the load resistance. As we know that our devices are strongly limited by the capacitance of the contact pad and the inductance of the wire bond, we leave a more detailed analysis for future work.
From the formula 4.17, we can infer that the heterodyne signal can be amplified into sidebands by the steepness of the responsivity-voltage curve, given in fig. 4.10 b) and c), and by P_u.
In figure 4.21, we report the microwave spectra without DC bias applied to the detector, while the injected microwave power increases from -5 dBm to 5 dBm. In this configuration, the heterodyne signal disappears and only the sidebands are observable as predicted by formula 4.16. Figure 4.21b, shows the sideband amplitude for increasing microwave power on a wide range from P_u = -18 dBm up to 5 dBm. The amplitude increases linearly with P_u, in agreement with the eq. 4.17. From the data at 0 DC bias voltage, we can plot the linear operating range of the receiver and extrapolate its first order compression point IP_{1dB}, which occurs at 4.5 dBm. It means that the linear dynamic range of our receivers is 31 dB. For large voltages, the responsivity reaches the saturation point, its derivative in equation 4.17 vanishes, and its modulation is no more possible: the sidebands disappear as visible in fig. 4.20b for V=0.7V.
These measurements illustrate that our QWIP heterodyne receiver acts also as a mixer, enabling to shift the heterodyne frequency to sidebands at any frequency within the bandwidth of the detector.

Active frequency stabilisation:preliminary results

In the SNR graph of fig. 4.17, the sensitivity is limited by the laser stability, which doesn't allow for further increase of the integration time. To this aim, active frequency stabilization techniques need to be implemented for the LO laser. In this work, we have stabilized the QCL by phase locking the beat note to a reference oscillator. The electronic equipment was supplied by the Laboratoire de Physique des Lasers (LPL). In this laboratory, a sub-Hz stabilization of a MIR QCL [108] has been notably achieved by employing an ultra-stable near-infrared laser as oscillator. The set-up,

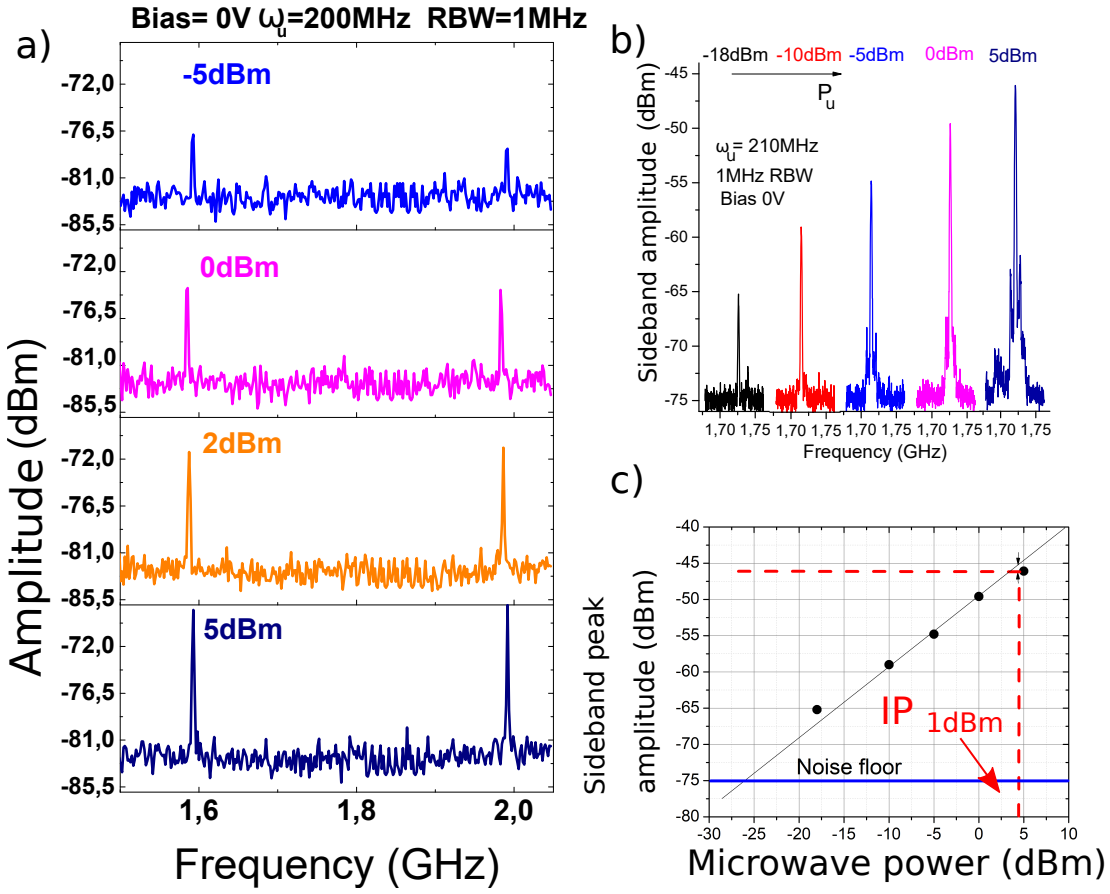

Figure 4.21: a) Microwave spectra with no DC applied bias on the detector, for four different injected RF powers at 200 MHz. The heterodyne signal at 1.8 GHz is no more visible and two sidebands can be observed at ±200 MHz from it. b) Sideband amplitude for increasing injected RF power from -18 dBm to 5 dBm. c) Sideband peak amplitude as a function of the injected microwave power. The linear dynamic range between the noise floor and the IP_{1dB} point is 31 dB.

including the servo loop is depicted in fig. 4.22a.
The beat note at frequency ω_h is filtered around 135 MHz, amplified (Mini-circuit ZFL-500-N+, 25 dB gain) and mixed with a RF signal coming from a commercial generator (Rohde-Schwarz SMA100A) to generate the error signal that drives a proportional-integrator phase-lock loop. The correction signal is applied to the QCL current.
In fig. 4.22b, we report an heterodyne signal (RBW=1 Hz), detected by the patch-antenna QWIP, fitted by a Gaussian curve with FWHM = 1 Hz: the QCL has a Hz-narrow line-shape instead of hundreds of kHz as in free-running mode. In this limit, the obtained SNR is 65 dB for a total impinging power of P = 3 mW, instead of 35 dB with LO in free-running mode. From a rough estimation of the SNR, we deduce that the NEP in this preliminary configuration is approximately 3 pW. The heterodyne signal as a function of the RBW is shown in fig. 4.22c. By decreasing the RBW from 30 kHz to 1 Hz, we reduce the noise by more than 15 dB. However these measurements show that there is still a residual technical noise, since:

- From RBW_1 to RBW_2, the noise level should decrease of $10\log(RBW_1/RBW_2)$;
- Without parasitic noise, the spectrum noise floor at RBW = 1 Hz is limited by the spectrum analyser noise floor (-110 dBm) or by the phase noise of the reference oscillator (-83 dBc at 100 MHz, 20 kHz offset), shown as a black curve in the first graph of fig. 4.22.

The noise of the reference and part of the optical feedback from the detector introduces a phase noise detrimental for the SNR. Moreover, SNR measurements are limited to a NEP of the order of µW, where the beating starts to be too weak to drive the PLL.
For future measurements, several improvements would be beneficial (beside developing an impedance matched detector):

- Use of an ultra stable frequency comb as RF reference;
- Narrow the linewidth of the laser by means of the feedback, under a fine controld through a piezoelectric transducer [109]. In this way the optical isolator can be removed and twice the current LO optical power can be used.
- Use of a down-mixing technique to lock in the GHz range. In particular, we can exploit the QWIP mixing properties, presented in the previous section and lock the laser frequency to a sideband. When the signal power is decreased, the microwave power can be adjusted to compensate it, while the NEP is measured on the heterodyne signal. Moreover the sideband can be shifted in frequency at will.

4.3 QCD for heterodyne detection

In the previous section, we presented the results of heterodyne detection obtained with a patch-antenna QWIP at room temperature and a DFB QCL as LO, with a maximum output power of P_{LO}=3 mW after the optical components. The measured NEP is severely limited by the QWIP dark current of I_{dark}=3.7 mA at room temperature: however, it is in these conditions that the amplification provided by the LO laser is strongly beneficial for the SNR. In fact, in a situation where the photocurrent dominates the dark current, we know from section 4.2.2 that saturation effects would occur in QWIP structures at much lower LO powers.
Following these considerations, the question naturally arises about the use of patch-antenna quantum cascade detectors as heterodyne receivers. Since these devices operate in a photovoltaic mode without dark current, no saturation effects are expected.
An even stronger local oscillator power can thus be used in a heterodyne set-up to reach the laser shot noise limited detection.

4.3.1 QWIP and QCD as heterodyne receivers

We revive for the heterodyne detection the comparison made in section 3.6 in chapter 3 between the patch-antenna QWIP and QCD we have fabricated in this work. The QWIP and QCD noise spectral densities are:

$$\begin{aligned} S_{QWIP} &= \frac{4k_BT}{r_{QWIP}} + 4e|I_{QWIP}|\frac{1}{N_{QW}p_c} \\ S_{QCD} &= \frac{4k_BT}{r_{QCD}} + 2e|I_{QCD}|\frac{1}{N_{QW}} \end{aligned} \tag{4.18}$$

where r is the resistance, N_{QW} the number of doped quantum wells and $g_{noise} = 1/(N_{QW}p_c)$ the QWIP noise gain where p_c the capture probability (see eq. 1.25 in chapter 1). The QCD noise spectral density was also defined in eq. 2.39 in chapter 2. The QWIP average shot noise current is composed of the photon shot noise and of the dark current shot noise, while the QCD one at 0 bias only of the photon shot noise current:

$$\begin{aligned} |I_{QWIP}| &= I_{dark} + \mathcal{R}_{QWIP}P_{LO} \\ |I_{QCD}| &= \mathcal{R}_{QCD}P_{LO} \end{aligned} \tag{4.19}$$

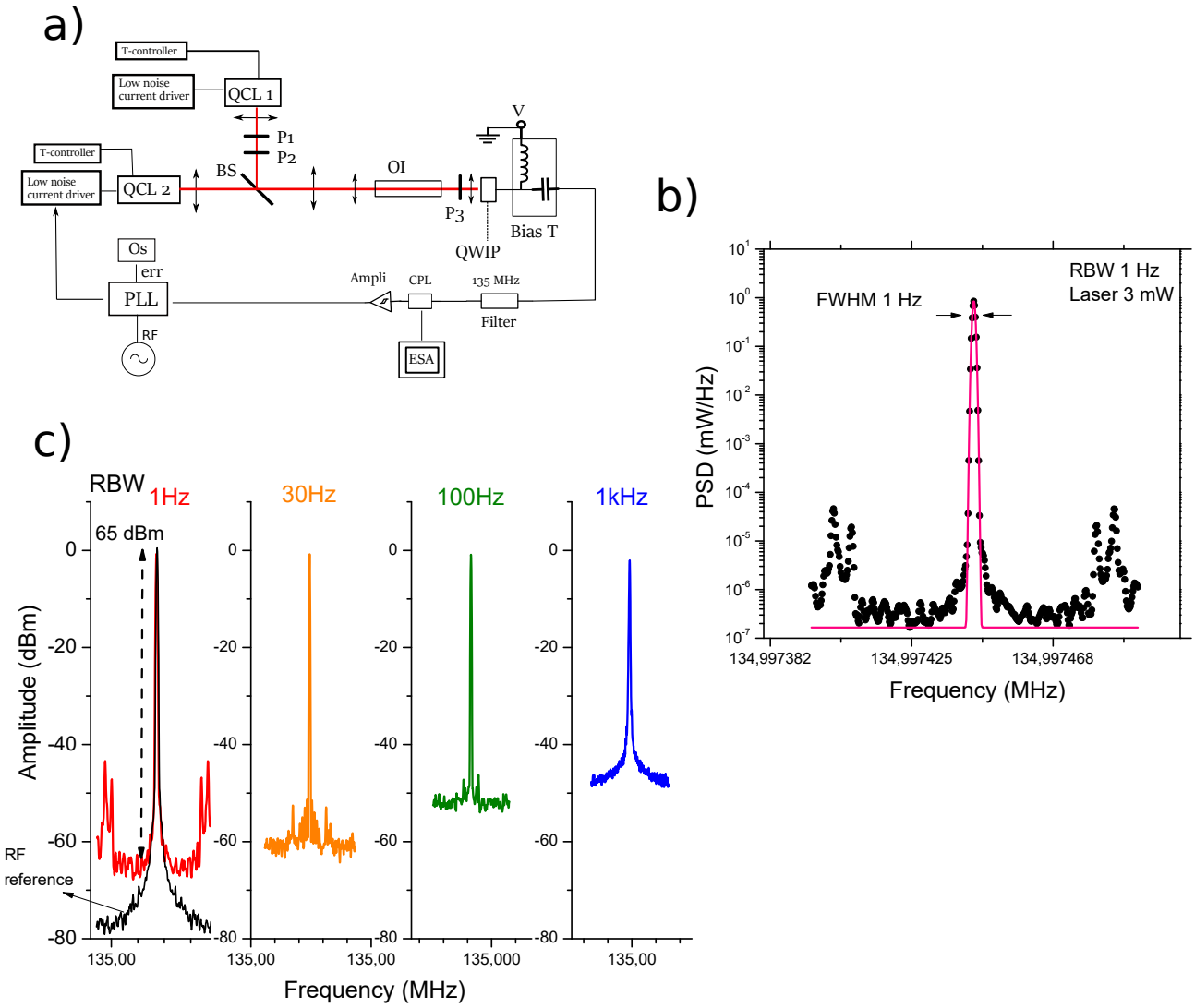

Figure 4.22: a) Set-up for the active stabilisation. OI-optical isolator, CPL -10 dB coupler, Os- Oscilloscope, PLL- phase locked loop b) Example of active-stabilized heterodyne signal measured by a patch-antenna QWIP (RBW=1 Hz). The pink curve represents the Gaussian fit with FWHM=1 Hz. c) Heterodyne signals for different RBWs. In the first graph, the reference oscillator is reported as a black curve.

where $\mathcal{R}$ is the responsivity, defined for the antenna coupled devices as:

$$\begin{aligned} \mathcal{R}_{QWIP} &= \frac{e}{E_{12}}\eta_{2D}g_{photo} = \frac{e}{E_{12}}\eta_{2D}\frac{p_e}{N_{QW}p_c} \\ \mathcal{R}_{QCD} &= \frac{e}{E_{12}}\eta_{2D}\frac{p_{ext}}{N_{QW}} \end{aligned} \tag{4.20}$$

where η_{2D} is the cavity absorption quantum efficiency defined in eq. 3.6 in chapter 3, p_{ext} is the extraction probability for one QCD period calculated in sec. 2.4.3 in chapter 2. The photoconductive gain for QWIP is defined by the capture and emission probability p_c and p_e of the well (eq. 1.27). For the QWIP detector, the photoconductive gain in the responsivity $\mathcal{R}$ and the noise gain differ in the escape probability p_e ([8]) which is sometimes approximated to 1 for good QWIP structures (chapter 1, eq. 1.25).
The noise spectral densities of eq. 4.18 for the patch antenna QWIP and QCD are presented in fig. 4.23 as a function of the temperature of the device. The estimated quantities in eq. 4.18

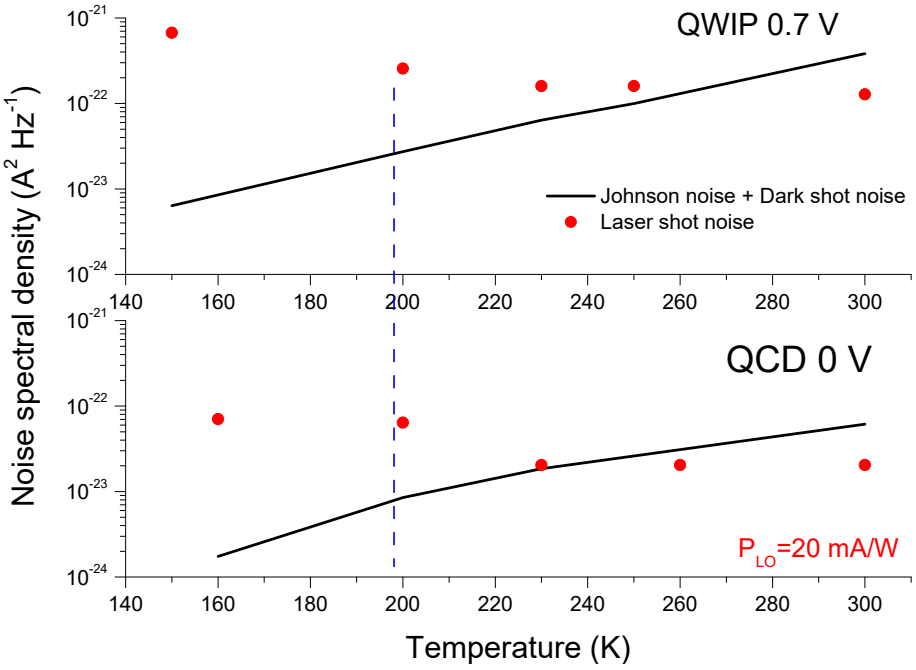

Figure 4.23: Noise spectral density for the patch-antenna QWIP (top) and QCD (bottom) as a function of the temperature. The red dots represent the laser shot noise, with a P_{LO}=20 mA/W and the black lines are the sum of the Johnson noise for the QCD and dark current shot noise for the QWIP. The blue dashed line indicates the temperature at which the laser shot noise is one order of magnitude greater than the other noises, that can be thus neglected.

are the QCD laser responsivity and a LO power of P_{LO}=20 mA/W, while the other quantities are measured. The laser responsivity for QCDs is estimated from the value of the responsivity calibrated with the blackbody and reported in sec. 3.5.2, by considering that the laser and the blackbody responsivities differ in a factor of 2.5, as discussed for QWIPs in section 4.2.2. In figure 4.23, the red points represent the laser shot noise, the black lines are the sum of the Johnson and dark current shot noises, as expressed in eq. 4.18. In this way, we enlighten at which temperature these detectors have to be eventually cooled down for the overall noise to be limited only by the laser shot noise. We can say that this ideal situation occurs when the laser shot noise is approx. 1 dB grater than the other detector's noises. In graph of eq. 4.23, we observe that the QWIP detector has a greater noise (almost 1 order of magnitude) but reaches the ideal heterodyne regime at the same temperature T=200 K of the patch-antenna QCD (blue dashed line).
The photon shot noise limited NEP value, achieved for strong P_{LO}, depends on the absorption quantum efficiency (see 4.6). For patch-antenna QWIP and QCD this limit is:

$$\begin{aligned} \mathrm{NEP}_{\mathrm{QWIP}} &= \frac{E_{12}\ \Delta f}{\eta_{2D}\ p_e} \\ \mathrm{NEP}_{\mathrm{QCD}} &= \frac{E_{12}\ \Delta f}{2\eta_{2D}\ p_{ext}} \end{aligned} \tag{4.21}$$

The ultimate NEP value in eq. 4.21 in our antenna-coupled QCDs is affected at room temperature by a low value of $p_{ext} \approx 0.3$ as studied in chapter 2, while we have demonstrated that p_e in QWIP is close to 1 [1]. The values necessary to estimate the NEP ideal limit of eq. 4.21 at room temperature are given in table 4.1.
In general, this comparison depends on the microscopic parameters characteristics of each sample: a precise knowledge of p_e for QWIP is elusive and p_{ext} is associated to the quantum design of the

QCD. For these considerations, we underline the importance of having a predictive model for the QCD photocurrent including quantum effects as tunnelling as the one described in chapter 2.

Table 4.1: Values for the estimation of the room temperature NEP of the patch-antenna QWIP and QCDs with 8 doped wells. *The laser responsivity is deduced from the blackbody responsivity.

Device	**Bias** (V)	I_{dark} (mA)	**Laser** $\mathcal{R}$ (mA W^{-1})	**Res.** (Ω)	η_{2D}	p_e-p_{ext}
QWIP	0.7	3.7	80	189	21%	$p_e \approx 1$
QCD	0	0	25*	263	22%	p_{ext} ≈0.3

In this work, we measured an heterodyne signal with the antenna-coupled QCD described in chapter 3, under a P_{LO}=3 mW and 13 dB amplification. The measurement is presented in figure 4.24. The signal is measured with a resolution bandwidth (RBW) of 1 MHz at an intermediate frequency IF of ω_h = 1.4 GHz and with no applied DC bias. The linewidth of the IF signal is again limited at 1 MHz, as for QWIPs, which determines the spectral resolution of the heterodyne detection system. The obtained SNR is 20 dBm, a factor of 10 less than the QWIP accordingly to the square of the ratio of their responsivities given in table 4.1.

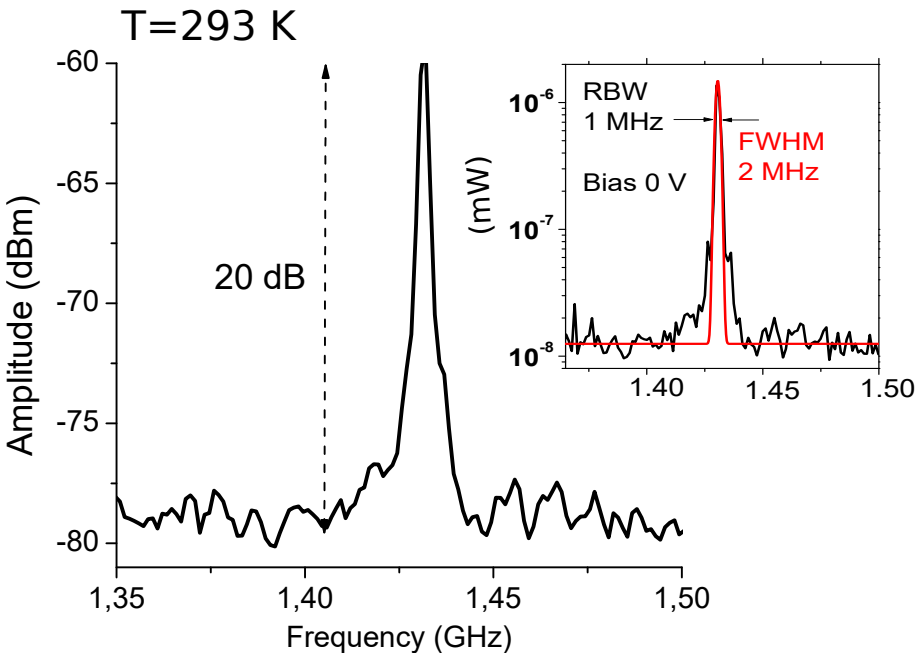

Figure 4.24: Heterodyne signal for the antenna-coupled QCD at room temperature and 0 bias. In the inset, the same spectrum in mW unit with a Gaussian fit as a red line.

For the QCD studied in this work, the tunnel coupled levels are resonant when a voltage is applied, hindering the best operations at 0 bias where the dark current noise vanishes (p_{ext} is only 0.3 at room temperature and 0 V, fig. 2.19). The best results for heterodyne were thus obtained with the patch-antenna QWIP. An optimised QCD, with the maximum responsivity at 0 bias (where the noise is very low), would approach the theoretical NEP limit closer to room temperature and would support without saturation strong local oscillator powers.
To conclude, in the last part of this chapter dedicated to the heterodyne experiments we present in the next sections two sets of measurements with interesting features for future developments. In the first one, a detector with a diffraction limited area has been studied. In the second one, a new set-up with more powerful QCLs has been mounted and tested with a patch-antenna QCD.

4.3.2 The sub-wavelength limit: a single patch QC heterodyne detection

The results presented up to now were performed with a detector composed of an array of 15 x 15 patches, corresponding to an electrical surface of σ=380 µm^2 and a photon collection area of A_{coll}=2250 µm^2. In fig. 3.7 in chapter 3 we have observed that in the array-shaped detector the

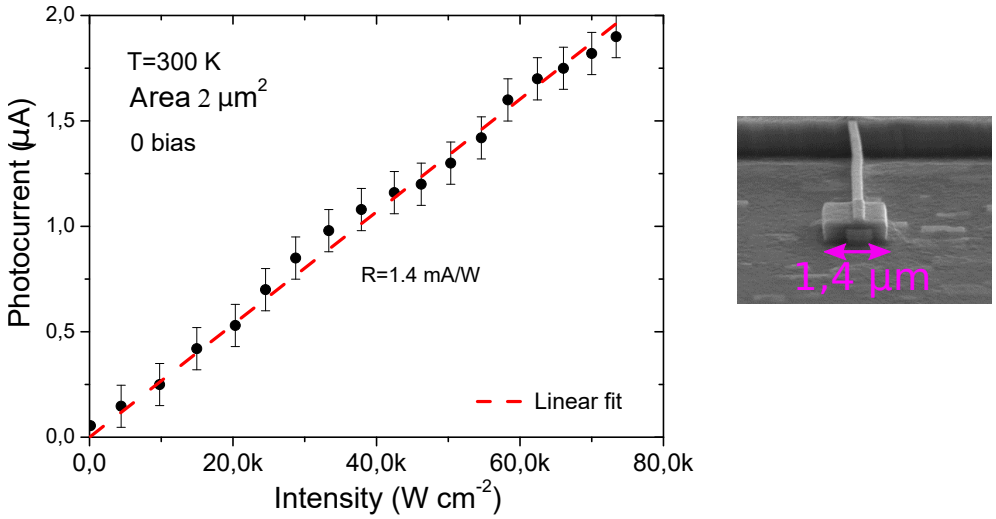

Figure 4.25: Photocurrent curve as a function the incident intensity for the single patch detector having an electrical surface of A=2 µm^2. The detector is without bias and at room temperature. From the linear fit (dashed line) we extrapolate a slope of 1.4 mA/W. On the side, a SEM image of the detector.

maximum photon collection area is reached by increasing the separation between individual patches (for a>4 µm). Therefore, the detectors presenting a smaller density of patches benefit at most of the ratio A_{coll}/σ.
Pushing this logic further, it's interesting to study the limit of a single QCD patch detector, that has a side dimension of only s=1.4 µm and a photon collection area of $A_{coll} \approx 14$ µm^2 as shown in chapter 2.
The laser photocurrent measurements together with a SEM image of the detector are reported in fig. 4.25. The photocurrent vs intensity characteristic at T=300 K is obtained by illuminating the QCD at 0 bias with the DFB QCL, using the same arrangement described in section 4.2.2. The collimated beam from the QCL is focused on the detector using an AR coated aspheric lens (NA = 0.56; 5 mm focal length) with a beam diameter of ≈ 20 µm. Since the laser beam spot area A_{spot} is larger than the photon collection area, we divided the power calibrated with a thermopile by a factor of A_{spot}/A_{coll} ≈20.
The photocurrent curve is linear, within the error, up to an intensity of 70 kW cm^{-2}. No saturation is observed (QCD does not suffer in principle from contact effects as QWIPs). This result confirms the advantage of a QCD structure with respect to a comparable QWIP in terms of the responsivity dynamical range.

The measured responsivity of the device is $\mathcal{R}$=1.4 mA/W and the resistance is r=30 kΩ. Compared to the array detector, the single patch electrical area is approximately 190 times smaller while its responsivity is only a factor of 35 less: the single patch detector maximizes the photon collection area, while its resistance scales as the ratio between the electrical surfaces.
The associated Johnson noise current in 1 Hz bandwidth is $\sqrt{4kT/r} \approx 7 \times 10^{-13}$A, while the photocurrent shot noise is $\sqrt{2eI_{photo}/N} \approx 1.5 \times 10^{-13}$A with N=8 number of doped quantum wells.

The shot-noise limited regime is not yet reached but closely approached, even though the single antenna has a dimension lower that the diffraction limit and can not couple all the impinging power.

Moreover, we have observed a peculiar feature related to the detector sub-wavelength dimensions. In fig. 4.26, we report heterodyne measurements performed with the single patch QCD at 0 bias, with four different resolution bandwidths. An amplifier with gain 20 dB was used (HILNA GV2-1). As the RBW it is decreased from 3 MHz to 30 kHz, the heterodyne signal linewidth, represented

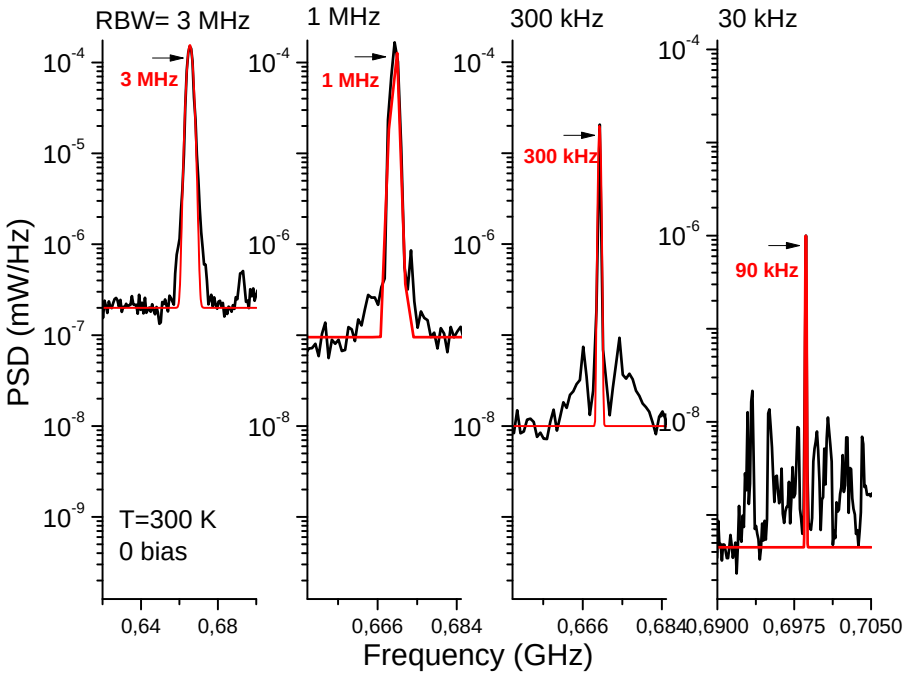

Figure 4.26: Heterodyne spectra for a single patch QCD at room temperature and 0 bias. The RBW is changed from 3 MHz to 1 MHz. The spectra are fitted with a Gaussian curve, represented in red.

in figure 4.26 by the FWHM of the Gaussian fit, is reduced from 3 MHz to 90 kHz (while the total SNR is conserved). When using a narrow RBW, the average noise level of the spectrum analyzer is lowered accordingly. Measurements with the array detector and free-running lasers report instead the broadening of the heterodyne lineshape for too long integration times, as the increased sweeping time implies an average over the frequency fluctuations of the signal. These anomalous linewidths are not due to an active frequency stabilisation: the peak signal indeed does not remain stable but decreases.
The used DFB lasers probably do not operate in a perfect single mode regime and suffer from a very high feedback ratio. The DFB grating eventually does not suppress the side modes, which compete and interfere and can induce a linewidth re-broadening. [110] One possible explanation is that the sub-wavelength detector acts as a shutter, by spatially filtering the incoming beam. It selects only a small portion of the beam where the phases of the overlapped modes are more correlated, thus reducing the phase noise in the beating signal. At RBW=30 kHz, where the linewidth is 90 kHz, we can observe in the spectrum other resolved heterodyne beatings, revealing the multimode nature of the lasers.

4.3.3 Towards an improved heterodyne set-up

We conclude this chapter by presenting some test measurements performed with more powerful and single-mode DFB QCLs.

We replaced the DFB lasers supplied by the Pr. Faist group, ETH with two new DFB customized commercial QCLs at $\lambda \approx 9$ µm, housed in a high heat load (HHL) package. This acquirement

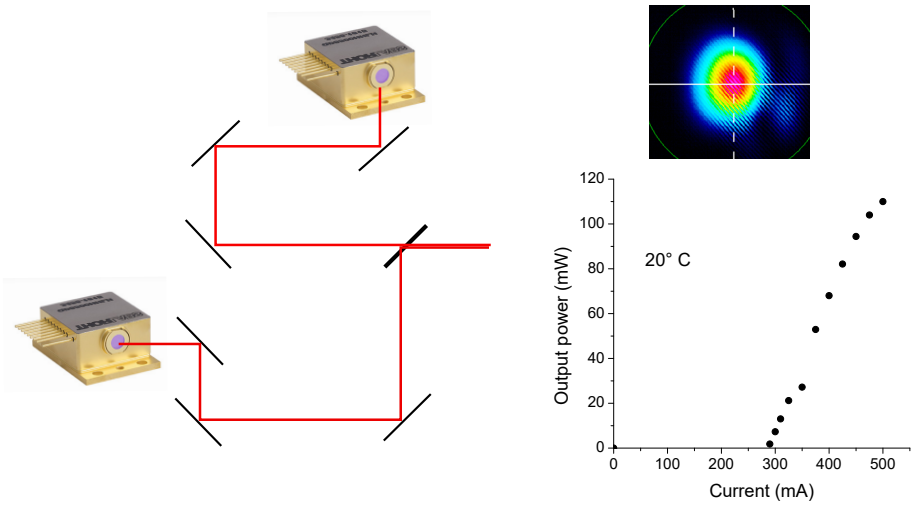

Figure 4.27: Schematic representation of the set up with the new DFB lasers (Thorlabs HHL). On the top, the camera image of the laser beam showing a single clean mode. At the bottom, the LI curve at 20C.

reflects the QCLs explosive commercial development of the last two years: on demand products are now available, while they were not at the time of our first work [1]. A sketch of the new DFB QCLs, together with an IR camera image of the beam and a LI curve of the laser taken in our laboratory, are provided in fig. 4.27. The new 9 µm DFB QCLs are highly mono-mode and can reach an output power up to 100 mW at 20°C. The HHL package greatly simplifies the alignment as the output beam is now collimated. Photocurrent and heterodyne measurements, taken with a 15x15

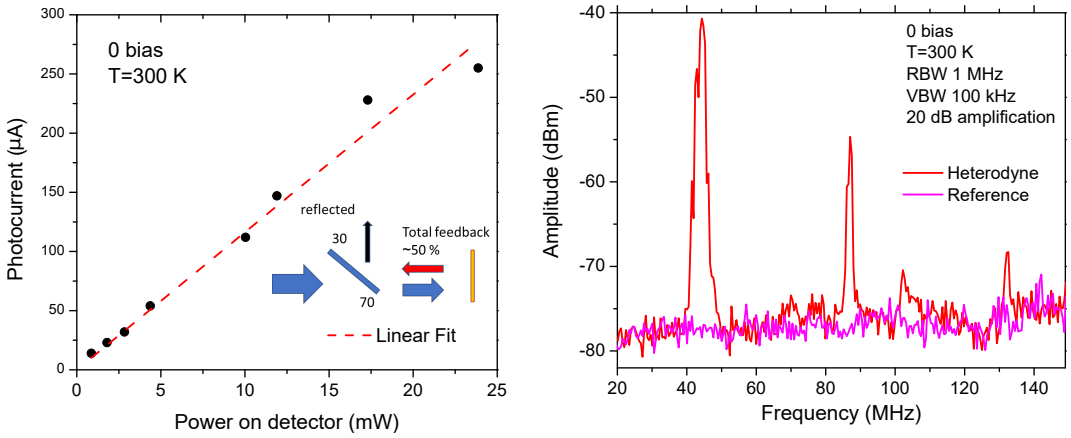

Figure 4.28: Photocurrent curve as a function of the effective power for a 15x15 patch antenna QCD at 0 bias and room temperature. The red dashed line is a linear fit. A severe feedback, represented by arrows in the diagram, limit an efficient power absorption. Heterodyne spectra (red), compared to a reference (pink), showing a main peak and two harmonics. The RBW is 1 MHz and the amplification 20 dB.

patch-antenna QCD at 0 bias and room temperature, are reported in fig. 4.28. The photocurrent as a function of the effective power incident onto the detector is fitted with a linear curve. However, a strong feedback severely degrades the performances, preventing the total power of the laser to couple into the detector. From a feedback measurement taken with a thermopile in the reflective side of the beam splitter (with ratio of 70/30), we infer that a fraction of nearly 50% of the power is

reflected back. At the same time, the heterodyne spectra present higher harmonics, visible in figure 4.28 against a background reference, starting at a beating frequency of 50 MHz, never observed before. All these limitations hinder the precise calibration of the NEP of the detector.
In conclusion, these attempts encourage and drive the research towards:

- High frequency processing of the patch-antenna QCD. The electrical bandwidth can thus reach the tens of GHz enabled by the unipolar operations [46]. Moreover, in a HF processing of the device, the bottom gold around the patches is replaced by an insulator layer such as SiO_2, which absorbs light impinging around the photon collection area and does not reflect it back (in progress at the time of the writing);
- Peltier cooling of the detector;
- Customized optical isolator;
- Low-losses single mode MIR/LWIR fibres, which start promisingly to appear now in the market.

Conclusion

Starting from the analysis of the device physics to the system implementation, I have examined how a sensitive infrared detection system can be achieved, while keeping the set-up compact. The choice of AlGaAs/GaAs QWIPs and QCDs is motivated by their fast response, unique among detectors at 9 µm wavelength, and their mature growth technology. To conclude, I will outline the scientific approaches used to describe in each chapter the specific physical aspects concerning the detectors (quantum design, light-matter coupling, coherent detection...). The combination of all these investigations opens the path to the conception of room temperature 9 µm detection systems having tens of GHz of bandwidth and quantum limited sensitive operations.

In **Chapter 1** I described the state of the art and the issues concerning the detection at λ=9 µm. The physics of semiconductor quantum wells is introduced, along with the theory of QWIP and QCD detectors. At the end of the chapter, I summarized the peculiarities of the heterodyne detection, reviewed the history of the available technology and mentioned some of its applications.

Chapter 2 is dedicated to the **physics of the QC detector**. The main interesting feature of these devices is that when they are operated in photovoltaic mode, the dark current noise vanishes. With the aim to optimize the detector's responsivity at 0 bias, I reported the development of a photocurrent transport model based on the density matrix formalism, which includes the effect of the resonant tunnelling as a function of the bias. In this way, the extraction probability, the fraction of the photoexcited electron collected by the external contacts, is precisely determined. Combining the calculation of the QCD absorption efficiency and of the extraction probability, the responsivity of the device is fully modelled. The main innovation of this formalism is the inclusion of the light excitation as a perturbation to the density matrix at equilibrium, which is fixed by the detailed balance and the Fermi statistics governing the carrier distribution on different subbands in the QCD. Within the diffusion transport theory of the Schottky diode-QCD analogy, I also reported the simulation of the resistance and of the activation energy, which set the noise properties of the device. All the models were successfully compared to the experimental data for the responsivity and resistance.

Chapter 3 is devoted to the **light coupling enhancement** by the geometry of the detector. In the described devices, the external radiation is collected by a meta-material composed of a double-metal patch antenna embedding the detector heterostructure. One advantage of the meta material is the possibility of distinguishing the photon collection area from the electrical area. By reducing the size of the device, the noise is decreased without reducing the size of the area sensitive to the impinging photons. The micrometric dimensions of the antenna require an accurate fabrication in clean room. In this work, I have realized the processing steps in order to secure highly reliable batches of devices. The efficient fabrication method has sustained the achievement of beyond-state-of-the-art performances of the patch-antenna QCD including a 78 K detectivity of D=5×10^{11}cmHz$^{0.5}$/W and a room temperature responsivity of $\mathcal{R}$=50 mA/W at 0 bias. These results have been published in [2]. The experimental data are validated by a general model based on the coupled mode theory (CMT), providing the estimation of the cavity absorption quantum ef-

ficiency. One of the main observations is that the maximum absorption occurs in the weak coupling regime, before the polaritonic splitting observable in strongly coupled oscillators. This feature is interesting because it enables the proposal of an optimisation procedure for increasing the absorption quantum efficiency up to a factor of 2 higher than that of the current devices, while keeping the same doping density.

Chapter 4 illustrates that the **heterodyne scheme** provides an efficient solution to the issue of detection in the LWIR. In this set-up a faint signal is amplified by the beating with a powerful laser, called the local oscillator, and detected by a fast power detector, as QWIPs and QCDs. In fact, despite the use of the meta-material to reduce the dark and Johnson noise of the detector, the direct detection still suffers from the thermal background noise. In heterodyne detection the bandwidth can be lowered to 1 Hz (instead of the MHz of direct detection), thus reducing the number of blackbody photons reaching the detector. The main novelty presented in this chapter is the implementation of a heterodyne system with all unipolar semiconductor devices operating at room temperature. The local oscillator is a QCL, while the receiver is an antenna coupled QWIP or QCD. By providing an accurate passive stabilization of the frequency of the LO laser, the heterodyne system reaches at room temperature the record value of NEP= 30 pW at λ=9 µm and in the GHz frequency range. It is also shown that the injection of a microwave signal into the detector shifts the heterodyne beating over the large bandwidth of the devices. This mixing property is an interesting function for signal processing in compact QCL-based systems. These results were published in [3].

4.3.4 Outlook

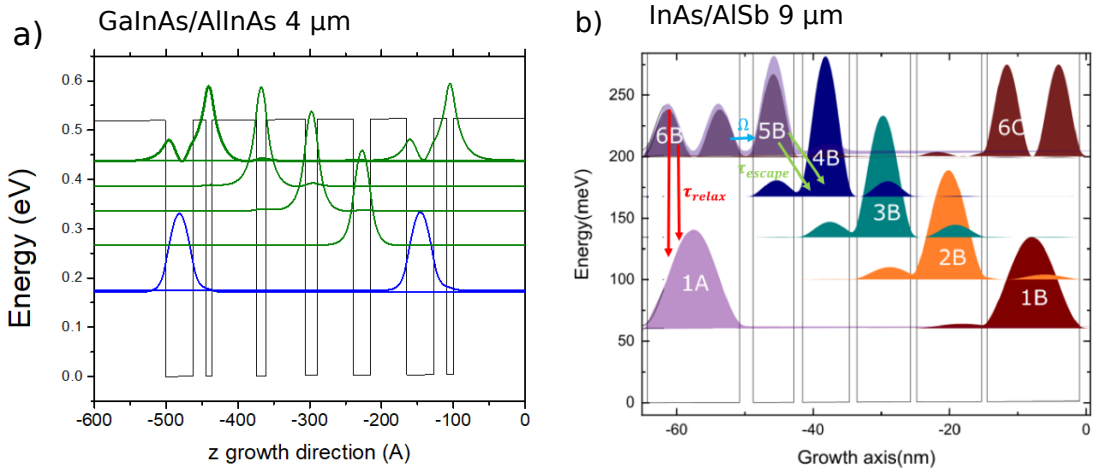

Figure 4.29: Band diagram of: a) 4 µm GaInAs/AlInAs QCD with thickness 3.8, **1.8**, 0.9, **6.2**, 5.5, **1.7**, 5.0, **2.4**. Its growth sheet is reported in appendix. b) 9 µm InAs/AlSb QCD with thickness 13.5, **2.7**, 6.0, **1.6**, 6.8, **1.5**, 7.9, **1.3**, 9.5. The barrier layers are in bold and the doped layer are underlined.

At the end of each chapter, I mentioned some optimisations that can lead to an even higher sensitivity of the patch-antenna detectors. To conclude this thesis, I briefly review these perspectives. The heterodyne quantum limited NEP in eq. 4.21 is determined for a QCD by the absorption quantum efficiency and the extraction probability. These two quantities could be optimised by, respectively, a better engineering of the quantum structure and by a dedicated geometry for the metamaterial. For the quantum design, a QCD band diagram with a diagonal optical transition, as the one at λ=4 µm reported in fig. 4.29a), could avoid the bias-dependent alignment of the

tunnel-coupled states of the vertical- transition devices (for a 9 µm version, see fig. 3.28). Most importantly, the maximum extraction probability p_{ext} should be at 0 bias, where the dark current noise is 0.
The proposal for an optimisation procedure for the meta-material was reported in sec. 3.4.5. Thicker structures having up to $N \approx 15$ periods and sparser array of patches enable the absorption quantum efficiency to reach a value of 40%, twice the current geometry.
Another substantial improvement concerns the realization of a new class of high-frequency patch-antenna devices, where the frequency bandwidth will no more be limited by the high-capacitance of the contact pad and by the electrical connections. Consequently, the intrinsic tens of GHz electrical bandwidth of QWIPs and QCDs could be fully exploited.

New perspectives for the heterodyne set-up are reported in section 4.3.3. In particular the issue of the strong spurious optical feedback could be mitigated by customized optical isolators. The single-photon power detection could be attained using very narrow laser frequencies imposed by an ultra-stable reference oscillator, implying longer integration times.

Other material systems exist that have complementary advantages for QCDs than AlGaAs/GaAs. In the literature Sb based III-V [111], GaN [112], II-VI semiconductors [113] QCDs were demonstrated mostly in the mid-IR (λ=4 µm). For the LWIR range, I analysed the possibility of using the InAs/AlSb material system. In InAs/AlSb heterostructures, the QWs are very deep (the conduction band offset is 2.1eV) and the effective mass of the electrons is $m^* \approx 0.023\ m_e$, a factor 3 lower than in GaAs. This is interesting because the low effective mass has a great impact on the absorption quantum efficiency: we have calculated that the single InAs well absorption efficiency of eq. 2.11 can theoretically reach the value of α_{2D}=3% instead of the 0.7% in GaAs, considering the same doping density of $n_{2D}=5 \times 10^{11}\text{cm}^{-2}$. The band diagram of a vertical-transition InAs/AlSb QCD is reported in fig. 4.29b (The diagonal transition design was hindered by the too small barriers required). Even though InAs/AlSb heterostructures suffer from less developed technology with respect to AlGaAs/GaAs heterostructures, considerable progresses have been recently attained, resulting in the first realization of a high performance InAs/AlSb-based QCL grown on a silicon substrate [114]. The Si integration is very appealing for the development of single-chip detection systems and mass scale applications.
A few words on the choice between QWIP or QCD in a heterodyne scheme. The two devices, if optimised have comparable performances when they reach the ultimate heterodyne NEP, limit that depends on the absorption quantum efficiency and on the probability to collect the excited electrons. Nevertheless, QCDs have two encouraging features. Firstly, they do not in principle exhibit the same saturation effects as QWIPs do, due to the field drop at the contacts when the photocurrent overcomes the dark current. Secondly, the complementarity of the QCD band diagram to the QCL active region is adapted to the engineering of a portable integrated heterodyne sensing platform with a combined QCL-QCD heterostructure in the same device [40]. The use of a patch antenna meta-material would greatly simplify the geometry and increase the performances of both laser and detector.

Appendix A

Growth sheets

A.1 QCD at 8.6 µm: wafer L1437

Layer	Material	Doping [cm^{-3}]	Thickness [nm]
n^+	GaAs	5×10^{18}	50
i	$Al_{0.35}Ga_{0.65}As$	-	3.2
i	GaAs	-	4.5
i	$Al_{0.35}Ga_{0.65}As$	-	3.3
i	GaAs	-	2.8
i	$Al_{0.35}Ga_{0.65}As$	-	2.5
i	GaAs	-	4.6
i	$Al_{0.35}Ga_{0.65}As$	-	2.0
i	GaAs	-	6.7
i	$Al_{0.35}Ga_{0.65}As$	-	1.0
n^+	GaAs	1×10^{18}	5.0
i	$Al_{0.35}Ga_{0.65}As$	-	1.0
			x 8
i	$Al_{0.35}Ga_{0.65}As$	-	3.2
n^+	GaAs	6×10^{18}	50
etch stop	$Al_{0.65}Ga_{0.65}As$	-	40
	semi-insulating GaAs substrate		

A.2 QWIP at 8.6 µm: wafer L1436

Layer	Material	Doping [cm^{-3}]	Thickness [nm]
n^+	GaAs	2×10^{18}	40
i	$Al_{0.25}Ga_{0.75}As$	-	33
i	GaAs	-	0.6
n^+	GaAs	1×10^{18}	4
i	GaAs	-	0.6
			x 8
i	$Al_{0.25}Ga_{0.75}As$	-	33
n^+	GaAs	6×10^{18}	40
etch stop	$Al_{0.50}Ga_{0.50}As$	-	400
semi-insulating GaAs substrate			

A.3 Diagonal transition QCD at 9 µm: wafer L1604

Layer	Material	Doping [cm^{-3}]	Thickness [nm]
n^+	GaAs	6×10^{18}	50
i	GaAs	-	8
i	$Al_{0.35}Ga_{0.65}As$	-	5.2
i	GaAs	-	2.3
i	$Al_{0.35}Ga_{0.65}As$	-	5.8
i	GaAs	-	1.7
i	$Al_{0.35}Ga_{0.65}As$	-	5.5
i	GaAs	-	1.4
i	$Al_{0.35}Ga_{0.65}As$	-	1.4
i	GaAs	-	0.5
n^+	GaAs	1×10^{18}	3.4
i	GaAs	-	0.5
			x 1
i	$Al_{0.35}Ga_{0.65}As$	-	4.8
i	GaAs	-	3.0
i	$Al_{0.35}Ga_{0.65}As$	-	5.2
i	GaAs	-	2.3
i	$Al_{0.35}Ga_{0.65}As$	-	5.8
i	GaAs	-	1.7
i	$Al_{0.35}Ga_{0.65}As$	-	5.5
i	GaAs	-	1.4
i	$Al_{0.35}Ga_{0.65}As$	-	1.4
i	GaAs	-	0.5
n^+	GaAs	1×10^{18}	3.4
i	GaAs	-	0.5
			x 12
i	$Al_{0.35}Ga_{0.65}As$	-	8
i	GaAs	-	8
n^+	GaAs	6×10^{18}	40
etch stop	$Al_{0.65}Ga_{0.65}As$	-	400
		semi-insulating GaAs substrate	

A.4 QCD at 4.6 μm: wafer G0616

Layer	Material	Doping [cm^{-3}]	Thickness [nm]
n^+	InGaAs	6×10^{18}	50
i	InGaAs	-	7
i	InAlAs	-	5.0
i	InGaAs	-	1.7
i	InAlAs	-	5.5
i	InGaAs	-	1.3
i	InAlAs	-	6.2
i	InGaAs	-	0.9
i	InAlAs	-	1.8
i	InGaAs	-	0.5
n^+	InGaAs	3×10^{18}	2.8
i	InGaAs	-	0.5
			x 1
i	InAlAs	-	3.8
i	InGaAs	-	2.4
i	InAlAs	-	5.0
i	InGaAs	-	1.7
i	InAlAs	-	5.5
i	InGaAs	-	1.3
i	InAlAs	-	6.2
i	InGaAs	-	0.9
i	InAlAs	-	1.8
i	InGaAs	-	0.5
n^+	InGaAs	3×10^{18}	2.8
i	InGaAs	-	0.5
			x 6
i	InAlAs	-	8
i	InGaAs	-	7
n^+	InGaAs	6×10^{18}	50
etch stop	InGaAs	-	400
semi-insulating InP:Fe substrate			

Bibliography

[1] D. Palaferri, Y. Todorov, A. Bigioli, A. Mottaghizadeh, D. Gacemi, A. Calabrese, A. Vasanelli, L. Li, A. G. Davies, E. H. Linfield, F. Kapsalidis, M. Beck, J. Faist, and C. Sirtori, "Room-temperature nine-µm-wavelength photodetectors and GHz-frequency heterodyne receivers," *Nature*, vol. 556, pp. 85–88, Apr. 2018.

[2] A. Bigioli, G. Armaroli, A. Vasanelli, D. Gacemi, Y. Todorov, D. Palaferri, L. Li, A. G. Davies, E. H. Linfield, and C. Sirtori, "Long-wavelength infrared photovoltaic heterodyne receivers using patch-antenna quantum cascade detectors," *Appl. Phys. Lett.*, vol. 116, p. 161101, Apr. 2020.

[3] A. Bigioli, D. Gacemi, D. Palaferri, Y. Todorov, A. Vasanelli, S. Suffit, L. Li, A. G. Davies, E. H. Linfield, F. Kapsalidis, M. Beck, J. Faist, and C. Sirtori, "Mixing Properties of Room Temperature Patch-Antenna Receivers in a Mid-Infrared ($\lambda \approx 9$µm) Heterodyne System," *Laser & Photonics Reviews*, p. 1900207, 2019.

[4] S. Fan, "Nighttime Radiative Cooling: Harvesting the Darkness of the Universe," p. 2, 2014.

[5] M. Planck and M. Masius, *The Theory of Heat Radiation.* Philadelphia, P. Blakiston's Son & Co, [c1914].

[6] A. Rogalski, *Infrared and Terahertz Detectors, Third Edition.* CRC Press, Jan. 2019.

[7] J. J. Talghader, A. S. Gawarikar, and R. P. Shea, "Spectral selectivity in infrared thermal detection," *Light: Science & Applications*, vol. 1, pp. e24–e24, Aug. 2012.

[8] H. Schneider and H. C. Liu, *Quantum Well Infrared Photodetectors: Physics and Applications.* No. 126 in Springer Series in Optical Sciences, Berlin ; New York: Springer, 2007.

[9] S. Steinkogler, H. Schneider, M. Walther, and P. Koidl, "Determination of the electron capture time in quantum-well infrared photodetectors using time-resolved photocurrent measurements," *Appl. Phys. Lett.*, vol. 82, pp. 3925–3927, May 2003.

[10] M. I. Hossain, Z. Ikonic, J. Watson, J. Shao, P. Harrison, M. J. Manfra, and O. Malis, "Strong heavy-to-light hole intersubband absorption in the valence band of carbon-doped GaAs/AlAs superlattices," *Journal of Applied Physics*, vol. 113, p. 053103, Feb. 2013.

[11] F. Capasso and H. C. Liu, *Intersubband Transitions in Quantum Wells: Physics and Device Applications*, vol. 62 of *Semiconductor and Semimetals.* Academic press, first ed., 1999.

[12] G. Bastard, *Wave Mechanics Applied to Semiconductor Heterostructures.* Wiley-Interscience, 1991.

[13] N. W. Ashcroft and N. D. Mermin, *Solid State Physics.* Cengage Learning, 2011.

[14] G. Pegolotti, *Quantum Engineering of Collective States in Semiconductor Nanostructures*. PhD thesis, Universite Paris Diderot-Paris VII, Dec. 2014.

[15] E. O. Kane, "Band structure of indium antimonide," *Journal of Physics and Chemistry of Solids*, vol. 1, pp. 249–261, Jan. 1957.

[16] Pegolotti Giulia, Vasanelli Angela, and Sirtori Carlo, "Active region design," 2014.

[17] C. Sirtori, F. Capasso, J. Faist, and S. Scandolo, "Nonparabolicity and a sum rule associated with bound-to-bound and bound-to-continuum intersubband transitions in quantum wells," *Phys. Rev. B*, vol. 50, pp. 8663–8674, Sept. 1994.

[18] P. Harrison, *Quantum Wells, Wires, and Dots: Theoretical and Computational Physics of Semiconductor Nanostructures*. Hoboken, NJ: Wiley, 2nd ed ed., 2005.

[19] T. Unuma, T. Takahashi, T. Noda, M. Yoshita, H. Sakaki, M. Baba, and H. Akiyama, "Effects of interface roughness and phonon scattering on intersubband absorption linewidth in a GaAs quantum well," *Appl. Phys. Lett.*, vol. 78, pp. 3448–3450, May 2001.

[20] B. F. Levine, K. K. Choi, C. G. Bethea, J. Walker, and R. J. Malik, "New 10 µm infrared detector using intersubband absorption in resonant tunneling GaAlAs superlattices," *Appl. Phys. Lett.*, vol. 50, pp. 1092–1094, Apr. 1987.

[21] H. C. Liu, "Photoconductive gain mechanism of quantum-well intersubband infrared detectors," *Appl. Phys. Lett.*, vol. 60, pp. 1507–1509, Mar. 1992.

[22] C. Schönbein, H. Schneider, G. Bihlmann, K. Schwarz, and P. Koidl, "A 10 µm intersubband photodetector operating at zero bias voltage," *Appl. Phys. Lett.*, vol. 68, pp. 973–975, Feb. 1996.

[23] H. Schneider, C. Schönbein, M. Walther, K. Schwarz, J. Fleissner, and P. Koidl, "Photovoltaic quantum well infrared photodetectors: The four-zone scheme," *Appl. Phys. Lett.*, vol. 71, pp. 246–248, July 1997.

[24] L. Consolino, F. Cappelli, M. S. de Cumis, and P. D. Natale, "QCL-based frequency metrology from the mid-infrared to the THz range: A review," *Nanophotonics*, vol. 8, pp. 181–204, Oct. 2018.

[25] J. Faist, F. Capasso, D. L. Sivco, C. Sirtori, A. L. Hutchinson, and A. Y. Cho, "Quantum Cascade Laser," *Science*, vol. 264, pp. 553–556, Apr. 1994.

[26] D. Hofstetter, M. Beck, and J. Faist, "Quantum-cascade-laser structures as photodetectors," *Appl. Phys. Lett.*, vol. 81, pp. 2683–2685, Sept. 2002.

[27] L. Gendron, M. Carras, A. Huynh, V. Ortiz, C. Koeniguer, and V. Berger, "Quantum cascade photodetector," *Appl. Phys. Lett.*, vol. 85, pp. 2824–2826, Oct. 2004.

[28] A. Delga, "8 - Quantum cascade detectors: A review," in *Mid-Infrared Optoelectronics* (E. Tournié and L. Cerutti, eds.), Woodhead Publishing Series in Electronic and Optical Materials, pp. 337–377, Woodhead Publishing, 2020.

[29] L. Li, P. Bai, Y. Zhang, W. Shen, and J. Cao, "Optical field simulation of edge coupled terahertz quantum well photodetectors," *AIP Advances*, vol. 8, p. 035214, Mar. 2018.

[30] K. K. Choi, "Electromagnetic modeling of edge coupled quantum well infrared photodetectors," *Journal of Applied Physics*, vol. 111, p. 124507, June 2012.

[31] H. C. Liu, R. Dudek, A. Shen, E. Dupont, C. Y. Song, Z. R. Wasilewski, and M. Buchanan, "High absorption (>90%) quantum-well infrared photodetectors," *Appl. Phys. Lett.*, vol. 79, pp. 4237–4239, Dec. 2001.

[32] R. Müller, V. Gramich, M. Wauro, J. Niemasz, L. Kirste, V. Daumer, A. Janaszek, J. Jureńczyk, and R. Rehm, "High operating temperature InAs/GaSb type-II superlattice detectors on GaAs substrate for the long wavelength infrared," *Infrared Physics & Technology*, vol. 96, pp. 141–144, Jan. 2019.

[33] "Photoconductive Mercury Cadmium Telluride Detectors." http://www.teledynejudson.com/prods/Pages/Photoconductive-Mercury-Cadmium-Telluride-Detectors.aspx.

[34] "InAsSb photovoltaic detector P13894-211MA."

[35] K. K. Choi, M. D. Jhabvala, D. P. Forrai, J. Sun, and D. Endres, "C-QWIPs for space exploration," *Infrared Physics & Technology*, vol. 54, pp. 170–176, May 2011.

[36] "PVMI, VIGO System S.A.."

[37] "52 RoHS 10 Restricted Substances." https://www.rohsguide.com/rohs-substances.htm.

[38] H. T. Miyazaki, T. Mano, T. Kasaya, H. Osato, K. Watanabe, Y. Sugimoto, T. Kawazu, Y. Arai, A. Shigetou, T. Ochiai, Y. Jimba, and H. Miyazaki, "Synchronously wired infrared antennas for resonant single-quantum-well photodetection up to room temperature," *Nature Communications*, vol. 11, p. 565, Jan. 2020.

[39] M. Hakl, Q. Y. Lin, S. Lepillet, M. Billet, J.-F. Lampin, S. Pirotta, R. Colombelli, W. J. Wan, J. C. Cao, H. Li, E. Peytavit, and S. Barbieri, "Ultra-fast quantum-well infared photodetectors operating at 10µm with flat response up to 70GHz at room temperature," *arXiv:2007.00299 [physics]*, Sept. 2020.

[40] B. Schwarz, C. A. Wang, L. Missaggia, T. S. Mansuripur, P. Chevalier, M. K. Connors, D. McNulty, J. Cederberg, G. Strasser, and F. Capasso, "Watt-Level Continuous-Wave Emission from a Bifunctional Quantum Cascade Laser/Detector," *ACS Photonics*, vol. 4, pp. 1225–1231, May 2017.

[41] M. Teich, "Infrared Heterodyne Detection," *Proceedings of the IEEE*, vol. 56, no. 1, 1968.

[42] D. L. Spears, "IR Detectors: Heterodyne and Direct," in *Optical and Laser Remote Sensing* (D. K. Killinger and A. Mooradian, eds.), Springer Series in Optical Sciences, pp. 278–286, Berlin, Heidelberg: Springer, 1983.

[43] M. Beck, D. Hofstetter, T. Aellen, J. Faist, U. Oesterle, M. Ilegems, E. Gini, and H. Melchior, "Continuous Wave Operation of a Mid-Infrared Semiconductor Laser at Room Temperature," *Science*, vol. 295, pp. 301–305, Jan. 2002.

[44] D. Wirtz, G. Sonnabend, and R. T. Schieder, "THIS: A tuneable heterodyne infrared spectrometer," *Spectrochimica Acta Part A: Molecular and Biomolecular Spectroscopy*, vol. 58, pp. 2457–2463, Sept. 2002.

[45] B. Parvitte, L. Joly, V. Zéninari, and D. Courtois, "Preliminary results of heterodyne detection with quantum-cascade lasers in the 9 µm region," *Spectrochimica Acta Part A: Molecular and Biomolecular Spectroscopy*, vol. 60, pp. 3285–3290, Dec. 2004.

[46] P. D. Grant, R. Dudek, M. Buchanan, and H. C. Liu, "Room-Temperature Heterodyne Detection up to 110 GHz With a Quantum-Well Infrared Photodetector," *IEEE Photon. Technol. Lett.*, vol. 18, pp. 2218–2220, Nov. 2006.

[47] G. Bourdarot, H. Guillet de Chatellus, and J.-P. Berger, "Toward a large bandwidth photonic correlator for infrared heterodyne interferometry: A first laboratory proof of concept," *A&A*, vol. 639, p. A53, July 2020.

[48] S. Kakuma, "Frequency-modulated continuous-wave laser radar using dual vertical-cavity surface-emitting laser diodes for real-time measurements of distance and radial velocity," *Opt Rev*, vol. 24, pp. 39–46, Feb. 2017.

[49] H. Timmers, A. Kowligy, A. Lind, F. C. Cruz, N. Nader, M. Silfies, G. Ycas, T. K. Allison, P. G. Schunemann, S. B. Papp, and S. A. Diddams, "Molecular fingerprinting with bright, broadband infrared frequency combs," *Optica, OPTICA*, vol. 5, pp. 727–732, June 2018.

[50] J. J. Liu, B. L. Stann, K. K. Klett, P. S. Cho, and P. M. Pellegrino, "Mid and long-wave infrared free-space optical communication," in *Laser Communication and Propagation through the Atmosphere and Oceans VIII*, vol. 11133, p. 1113302, International Society for Optics and Photonics, Sept. 2019.

[51] K. M. Judd, M. P. Thornton, and A. A. Richards, "Automotive sensing: Assessing the impact of fog on LWIR, MWIR, SWIR, visible, and lidar performance," in *Infrared Technology and Applications XLV*, vol. 11002, p. 110021F, International Society for Optics and Photonics, May 2019.

[52] D. D. S. Hale, M. Bester, W. C. Danchi, W. Fitelson, S. Hoss, E. A. Lipman, J. D. Monnier, P. G. Tuthill, and C. H. Townes, "The Berkeley Infrared Spatial Interferometer: A Heterodyne Stellar Interferometer for the Mid-Infrared," *ApJ*, vol. 537, p. 998, July 2000.

[53] L. Mandel and E. Wolf, *Optical Coherence and Quantum Optics*. Cambridge: Cambridge University Press, 1995.

[54] N. Pinchon, O. Cassignol, A. Nicolas, F. Bernardin, P. Leduc, J.-P. Tarel, R. Brémond, E. Bercier, and J. Brunet, "All-Weather Vision for Automotive Safety: Which Spectral Band?," in *Advanced Microsystems for Automotive Applications 2018* (J. Dubbert, B. Müller, and G. Meyer, eds.), pp. 3–15, Cham: Springer International Publishing, 2019.

[55] S. Saha and J. Kumar, "Rate equation modelling and investigation of quantum cascade detector characteristics," *Superlattices and Microstructures*, vol. 98, pp. 70–77, Oct. 2016.

[56] R. Terazzi and J. Faist, "A density matrix model of transport and radiation in quantum cascade lasers," *New J. Phys.*, vol. 12, p. 033045, Mar. 2010.

[57] H. Callebaut and Q. Hu, "Importance of coherence for electron transport in terahertz quantum cascade lasers," *Journal of Applied Physics*, vol. 98, p. 104505, 2005.

[58] S. Kumar and Q. Hu, "Coherence of resonant-tunneling transport in terahertz quantum-cascade lasers," *Phys. Rev. B*, vol. 80, p. 245316, Dec. 2009.

[59] C. Koeniguer, G. Dubois, A. Gomez, and V. Berger, "Electronic transport in quantum cascade structures at equilibrium," *Phys. Rev. B*, vol. 74, p. 235325, Dec. 2006.

[60] A. Delga, M. Carras, V. Trinité, V. Guériaux, L. Doyennette, A. Nedelcu, H. Schneider, and V. Berger, "Master equation approach of classical noise in intersubband detectors," *Phys. Rev. B*, vol. 85, p. 245414, June 2012.

[61] T. Unuma, M. Yoshita, T. Noda, H. Sakaki, and H. Akiyama, "Intersubband absorption linewidth in GaAs quantum wells due to scattering by interface roughness, phonons, alloy disorder, and impurities," *Journal of Applied Physics*, vol. 93, pp. 1586–1597, Feb. 2003.

[62] P. Harrison, "The nature of the electron distribution functions in quantum cascade lasers," *Appl. Phys. Lett.*, vol. 75, pp. 2800–2802, Oct. 1999.

[63] A. Vasanelli, A. Leuliet, C. Sirtori, A. Wade, G. Fedorov, D. Smirnov, G. Bastard, B. Vinter, M. Giovannini, and J. Faist, "Role of elastic scattering mechanisms in GaInAs/AlInAs quantum cascade lasers," *Appl. Phys. Lett.*, vol. 89, p. 172120, Oct. 2006.

[64] Claude Cohen-Tannoudji, Bernard Diu, and Franck Laloe, *Quantum Mechanics, Volume 1: Basic Concepts, Tools, and Applications, 2nd Edition | Wiley*, vol. 1. Wiley, second ed., 2019.

[65] R. L. Terazzi, *Transport in Quantum Cascade Lasers.* Doctoral Thesis, ETH Zurich, 2012.

[66] E. Dupont, S. Fathololoumi, and H. C. Liu, "Simplified density-matrix model applied to three-well terahertz quantum cascade lasers," *Phys. Rev. B*, vol. 81, p. 205311, May 2010.

[67] F. Eickemeyer, K. Reimann, M. Woerner, T. Elsaesser, S. Barbieri, C. Sirtori, G. Strasser, T. Müller, R. Bratschitsch, and K. Unterrainer, "Ultrafast Coherent Electron Transport in Semiconductor Quantum Cascade Structures," *Phys. Rev. Lett.*, vol. 89, p. 047402, July 2002.

[68] H. Schneider, T. Maier, M. Walther, and H. C. Liu, "Two-photon photocurrent spectroscopy of electron intersubband relaxation and dephasing in quantum wells," *Appl. Phys. Lett.*, vol. 91, p. 191116, Nov. 2007.

[69] R. Kazarinov and R. Suris, "Possibility of the Amplification of Electromagnetic Waves in a Semiconductor with a Superlattice," *Soviet Physics-Semiconductors*, vol. 5, no. 4, p. 707, 1971.

[70] C. Sirtori, F. Capasso, J. Faist, A. Hutchinson, D. Sivco, and A. Cho, "Resonant tunneling in quantum cascade lasers," *IEEE J. Quantum Electron.*, vol. 34, no. 9, pp. 1722–1729, Sept./1998.

[71] K. L. Campman, H. Schmidt, A. Imamoglu, and A. C. Gossard, "Interface roughness and alloy-disorder scattering contributions to intersubband transition linewidths," *Appl. Phys. Lett.*, vol. 69, pp. 2554–2556, Oct. 1996.

[72] P. Reininger, B. Schwarz, H. Detz, D. MacFarland, T. Zederbauer, A. M. Andrews, W. Schrenk, O. Baumgartner, H. Kosina, and G. Strasser, "Diagonal-transition quantum cascade detector," *Appl. Phys. Lett.*, vol. 105, p. 091108, Sept. 2014.

[73] A. Delga, L. Doyennette, M. Carras, V. Trinité, and P. Bois, "Johnson and shot noises in intersubband detectors," *Appl. Phys. Lett.*, vol. 102, p. 163507, Apr. 2013.

[74] R. Landauer, "Solid-state shot noise," *Phys. Rev. B*, vol. 47, pp. 16427–16432, June 1993.

[75] C. Koeniguer, *Transport électronique dans les détecteurs à cascade quantique*. Physics, Université Paris-Diderot - Paris VII, 2008.

[76] S. M. Sze and K. K. Ng, *Physics of Semiconductor Devices*. Hoboken, N.J: Wiley-Interscience, 3rd ed ed., 2007.

[77] M. Grundmann, *The Physics of Semiconductors: An Introduction Including Nanophysics and Applications*. Graduate Texts in Physics, Berlin Heidelberg: Springer-Verlag, second ed., 2010.

[78] G. Armaroli, *Experimental Investigation and Modelling of Mid-Infrared Quantum Cascade Detectors Operating at High Temperature*. Tesi di laurea, Nov. 2019.

[79] A. Buffaz, A. Gomez, M. Carras, L. Doyennette, and V. Berger, "Role of subband occupancy on electronic transport in quantum cascade detectors," *Phys. Rev. B*, vol. 81, p. 075304, Feb. 2010.

[80] Y. Todorov, L. Tosetto, J. Teissier, A. M. Andrews, P. Klang, R. Colombelli, I. Sagnes, G. Strasser, and C. Sirtori, "Optical properties of metal-dielectric-metal microcavities in the THz frequency range," *Opt. Express*, vol. 18, p. 13886, June 2010.

[81] D. Palaferri, "Ultra-subwavelength resonators for high temperature high performance quantum detectors," *New J. Phys.*, p. 13, 2016.

[82] M. Jeannin, T. Bonazzi, D. Gacemi, A. Vasanelli, L. Li, A. G. Davies, E. Linfield, C. Sirtori, and Y. Todorov, "Absorption Engineering in an Ultrasubwavelength Quantum System," *Nano Lett.*, vol. 20, pp. 4430–4436, June 2020.

[83] Y. Nga Chen, Y. Todorov, B. Askenazi, A. Vasanelli, G. Biasiol, R. Colombelli, and C. Sirtori, "Antenna-coupled microcavities for enhanced infrared photo-detection," *Appl. Phys. Lett.*, vol. 104, p. 031113, Jan. 2014.

[84] Y. Todorov, I. Sagnes, I. Abram, and C. Minot, "Purcell Enhancement of Spontaneous Emission from Quantum Cascades inside Mirror-Grating Metal Cavities at THz Frequencies," *Phys. Rev. Lett.*, vol. 99, p. 223603, Nov. 2007.

[85] D. Dini, R. Köhler, A. Tredicucci, G. Biasiol, and L. Sorba, "Microcavity Polariton Splitting of Intersubband Transitions," *Phys. Rev. Lett.*, vol. 90, p. 116401, Mar. 2003.

[86] Haus, Hermann A, *Waves And Fields in Optoelectronics*. Prentice-Hall, 1984.

[87] S. Fan, W. Suh, and J. D. Joannopoulos, "Temporal coupled-mode theory for the Fano resonance in optical resonators," *J. Opt. Soc. Am. A*, vol. 20, p. 569, Mar. 2003.

[88] S. Zanotto, F. P. Mezzapesa, F. Bianco, G. Biasiol, L. Baldacci, M. S. Vitiello, L. Sorba, R. Colombelli, and A. Tredicucci, "Perfect energy-feeding into strongly coupled systems and interferometric control of polariton absorption," *Nature Phys*, vol. 10, pp. 830–834, Nov. 2014.

[89] M. Jeannin, G. Mariotti Nesurini, S. Suffit, D. Gacemi, A. Vasanelli, L. Li, A. G. Davies, E. Linfield, C. Sirtori, and Y. Todorov, "Ultrastrong Light–Matter Coupling in Deeply Subwavelength THz LC Resonators," *ACS Photonics*, vol. 6, pp. 1207–1215, May 2019.

[90] C. Feuillet-Palma, Y. Todorov, A. Vasanelli, and C. Sirtori, "Strong near field enhancement in THz nano-antenna arrays," *Scientific Reports*, vol. 3, p. 1361, Mar. 2013.

[91] Balanis, A. Constantin, *Antenna Theory. Analysis and Design.* John Wiley and Sons, Inc., second ed., 1992.

[92] R. H. Dicke, "Coherence in Spontaneous Radiation Processes," *Phys. Rev.*, vol. 93, pp. 99–110, Jan. 1954.

[93] J. Keller, J. Haase, F. Appugliese, S. Rajabali, Z. Wang, G. L. Paravicini-Bagliani, C. Maissen, G. Scalari, and J. Faist, "Superradiantly Limited Linewidth in Complementary THz Metamaterials on Si-Membranes," *Advanced Optical Materials*, vol. 6, p. 1800210, Aug. 2018.

[94] A. Delga, L. Doyennette, V. Berger, M. Carras, V. Trinité, and A. Nedelcu, "Performances of quantum cascade detectors," *Infrared Physics & Technology*, vol. 59, pp. 100–107, July 2013.

[95] P.-B. Vigneron, S. Pirotta, I. Carusotto, N.-L. Tran, G. Biasiol, J.-M. Manceau, A. Bousseksou, and R. Colombelli, "Quantum well infrared photo-detectors operating in the strong light-matter coupling regime," *Appl. Phys. Lett.*, vol. 114, p. 131104, Apr. 2019.

[96] R. Sarma, D. de Ceglia, N. Nookala, M. A. Vincenti, S. Campione, O. Wolf, M. Scalora, M. B. Sinclair, M. A. Belkin, and I. Brener, "Broadband and Efficient Second-Harmonic Generation from a Hybrid Dielectric Metasurface/Semiconductor Quantum-Well Structure," *ACS Photonics*, vol. 6, pp. 1458–1465, June 2019.

[97] H. A. Haus, *Electromagnetic Noise and Quantum Optical Measurements.* Springer Science & Business Media, Sept. 2000.

[98] J. Faist, *Quantum Cascade Lasers.* Oxford University Press.

[99] M. Ershov, H. C. Liu, M. Buchanan, Z. R. Wasilewski, and V. Ryzhii, "Photoconductivity nonlinearity at high excitation power in quantum well infrared photodetectors," *Appl. Phys. Lett.*, vol. 70, pp. 414–416, Jan. 1997.

[100] C. Mermelstein, H. Schneider, A. Sa'ar, C. Schönbein, M. Walther, and G. Bihlmann, "Low-power photocurrent nonlinearity in quantum well infrared detectors," *Appl. Phys. Lett.*, vol. 71, pp. 2011–2013, Oct. 1997.

[101] D. Palaferri, Y. Todorov, D. Gacemi, S. Barbieri, L. H. Li, A. G. Davies, E. H. Linfield, and C. Sirtori, "Noise characterization of patch antenna THz photodetectors," *Appl. Phys. Lett.*, vol. 113, p. 161105, Oct. 2018.

[102] A. E. Siegman, "The Antenna Properties of Optical Heterodyne Receivers," *Appl. Opt., AO*, vol. 5, pp. 1588–1594, Oct. 1966.

[103] M. S. Taubman, "Low-noise high-performance current controllers for quantum cascade lasers," *Review of Scientific Instruments*, vol. 82, p. 064704, June 2011.

[104] D. Weidmann, K. Smith, and B. Ellison, "Experimental investigation of high-frequency noise and optical feedback effects using a 9.7 µm continuous-wave distributed-feedback quantum-cascade laser," *Appl. Opt., AO*, vol. 46, pp. 947–953, Feb. 2007.

[105] L. Jumpertz, M. Carras, K. Schires, and F. Grillot, "Regimes of external optical feedback in 5.6 µm distributed feedback mid-infrared quantum cascade lasers," *Appl. Phys. Lett.*, vol. 105, p. 131112, Sept. 2014.

[106] S. Schilt, L. Tombez, G. Di Domenico, and D. Hofstetter, "Frequency Noise and Linewidth of Mid-infrared Continuous-Wave Quantum Cascade Lasers: An Overview," *The Wonders of Nanotechnology: Quantum and Optoelectronic Devices and Applications (chapter 12)*, pp. 261–287, 2013.

[107] S. Bartalini, S. Borri, P. Cancio, A. Castrillo, I. Galli, G. Giusfredi, D. Mazzotti, L. Gianfrani, and P. De Natale, "Observing the Intrinsic Linewidth of a Quantum-Cascade Laser: Beyond the Schawlow-Townes Limit," *Phys. Rev. Lett.*, vol. 104, p. 083904, Feb. 2010.

[108] B. Argence, B. Chanteau, O. Lopez, D. Nicolodi, M. Abgrall, C. Chardonnet, C. Daussy, B. Darquié, Y. Le Coq, and A. Amy-Klein, "Quantum cascade laser frequency stabilization at the sub-Hz level," *Nature Photon*, vol. 9, pp. 456–460, July 2015.

[109] B. Zhao, X. Wang, and C. Wang, "Strong Optical Feedback Stabilized Quantum Cascade Laser," *ACS Photonics*, vol. 7, pp. 1255–1261, May 2020.

[110] X. Pan, B. Tromborg, and H. Olesen, "Linewidth rebroadening in DFB lasers due to weak side modes," *IEEE Photonics Technology Letters*, vol. 3, pp. 112–114, Feb. 1991.

[111] P. Reininger, T. Zederbauer, B. Schwarz, H. Detz, D. MacFarland, A. M. Andrews, W. Schrenk, and G. Strasser, "InAs/AlAsSb based quantum cascade detector," *Appl. Phys. Lett.*, vol. 107, p. 081107, Aug. 2015.

[112] Y. Song, R. Bhat, T.-Y. Huang, P. Badami, C.-E. Zah, and C. Gmachl, "III-nitride quantum cascade detector grown by metal organic chemical vapor deposition," *Appl. Phys. Lett.*, vol. 105, p. 182104, Nov. 2014.

[113] A. P. Ravikumar, T. A. Garcia, J. D. Jesus, M. C. Tamargo, and C. F. Gmachl, "High detectivity short-wavelength II-VI quantum cascade detector," *Appl. Phys. Lett.*, vol. 105, p. 061113, Aug. 2014.

[114] H. Nguyen-Van, A. N. Baranov, Z. Loghmari, L. Cerutti, J.-B. Rodriguez, J. Tournet, G. Narcy, G. Boissier, G. Patriarche, M. Bahriz, E. Tournié, and R. Teissier, "Quantum cascade lasers grown on silicon," *Scientific Reports*, vol. 8, p. 7206, May 2018.

Acknowledgements

I would like to thank my referees, Harald Schneider and Jaime Gómez Rivas, for accepting the task of reviewing the manuscript and for accurately reading it. I am grateful to the examiners, Agnès Dolfi-Bouteyre and Jean-Philippe Berger for the interest they have shown in my work and for the time they have devoted to it. I thank Giuseppe Leo for vibrantly presiding my jury. I would like to thank all the jury for the precious feedback I received and for the inspiring scientific discussions that made the defence day unforgettable for me.

I would like to thank my supervisor Carlo. I have learnt a lot from his broad and deep knowledge of device physics and from his wisdom in data analysis and experiments. I am grateful for the time he spent writing with me the articles and for carefully and promptly correcting the manuscript and the presentation. Carlo was a demanding supervisor, who drove me to be aware of the marvellous freedom of the intellectual autonomy.

I am thankful to Angela. With her profound scientific competence, she supported my thesis from the doctoral school application until the defence day. I am grateful to her for her last rigorous correction of this manuscript.
I acknowledge the group of Edmund Linfield (University of Leeds) for the excellent growth of the samples. The processing was performed in the clean room of Laboratoire Matériaux et Phénomènes Quantiques. I am grateful to Stephan Suffit, Christophe Manquest and Pascal Filloux for the support and for the ideal working environment.
I thank Jérôme Faist and his group (ETH, Zurich), for providing the two DFB lasers for the first heterodyne experiment, for the scientific discussions and for hosting me in Zurich: I was amazed by their laboratory.
I thank Benoît Darquié and Olivier Lopez (Laboratoire de Physique des Lasers) for providing the electronics for the laser frequency stabilisation.
I am grateful to Wang Qijie (NTU Singapore) for hosting me and showing me his laboratory in Singapore.
I would like to thank Jean-Philippe Berger and Guillaume Bourdarot (Université de Grenoble) for the very interesting visions about infrared heterodyne detection I learned from them, their competence and curiosity and for supporting me for my future.
I thank Djamal and Grégoire in the QUAD group: I learnt a lot from their expertise in optics and signal analysis.

I am very grateful to the students who collaborated with me: Pierre and Raphael for their enthusiasm; Giovanni, for his help in lab and for helping me understanding many things with his strong interest for theoretical investigations; Juliette for her help in measurements and her remarkable skills for experiences; Minoosh for sharing with me the unlucky confinement months. I would like to thank Daniela Cavalcoli (University of Bologna). Daniela introduced me to the Physics of Semiconductor and supported my desire of studying abroad during my master. I thank her for the

chance of supervising and participating to the excellent master-thesis of Giovanni in Bologna.

I would like to thank all the past and current research mates of the QUAD team: in particular Mathieu for his remarkable ability and motivation in clean room, python, experiments; Allegra for her deep knowledge of physics and her sense of humour; Étienne for guiding me in Singapore, for his skills and optimism; Alireza and Giulia for their very elegant way of doing experiments and their kindness; Baptiste D. and Baptiste C., for the interesting scientific discussions. Thanks to Thomas and Hamza, in particular for the very last heterodyne experiment the week before the defence. Further thanks to, in random order: Daniele, Yanko, Andy, Sébastien, Zahra, Benjamin, Pierre and Jean Charles from Lytid. I wish to the first year PhDs Mohammadreza, Tung, Mohsen a successful and joyful experience.

During these three years, in the darkest moments, I had the chance to be supported by people who have always believed in me as a physicist. I thank François, Simon, Jean and Fabrizio for reading parts of the manuscript and giving me an important feedback. I am grateful to Fabrizio, for the illuminating discussions we have about tutto. Even from Japan, his wholehearted presence was precious, replacing every time my anger with laughters. I thank François and Nicole for always being so supportive to me and to my work, I felt at home. I am grateful to Simon, for introducing me to the methods of computational physics and for inspiring me with his outstanding analytical vision and with his strong sense of ethics in research. I thank Patrick Nayman for introducing me to the issue of electromagnetic noise in experiments, in an admirable clear way.
I thank my dearest and intimate friends in Paris: Hamid, Samantha, Carlo, Jasmine, Yara, Jean, Charlie, Allegra, Felix, Laura, Ilaria. Merci à Marième, Thomas, Lucas, Francette et le reste de la famille. Merci à Esther. Grazie a Laura, Savino, Andrea, Davide, Stefania. Grazie a Ambra. Eux tous, chacun avec son bagage, ont été tellement importants pour ce travail.

Grazie a Simon, per ridarmi speranza.
Grazie Rosa.
Grazie a Uliana e a Stefano, al loro bene senza fine.